

PLANT BASED SYNTHESIS AND CHARACTERISATION
OF IRON- AND SILVER-DOPED ZINC OXIDE
NANOPARTICLES FOR SONOCATALYTIC
DEGRADATION OF MALACHITE GREEN

CHAN YIN YIN

DOCTOR OF PHILOSOPHY (ENGINEERING)

LEE KONG CHIAN
FACULTY OF ENGINEERING AND SCIENCE
UNIVERSITI TUNKU ABDUL RAHMAN
JUNE 2023

**PLANT BASED SYNTHESIS AND CHARACTERISATION OF IRON-
AND SILVER-DOPED ZINC OXIDE NANOPARTICLES FOR
SONOCATALYTIC DEGRADATION OF MALACHITE GREEN**

By

CHAN YIN YIN

A thesis submitted to the Department of Chemical Engineering,
Lee Kong Chian Faculty of Engineering and Science,
Universiti Tunku Abdul Rahman,
in partial fulfillment of the requirements for the degree of
Doctor of Philosophy in Engineering
June 2023

ABSTRACT

PLANT BASED SYNTHESIS AND CHARACTERISATION OF IRON- AND SILVER-DOPED ZINC OXIDE NANOPARTICLES FOR SONOCATALYTIC DEGRADATION OF MALACHITE GREEN

Chan Yin Yin

The discharge of dye-containing wastewater such as MG from industry into environment is a hot topic among society nowadays due to the high persistent and carcinogenic effect of dye molecules. Besides, high consumption of chemical in the synthesis of nanomaterial is one of the main concerns in the research field. In this study, sonocatalysis was proposed to degrade the organic dyes using metal doped zinc oxide (ZnO) nanoparticles which were obtained via green synthesis process. Characterization of plant extract and the green synthesized ZnO samples were carried out to determine the plausible mechanism of green synthesis and their effects towards the sonocatalytic performance, respectively. The results confirmed that high phytochemical content was present in plant extract and involved in the green synthesis of ZnO nanoparticles. Metal doping successfully lowered down the band gap energy, reduced particle size as well as increased the surface area of the green synthesized ZnO nanoparticles. In this work, 5 wt% silver-doped ZnO (Ag-ZnO) with the highest sonocatalytic activity was selected to evaluate sonocatalytic dye degradation through parameter study. By the means of response surface methodology (RSM), a central composite design (CCD) model was successfully constructed to predict the sonocatalytic degradation efficiency

and the optimum degradation efficiency of MG was found to be 89.21% within 15 mins using Ag-ZnO with 0.75 g/L of catalyst loading under 500 mg/L of initial dye concentration, 40 W of ultrasonic power and 1.75 mM of oxidant concentration. The reusability test also confirmed that the green synthesized samples exhibited excellent stabilities which could retain the degradation efficiency of MG up to 76.6% even after 5 cycles of sonochemical reaction. The kinetic study showed that the sonocatalytic degradation of MG was fitted well into second-order kinetic model with high R^2 value (0.953). Furthermore, thermodynamic study confirmed the feasibility and efficiency of sonocatalysis reaction in the degradation of MG with low value of activation energy (+ 24.43 kJ/mol) by using the green synthesized Ag-ZnO. This research marked the great breakthrough of wastewater treatment by using the green nanomaterials as a sonocatalyst.

ACKNOWLEDGEMENT

Firstly, I would like to mention that this project would not be achieved successfully without the participation of all the parties. I would like to express my deep sense of gratitude to my supervisor, Dr Pang Yean Ling and co-supervisor Dr Steven Lim. Throughout my postgraduate study, they provided an infinite number of valuable advice, suggestion and comments to develop and improve my research and report writing.

Besides, many thanks to Universiti Tunku Abdul Rahman (UTAR) for providing the financial assistance in this project as well as a suitable environment to conduct my research. I would like to acknowledge all the officers from Department of Laboratory Management and Safety Administrative who provided technical assistance during my research.

Last but not least, I am thankful to have all the moral support and encouragement words from my family and friends during my up and down. I would like to extend my sincere regards to all the parties who helped me in many different ways during this project.

LEE KONG CHIAN FACULTY OF ENGINEERING AND SCIENCE
UNIVERSITI TUNKU ABDUL RAHMAN

Date: 21 June 2023

SUBMISSION OF FINAL YEAR PROJECT /DISSERTATION/THESIS

It is hereby certified that CHAN YIN YIN (ID No: 18UED06819) has completed this final year project/ dissertation/ thesis* entitled “ PLANT BASED SYNTHESIS AND CHARACTERISATION OF IRON- AND SILVER-DOPED ZINC OXIDE NANOPARTICLES FOR SONOCATALYTIC DEGRADATION OF MALACHITE GREEN ” under the supervision of DR PANG YEAN LING (Supervisor) from the Department of CHEMICAL ENGINEERING, Lee Kong Chian Faculty of ENGINEERING AND SCIENCE, and DR STEVEN LIM (Co-Supervisor)* from the Department of CHEMICAL ENGINEERING, Lee Kong Chian Faculty of ENGINEERING AND SCIENCE.

I understand that University will upload softcopy of my final year project / dissertation/ thesis* in pdf format into UTAR Institutional Repository, which may be made accessible to UTAR community and public.

Yours truly,



(Chan Yin Yin)

DECLARATION

I hereby declare that the dissertation is based on my original work except for quotations and citations which have been duly acknowledged. I also declare that it has not been previously or concurrently submitted for any other degree at UTAR or other institutions.

Name CHAN YIN YIN

Date 21 JUNE 2022

TABLE OF CONTENTS

	Page
ABSTRACT	iii
ACKNOWLEDGEMENT	v
APPROVAL SHEET	vi
DECLARATION	viii
TABLE OF CONTENTS	ix
LIST OF TABLES	xiii
LIST OF FIGURES	xv
LIST OF ABBREVIATIONS	xx

CHAPTER

1.0	INTRODUCTION	1
1.1	Water Pollution	1
1.2	Dye Production and its Environmental Impacts	2
1.3	Classification of Textile Manufacturing Processes	4
1.4	Problem Statement	5
1.5	Research Objectives	8
1.6	Scope of Study	9
2.0	LITERATURE REVIEW	11
2.1	Classification of Organic Dyes	11
2.2	Dye Removal Method	13
	2.2.1 Physical Method	13
	2.2.2 Biological Method	16
	2.2.3 Chemical Method	18
2.3	Principle of Sonocatalysis	20
2.4	Properties of ZnO Nanoparticles	23
2.5	The Common Synthesis Approaches of ZnO Nanoparticles	28
	2.5.1 Pyrometallurgy	33
	2.5.2 Hydrometallurgy	34
	2.5.3 Co-precipitation	35
	2.5.4 Sol-gel	39

2.5.5	Hydrothermal	44
2.5.6	Mechanochemical	48
2.5.7	Thermal Decomposition	53
2.6	Emerging Green Synthesis Approach of ZnO Nanoparticles	58
2.6.1	Green Synthesis of ZnO nanoparticles using Plant Extract	59
2.6.2	Green Synthesis of ZnO Nanoparticles using Bacteria	66
2.6.3	Green Synthesis of ZnO Nanoparticles using Algae	71
2.6.4	Green Synthesis of ZnO Nanoparticles using Fungus	78
2.7	Proposed Mechanism of Green Synthesis	79
2.8	Modification of Green Synthesized ZnO Nanoparticles	81
2.8.1	Metal Doping	81
2.8.2	Polymer Coating	90
2.8.3	Others	92
3.0	METHODOLOGY	94
3.1	Chemicals and Materials	95
3.2	Instruments and Equipment	100
3.3	Synthesis of ZnO Nanoparticles	105
3.3.1	Preparation of Plant Extract	105
3.3.2	Green Synthesis of Pure and Metal Doped ZnO Nanoparticles	105
3.4	Characterization of Plant Extract	106
3.5	Characterization of ZnO Nanoparticles	108
3.5.1	X-ray Diffraction (XRD)	108
3.5.2	Field Emission Scanning Electron Spectroscopy (FESEM), Transmission Electron Spectroscopy (TEM) and Energy Dispersive X-ray Spectroscopy (EDX)	110
3.5.3	Surface Analysis	110
3.5.4	FTIR	111
3.5.5	Zeta Potential	111
3.5.6	Thermogravimetric Analysis (TGA)	112
3.5.7	UV-Vis Diffuse Reflectance Spectroscopy (UV-Vis DRS)	112
3.5.8	Photoluminescence Spectroscopy (PL)	113
3.5.9	Raman Analysis	114
3.5.10	X-ray Photoemission Spectroscopy (XPS)	114
3.5.11	Antibacterial Activity	114

3.6	Evaluation of Sonocatalytic Performance of ZnO Nanoparticles	115
3.7	RSM Modelling and Optimization	118
3.8	Reusability Test of Ag-ZnO Nanoparticles	121
3.9	Mechanism Study of Sonocatalytic Degradation of MG	121
3.10	Kinetic Study	122
3.11	Thermodynamic Study	123
4.0	RESULTS AND DISCUSSION	126
4.1	Characterization of ZnO	126
4.1.1	XRD	126
4.1.2	FESEM, TEM and EDX	130
4.1.3	Surface Analysis	136
4.1.4	FTIR	139
4.1.5	Zeta Potential	141
4.1.6	TGA	143
4.1.7	UV-Vis DRS	145
4.1.8	Photoluminescence Analysis	146
4.1.9	Raman Analysis	148
4.1.10	XPS	151
4.1.11	Antibacterial Activity	153
4.2	Characterization of Plant Extracts	159
4.2.1	UV-Vis Spectroscopy	159
4.2.2	TPC and TFC analysis	160
4.2.3	FTIR	162
4.2.4	GC-MS	164
4.2.5	Possible Mechanism of Green Synthesis of ZnO	168
4.3	Evaluation of Sonocatalytic Performance of ZnO	169
4.3.1	Type of Plant	169
4.3.2	Synthesis Temperature of ZnO	171
4.3.3	Synthesis Duration of ZnO	173
4.3.4	Type of Catalyst	174
4.3.5	Initial Dye Concentration	179
4.3.6	Catalyst Loading	180
4.3.7	Ultrasonic Power	182
4.3.8	Ultrasonic Frequency	184
4.3.9	Type of Anion	186

4.3.10	Solution pH	189
4.3.11	Oxidant Concentration	191
4.3.12	Type of Organic Dyes	192
4.4	RSM Modelling and Optimization of Sonocatalytic MG Degradation Efficiency	196
4.4.1	Effect of Experimental Variables on the Degradation Efficiency	202
4.4.2	Model Validation and Optimization	209
4.5	Reusability Test	218
4.6	Mechanism Studies of Sonocatalysis	226
4.7	Kinetic and Thermodynamic Studies	234
4.7.1	Reaction Kinetic Study	234
4.7.2	Thermodynamic Study	237
5.0	CONCLUSIONS AND FUTURE PERSPECTIVES	243
5.1	Conclusions	243
5.2	Future Perspectives	245
	REFERENCES	247
	LIST OF PUBLICATIONS	296

LIST OF TABLES

Table		Page
2.1	Advantages and Drawbacks of the Techniques Applied for Synthesis of ZnO Nanoparticles.	29
2.2	Synthesis of ZnO Nanoparticles by the Means of Co-precipitation.	37
2.3	Synthesis of ZnO Nanoparticles through Sol-gel Method.	41
2.4	Synthesis of ZnO Nanoparticles using Hydrothermal Method.	45
2.5	Synthesis of ZnO Nanoparticles through Mechanochemical Method.	50
2.6	Synthesis of ZnO Nanoparticles by the Means of Thermal Decomposition.	54
2.7	Green Synthesis of ZnO Nanoparticles using Plant Extract.	61
2.8	Green Synthesis of ZnO Nanoparticles using Bacteria.	68
2.9	Algae and Fungus Mediated ZnO Nanoparticles.	73
2.1	Doping of Green Synthesized ZnO Nanoparticles.	82
3.1	List of Chemicals and Materials.	97
3.2	List of Instruments and Equipment Applied throughout the Research.	101
3.3	Experimental Factors with Their Unit, Code and Level.	119
3.4	Kinetic Models Adopted to Evaluate Sonocatalytic Degradation of MG.	122
4.1	XRD Parameter Values of ZnO Samples.	129
4.2	EDX Results of ZnO Samples.	135

4.3	BET Surface Area and Pore Volume of ZnO Samples.	138
4.4	TPC and TFC of Plant Extract.	161
4.5	Identification of Biomolecules Present in Clitoria ternatea Linn extract through GC-MS.	166
4.6	Molecular Weight and Molecular Structure of Organic Dyes.	194
4.7	ANOVA Results for Sonocatalytic Degradation Efficiency of MG Dye.	197
4.8	ANOVA Results for Sonocatalytic Degradation Efficiency of MG Dye after Backward Elimination.	198
4.9	Designed Matrix of CCD Together with the Predicted and Experimental Results.	200
4.1	Comparative Results of Experimental and Predicted Values for Model Validation.	210
4.11	Comparative Data on the Removal of MG.	216
4.12	Elemental Composition of Fresh and Reused Ag-ZnO.	225
4.13	Kinetic Modelling for Sonocatalytic Degradation of MG.	235
4.14	Thermodynamic parameters for the sonocatalytic degradation of MG.	239

LIST OF FIGURES

Figure	Page
1.1 Trend of River Water Quality in Malaysia from 2011 to 2020 (Department of Environment Malaysia, 2021).	2
1.2 Distribution of Water Usage in Each Step of Textile Processing (Panda, Sen and Mukhopadhyay, 2021; Ismail and Sakai, 2022).	4
2.1 Number of Research Paper Related to Sonocatalysis Published in ScienceDirect from 2013 to 2022.	20
2.2 Acoustic Cavitation Phenomenon under Ultrasound Irradiation (Vyas et al., 2019).	22
2.3 Crystal Structure Models of ZnO: (a) Zinc Blende, (b) Wurtzite and (c) Rocksalt (Özgür, Avrutin and Morkoç, 2018).	24
2.4 Morphologies of ZnO: (a) Nanocombs, (b) Nanobelts (Zhang and Bai, 2011), (c) Nanoflowers (Nagar et al., 2020) and (d) Nanorings (Alenezi, 2018).	27
2.5 Preparation Steps of Biological Extract for the Green Synthesis of ZnO Nanoparticles.	59
3.1 Flowchart for Research Overview.	95
3.2 Schematic Diagram of Sonocatalytic Reaction.	116
4.1 XRD Patterns of Com-ZnO, Che-ZnO, Bio-ZnO, Ag-ZnO and Fe-ZnO.	127
4.2 FESEM Images of (a) Com-ZnO, (b) Che-ZnO, (c) Bio-ZnO, (d) Ag-ZnO and (e) Fe-ZnO Captured at Magnification x50 000 and (f) TEM Image of Ag-ZnO Obtained at Magnification x43 000.	132
4.3 Nitrogen Adsorption-desorption Isotherms of (a) Com-ZnO, (b) Che-ZnO, (c) Bio-ZnO, (d) Ag-ZnO and (e) Fe-ZnO, and (f) BJH Pore Distribution Plots of ZnO Samples.	137
4.4 FTIR Spectra of Com-ZnO, Che-ZnO, Bio-ZnO, Ag-ZnO and Fe-ZnO.	140

4.5	Zeta Potential of ZnO Samples.	142
4.6	TGA Plots of ZnO Nanoparticles.	144
4.7	Tauc Plots of ZnO Nanoparticles.	146
4.8	Photoluminescence Spectra of (a) Com-ZnO, (b) Bio-ZnO and (c) Ag-ZnO.	147
4.9	Raman Spectra of Com-ZnO and Ag-ZnO.	150
4.1	High Resolution Elemental Spectra of (a) Zn 2p, (b) O1s and (c) Ag 3d in Ag-ZnO.	153
4.11	Antibacterial Activities over (a) Control, (b) Com-ZnO, (c) Che-ZnO, (d) Bio-ZnO, (e) Ag-ZnO and (f) Fe-ZnO towards <i>E. coli</i> .	155
4.12	Study of Antibacterial Activity over (a) Control and (b) Ag-ZnO against <i>E. Coli</i> under SEM.	156
4.13	Plausible Mechanism of Antibacterial Activity in the Presence of ZnO Nanoparticles on the Bacterial Cell Membrane.	157
4.14	UV-Vis Spectra of (i) <i>Clitoria ternatea</i> Linn Extract and (ii) Ag-ZnO Nanoparticles.	160
4.15	FTIR Spectra of (i) <i>Clitoria ternatea</i> Linn Extract, (ii) Uncalcined Ag-ZnO and (iii) Calcined Ag-ZnO nanoparticles.	164
4.16	GC-MS Spectrum of <i>Clitoria ternatea</i> Linn extract.	165
4.17	Plausible Mechanism of Green Synthesis to Obtain ZnO Nanoparticles.	169
4.18	Effect of Various Plant Extract on the Sonocatalytic Performance of ZnO Nanoparticles in the Degradation of MG (Catalyst Loading: 0.5 g/L; Initial Dye Concentration: 500 mg/L; Ultrasonic Power: 40 W; Solution pH: 3; Irradiation Time: 60 mins).	171
4.19	Effect of Synthesis Temperature on the Sonocatalytic Performance of ZnO Nanoparticles in the Degradation of MG (Catalyst Loading: 0.5 g/L; Initial Dye Concentration:	172

	500 mg/L; Ultrasonic Power: 40 W; Solution pH: 3; Irradiation Time: 60 mins).	
4.2	Effect of Synthesis Duration on the Sonocatalytic Performance of ZnO Nanoparticles in the Degradation of MG (Catalyst Loading: 0.5 g/L; Initial Dye Concentration: 500 mg/L; Ultrasonic Power: 40 W; Solution pH: 3; Irradiation Time: 60 mins).	174
4.21	Sonocatalytic Degradation of MG using Different Catalyst (Catalyst Loading: 0.5 g/L; Initial Dye Concentration: 500 mg/L; Ultrasonic Power: 40 W; Irradiation Time: 60 mins).	175
4.22	Effect of Initial Dye Concentration on the Sonocatalytic Degradation of MG (Catalyst Loading: 0.5 g/L; Ultrasonic Power: 40 W; Solution pH: 3; Irradiation Time: 30 mins).	180
4.23	Effect of Catalyst Loading on the Sonocatalytic Degradation of MG (Initial Dye Concentration: 500 mg/L; Ultrasonic Power: 40 W; Solution pH: 3; Irradiation Time: 30 mins).	181
4.24	Effect of Ultrasonic Power on the Sonocatalytic Degradation of MG (Catalyst Dosage: 1.0 g/L; Initial Dye Concentration: 500 mg/L; Solution pH: 3; Irradiation Time: 30 mins).	183
4.25	Effect of Ultrasonic Frequency on the Sonocatalytic Degradation of MG (Catalyst Loading: 1.0 g/L; Initial Dye Concentration: 500 mg/L; Ultrasonic Power: 80 W; Solution pH: 3; Irradiation Time: 30 mins).	185
4.26	Effect of Anions on the Degradation Efficiency of MG (Catalyst Loading: 1.0 g/L; Initial Dye Concentration: 500 mg/L; Ultrasonic Power: 80 W; Solution pH: 3; Irradiation Time: 30 mins).	186
4.27	Effect of Solution pH on the Sonocatalytic Degradation of MG (Catalyst Loading: 1.0 g/L; Initial Dye Concentration: 500 mg/L; Ultrasonic Power: 80 W; Irradiation Time: 30 mins).	190
4.28	Effect of Sodium Persulfate Concentration in the Sonocatalytic Degradation of MG (Catalyst Loading: 1.0 g/L; Initial Dye Concentration: 500 mg/L; Ultrasonic Power: 80 W; Solution pH: 3; Irradiation Time: 30 mins).	192

4.29	The Sonocatalytic Activity of Ag-ZnO in the Presence of Different Organic Dyes (Catalyst Loading: 1.0 g/L; Initial Dye Concentration: 500 mg/L; Ultrasonic Power: 80 W; Sodium Persulfate Concentration: 2.0 mM; Irradiation Time: 60 mins).	193
4.3	The Relationship between Predicted and Experimental Data of Sonocatalytic Degradation Efficiency.	202
4.31	Interactive Effects of (a) Catalyst Loading and Initial Dye Concentration, (b) Catalyst Loading and Ultrasonic Power, (c) Catalyst Loading and Oxidant Concentration, (d) Initial Dye Concentration and Ultrasonic Power, (e) Initial Dye Concentration and Oxidant Concentration and (f) Ultrasonic Power and Oxidant Concentration.	204
4.32	Absorption Spectra of MG in the Sonocatalytic Degradation of MG under the Optimized Condition (Initial Dye Concentration: 500 mg/L, Catalyst Loading: 0.75 g/L, Concentration of Oxidant: 1.75 mM, Ultrasonic Power: 40 W).	212
4.33	COD and TOC Removal Efficiencies in the Sonocatalytic Degradation of MG under Optimum Condition (Initial Dye Concentration: 500 mg/L, Catalyst Loading: 0.75 g/L, Concentration of Oxidant: 1.75 mM, Ultrasonic Power: 40 W).	213
4.34	Reusability Study of Ag-ZnO in the Sonocatalytic Degradation of MG under Optimum Condition (Initial Dye Concentration: 500 mg/L, Catalyst Loading: 0.75 g/L, Concentration of Oxidant: 1.75 mM, Ultrasonic Power: 40 W).	219
4.35	XRD Spectra of Fresh and Recycled Ag-ZnO.	220
4.36	FTIR Spectra of (a) MG Molecules, (b) Fresh Ag-ZnO, (c) Recycled Ag-ZnO after 1st Cycle, (d) 5th Cycle and (e) 10th Cycle of Sonocatalytic Reaction.	222
4.37	TGA Curves of Fresh Ag-ZnO and Recycled Ag-ZnO Samples.	224
4.38	Pore Distribution for the Fresh and Reused Ag-ZnO.	226
4.39	Effect of Chemical Scavengers on the Sonocatalytic Degradation of MG Dye in the Presence of Ag-ZnO as Catalyst and Sodium Persulfate as Oxidant.	227

4.4	Absorption Spectra of Bio-ZnO and Ag-ZnO.	233
4.41	(a) Zero order, (b) First Order, (c) Second Order and (d) Third Order Kinetic Models for the Sonocatalytic Degradation of MG.	235
4.42	Sonocatalytic Degradation of MG under Optimum Condition (Initial Dye Concentration: 500 mg/L, Catalyst Loading: 0.75 g/L, Concentration of Oxidant: 1.75 mM, Ultrasonic Power: 40 W).	237
4.43	(a) Van't Hoff Plot of Sonocatalytic Degradation of MG and (b) Standard Gibbs Energy at Various Temperature.	238
4.44	Eyring Plot for Sonocatalytic Degradation of MG.	240
4.45	Arrhenius Plot for Sonocatalytic Degradation of MG.	241

LIST OF ABBREVIATIONS

•Cl	Chlorine radicals
•H	Hydrogen radicals
•O ₂ ⁻	Superoxide radicals
•OH	Hydroxyl radicals
ΔG [‡]	Activated Gibbs energy
ΔG [°]	Standard Gibbs energy
ΔH [‡]	Enthalpy of activation
ΔH [°]	Standard enthalpy
ΔS [‡]	Entropy of activation
ΔS [°]	Standard entropy
Ag	Silver
Ag-ZnO	Silver-doped zinc oxide
Al	Aluminium
AMT	2-amino-5-mercapto-1,3,4-thiadiazole
ANOVA	Analysis of variance
AOP	Advanced oxidation process
AOS	average oxidation state
ATR	Attenuated total reflectance
Au	Gold
BJH	Barrett-Joyner-Halenda
BOD	Biological oxygen demand
BQ	Benzoquinone

CB	Conduction Band
CCD	Central composite design
CH ₃ COO ⁻	Acetate anions
Che-ZnO	Chemically synthesized zinc oxide
Cl ⁻	Chloride anions
CO ₃ ^{-•}	Carbonate radicals
CO ₃ ²⁻	Carbonate anions
COD	Chemical oxygen demand
Com-ZnO	Commercial zinc oxide
COS	Carbon oxidation state
CR	Congo red
Cu	Copper
CuO	Copper oxide
DMSO	Dimethyl sulfoxide
DOE	Department of Environment
e ⁻	electron
<i>E_a</i>	Activation energy
EDTA-2Na	Ethylenediaminetetraacetic acid disodium
EDX	Energy dispersive X-ray spectroscopy
FDA	Food and Drug Administration
Fe	Iron
FESEM	Field emission scanning electron spectroscopy
Fe-ZnO	Iron-doped zinc oxide
FTIR	Fourier transform infrared spectroscopy
Ga	Gallium

GC-MS	Gas chromatography-mass spectrometry
h^+	hole
H^+	Hydrogen ions
H_2Q	Hydroquinone
HCO_3^-	Bicarbonate anions
IBA	Isobutanol
ICP-OES	Inductively coupled plasma-optical emission spectroscopy
La	Lanthanum
LED	Light-emitting diodes
LO	Longitudinal optical
LOF	Lack of fit
MB	Methylene blue
MetOH	Methanol
MG	Malachite Green
Mg	Magnesium
Mn	Manganese
MnO_3	Manganese oxide
MO	Methyl orange
Mo_3O	Molybdenum oxide
MOF	Metal organic framework
NaCl	Sodium chloride
NaI-PPy	Sodium iodide-polypyrrole
NaOH	Sodium hydroxide
Ni	Nickel
OH^-	Hydroxyl ions

PDA	Polydopamine
pH _{zpc}	Zero point charge
PL	Photoluminescence spectroscopy
R^2	Regression coefficient
RB	Rhodamine B
rGO	Reduced graphene oxide
ROS	Reactive oxygen species
RSM	Response surface methodology
S ₂ O ₈ ²⁻	Persulfate ions
Sm	Samarium
SMA	Styrene maleic anhydride
SO ₄ ^{-•}	Sulfate radicals
SPR	Surface plasmon resonance
TEM	Transmission electron spectroscopy
TFC	Total flavonoid content
TGA	Thermogravimetric analysis
TO	Transverse optical
TOC	Total organic carbon
TPC	Total phenolic content
TTDMM	Trimesoyl 1,3,5-trimethyl malonate ester
UV	Ultraviolet
UV-Vis DRS	UV-Vis diffuse reflectance spectroscopy
VB	Valence Band
WHO	World Health Organization
XPS	X-ray photoemission spectroscopy

XRD	X-ray diffraction
Zn	Zinc
ZnAc	Zinc acetate
ZnCl	Zinc chloride
ZnNO ₃	Zinc nitrate
ZnO	Zinc oxide
ZnSO ₄	Zinc sulphate

CHAPTER 1

INTRODUCTION

1.1 Water Pollution

In this new era, the increase in the water pollution index is accelerated by the rapid growth of urbanization and industrialization. As reported by the World Health Organization (WHO), it was expected that at least half of the population will be staying in water-stressed region by 2025 due to the water contamination and shortage of clean water supply (World Health Organization, 2019). The discharge of industrial wastewater into the water bodies becomes a hot topic among the society due to the content of chemical waste especially organic dye which exhibits high persistency and stability in the environment and harmful to human being and the ecosystem (Ahmadi et al., 2020b).

According to The Sustainable Development Goal Report 2022, there was only 60% of water bodies complying the standard of good water quality among the 97 reporting countries (United Nations, 2022). United Nations General Assembly urged that it is mandatory to develop and accelerate the progress of global wastewater treatment to achieve the Sustainable Development Goal 6 which was known as “Clean Water and Sanitation”. **Figure 1.1** presents the water river quality trend in Malaysia over the past 10 years. It

is a good sign to observe an increasing trend in the number of rivers with good quality. However, there were about 34 out of 672 rivers found to be highly polluted in Malaysia while 29% of the rivers were slightly polluted. The polluted water sources may create potential hazards towards public health and ecosystem. Therefore, the establishment of an efficient wastewater remediation method is necessary to remove targeted water pollutants from the environment.

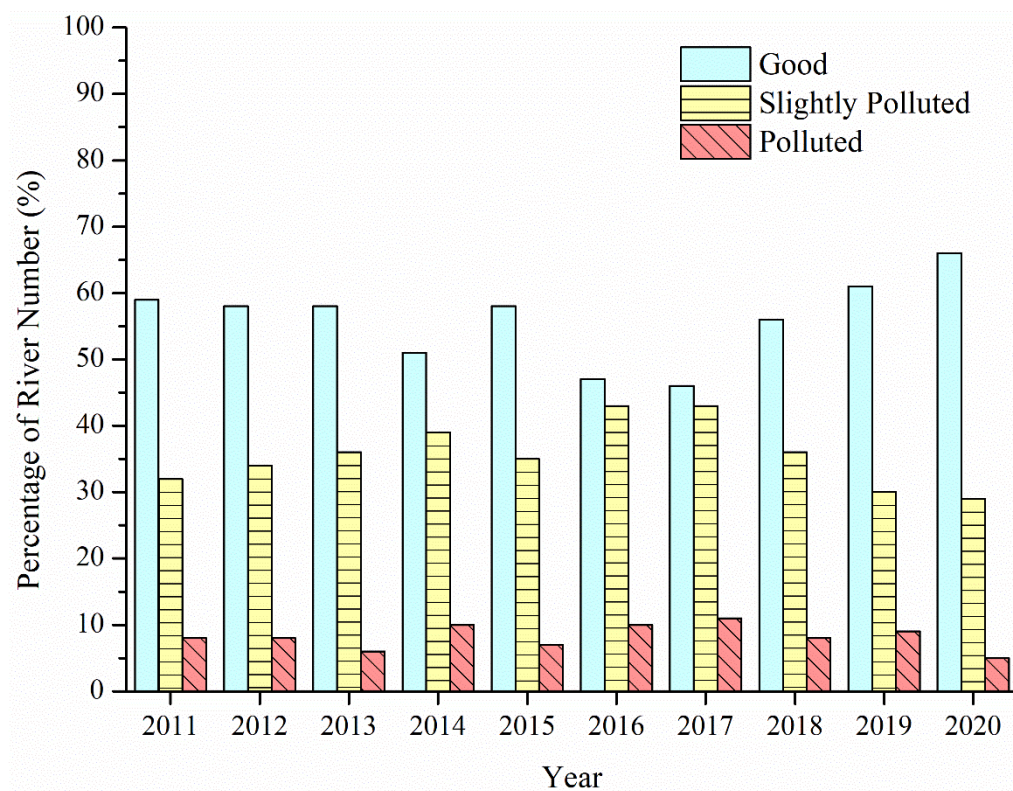


Figure 1.1: Trend of River Water Quality in Malaysia from 2011 to 2020 (Department of Environment Malaysia, 2021).

1.2 Dye Production and its Environmental Impacts

Numerous organic substances such as organic dyes and fertilizers originated from plantations, industry sites and household wastes are discharged into water source due to the rapid growth of population and globalization.

Nowadays, there are about 100,000 types of dye available commercially and around 700,000 tonnes of dye are being produced annually (Moon et al., 2023). The textile industry is the principal consumer of dye substances that can generate up to 100 tonnes of dye-contaminated wastewater into the environment per year (Katheresan, Kansedo and Lau, 2018). Textile market is expected to undergo a 4.4% of annual growth rate from 2021 to 2028 indicating that it is predicted to have higher annual production of textile products (Panda, Sen and Mukhopadhyay, 2021). The usage of organic dyes will definitely increase with the growth of textile market which will eventually cause higher discharge of dye-contaminated water into environment.

The release of dye-contaminated wastewater into environment is a detrimental practice because dye molecules are toxic and carcinogenic. Together with its persistent nature, dye contamination will cause bio-accumulation hazard in the food chain leading to numerous health problems such as allergic, destroy of chromosome and abnormal cell growth (Al-Tohamy et al., 2022). In addition, the presence of dye molecules will downgrade the water quality by increasing chemical oxygen demand (COD) and biological oxygen demand (BOD) values, alternating water pH and showing undesirable coloration (Tanveer et al., 2022). Aquatic organisms are also direct victims of dye contamination. This can be elucidated by the blocking of sunlight by the dye molecules present in water bodies. This will then inhibit the photosynthesis activity of aquatic plant (Khor, Khan and Harunsani, 2022). As a consequence, the food chain of aquatic organism is greatly affected.

1.3 Classification of Textile Manufacturing Processes

Textile industry usually operates under extremely high water consumption in which the distribution of water usage in each operation is illustrated in **Figure 1.2**. According to the chart, dyeing stage consumes the highest amount of water in textile processing followed by scouring, mercerisation, bleaching, printing, desizing and sizing. In textile manufacturing, the average water consumption per kg product is estimated to be 200 L (Behera et al., 2021). High consumption of water reflects large generation of wastewater. The discharge of textile wastewater had created public awareness because the high volume of wastewater may contain enormous amount of potential hazardous pollutants which pose intimidating threat to health and environment.

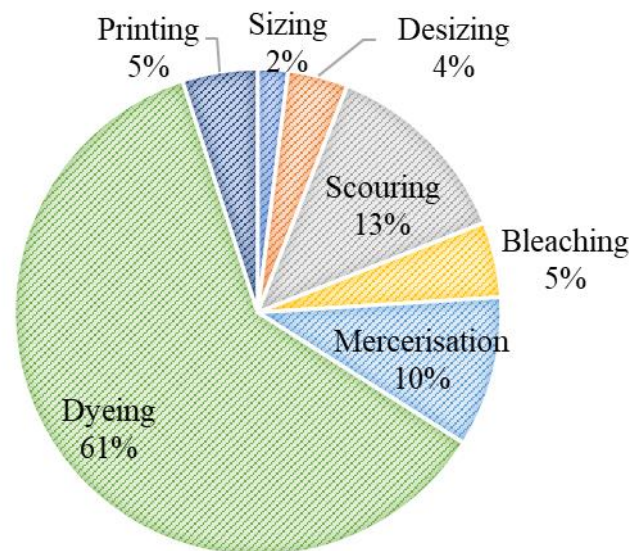


Figure 1.2: Distribution of Water Usage in Each Step of Textile Processing (Panda, Sen and Mukhopadhyay, 2021; Ismail and Sakai, 2022).

Dyeing is the main stage in textile manufacturing which applies coloring materials to colorize the fabrics. In a typical dyeing process, the fabrics are immersed in a dyebath according to the desired color. In addition, chemical auxiliaries such as formaldehyde, phthalates, urea and alkali are applied to inhibit the formation of foam, manipulate pH and ensure even dyeing. Dyeing process is the major contributor of textile wastewater owing to its extremely high water usage which can reach up to 300 L per kg of fabric products. Printing process is performed after completion of fabric dyeing. The purpose of printing is to outline a specific pattern and design on the fabrics by applying dye materials to a definite location. Basically, printing effluent contains similar pollutants as found in dyeing wastewater which is mainly consisted of dyestuffs. According to China Environment Statistical Yearbook in 2016, textile industry in China generated more than 4.5 million tons of dye-containing sludge per year (Artifon et al., 2021). Hence, it is mandatory to remediate dye-containing wastewater prior to discharge into environment.

1.4 Problem Statement

In order to get rid of the organic pollutants from water, several conventional methods are employed such as adsorption, coagulation, and ion exchange. These techniques have some drawbacks that affect their feasibility in large scale operation such as large amount of sludge generated, non-economic favorable and solid waste handling problems (Ayanda et al., 2021). In addition, it is found that organic dyes from wastewater are hard to be removed due to its high resistance to aerobic digestion and recalcitrant in nature (Maučec et al.,

2018). Thus, remediation strategy is absolutely challenging to remove these organic dye compounds from wastewater. Recent studies show that sonocatalysis is a potential advanced oxidation process (AOP) that is able to degrade organic dyes in the presence of catalyst under ultrasonic irradiation (Chang et al., 2019). Zinc oxide (ZnO) nanoparticle is one of the promising semiconductors applied as catalyst owing to its non-toxicity, high catalytic activity with physically and chemically stable behaviors (Madhumitha et al., 2019). The energy transmitted by ultrasound waves will trigger the excitation of electron present on the surface of ZnO nanoparticles which will in turn lead to the formation of electron-hole pairs. The reaction between the charge carriers and water or oxygen molecules causes the generation of free radicals which have high oxidizing power to decompose the organic pollutants.

Over the last decade, the prevailing methods for ZnO nanoparticles synthesis include sol-gel technique, hydrothermal, metallurgic, thermal processing and mechanochemical involve either the utilization of hazardous chemicals, generation of unwanted wastes and energy-intensive processes (Bhattacharya et al., 2020). Thus, much attention has been drawn to the development of an eco-friendly process for the synthesis of ZnO nanoparticles through that is known as a green synthesis process. Green synthesis of nanoparticles using plant extract or microorganisms as reductants and stabilizer instead of toxic chemical compounds such as triethyl amine and sodium hydroxide (NaOH) is an eco-friendly and cost effective alternative (Shubha et al., 2019). Bioactive compounds which consisted of electron-donating groups such as hydroxyl and amine are capable to reduce Zn^{2+} ions to zero valent Zn

during the green synthesis process. In addition, the phytochemicals can also induce the chelating effect to stabilize the growth of nanoparticles. Green synthesis is consistent with one of the green chemistry principles i.e. to minimize the environmental hazards as compared to conventional chemical synthesis processes.

In addition to the synthesis method, modification of ZnO catalyst has become one of the greatest challenges in this research area. This is because ZnO has a wide band gap energy that may lower its quantum efficiency and limiting its feasibility in industrial application. Metal doping of ZnO nanoparticles will alter the particle structure through the introduction of dopants. This will in turn cause the reduction of band gap energy and inhibition of the recombination rate of electron-hole pairs during AOPs (Janani Archana, Christy Preetha and Balasubramanian, 2022). A significant band gap narrowing of ZnO was observed in the work done by Munawar et al. (2020) as a result Ag doping which enhanced the formation of charge carriers under catalytic process. Acar et al. (2022) also reported Ag doping on photocatalyst could improve the dye degradation efficiency significantly. Hence, this study is proposed to synthesize, characterize metal-doped ZnO nanoparticles using different plant extracts via green route.

In addition, there was limited study reported on the optimization of sonocatalytic activity using green synthesized ZnO nanoparticles. Therefore, parameter study was proposed to optimize the catalytic activity of ZnO nanoparticles in the degradation of organic dye through response surface

methodology (RSM). RSM is an effective and powerful statistical tool used for optimization by considering the interaction of operating variables in the design of experiments. The influences of several experimental variables on the outcomes can be evaluated simultaneously by the means of RSM approach leading to the reduction in laborious work (Zulfiqar et al., 2020). Besides, the reusability of sonocatalyst is an important parameter in the economical perspective. The application of materials with high stability was favoured in commercial platform due to cost-saving. However, there was limited work done on the reusability test of green synthesized ZnO nanoparticles in sonocatalysis. Mechanism, kinetic and thermodynamic of the sonocatalytic degradation of organic dye in the presence of ZnO nanoparticles was also studied in this research due to the limited information available in the literature. This information was important to have a better understanding on the nature of the sonocatalytic reaction prior to the upscale of the application.

1.5 Research Objectives

This research aims to fabricate ZnO nanoparticles as sonocatalyst in the water treatment through green synthesis. The objectives of this study are listed as following:

- a. To synthesize and characterize pure and metal-doped zinc oxide (ZnO) nanoparticles by using different plant extracts and by varying the synthesis parameters via green route.

- b. To investigate the performance of sonocatalytic degradation efficiency of dye in the presence of ZnO nanoparticles under different process parameters in order to maximize the degradation performance.
- c. To study the reusability of the synthesized ZnO nanoparticles in the sonocatalytic degradation of organic dye.
- d. To elucidate the reaction mechanism, kinetic and thermodynamic studies of the sonocatalytic degradation of dye in the presence of ZnO nanoparticles.

1.6 Scope of Study

In this work, green synthesis of silver-doped ZnO (Ag-ZnO) and iron-doped ZnO (Fe-ZnO) nanoparticles were proposed by using various types of plant extracts such as black tea waste, *Clitoria ternatea* Linn flower, hibiscus leaves and palm leaves. To the best of our knowledge, there is no work reported on the application of green synthesized ZnO in the sonocatalytic degradation of organic dye including parameter, kinetic and thermodynamic studies. Hence, the first part of this study involved the preparation of metal-doped ZnO nanoparticles through green synthesis. The characterization of the samples was then conducted to determine their chemical, physical and optical properties. Together with the characterization of plant extract, a plausible mechanism of green synthesis was proposed in this study. In addition, the sonocatalytic performance of the green synthesized ZnO nanoparticles was evaluated through the treatment of dye-containing water.

The best sonocatalyst was chosen for the subsequent parameter studies to explore the effects of operating parameters on the sonocatalytic degradation efficiency of organic dyes. Besides, RSM modelling was performed to optimize the sonocatalytic performance of the green synthesized ZnO nanoparticles in the degradation of organic dyes. Reusability test of the green synthesized nanomaterials was then carried out for up to 10 sonocatalytic cycles. The properties of the reused sonocatalyst were also characterized and analysed to determine the stability of the samples. Mechanism study of the sonocatalytic reaction was conducted through radical scavenging test. Besides, the kinetic of the sonocatalytic reaction was evaluated by the means of zero order, first order, second order and third order kinetic models while the thermodynamic of the reaction was evaluated using Van't Hoff, Eyring and Arrhenius equations.

CHAPTER 2

LITERATURE REVIEW

2.1 Classification of Organic Dyes

Organic dyes are widely used as colorant to impart color to textile, leather and paper products. Basically, organic dyes are made up of two major components which are known as auxochromes and chromophores. Chromophore components of dye are electron receivers which are responsible in the color formation. The examples of chromophore involve azo ($-N=N-$), carbonyl ($C=O$), nitroso ($N-OH$) and sulphur ($C=S$) (Tanveer et al., 2022). The role of auxochromes present in dyes is to enhance the color intensity by varying the solubility of dye and adhesion on the fabric products. In contrast to chromophore, auxochromes are electron donor consisting of functional group such as NH_2 , $-COOH$, $-SO_3H$ and $-OH$ (Benkhaya, M'rabet and El Harfi, 2020).

Organic dyes can be classified into two main categories which are natural and synthetic dyes. Natural dyes can be further categorized according to the origin of color materials such as plant (Jackfruit, Onion, Indigo), animal (Lac insect, Cochineal) and mineral (Red clay, Ball clay, Mineral ore) (Gupta, 2019). Although natural dyes are more eco-friendly and safer than synthetic dyes, its application in textile industry is less favourable than the latter due to its poor attachment on the fabrics products and poor fastness to light and

washing (Moyo, Makhanya and Zwane, 2022). Therefore, numerous types of synthetic dyes are invented and produced to mitigate the limitations of natural dyes.

Other than the source of dyes, the classification of dye is commonly performed based on the particle charge including anionic, cationic and non-ionic dyes (Sankar Sana et al., 2022). Anionic dyes are negatively charged with the functional groups such as sulfonate, triphenylmethane and azo groups. The examples of anionic dye are congo red (CR), acid blue, methyl orange (MO) and Eriochrome Black T. The attachment of anionic dyes is favourable over the positively charged surface of adsorbent due to the electrostatic interaction. Cationic dyes are positively charged dyes including methylene blue (MB), malachite green (MG) and rhodamine B (RB). This type of dye can adhere easily onto the adsorbent with negatively charged surface. Disperse and vat dyes are non-ionic and water insoluble dyes which are bonded to the fabric materials through Van der Waals force and hydrogen bonding (Tanveer et al., 2022).

Besides, categorization of organic dyes can be done based on the chemical structure of dyes (Benkhaya, M' rabet and El Harfi, 2020). For instance, organic dyes which consist of azo groups bonded to aromatic ring are known as azo dyes while triarylmethane dye is the group of dyes which made up of a central carbon connecting to three aromatic rings. Other examples of dye with different chemical structures are indigo dyes, cyanine dyes and anthraquinone dyes. Organic dyes can also be divided into different groups according to their principal substrates. For example, solvent dyes are widely

used for plastic dyeing while reactive dye are mainly applied on textile products such as silk, cotton and nylon (Hasanpour and Hatami, 2020).

2.2 Dye Removal Method

Owing to the disadvantages of dye contamination, the development of an effective remediation method is crucial to overcome the pollution problems and eliminate the hazard substances from environment. Basically, dye removal techniques are divided into three groups which are physical, chemical and biological methods.

2.2.1 Physical Method

In physical dye removal method, dye substances are separated physically from wastewater. For instance, flocculation is a physical technique which facilitates the elimination of dye molecules by binding the pollutants into flocs in bigger size using flocculant. During flocculation process, gentle mixing is involved to bring the targeted substance close to flocculant. This would in turn increases the frequency of collision and bonding formation between pollutants and flocculation agent which induce the generation of flocs. It is then followed by the growth of flocs into larger size and settle at the bottom of process tank. The last step of flocculation is the separation of suspended particles from wastewater medium when the flocs achieve the optimum size. According to the research conducted by Sun et al. (2022b), the factors that affect the performance of flocculation includes type of flocculant, flocculant dosage,

solution pH, stirring intensity and the presence of coexisting cations. They also highlighted that mixing at optimum speed could enhance the efficiency of flocculation. In contrast, aggressive mixing would compromise the flocculation performance due to the breaking of particle into smaller size. In addition, Sultana, Usman and Farooqi (2021) proposed the modification of traditional flocculation method by introducing base soap as anionic surfactant onto flocculant. The results revealed that the addition of surfactant could enhance the flocculation process by improving the bonding between flocculants and dye molecules.

Adsorption is another common physical method applied for dye removal which transfers dye molecules from an aqueous phase to a surface of solid material. The key elements of a good adsorbent are high specific surface area and good affinity towards adsorbate. According to Iqbal et al. (2022), the efficiency of dye adsorption was varied with the duration of contact between adsorbent and adsorbate, solution pH, dosage of adsorbent and initial dye concentration. It is noteworthy that the decrement of dye removal efficiency was observed after the achievement of adsorption-desorption equilibrium. The authors claimed that the reduction effect was owing to the desorption of dye molecules from adsorbent particles as well as the overloading of adsorbent surface. Activated carbon is one of the popular adsorbents to be used in commercial water remediation due to its porous structure which provides large specific surface area for adsorption (Jawad et al., 2022). Ngoc et al. (2022) suggested the application of transition metal oxide nanoparticles, cobalt chromite as adsorbent for dye removal. In the study, the nanomaterials showed

high selectivity towards anionic dye as compared to cationic dye. Other common types of adsorbent materials include cellulose, silica and metal-organic framework (El Bendary, Radwan and El-Shahat, 2021; Caesario et al., 2022; Sun et al., 2022a).

Membrane filtration is also widely applied in the treatment of dye-contaminated effluent. By the means of membrane filtration, a barrier is inserted to separate dye molecules from the raw wastewater. The performance of a membrane in water remediation is highly dependent on its hydrophilicity property, fouling effect, membrane thickness, porous structure and chemical stability (Jankowski et al., 2022). Polymer-based membrane such as polysulfone, polyimide and polyethersulfone is always favourable in the application of dye removal due to its cost effectiveness, high mechanical strength, high thermal resistance and good chemical stability (Benkhaya et al., 2021b; Nasr and Ali, 2022; Zheng et al., 2022). The current trend of research focuses on modification or blending of membrane materials to further improve the compatibility of membrane filtration in commercial practice. For instance, Benkhaya et al. (2021a) proposed the mixing of polysulfone with polyetherimide prior to the fabrication of membrane. The research outcomes confirmed that the presence of polyetherimide increased the hydrophilicity of polysulfone membrane leading to the improvement on the water flux. Besides, the addition of polyetherimide resulted in a denser structure of membrane top layer which caused higher rejection rate of dye molecules. According to Yu et al. (2022), the filtration performance of polyetherimide membrane in dye removal could be enhanced by the modification with polyetheretherketone.

2.2.2 Biological Method

Biological-based dye removal method is a sustainable approach which degrade the complex dye molecules into simpler products such as ammonia, carbon dioxide and water. In a typical biological wastewater treatment, microorganisms such as bacteria, algae, fungi and yeast are commonly used in bioremediation of dye-containing wastewater. Dye molecules can be removed biologically from wastewater through adsorption and degradation. This biological method can be conducted under aerobic and anaerobic conditions (Fan et al., 2022b; Nguyen et al., 2022). Zhang et al. (2022a) proposed a rotary algae biofilm which could achieve up to 95% of degradation efficiency of 600 mg/L Acid Orange. Moradi et al. (2021) had explored that both living and dead algae could eliminate dye substances via different routes. In the research, biosorption took place in the remediation of dye-containing wastewater using dead *S. platensis* while living *S. platensis* decomposed dye molecules by the secreted enzymes such as laccase and peroxidase.

According to Gul et al. (2023), the performance of fungi species such as *A. flavus* and *A. niger* in the dye decolorization was affected significantly by various operating conditions including type of carbon and nitrogen sources present as nutrients to fungi, shaking of reaction medium and incubation time. Besides, Saravanan et al. (2021) suggested that the application of fungal biomass as bio-adsorbent was a promising alternative for dye elimination process. The study revealed that there were different types of functional group

with both positive and negative charge present on the immobilized mixed fungal biomass. In addition, the surface morphology of the fungal biomass exhibited porous structure. These properties provided good adsorption activity of fungal biomass in the removal of dyestuffs. Besides, Artifon et al. (2022) applied the spent brewer's yeast as bio-flocculant in the treatment of dye-containing effluent. By the means of centesimal analysis, the data showed that the residue collected from brewing industry was enriched with two major chemical components which are polysaccharides and proteins. Spent yeast was recognized as a potential natural source of flocculant owing to enrichment of sugar and protein contents with long molecular chain and various functional groups. Besides, Saravanan et al. (2021b) mentioned that the production of yeast was easier as compared to bacteria and fungi. This is an attractive point of yeast in the commercial application because it can achieve higher production per unit time.

Other than algae, fungi and yeast, bacteria are another common biological source which are widely applied in wastewater treatment. The usage of extracellular polymeric substances generated by *Lysinibacillus sp* in the dye removal was recommended by Kamath Miyar, Pai and Goveas (2021). The biological polymer with high molecular weight showed the highest adsorption efficiency in MG solution as compared to MO, CR and Coomassie Blue. The results elucidated that agitation speed was a key parameter in the bio-adsorption of dye in which enhanced mass transfer and decrement in the resistance of boundary layer could be done by increasing the agitation speed. This would in turn lead to the improvement in the adsorption removal of dye. Srinivasan and

Sadasivam (2021) also reported on the application of bacterial species in biological remediation of dye-containing wastewater. Based on the findings recorded in the study, azoreductase secreted by *A. hydrophila* was a potential enzyme assays which could degrade dye molecules into simpler products.

2.2.3 Chemical Method

Chemical dye removal technique is also widely published in research paper which shows competitive results as compared to physical and biological methods. Ion exchange is one of the examples for chemical dye removal methods which involves the swap of ions between dye molecules and an ionic substance. Kumar Sinha et al. (2021) suggested the application of ammonium phosphomolybdate in the remediation of dye-containing effluent in which the resin will bind to cationic dye molecules electrostatically through ion exchange reaction. The experiment showed that the ion exchanger exhibited the highest affinity towards cationic dye as compared to anionic and neutral dyes. The selectivity of the reaction makes it less favourable in commercial wastewater treatment because there are various types of dye existing in the real wastewater. Another example of chemical dye removal methods is coagulation. According to Ren et al. (2022), iron chloride is an effective coagulant which performs better in dye elimination under alkaline condition than that in acidic medium. The constructed coagulation model showed that dye removal was mainly contributed by both electrostatic and hydrogen bonding adsorption.

Among chemical dye removal methods, AOP is on the research trending

nowadays. During AOP, dyestuffs are degraded rapidly by reactive oxygen species (ROS) with high oxidizing power. AOP techniques can be distinguished based on the source of energy used to generate ROS. Electrochemical is one of the examples for AOP which employs electric current to trigger the formation of ROS which in turn decompose toxic dye substances into less harmful product such as water and carbon dioxide. Saxena, Ruparelia and Saxena (2022) prepared a dimensionally stable anode by using titanium as base precursor and coated the electrode with mixed metal oxides via thermal decomposition. The experiment recorded an excellent efficiency of dye degradation by the means of the prepared anode under electrochemical reaction. Ma et al. (2021) emphasized that the selection of electrode materials is an important factor which will influence the performance of an electrocatalytic reaction. The authors proposed that the electrochemical characteristics of a lead oxide electrode can be enhanced by embedding with both metal materials and organic polymer. The results of the experiment showed that 100 mg/L of Acid Blue 9 was decolorized completely within 2 hours of electrochemical process using the prepared electrode. Besides, the efficiency of electrocatalysis was also highly affected by the operating parameters such as current density, pulse frequency and pulse duty cycle.

Other examples of AOP include photocatalysis, Fenton reaction and ozonation (Dalponte Dallabona, Mathias and Jorge, 2021; Li et al., 2021a; Zhang et al., 2022c). In recent years, sonocatalysis had been also explored to be a promising AOP in the elimination the organic pollutants from water bodies (Nas, 2021). This is because the ultrasound waves generated may activate the

sonocatalyst, enhance the mass transfer within the reaction medium, inhibit the agglomeration of particles and provide continuous cleaning of particles surface (Saleh and Taufik, 2019). **Figure 2.1** illustrates the number of research papers published in ScienceDirect in the past 10 years as per entering “Sonocatalysis” as the keyword. The graph shows an increasing trend in the topic related to sonocatalysis. In other words, sonocatalysis garners more attraction in the research field from year to year. Among this, ZnO nanoparticle is a potential semiconductor which is widely applied as sonocatalyst due to its chemical stability, high efficiency to produce electron-hole pairs and non-toxicity nature (Gholami et al., 2019a).

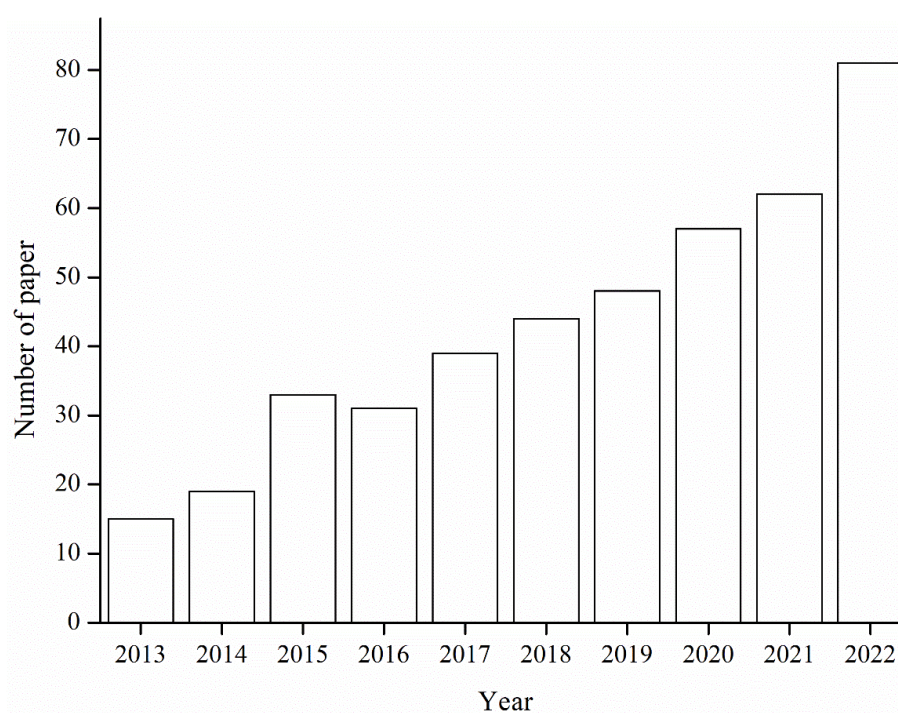


Figure 2.1: Number of Research Paper Related to Sonocatalysis Published in ScienceDirect from 2013 to 2022.

2.3 Principle of Sonocatalysis

Sonocatalysis employs ultrasound as energy source to initiate the chemical reaction between reactants. The occurrence of sonocatalysis can be well-elucidated by the fundamental of sonochemistry. Transient cavitation will induce the generation of ROS with high oxidizing power while the fluid is sonicated under ultrasound irradiation. **Figure 2.2** illustrates the acoustic cavitation phenomenon including the nucleation, growth and collapse of microbubbles under ultrasound irradiation. Firstly, the formation of microbubble is triggered under the propagation of ultrasound wave with a series of alternating compression and rarefaction (Abdi et al., 2022). During compression period, the size of microbubble will reduce due to positive pressure within the liquid medium. The growth of microbubbles take place during the rarefaction phase in which the pressure is minimum. The microbubble will eventually collapse violently when the critical size is achieved after undergoing successive cycles of oscillating ultrasound wave (Merabet and Kerboua, 2022). The implosion of microbubble is known as acoustic cavitation phenomenon which generates a localized hotspot with extremely high temperature (up to 5000 K) and pressure (up to 1000 atm) (Shojaeiarani, Bajwa and Holt, 2020). The thermal energy produced during the collapse of microbubble will then lead to water cleavage. This process is known as sonolysis where ROS will be generated due to water pyrolysis.

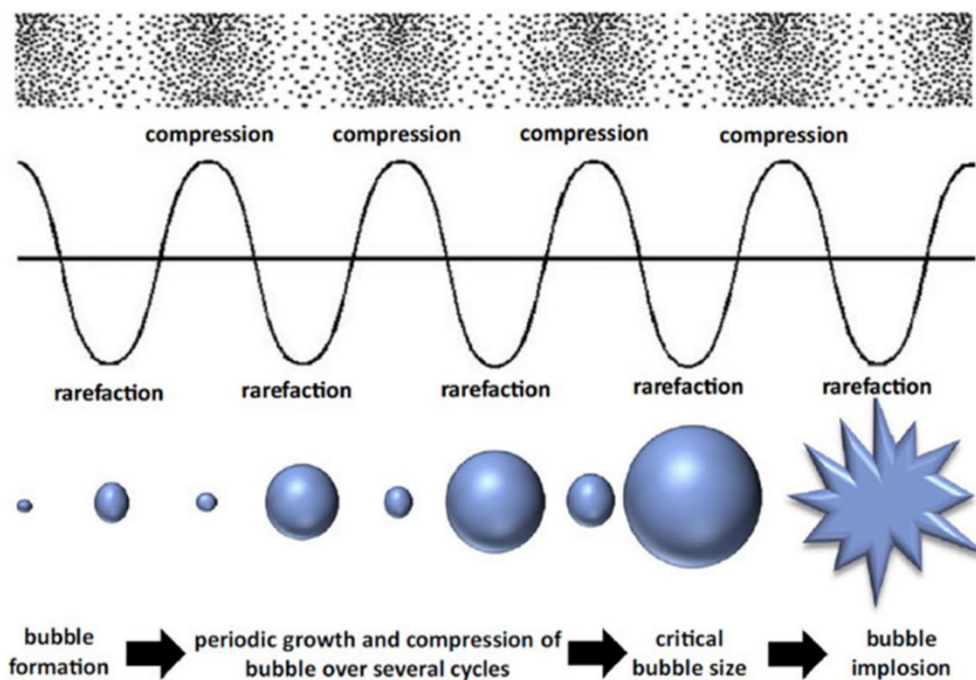


Figure 2.2: Acoustic Cavitation Phenomenon under Ultrasound Irradiation (Vyas et al., 2019).

In addition to thermal energy, the implosion of microbubble will also cause the emission of sonoluminescence in the form of light (Abdurahman, Abdullah and Shoparwe, 2021). According to Khataee et al. (2020) and Wang et al. (2008), the wavelength of sonoluminescence generated during acoustic cavitation is below 375 nm. In other words, the light energy emitted under ultrasound irradiation is greater than or equal to 3.3 eV. Heterogeneous catalysis will then be triggered by the transmission of photon energy in the presence of solid particle with band gap energy lower than 3.3 eV. Excitation of electron (e^-) located at the valence band (VB) of sonocatalyst to the conduction band (CB) take place when the energy of sonoluminescence is higher than the band gap energy of sonocatalyst. This will in turn leave a positively charged hole (h^+) in CB. The formation of charge carriers will react with the water and oxygen molecules adsorbed on the surface of sonocatalyst to form ROS which exhibit

high oxidizing ability to decompose organic substances into simpler products. Other than chemical reaction, ultrasound irradiation could assist the degradation of organic substances through mechanical motion. For instance, ultrasound wave will induce turbulent flow which will enhance the mass transfer within the reacting medium (Li et al., 2021d). The frequency of collision between reactant and catalyst will increase consequently leading to the improvement in the catalytic activity. The microjet effect of ultrasound wave will also inhibit the agglomeration of sonocatalyst and clean the surface of catalyst continuously (Pirsaheb and Moradi, 2021). This will in turn increase the surface area of sonocatalyst available for the chemical reaction.

2.4 Properties of ZnO Nanoparticles

ZnO is a Group II – VI semiconductor compound which is made up of zinc (Zn) and oxygen (O) elements that arranged in a tetrahedral bonding configuration. Due to the unique and distinctive properties of ZnO, it has garnered broad attention for their diverse applications in various areas such as catalysis, food packaging, electronics, biomedical, sunscreens and pigments. As accompany with the establishment of nanotechnology, the synthesis of ZnO undergoes rapid development from thin films to nanostructures in the past decades to exhibit the distinguished optical, electrical, chemical and mechanical properties of ZnO. Hence, their performance and broadness of applications are improved by having reduced size and better properties (Lin et al., 2019; Moatamed et al., 2019).

ZnO can be synthesized into 3 possible crystal structures which are zinc blende, wurtzite and rocksalt as illustrated in **Figure 2.3**. Under ambient conditions, ZnO exhibits the greatest thermodynamic stability in wurtzite arrangement. ZnO growing on cubic substrate displays zinc blende structure while ZnO with rocksalt lattice is quite rare as it can only be obtained through fabrication under extreme high pressure which is at about 10 GPa (Norek, 2019). Wurtzite, the most common crystal structure of ZnO, is a hexagonal structure in which one zinc atom is tetrahedrally coordinated to four oxygen atoms and the ions are arranged in alternate pattern along c-axis. The oppositely charged ions induce the polar surfaces which are Zn-(0001) and O-(000 $\bar{1}$). The formation of the polar planes allows the creation of a polar c-axis. The space group of ZnO arranged in hexagonal wurtzite lattice is categorized as P6₃mc with lattice constants of $a = 0.3296$ nm and $c = 0.52065$ nm. The feature of wurtzite ZnO with asymmetric center gives rise to its piezoelectricity and pyroelectricity properties (Kaur and Singh, 2020). These properties increase the application potential of ZnO such as mechanical actuator and piezoelectric sensor (Hao et al., 2019).

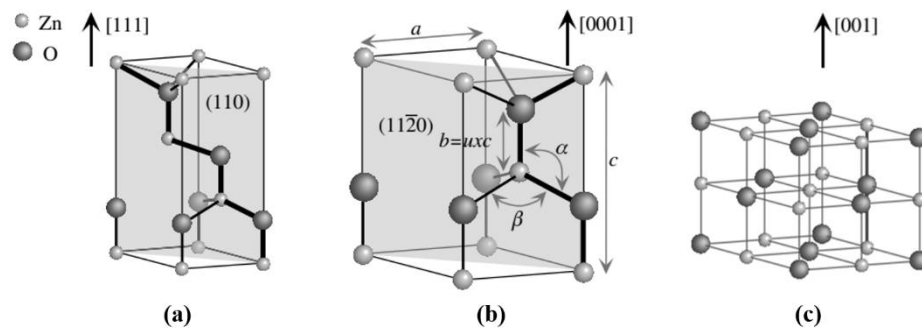


Figure 2.3: Crystal Structure Models of ZnO: (a) Zinc Blende, (b) Wurtzite and (c) Rocksalt (Özgür, Avrutin and Morkoç, 2018).

ZnO nanoparticles can be grown into a wide variety of morphologies such as nanobelts, nanocombs, nanoflowers and nanorings as shown in **Figure 2.4** which is mainly affected by the growth rate of certain directions. Basically, wurtzite ZnO has three primary growth surfaces which are *c*-plane, *a*-plane and *m*-plane. The formation of various nanostructures can be achieved by varying the synthesis parameters such as temperature and type of solvents used (Goswami, Adhikary and Bhattacharjee, 2018; Marlinda et al., 2019). Recent research works have paid high focus on the application of ZnO nanoparticles especially in the biomedical field due to its extremely low toxicity property. The toxicity of ZnO nanoparticles had been studied by Sudhakaran et al. (2020) using adult healthy Wistar rats which exhibited similar properties as compared to human in terms of biochemical, physiological and metabolic pathways. The findings revealed that there were no significant toxic responses observed in rats after exposing to 10 mg/kg-body weight ZnO nanoparticles. According to Pallela et al. (2020), human embryonic kidney 293 (HEK-293) exhibited high cell viability (81 %) under high exposure of green synthesized ZnO nanoparticles (100 µg/mL). The results indicated the low toxicity and biocompatibility of ZnO nanoparticles towards human body. Alves et al. (2019) had also evaluated the cytotoxicity of ZnO nanoparticles using human dermal fibroblasts. The cells exhibited insignificant change in cell viability as a consequence of exposure to ZnO nanoparticles for 24 h. Vijayakumar et al. (2020) also reported on the non-toxicity behavior of ZnO nanoparticles to the mouse embryonic fibroblast cells. It is interesting to notice that no apoptotic activity of fibroblast cells was observed through flow cytometry at the

concentration of ZnO nanoparticles up to 120 $\mu\text{g}/\text{mL}$. In addition, Zare et al. (2019) had unravelled the biocompatibility of green synthesized ZnO nanoparticles through the investigation of haemolysis effect. There was only 3 % haemolysis observed at 6 mg/mL of ZnO nanoparticles which did not exceed the permissible limit (5 %). Therefore, ZnO nanoparticles with low toxicity are safe to be used as drug carriers in human body (Akbarian et al., 2020). Besides, the biocompatibility of ZnO nanoparticles accompanied with the ability to produce ROS make them applicable in killing targeted cancer cells and bacteria. Besides, ZnO nanoparticles are also useful in anti-inflammatory activity and wound healing as the presence of Zn is capable to enhance the generation of Immunoglobulin E antibodies and trigger the epithelialization activity.

Another attractive point of ZnO nanoparticles is the wide band gap (3.2 eV) which is advantageous in the application of optoelectronic applications. In combination with the high excitation energy of ZnO (60 meV), it is a potential material to be employed in the light-emitting diodes (LED) to generate high photon energy and emit visible light with short-wavelength (Li et al., 2020). The application of ZnO in photovoltaic cell is also ideal attributed to the wide band gap which is important to have more efficient energy harvesting by converting the visible light into electricity (Ganesan et al., 2019). In addition to the wide band gap, ZnO also has high thermal conductivity which enables it to be suitable in the devices operated at extremely high temperature such military, gas sensors and aerospace (Ullah et al., 2019). This is because ZnO is less readily to be activated by thermal energy and able to remove heat easily.

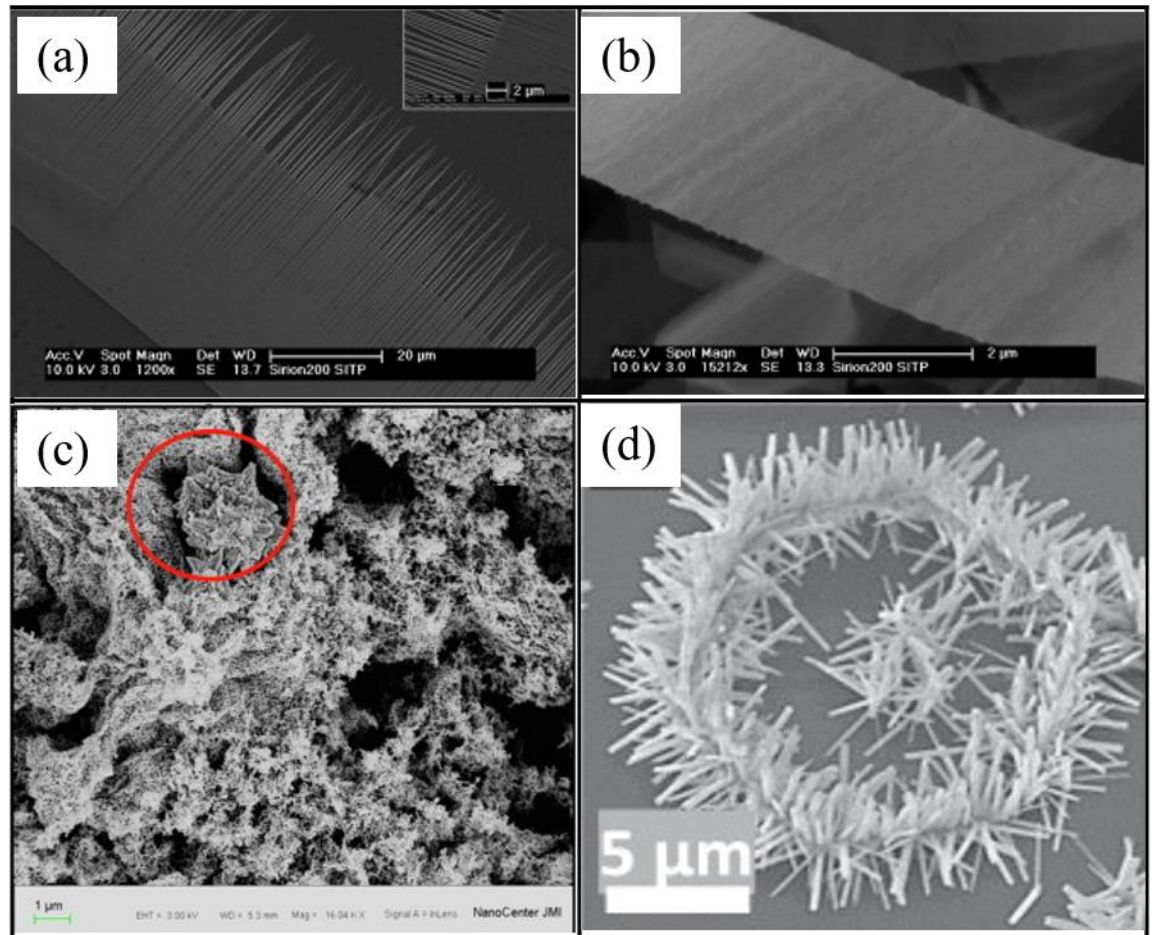


Figure 2.4: Morphologies of ZnO: (a) Nanocombs, (b) Nanobelts (Zhang and Bai, 2011), (c) Nanoflowers (Nagar et al., 2020) and (d) Nanorings (Alenezi, 2018).

ZnO also exhibits beneficial effect on the fabrication of food packaging due to its high optical transmittance in visible light region and antimicrobial property (Gomez-Gomez, Perez-Corona and Madrid, 2020). According to the Food and Drug Administration (FDA), ZnO has been included in the “generally recognized as safe” (GRAS) list implying that ZnO is a safe and promising material to be used in the food packaging (Kumar et al., 2019c). The application of ZnO in optoelectronic devices is further strengthened by its good transparency to visible light and electrical conductivity which are desirable properties of material for the transparent conducting film (Özgür et al., 2019).

With the advantageous properties as mentioned, recent works have focused on the application of ZnO as catalyst in AOP (Maleki et al., 2020; Sultana et al., 2020). In the presence of external energy such as ultraviolet (UV) and ultrasound irradiation, e^- is excited from VB to CB creating electron-hole pair. This phenomenon accelerates the generation of ROS which have strong oxidizing power to mineralize organic substance (Rueda-Salaya et al., 2020).

2.5 The Common Synthesis Approaches of ZnO Nanoparticles

The traditional techniques which are commonly used to synthesis ZnO nanoparticles includes pyrometallurgy, hydrometallurgy, co-precipitation, sol-gel, hydrothermal, mechanochemical and thermal decomposition. A typical synthetic method of ZnO nanoparticles involves the consumption of various chemicals which are mainly used as Zn precursor, reducing agent and stabilizing agent. Basically, the differences between these synthetic methods are the intermediates formed during the synthesis process and the preparation techniques. For instance, Zn-containing precipitate is formed as intermediate during co-precipitation process while the intermediate product is obtained in gel-form during sol-gel method. In term of preparation technique, mechanical force is applied in mechanochemical process while heat energy is the key driver to obtain ZnO nanoparticles in thermal decomposition. Biological method, i.e. green synthesis has evolved into the focus of recent research to minimize the usage of chemical in the production of ZnO nanoparticles. **Table 2.1** presents the advantages and disadvantages of ZnO nanoparticles synthetic methods.

Table 2.1: Advantages and Drawbacks of the Techniques Applied for Synthesis of ZnO Nanoparticles.

Methods	Advantages	Disadvantages	Reference
Pyrometallurgy	<ul style="list-style-type: none"> - No pre-treatment is required. - High potential of zinc recovery from e-waste. 	<ul style="list-style-type: none"> - Energy intensive process. - Cause air pollution: Generate greenhouse gases, dust and harmful substance such as dioxins and furans. - Dispose significant amount of solid waste. 	<p>(Dutta et al., 2018; Spooren et al., 2020)</p>
Hydrometallurgy	<ul style="list-style-type: none"> - Able to recover zinc present in complex mices and at low concentration. - Can be applied to e-waste stream for zinc recovery. - Can be controlled more easily than pyrometallurgy. 	<ul style="list-style-type: none"> - High consumption of acid. - Utilize large amount of water. - Discharge huge quantity of wastewater. - High capital cost: Corrosive-resistant equipment is required. - ZnO produced is less pure and contains a 	<p>(Moezzi, McDonagh and Cortie, 2012; Dominguez-Benetton et al., 2018; Baniasadi et al., 2019; Xiong et al.,</p>

		significant amount of water.	2019)
Co-precipitation	<ul style="list-style-type: none"> - Cost effective: Does not involve complex process and expensive equipment. - High yield at low synthesis temperature. - The properties of product can be easily controlled by tuning the process variables. 	<ul style="list-style-type: none"> - Agglomerated particles is obtained. - Eco-unfriendly: High chemical usage. 	(Hairom, Mohammad and Kadhum, 2015; Raj and Sadayandi, 2016; Kaur et al., 2018)
Sol-gel	<ul style="list-style-type: none"> - Simple and repeatable process. - Able to obtain product with high purity. - Morphology of product is tunable by adjusting the synthesis parameters. 	<ul style="list-style-type: none"> - Agglomerated particles is obtained. - Not suitable for large scale production. - Eco-unfriendly: High chemical usage. 	(Mahamuni-Badiger et al., 2020; Phin, Ong and Sin, 2020)
Hydrothermal	<ul style="list-style-type: none"> - High potential to obtain product with high degrees of crystallinity and purity. - Cost effective: Simple lab equipment. 	<ul style="list-style-type: none"> - High pressure and temperature are required. - Problem on reproducibility and reliability. - Eco-unfriendly: High chemical usage. 	(Jamkhande et al., 2019; Mahamuni-Badiger et al., 2020)

	<ul style="list-style-type: none"> - Product properties can be controlled easily by simple tuning of the experimental variables. 		
Mechanochemical	<ul style="list-style-type: none"> - Applicable in large scale production. - Low production cost. 	<ul style="list-style-type: none"> - May get contaminated easily from impurities present in milling media and atmosphere. - Long milling time is needed to synthesis smaller particles. - Eco-unfriendly: High chemical usage. 	<p>(Ao et al., 2006; Jamkhande et al., 2019)</p>
Thermal decomposition	<ul style="list-style-type: none"> - Time saving process. - Easy handling process for the large-scale production - Cost-effective: No complicated instruments and expensive raw materials are needed. 	<ul style="list-style-type: none"> - Eco-unfriendly: High chemical usage. - Energy intensive: High annealing temperature is required. 	<p>(Purkayastha, Sarma and Bhattacharjee, 2014; Singh, Das and Sil, 2020)</p>

Green synthesis	<ul style="list-style-type: none">- Utilization of renewable and biosafe sources.- Prevent the discharge of toxic waste.- High reproducibility and stability.- Cost effective: Does not involve expensive raw materials.	<ul style="list-style-type: none">- Lack of uniform size distribution.	(Mahamuni-Badiger et al., 2020; Singh, Das and Sil, 2020)
-----------------	---	--	---

2.5.1 Pyrometallurgy

Pyrometallurgical process is a high temperature heating process used to produce ZnO nanoparticles in industry. It can be categorized into two classes which are direct process and indirect process. The direct process which is also known as American process involves the reduction of zincite via the reaction with coal under high temperature condition. Next, the obtained Zn vapor is oxidized into ZnO in the batch mode (Kołodziejczak-Radzimska and Jesionowski, 2014). This technique is less likely to be applied due to the lower purity of yield obtained at the end of the process as compared to indirect process (Lungu et al., 2017).

Indirect process, which is also known as French process, is applied to yield ZnO nanoparticles using molten Zn. Firstly, metallic Zn present in molten form is vaporized at temperature above 900 °C. Next, the Zn vapor is oxidized into ZnO via the reaction with oxygen present in the air supply. The resulting product is then conveyed through a cooling duct to a collection point (Mahmud et al., 2006). Luptáková, Pešlová and Kliber (2015) investigated the structure and chemical composition of ZnO powder produced by means of French process. In the research, impurities such as iron (Fe) and manganese (Mn) are detected on the final product of ZnO. In addition, the yields are present in non-uniform grain distribution which may be attributed to the different crystallization rate of grain. The indirect pyrometallurgical process was also carried out by Zhan, Li and Xu (2020) to synthesis ZnO nanoparticles through the recovery from spent Zn-Mn battery. ZnO nanoparticles with different

morphology are obtained by varying the oxygen content supplied to the system and type of collection substrate used. In addition, the synthesis parameters such as nitrogen flow rate, evaporation temperature and condensation distance from the heating part affects the particle size of ZnO powder significantly. ZnO nanoparticles obtained through the proposed French process from spent battery is found to have high purity and good UV absorption performance.

2.5.2 Hydrometallurgy

Hydrometallurgy is an alternative used to synthesize ZnO nanoparticles involving the separation and extraction of zinc metal in liquid medium. Basically, the first step of hydrometallurgical process is the addition of leachate such as ammonia solution, iminodiacetic acid and NaOH into Zn-enriched sources (Dou, 2016; Antuñano, Cambra and Arias, 2017; Palimakaa et al., 2018). It is then followed by the removal of impurities and precipitation of ZnO or electrolysis prior to the calcination process. In the work done by Gallegos et al. (2018), ZnO nanoparticles were obtained from the spent alkaline battery via hydrometallurgy. In the presence of biogenerated sulphuric acid as leaching agent with the application of either sodium carbonate or oxalic acid as precipitation agent, platelet-shaped ZnO nanoparticles with the particle size range from 12.9 to 18.9 nm were successfully synthesized and found to have excellent photocatalytic activity in the degradation of MB.

In addition, Deep et al. (2016) proposed a modified hydrometallurgical technique to yield ZnO nanoparticles from the electrode of spent battery which

contains great amount of Zn and Mn. In this research, one-pot technique was studied with the combination of leaching and impurity removal steps. Besides, the calcination step had been eliminated by the ethanolic precipitation of ZnO nanoparticles. As a result, ZnO nanoparticles with particle size of around 5 nm were obtained by using hydrochloric acid and Cyanex-923 as extractants. The synthesized ZnO nanoparticles were proved to exhibit fluorescent property which was suitable in the application of biosensors and solar cells. It is also noteworthy that the findings displayed the positive influences of liquid-to-solid ratio, reaction temperature and time on the yield of ZnO nanoparticles.

2.5.3 Co-precipitation

Co-precipitation is a well-known method applied to prepare ZnO nanoparticles from Zn salt solution involving the usage of chemical reducing agents in which NaOH is commonly used (Soren et al., 2018). In a typical co-precipitation process, precipitate can be obtained by the mixing of Zn precursor and reducing agent. Washing using distilled water or ethanol and calcination steps are then applied to remove the impurities present (Ahmad et al., 2020c).

Some examples of co-precipitation reported by researchers are presented in **Table 2.2**. In the work done by Thambidurai et al. (2020), co-precipitation technique was applied to obtain ZnO nanoparticles with spherical shape and size ranges from 25 to 200 nm. The synthesized ZnO nanoparticles exhibited good catalytic activity which had degraded 61.45% of MB after exposure to natural sunlight irradiation for 45 mins. Goswami, Adhikary and Bhattacharjee (2018)

also synthesized spherical ZnO nanoparticles successfully through co-precipitation and studied the effect of annealing temperature on the formation of ZnO nanoparticles. The findings indicated that the increment in calcination temperature from 200 °C to 600 °C leads to the enlargement in the crystallite size from 16.3 nm to 23 nm and the improvement in the crystallinity of the nanoparticles. Besides, the increment in the degree of agglomeration could be noticed significantly with the increasing annealing temperature.

Modified co-precipitation technique was proposed by Huy et al. (2019) in which ultrasound irradiation was applied during the preparation of ZnO nanoparticles while the post-annealing step was eliminated. The investigation showed that the incorporation of ultrasound irradiation was able to synthesis ZnO nanoparticles with good crystallinity and no cluster formed. The results demonstrated that high-energy jet generated by ultrasound irradiation could accelerate the nucleation of ZnO nanoparticles and dehydration process leading to the restriction in agglomeration and cluster formation. In addition, it is noteworthy that the incorporation of ultrasound irradiation in the precipitation process could increase the surface area of ZnO nanoparticles from 3.75 m²/g to 20.02 m²/g which is beneficial to the adsorption of hydrogen sulphide in air.

Table 2.2: Synthesis of ZnO Nanoparticles by the Means of Co-precipitation.

Starting materials	Synthesis condition	Morphology	Particle size	Application	Reference
Zinc nitrate (ZnNO ₃) NaOH	Precipitation + Calcination temperature at 400 °C for 2h	Spherical	25 - 200 nm	Photocatalytic degradation and antibacterial activity	(Thambidurai et al., 2020)
ZnNO ₃ Sodium borohydride	Precipitation + Calcination at 600 °C for 1 h	Flower	200 - 400 nm	Red emitting phosphor material	(Singh, King and Nayak, 2019)
Zinc chloride (ZnCl) NaOH	Precipitation at 60 °C for 2 h	Cubic	37.5 - 74.7 nm	Food packaging and biomedical applications	(Shankar, Wang and Rhim, 2018)
Zinc sulphate (ZnSO ₄) NaOH	Precipitation at 90 °C for 2 h	Spherical	43 nm	Bioavailability and toxicity studies	(Sudhakaran et al., 2020)

ZnSO ₄	Precipitation at 55 °C +	Flower and star	148.9 -	Enhance enzyme activity	(Khan et al.,
NaOH	Calcination at 500 °C for 2 h		165.9 nm	in detergent	2019a)
Zinc acetate (ZnAc)	Precipitation at 60 °C for 2 h	Spherical	140 nm	Photocatalytic	(Adam et al.,
NaOH				degradation	2018)
ZnAc	Precipitation at 80 °C for 2 h	Spherical	30 - 45 nm	Photocatalytic	(Singh et al.,
NaOH				degradation	2019b)
Polyethylene glycol					
ZnAc	Precipitation at 70 °C for 2 h	Spherical	20 nm	Genotoxicity study on	(Salama et al.,
NaOH	+ Calcination at 500 °C for 2			plant growth	2019)
Ethanol	h				
ZnAc	Precipitation at 80 °C for 6 h	Spherical and	-	Sensing material	(Khansili et al.,
Ammonia		flower			2020)
Trisodium citrate					

2.5.4 Sol-gel

Sol-gel technique is a low cost and simple method used to synthesis ZnO nanoparticles. This method includes the formation of colloidal sol from Zn precursor through hydrolysis and polymerization catalysed by acid or base and the transformation of the liquid phase into viscous gel via condensation. **Table 2.3** lists the examples of sol-gel method reported in literature. A typical sol-gel method can be divided into two main steps which are solvation and polymerization. Zn precursor is first dissolved in a solvent and then chelating agent is added for reaction. The mixture is left until gel-like substances are obtained at the end (Belay, Bekele and Reddy, 2019). The surface properties of ZnO nanoparticles can be tuned easily by controlling the synthesis parameters of sol-gel method such as the calcination temperature and type of chelating agent used. For instance, Nagar et al. (2020) successfully fabricated ZnO nanoparticles in flower shape by means of triton X-100 as surfactant through sol-gel method. According to the results obtained, the nanoflower shape of particle contributed to the good performance as field emitters by having high current density of 30.5 mA/cm^2 and excellent enhancement factor.

In addition, the research done by Narjis et al. (2020) proved that annealing temperature has positive effect on the crystallite size of ZnO nanoparticles synthesized via sol-gel technique. Ismail et al. (2019) also investigated the influence of calcination temperature on the structure of ZnO nanoparticles synthesized using sol-gel method. In their study, rod-shape ZnO nanoparticles were obtained with the involvement of polyethylene glycol as

surfactant. The synthesized ZnO nanoparticles were found to have bigger size and higher degree of agglomeration with the increasing calcination temperature. Mahdavi and Ashraf Talesh (2017) modified the typical sol-gel process by applying ultrasonic irradiation instead of magnetic stirring to attain the formation of gel. By means of characterization techniques, the synthesized ZnO nanoparticles was found to have decrement in particle size from 50 nm to 15 nm with less agglomeration as both the sonication power and duration increase from 0 to 200 W and from 0 to 20 minutes, respectively. Besides, it is noteworthy that the incorporation of ultrasound irradiation during the synthesis of ZnO nanoparticles induced cavitation phenomenon leading to the improvement in the purity of product. Sonication also improved the optical properties of ZnO nanoparticles which was observed from the enhancement in the photocatalytic degradation of MO.

Table 2.3: Synthesis of ZnO Nanoparticles through Sol-gel Method.

Starting materials	Synthesis condition	Morphology	Particle size	Application	Reference
ZnAc NaOH	Sol-gel reaction at 80 °C + Calcination at 300 °C for 2 h	Spherical	60 - 120 nm	Trap distribution study	(Delice, Isik and Gasanly, 2019)
ZnAc NaOH Ethanol	Sol-gel reaction for 24 h + Calcination at 600 °C for 90 mins	Wires, cuboids and spherical	40 - 90 nm	Electrocatalytic for hydrogen evolution	(Sofianos et al., 2021)
ZnAc NaOH Polyethylene glycol	Sol-gel reaction + Calcination temperature at 70 - 800 °C	Rod	73 nm	Antibacterial activity	(Ismail et al., 2019)
ZnAc	Sol-gel reaction at room	Flower	30 - 60 nm	Field emission displays	(Nagar et al.,

Ammonia	temperature for 3 h +					2020)
Triton X-100	Calcination at 400 °C					
ZnAc	Sol-gel reaction at 80 °C +	Flower	59 nm	Fertilizer		(Yusefi-
Citric acid	Calcination at 800 °C or 1000 °C					Tanha et al., 2020)
ZnAc	Sol-gel reaction at 50 °C for 2	Spherical	2 - 9 nm	Coating material on film		(Rawat et al.,
Lithium hydroxide	h					2018)
Ethanol						
3-(trimethoxysilyl)propyl methacrylate						
ZnNO ₃	Sol-gel reaction at 70 °C for 2	Spherical	20.2 nm	Photocatalytic		(Khan et al.,
Citric acid	h + Calcination at 450 °C for 6 h			degradation		2018a)

Zinc acetylacetonate hydrate	Sol-gel reaction for 2 h +	Rod	< 100 nm	Photocatalytic	(Uribe-
Ethanol	Calcination at 500 °C for 4 h			degradation	López et al.,
Ammonium hydroxide					2021)
Zinc methoxide	Sol-gel reaction at room	Spherical	15 -40 nm	Photocatalytic	(Mohamed et
Nitric acid	temperature + Calcination at			degradation	al., 2016)
Methyl alcohol	550 °C for 5 h				

2.5.5 Hydrothermal

Hydrothermal is one of the facile methods that can be employed to synthesize ZnO nanoparticles. The formation of ZnO nanoparticles is resulted from the crystallization of high moisture material containing Zn precursor under high temperature and pressure. **Table 2.4** presents the examples of ZnO nanoparticles synthesis through hydrothermal. ZnO nanoparticles with high purity and controlled surface properties can be obtained by varying the synthesis parameters via hydrothermal methods. For instance, Marlinda et al. (2019) found that the variation of reaction pH could induce the formation of ZnO nanoparticles with different morphology such as baton, star, flower and rod shapes and hence affects the photoelectrochemical properties of ZnO nanoparticles. In the hydrothermal process, the mixture of precursor solutions is usually transferred into a Teflon-lined autoclave and treated thermally in an oven to obtain the product (Mahendiran et al., 2019).

Table 2.4: Synthesis of ZnO Nanoparticles using Hydrothermal Method.

Starting materials	Synthesis condition	Morphology	Particle size	Application	Reference
ZnAc NaOH	Hydrothermal at 60 °C for 10 - 15 h in autoclave	Rod	20 - 100 nm	Reflectance study	(Dhasmana et al., 2020)
ZnAc NaOH Ethanol	Hydrothermal at 140 °C for 24 h in Teflon-lined autoclave	Plates	30 - 58 nm	Photocatalytic degradation	(Van Tuan et al., 2020)
ZnAc NaOH Oleylamine	Hydrothermal at 150 °C for 10 h	Tube	-	Photonic properties study	(Vinoditha et al., 2020)
ZnAc Dimethyl sulfoxide (DMSO)	Hydrothermal at 30 °C for 1 h	Spherical	2.6 - 4.8 nm	Optoelectronic devices	(Liu et al., 2020)

Tetramethyl ammonium
hydroxide pentahydrate
Ethanol

ZnCl ₂	Hydrothermal at 150 °C for 3 h in Teflon-lined autoclave + Calcination at 400 °C for 3 h	Rod, hexagonal and flower	95 - 215 nm	Photocatalytic degradation	(Kumaresan et al., 2017)
ZnCl ₂ NaOH	Hydrothermal at 60 °C for 48 h	Spherical	50 nm	Antibacterial activity	(Akbar and Anal, 2014)
ZnNO ₃ NaOH	Hydrothermal at 160 °C for 4 h in Teflon-lined reactor	Flakes	50 - 300 nm	Electromagnetic study	(Wang et al., 2020c)
ZnNO ₃ Urea Polyethylene glycol	Hydrothermal at 180 °C for 24 h under autogenous pressure in Teflon-lined	Spherical	125 - 300 nm	Photodetector	(Ahmad et al., 2018)

D-glucose	autoclave + Calcination at 25 - 550 °C					
ZnAc	Hydrothermal at room temperature for 3 h	Triangular	-	-		(Amirthavalli, Manikandan and Prince, 2018)
Cetyltrimethylammonium bromide						

In the work reported by Ahmad et al. (2018), ZnO nanoparticles capped with polyethylene glycol was synthesized hydrothermally. The resulting product was found to be potentially applicable in photodetector with shorter response and recovery duration due to the superior optical properties of ZnO. It is interesting that Dhasmana et al. (2020) proposed modification on the hydrothermal technique by the incorporation of sonication and vacuum drying. The obtained results implied that vacuum drying could enhance the crystallinity and reduce the size of particles while sonication could foster the deagglomeration of particle by inducing mechanical and thermal energy. The synthesized ZnO nanoparticles was found to be in nanorod shape and exhibit significant change on the optical properties of textured silicon by improving the reflectance in visible region and quenching the reflectance in UV region.

2.5.6 Mechanochemical

Mechanochemical is a convenient and fast process which is frequently applied to obtain ZnO nanoparticles. Some of the works reported on the preparation of ZnO nanoparticles using mechanochemical method are shown in **Table 2.5**. In this technique, mechanical milling or grinding is involved to enhance the reaction kinetics between the precursors in a planetary ball mill. Meanwhile, diluent such as sodium chloride (NaCl) is added into the system to control the growth kinetic of particles (Sabri, Yahya and Talari, 2012). As highlighted by Yang et al. (2004), the synthesis parameters such as milling time, molar ratio of reacting materials and calcination temperature would affect the crystal size of ZnO nanoparticles formed by mechanochemical process. Besides,

type of Zn precursor used in mechanochemical process is an important factor which would influence the properties of ZnO nanoparticles such as morphology, lattice imperfections and magnetic properties (Tóthová et al., 2019).

According to the research done by Čech Barabaszová et al. (2018), ZnO nanoparticles present in plate-like shape with crystallite size of around 45 nm were successfully synthesized through mechanochemical process by using ZnCl and ZnAc as zinc precursor. The findings explained the excellent antibacterial activity of the obtained nano-sized ZnO against *Staphylococcus aureus*. Furthermore, the influences of NaCl present as diluent during the mechanochemical process, milling time and involvement of heat treatment on the formation of ZnO nanoparticles had been studied by Kakhaki, Youzbashi and Naderi (2015). The crystallite size could be reduced from 10.9 nm to 8.8 nm by lengthening the milling time from 30 minutes to 40 minutes attributed to the higher frequency of collision between the particles involved. In addition, bigger particle size was found with increasing annealing temperature due to the promotion of crystal growth by higher thermal energy. The findings also prove that the presence of NaCl resulted in the inhibition of agglomeration and the increment in the amount of oxygen vacancy. These properties beneficial the application of ZnO nanoparticles as photocatalyst because higher surface area was available for the adsorption of reactants and greater amount of oxygen vacancy present as e^- trap was able to improve the separation efficiency of electron-hole pair.

Table 2.5: Synthesis of ZnO Nanoparticles through Mechanochemical Method.

Starting materials	Synthesis condition	Morphology	Particle size	Application	Reference
ZnAc NaOH	Ball mill at 500 rpm for 30 mins + Calcination at 350 °C or 650 °C	Cubic, Plates	-	Antibacterial activity	(Čech Barabaszová et al., 2018)
ZnAc NaOH N-cetyl-N,N,N-trimethyl ammonium bromide	Ball mill at 300 rpm for 30 mins - 5 h + Calcination at 500 °C for 1 h	Rod	60 - 135 nm	-	(Dhara and Giri, 2011)
ZnAc Oxalic acid	Ball mill for 1 h + Calcination at 450 °C for 30 mins	Spherical	20 - 30 nm	As catalyst during synthesis of 2,3-disubstituted	(Safaei-Ghomi and Ghasemzadeh,

				benzo[b]furan	2017)
ZnAc	Ball mill for 1 h +	Spherical	38 nm	Fertilizer	(Yusefi-Tanha
Citric acid	Calcination at 530 °C for 10 h				et al., 2020)
ZnCl	Ball mill + Calcination at	Rod	62 - 181 nm	Optical and electrical	(Çolak,
Citric acid / Maleic acid /	400 °C or 600 °C for 5 h			studies	Karaköse and
Sodium oxalate /Salicylic acid /					Derin, 2017)
Tartaric acid / Urea					
ZnCl	Ball mill at 200 - 300 rpm for	Spherical	36 nm	Magnetic study	(Zargar
Sodium carbonate	7 - 9 h + Calcination at 250 -				Shoushtari,
Sodium chloride	350 °C				Poormoghadam
					and Farbod,
					2017)

Zinc carbonate hydroxide	Ball mill at 500 rpm or 1000 rpm for 1 - 10 h + Calcination at 200 °C or 400 °C for 2 h	Spherical	50 nm	Photocatalytic degradation	(Dimitriev, Gancheva and Iordanova, 2012)
ZnNO ₃ Urea / Acetamide	Ball mill at 1800 rpm for 160 mins + Calcination at 450 °C or 550 °C for 3 h	Hexagonal / Timber / Disk	45 - 52 nm	Photocatalytic degradation	(Tadjarodi et al., 2015)
ZnNO ₃ Lithium hydroxide / NaOH	Ball mill at 350 rpm for 90 mins	Spherical	10 nm	Photocatalytic degradation	(Mendoza-Mendoza et al., 2018)

2.5.7 Thermal Decomposition

Thermal decomposition is also a possible way that can be employed to synthesis ZnO nanoparticles by heating Zn precursor at high temperature. **Table 2.6** presents the examples of research conducted on the yield of ZnO nanoparticles using thermal decomposition technique. Zn-based metal organic framework (MOF) and Zn-based complex are usually prepared and used as a precursor of ZnO in thermal decomposition process. In a typical preparation of Zn-complex, Zn salt such as $ZnNO_3$ and ZnAc is mixed with organic bridging ligand substance in a solvent for reaction. Next, the complex undergoes thermal decomposition at elevating temperature to break the ligands of complex leading to the nucleation of ZnO nanoparticles (Hayami et al., 2018). According to the research performed by Hajiashrafi and Motakef Kazemi (2019), Zn-based MOF was produced by using ZnAc as precursor and dehydrate benzene-1,4-dicarboxylate as ligating agent through solvothermal process. Besides, the authors proposed the use of tri-ethylamine as capping agent in the thermal decomposition of Zn-based MOF. The presence of stabilizer could reduce the particle size of ZnO from 100 nm to 80 nm by inhibiting the particle growth. Thermal decomposition can also be carried out by using salt of Zn. In the work reported by Kontopoulou, Angelopoulou and Bouropoulos (2016), ZnO nanoparticles were successfully synthesized via thermal decomposition of Zn palmitate in which the products were having spherical shape with various particle size based on the setting of decomposition temperature. Shamsipur et al. (2013) also suggested the formation of nano-sized ZnO with high crystallinity and purity through thermal decomposition of zinc carbonate.

Table 2.6: Synthesis of ZnO Nanoparticles by the Means of Thermal Decomposition.

Starting materials	Intermediates	Synthesis condition	Morphology	Particle size	Application	Reference
ZnNO ₃	Bis(2-aminonicotinato) zinc	Thermal decomposition at	Spherical	30 nm	Photocatalytic degradation	(Bijan zad, Tadjarodi and Akhavan, 2015)
Potassium hydroxide	(II)	550 °C for 4 h				
2-aminonicotinic acid						
Ethanol						
ZnNO ₃	(Bis1,7-bis[4-hydroxy-3-methoxyphenyl]-1,6-heptadiene-3,5-dionato)hydroxide zinc(II)	Thermal decomposition at	Spherical	123 - 131 nm	-	(Khalil et al., 2014)
Curcumin		500 °C				
Triethyl amine						
Methanol						
Zinc carbonate	[Zn(OH) ₄] ²⁻ complex	Thermal decomposition at	Spherical	24 nm	Photocatalytic degradation,	(Mousa, Bayoumy and

		700 °C for 5 h				solar cell, antibacterial and antifungal activity	Khairy, 2013)
ZnAc	Zn ₄ O(BDC) ₃	Thermal decomposition at 550 °C for 5 h	Spherical	80 - 110 nm	Antibacterial activity	(Hajiafrafi and Motakef Kazemi, 2019)	
Terephthalic acid							
Tri-ethylamine							
Dimethylformamide							
ZnAc	-	Thermal decomposition at 250 °C for 3 - 36 h	Spherical	12 - 35 nm	Photocatalytic degradation	(Alp et al., 2018)	
Ethylene glycol							
ZnAc	-	Thermal decomposition at	Bushes	10 - 12 nm	-	(Freedman et al., 2010)	
Sodium bicarbonate							

Triton-X 100		200 °C for 3 h					
ZnAc	Bis(2-hydroxy-1-	Thermal	Spherical	30 - 45	-		(Mir et al.,
2-hydroxo-1-	naphthaldehydato)zinc(II)	decomposition at		nm			2015)
naphthaldehyde		247 °C for 65 mins					
Oleyamine							
Methanol							
Zinc (II) acetylacetonate	Zn(C ₅ H ₇ O ₂) ₂ (octadecylamine) ₂	Thermal	Rod	65 nm	-		(Purkayastha,
monohydrate		decomposition at 140					Sarma and
Octadecylamine		- 200 °C for 1 h					Bhattacharjee,
							2014)
Zinc acetylacetonate	-	Thermal	Plates	60 nm	Magnetic study		(Sun et al.,
hydrate		decomposition at					2017)
Oleic acid		120 °C for 1 h then					

Oleylamine	200 °C for 1 h then
1-octadecene	300 °C for 2h

2.6 Emerging Green Synthesis Approach of ZnO Nanoparticles

In recent years, green synthesis of nanomaterials such as silver (Ag), gold (Au), copper oxide (CuO) and zirconium dioxide (ZrO₂) garners considerable attention due to the elimination of the usage of hazardous chemicals in conventional synthesis methods (da Silva et al., 2019; Thangamani and Bhuvaneshwari, 2019; Manik et al., 2020; Mohamed, 2020). This method is able to prevent further contamination in the application of wastewater treatment and also practice sustainable engineering by converting biological wastes such as leaves and fruit peels into useful materials (Chandra Joshi and Singh, 2020; Gao et al., 2020). Green synthesis approach can be considered as an environmentally friendly, cost effective and simple method without compromising the properties and applications of the products. Besides, milder condition is required to facilitate to prepare nanomaterials through green synthesis as compared to chemical and mechanical methods.

In the green synthesis of ZnO nanoparticles, the naturally available resources such as plant, bacteria and fungus are employed instead of toxic chemicals due to their enrichment in various biocompounds which are able to act as reductants and stabilizers. The general preparation steps of biological extract are presented in **Figure 2.5**. As reported by Vinayagam et al. (2020), *Calliandra haematocephala* leaves contain enormous amount of phytochemicals such as imino acid and pipecolic acid which are involved in the formation of ZnO nanoparticles via green route. In addition, Barsainya and Singh (2018) proposed the green synthesis of ZnO nanoparticles using the

pyoverdine metabolite produced by *Pseudomonas aeruginosa* which is categorized as gram-negative bacteria. The biomolecules such as protein and peptide moiety present in the siderophore act as reducing and stabilizing agents in the green synthesis of ZnO nanoparticles. Based on the research done by Ishwarya et al. (2018), bioactive compounds containing phenolic and aromatic structures were found in *Ulva lactuca* seaweed in which the involvement of biomolecules in the yield of ZnO nanoparticles was confirmed.

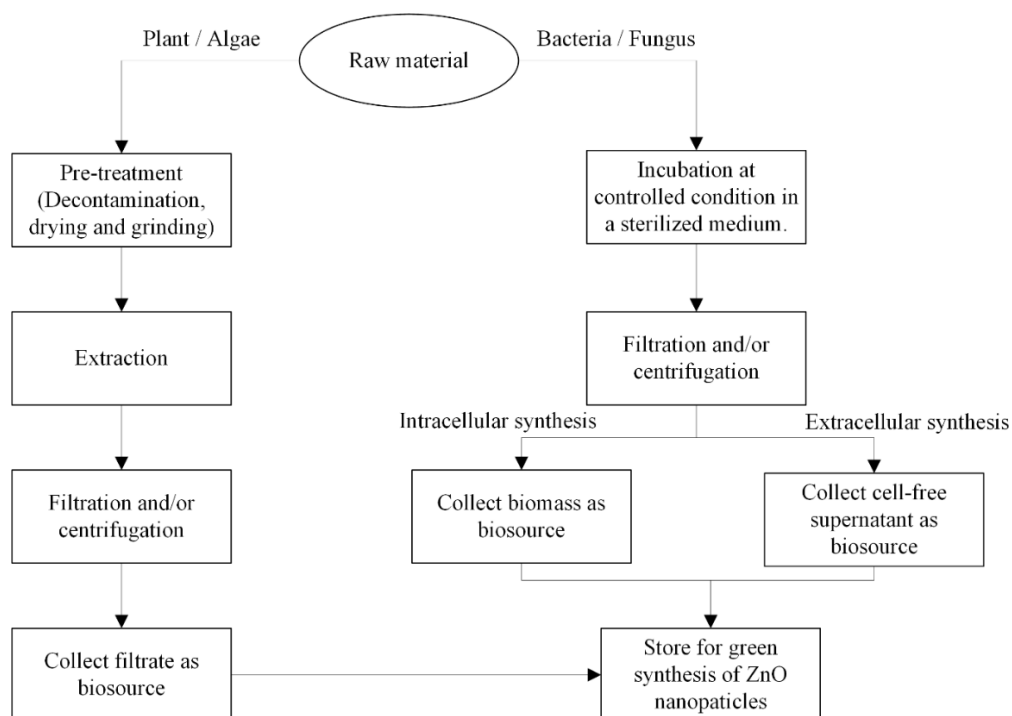


Figure 2.5: Preparation Steps of Biological Extract for the Green Synthesis of ZnO Nanoparticles.

2.6.1 Green Synthesis of ZnO nanoparticles using Plant Extract

Among various types of green sources, plant extract is the most common biomaterial used in the green synthesis of ZnO nanoparticles due to the simple

and easy handling during preparation and storage. **Table 2.7** shows the list of plant that had been studied by researchers to synthesis ZnO nanopowder through green route. In a typical green synthesis of ZnO nanoparticles, different parts of plant can serve as biosources such as flower (Jamdagni, Khatri and Rana, 2018), fruit (Ramanarayanan et al., 2018), leaf (Vinayagam et al., 2020), peel (Gao et al., 2020) and root (Chen et al., 2019). Extraction of phytochemicals is typically carried out through heating in particular solvent such as water (Chemingui et al., 2019), ethanol (Quek et al., 2020) and hexane (Ansari et al., 2020). The common extraction techniques included maceration, digestion, decoction. The difference among these processes is the temperature of synthesis (Patra et al., 2018). In maceration, the plant source is immersed in solvent at room temperature for a long period. Digestion involves the heating of plant source in solvent at temperature higher than room temperature but lower than boiling point of solvent while decoction process boils the plant source in the solvent (Belwal et al., 2018).

Table 2.7: Green Synthesis of ZnO Nanoparticles using Plant Extract.

Plant	Parts	Zn source	Extraction method	Functional group	Particle size	Shape	Application	Reference
Aegle marmelos (Indian bael)	Juice	ZnNO ₃	Maceration	Alkane	20 nm	Hexagonal wurtzite	Photocatalytic degradation, antibacterial and antioxidant activity	(Mallikarjunaswamy et al., 2020)
Aloe barbadensis Mill	Leaves	ZnAc	Decoction at 110 °C for 1 h	Amine, alkene, alkane, carbonothioyl	30 - 40 nm	Spherical	Seedling growth and germination	(Singh et al., 2019a)

Camellia sinensis L.	Leaves	ZnNO ₃	Solvent extraction	Hydroxyl, amide, alkene	18 - 30 nm	Spherical	Drug delivery	(Akbarian et al., 2020)
Cinnamomum verum	Bark	ZnNO ₃	Solvent extraction	Hydroxyl	45 nm	Hexagonal wurtzite	Antibacterial activity	(Ansari et al., 2020)
Citrus sinensis (Navel orange)	Peel	ZnNO ₃	Digestion at 80 °C for 1 h	Hydroxyl, carbonyl	33.1 nm	Hexagonal	Fruit preservation	(Gao et al., 2020)
Daucus carota (Carrot)	Vegetable	ZnNO ₃	-	Alkane	16 - 21 nm	Spherical and polyhedral	Photocatalytic degradation	(Luque et al., 2018a)
Nyctanthes arbor-tristis	Flower	ZnAc	Decoction for 15 mins	Hydroxyl, amine, alkyne,	12 - 32 nm	Spherical	Antifungal activity	(Jamdagni, Khatri and Rana, 2018)

carbonyl								
Punica granatum	Epicarp	ZnNO ₃	Maceration	Nitro, nitrate	50 nm	Hexagonal wurtzite	Antibacterial activity	(Akash, Ahalya and Dhamodhar, 2020)
Quince seed	Mucilage	ZnNO ₃	Digestion at 60 °C for 4 h	Hydroxyl	25 nm	Spherical	Photocatalytic degradation	(Tabrizi Hafez Moghaddas, Javanbakht and Elahi, 2020)
Sphagneticola trilobata	Roots	ZnAc	Digestion at 60 °C for 20 mins	Carbonyl, amine, amide	65 - 80 nm	Irregular and complex	Heavy metal adsorption, seed germination and plant	(Shaik, David Raju and Rama Sekhara Reddy, 2020)

								growth
Syzygium Cumini	Seed	ZnAc	Digestion at 60 °C for 30 mins	Carboxyl, hydroxyl	50 - 60 nm	Spherical	Larvicidal activity	(Roopan et al., 2019)
Zingiber zerumbet	Rhizome	ZnAc	Solvent evaporation	Alkene, hydroxyl, carbonyl	-	Hexagonal	Heavy metal adsorption	(Azizi, Shahri and Mohamad, 2017)
Zizyphus jujube	Fruit	ZnNO ₃	Reflux at 80 °C for 30 mins	Hydroxyl, carbonyl, carboxyl	21 - 37 nm	Spherical	Photocatalytic degradation	(Golmohammadi, Honarmand and Ghanbari, 2020)

It is noteworthy that Singh et al. (2019a) proposed one-pot green synthesis method to produce ZnO nanoparticles using leaf extract of *Aloe barbedensis* Mill. The plant extract was successfully obtained through boiling in deionized water while ZnAc was used as Zn sources in the preparation of ZnO nanoparticles. The phytochemical contents in the plant extract especially flavonoids and phenol compounds with the amount of 1.9% and 13.11%, respectively played the roles of reductants and stabilizers during the synthesis of ZnO nanoparticles. In other words, the biomolecules would form complex with Zn precursor and donate e^- to Zn^{2+} leading to the reduction and formation of ZnO nanoparticles. Meanwhile, the presence of biomolecules in the formation of Zn complex would restrict the growth of nanoparticles and hence act as a stabilizer to control the particle size. In addition, this work has revealed the potential of the green approach to synthesis ZnO nanoparticles with excellent performance in the seedling growth and seed germination activity of wheat plant. Roopan et al. (2019) had also synthesized ZnO nanoparticles using the seed extract of *Syzygium cumini* which is a type of medicinal plant composed of numerous bioactive compounds such as glucoside, anthocyanins and myricetin. This green approach successfully produced ZnO nanoparticles with average size range from 55 to 60 nm. Besides, the larvicidal and ovicidal activities of the green synthesized ZnO nanoparticles were observed against *Aedes aegypti* which is the transmission vector of dengue. The investigation illustrates that a maximum mortality rate of 80 % could be achieved at the maximum concentration of phyto-mediated ZnO nanoparticles.

In the work done by Gao et al. (2020), nano-sized ZnO particles were

synthesized by the means of green synthesis using peel extract of *Citrus sinensis* which was enriched with biological constituents including flavonoid, vitamin C, carotenoids and phenolic acids. The findings have shown that the green synthesized ZnO nanoparticles exhibited high degree of crystallinity and regular structure indicating the feasibility of green synthesis in the production of ZnO nanoparticles using non-toxic and naturally available sources. It is surprising that the green ZnO nanoparticles could be applied in the preservation of strawberry through coating. By the means of research, the incorporation of ZnO nanoparticles with good antibacterial and antifungal properties was found useful in the reduction of rotting rate and the enhancement of postharvest quality of strawberry. Luque et al. (2018b) also synthesized ZnO nanoparticles successfully using *Citrus sinensis* peel extract. The obtained ZnO nanoparticles had similar particle size as reported by Gao et al. (2020) which was around 30 nm. This study reveals that the particle size of ZnO powder decreases from 20 nm to 10 nm with the increasing concentration of plant extract from 1 wt% to 4 wt% due to the higher amount of phytochemicals present. Besides, ZnO nanoparticles synthesized through the green method were found to have high photocatalytic activity in the degradation of organic dye.

2.6.2 Green Synthesis of ZnO Nanoparticles using Bacteria

Microbial synthesis is also applied to obtain biocompatible ZnO nanoparticles as the green method employs bacteria as biological reductants and stabilizers instead of toxic and expensive chemical substances. **Table 2.8** present the types of bacteria which had been utilized successfully in the green

synthesis of ZnO nanoparticles. Basically, microbial synthesis of ZnO nanoparticles can be divided into two main categories which are intracellular synthesis and extracellular synthesis. In the case of intracellular synthesis, the process involves the transport of zinc precursor into the cell, the reduction and formation of ZnO nanoparticles within the cell and the penetration of product out of the cell. Król et al. (2018) used *Lactobacillus paracasei* isolated from dairy products to synthesis spherical ZnO nanoparticles intracellularly. Based on the Fourier Transform Infrared Spectroscopy (FTIR) analysis, carboxyl and amino acid were the biocomponents found in the bacteria which were responsible in the reduction of ZnNO₃ to obtain ZnO nanoparticles. The green synthesized ZnO nanoparticles using the lactic acid bacteria exhibited superior antibacterial activity against drug-resistant strains implying the plausible route of intracellular synthesis to obtain ZnO nanoparticles without using harmful chemicals. Tripathi et al. (2014) also produced ZnO nanoparticles using *Bacillus licheniformis* by the means of intracellular synthesis. The research illustrates that the nano-structured ZnO particles present in flower shape could be applied as a good photocatalyst in the degradation of organic dye under UV-irradiation.

Table 2.8: Green Synthesis of ZnO Nanoparticles using Bacteria.

Bacteria	Zn source	Extraction method	Functional group	Particle size	Shape	Application	Reference
<i>Bacillus haynesii</i>	ZnSO ₄	Cultivation at 55 °C and centrifugation to obtain cell-free filtrate	Ether, hydroxyl	45 - 55 nm	Spherical	Antibacterial activity	(Rehman et al., 2019)
<i>Bacillus megaterium</i>	ZnNO ₃	Cultivation and centrifugation to obtain cell-free filtrate	Hydroxyl, carbonyl, carboxyl, amine	45 - 95 nm	Cubic and rod	Antibacterial activity	(Saravanan et al., 2018)
<i>Halomonas elongata</i>	ZnCl	Cultivation at 37 °C for 1 week and centrifugation to obtain cell-free filtrate	Hydroxyl, alkene, alkyne, alkyl halide	10 - 27 nm	Spherical	Antibacterial activity	(Taran, Rad and Alavi, 2018)

<i>Lactobacillus paracasei</i>	ZnNO ₃	Cultivation at 37 °C for 1 day and centrifugation to obtain bacterial biomass	Carbonyl, carboxyl, amide	1180 nm	Spherical	Antibacterial activity	(Król et al., 2018)
<i>Pseudomonas aeruginosa</i>	ZnNO ₃	Cultivation at 33 - 37 °C for 1 day, centrifugation to obtain cell-free filtrate and solvation using chloroform	Hydroxyl, amine, amide, carbonyl	50 - 100 nm	Pseudospherical	Antibacterial and antifungal activity	(Barsainya and Singh, 2018)
<i>Pseudomonas putida</i>	ZnNO ₃	Cultivation at 37 °C for 1 day and collect	Hydroxyl, amine, carboxyl,	44.5 nm	Spherical	Antibiofilm and antibacterial	(Jayabalan et al.,

		culture solution	carbonyl, ether			activity	2019)
<i>Rhodococcus pyridinivorans</i>	ZnSO ₄	Cultivation at 30 °C for 1 day and collect culture solution	Amide, amine, alkane, alkyne, hydroxyl, ether	100 - 120 nm	Spherical	Textile finishing and drug delivery	(Kundu et al., 2014)
<i>Streptomyces enissocaesilis</i>	ZnSO ₄	Cultivation at 30 °C for 3 days and centrifugation to obtain cell-free filtrate	Hydroxyl, carbonyl, amide, amine, nitrile, alkyne	5 - 20 nm	Spherical	Antibacterial activity	(Shaaban and El-Mahdy, 2018)

On the contrary of intracellular synthesis, extracellular synthesis of ZnO nanoparticles is conducted outside the bacterial cell by the metabolite substances. For instance, Barsainya and Singh (2018) utilized siderophore pyoverdine secreted by *Pseudomonas aeruginosa* to obtain ZnO nanoparticles with particle size ranging from 50 nm to 100 nm. The extracellular secondary metabolites pyoverdine contains amino and hydroxamate groups which are involved in the reduction of zinc ions to form ZnO nanoparticles. The metal oxide product obtained via the green approach possessed potential in the application as bactericides and fungicides. In addition, Saravanan et al. (2018) has successfully synthesized ZnO nanoparticles using the metabolite products of *Bacillus megaterium*. The cell-free extract is enriched with bioactive compounds which are composed of different functional groups such as carboxyl, aromatic and amine groups. The interaction between the bioreductants and Zn precursor results in the formation of ZnO nanoparticles present in cubic and rod shapes with particle size ranging from 45 nm to 95 nm. Shaaban and El-Mahdy (2018), Taran, Rad and Alavi (2018), Jayabalan et al. (2019) and Rehman et al. (2019) had also proposed the bacterial extracellular synthesis of ZnO nanoparticles which exhibited excellent performance in the inhibition of bacterial growth.

2.6.3 Green Synthesis of ZnO Nanoparticles using Algae

Algae is also a candidate that can be utilized as biosources in the effective green synthesis of ZnO nanoparticles due to their high contents of biomolecules such as sugar and protein (Ishwarya et al., 2018). **Table 2.9** lists

the types of algae which are applicable in the synthesis of ZnO nanoparticles. The preparation steps of algal extract are similar to the preparation of plant extract in which the natural sources are firstly washed for decontamination followed by powdering, dehydration and extraction (Sanaeimehr, Javadi and Namvar, 2018). ZnO nanoparticles with the rod-like shape has been successfully obtained via green synthesis by using *Ulva fasciata* as bioreductants in the literature reported by Hamouda et al. (2020). The research revealed that ZnO nanoparticles were formed through the interaction between the zinc precursor and the potentially bioactive compounds present in the green algae which were composed of amine, carbonyl and nitro groups. It was surprising that the algae mediated ZnO nanoparticles exhibited better antibacterial activity than the wet-chemical synthesized ZnO nanoparticles. In addition, Bhattacharya et al. (2020) had applied ZnO nanoparticles synthesized using *Spirulina sp.* on the ultrafiltration membrane for drug removal. The results indicated that green synthesized ZnO nanoparticles had improved the performance of the membrane through the enhancement of hydrophilicity and antifouling properties. Again, this study emphasized the feasibility of green synthesis using algal extract on the preparation of ZnO nanoparticles.

Table 2.9: Algae and Fungus Mediated ZnO Nanoparticles.

Biosource	Category	Zn source	Extraction method	Functional group	Particle size	Shape	Application	Reference
<i>Kappa carrageenan</i>	Algae	ZnAc	-	Amide, hydroxyl, carbonyl, alkane	97.03 nm	Oval	Drug delivery	(Vijayaku mar et al., 2020)
<i>Sargassum muticum</i>	Algae	ZnAc	Decoction	Hydroxyl, carbonyl, amide, sulphate	30 – 57 nm	Hexagonal	Anticancer activity	(Sanaeime hr, Javadi and Namvar, 2018)

<i>Spirulina sp.</i>	Algae	ZnSO ₄	Decoction	Carboxyl, carbonyl, hydroxyl, amide, alkane	-	-	Drug removal	(Bhattachar ya et al., 2020)
<i>Ulva fasciata</i>	Algae	ZnAc	Decoction for 1 h	Nitro, amine, alkene, carbonyl	50 - 150 nm	Rod shape	Antibacterial activity	(Hamouda et al., 2020)
<i>Ulva lactuca</i>	Algae	ZnAc	Decoction for 20 mins	Hydroxyl, alkane	10 - 50 nm	Sponge	Photocatalytic degradation, antibacterial and larvicidal activity	(Ishwarya et al., 2018)

<i>Alternaria tenuissima</i>	Fungus	ZnSO ₄	Cultivation at 30 °C for 10 days and filtration to obtain cell-free filtrate	Carbonyl, carboxyl, amine, hydroxyl	10 - 30 nm	Spherical	Photocatalytic degradation, antibacterial, anticancer, antifungal and antioxidant activity	(Abdelhaki m, El-Sayed and Rashidi, 2020)
<i>Aspergillus niger</i>	Fungus	ZnAc	Cultivation at 28 °C and filtration to obtain fungal biomass	Hydroxyl, carbonyl, alkene	80 - 130 nm	Rod	Antibacterial activity	(Gao et al., 2019)
<i>Aspergillus niger</i>	Fungus	ZnAc	Cultivation at 26 - 30 °C for 5 days,	Hydroxyl, amine, amide,	8 - 38 nm	Rod shape	Textile finishing	(Mohamed et al.,

			filtration and	alkene				2019)
			centrifugation to					
			obtain cell-free					
			filtrate					
<i>Aspergillus terreus</i>	Fungus	ZnAc	Cultivation at 26 - 30 °C for 3 days and filtration to obtain cell-free filtrate	Carbonyl, hydroxyl, amide, amine	10 - 45 nm	Spherical	Textile finishing	(Fouda et al., 2018)
<i>Fusarium keratoplasticum</i>	Fungus	ZnAc	Cultivation at 26 - 30 °C for 5 days, filtration and centrifugation to	Hydroxyl, amine, amide, alkene	10 - 42 nm	Hexagonal	Textile finishing	(Mohamed et al., 2019)

			obtain cell-free filtrate					
<i>Periconium sp.</i>	Fungus	ZnNO ₃	Cultivation for 3 weeks, pulverization fungal biomass and boil in deionized water	Hydroxyl, carbonyl, alkene, carboxyl, amine, amide, nitro, ester	16 - 78 nm	Spherical	Antibacterial and antifungal activity	(Ganesan et al., 2020)

2.6.4 Green Synthesis of ZnO Nanoparticles using Fungus

Fungus is a renewable feedstock that is easy-to-obtain for the synthesis of nanostructured ZnO via green synthesis approach. **Table 2.9** also summarizes the works done on the green synthesis of ZnO nanoparticles using fungus. The fungal synthesis is deemed to be similar as microbial synthesis of ZnO nanoparticles in which isolation and sub-culturing of fungus are carried out in a typical preparation of fungal extract (Ganesan et al., 2020). During cultivation process, the strain of fungus is incubated in a sterilized medium at optimum temperature for a period of time. The cell-free supernatant enriched with fungal metabolites is then collected through filtration and centrifugation for further use in the preparation of ZnO nanoparticles (Abdelhakim, El-Sayed and Rashidi, 2020).

Among a wide variety of fungus, *Aspergillus niger* is one of the common types to be utilized in the green synthesis of ZnO nanoparticles. For instance, Ibrahim et al. (2017), Kalpana et al. (2018), Gao et al. (2019) and Mohamed et al. (2019) had successfully synthesized nanosized ZnO using *Aspergillus niger* as a biological reducing and capping agents. The green synthesized products were found to have good UV protection, effective antimicrobial activity and excellent catalytic performance. Furthermore, Fouda et al. (2018) had suggested the synthesis of ZnO nanoparticles using *Aspergillus terreus* which was isolated from contaminated soil. This fungus is able to harness an enormous amount of metabolite substances such as enzyme and protein which are bioactive phytochemicals in the reduction and stabilization of ZnO nanoparticles. The

study presents the attractive application of the green synthesized ZnO nanoparticles in the medical textile finishing due to their effective antibacterial activity and UV protection properties.

2.7 Proposed Mechanism of Green Synthesis

Green synthesis process is basically divided into three steps which are hydrolysis, complexation and decomposition. Bioactive molecules such as polyphenolic compounds and amino acid acts as reducing agent in the synthesis of ZnO nanoparticles by donating π -electrons from carbonyl groups. This results in the formation of Zn complex and reduction of Zn^{2+} ions to zero valent Zn. It is then followed by the decomposition of Zn complex to ZnO nanoparticles through annealing process (Azizi, Shahri and Mohamad, 2017; Chemingui et al., 2019).

Nava et al. (2017) had discussed the mechanism of green synthesis of ZnO nanoparticles using *Camellia sinensis* extract. Firstly, the deprotonation of hydroxyl groups present in the polyphenolic compound of plant extract occurs. It is then followed by the complexation of zinc ions by the deprotonated polyphenolic compounds as ligation agent. ZnO nanoparticles is eventually obtained through thermal decomposition. In this study, the findings discovered the presence of polyphenol compounds as reducing agent which had involved in the formation of ZnO nanoparticles. Furthermore, the role of biomolecules as capping agent had been confirmed attributed to the decrement of crystallite size from 17.47 nm to 9.04 nm with the increasing plant extract amount from 10 mL

to 40 mL.

Besides, Król et al. (2018) suggested that the formation of ZnO nanoparticles via green synthesis was initiated by the complexation of zinc with water molecules in acidic medium. Next, the zinc aqua complex received e^- donated by the deprotonated carboxyl group of bioactive compounds present in the bacteria such as peptidoglycan and enzymes. This results in the formation of aqua-hydroxo-complex which was then transformed into ZnO nanoparticles. The FTIR assay had shown the increment of deprotonated carboxyl group amount with time implying the involvement of biomolecules such as protein and peptidoglycan in the synthesis of ZnO nanoparticles.

Moghaddam et al. (2017) had also related the mechanism of green synthesis to the interaction between hydroxyl groups of amino acids and zinc ions. The secreted amino acid also assisted in the stabilization of ZnO nanoparticles by controlling the growth and minimizing the aggregation of particles. This is further supported by Da'na, Taha and Hessian (2020) which had proved that ZnO nanoparticles exhibited less aggregation with the involvement of *Azadirachta indica* leaves in the synthesis process. In addition, Tripathi et al. (2014) discussed the mechanism of green synthesis involving protein as capping agent of ZnO nanoparticles. The growth of ZnO nuclei induced the stress condition leading to the secretion of protein by the bacterial biomass. The presence of amine and deprotonated carboxyl groups in the ZnO nanoflowers indicated the role of protein as stabilizer during the crystal growth.

2.8 Modification of Green Synthesized ZnO Nanoparticles

2.8.1 Metal Doping

Table 2.10 shows the surface modification of green synthesized ZnO nanoparticles reported in literature. Metal doping is the most common method used in the surface modification of ZnO nanoparticles in order to improve its optical, physical and electrical properties. The introduction of metal such as Ag, magnesium (Mg) and copper (Cu) provides synergistic effect with the semiconductor in a wide variety of applications such as wastewater treatment, optical and electronic devices. Babu and Antony (2019) had investigated the effect of Ag doping on the ZnO nanoparticles synthesized using *Sida Rhombifolia* leaves via green approach. In term of morphology, Ag doping increased the crystallite size of ZnO nanoparticles from 3.42 nm to 4.21 nm and caused more agglomerated structure as compared to pristine ZnO nanoparticles. The research had also revealed that the presence of Ag dopants could promote the photocatalytic efficiencies of ZnO nanoparticles from 87% to 95% and from 55% to 95% in the degradation of MG and MB respectively after 2 hours of exposure to UV irradiation. This was attributed to the role of Ag as e^- sink that improved the separation efficiency of electron-hole pair and hence enhanced the generation of free radicals to mineralize the organic compounds.

Table 2.10: Doping of Green Synthesized ZnO Nanoparticles.

Dopant	Type of dopant	Green source	Particle size	Shape	Band gap	Change in particle size	Change in band gap energy	Application	Reference
Aluminium (Al)	Metal	Cucum sativa fruit	50 nm	Spherical	3.01 eV	Decreased from 100 nm to 50 nm	Decreased from 3.14 eV to 3.01 eV	Solar cell and optoelectronic devices	(Srimathi et al., 2020)
Chitosan	Polymer	Rosa canina fruit	33 - 49 nm	Rod	-	Increased from 29 nm to 41 nm	-	Antibacterial activity	(Hemmati et al., 2020)

Gallium (Ga)	Metal	Azadirachta indica leaves	17 nm	Spherical	-	Decreased from 25 nm to 17 nm	-	Diode	(Annathurai et al., 2019)
Au	Transition metal	Carya illinoensis leaves	-	Irregular shapes	2.91 eV	-	Decreased from 3.02 eV to 2.91 eV	Photocatalytic degradation	(Ahmad et al., 2020b)
Fe	Transition metal	Hibiscus rosa-sinensis leaves	35 - 170 nm	Spherical	3.25 eV	Decreased from 137.5 nm to 102.5 nm	Decreased from 3.39 eV to 3.25 eV	Photocatalytic degradation and antibacterial activity	(Lam et al., 2020)

Lanthanum (La)	Transition metal	Aloe vera leaves	-	Spherical	-	Decreased	-	Fluorescent labels in fingerprints	(Shivananjaiah, Sailaja Kumari and Geetha, 2020)
La Copper oxide (CuO)	Transition metal	Strobilanthes crispus (B.) leaves	62.1 nm	Spherical	2.87 eV	Increased from 58.9 nm to 62.1 nm	Decreased from 3.2 eV to 2.87 eV	Photocatalytic degradation	(Yulizar, Apriandanu and Ashna, 2020)
Mn Mg	Transition metal Alkaline-earth metal	Ocimum tenuiflorum leaves	-	Spherical	3.96 eV	Decreased	Decreased from 3.99 eV to 3.96 eV	Photocatalytic degradation	(Subbiah, Muthukumaran and Raja, 2020)
Manganese oxide	Lanthanide	Vitis vinifera	< 80 nm	Spherical	3.25	-	-	Electrochemical	(Valian,

(MnO ₃)		juice			- 3.6			sensor	Khoobi and
Dysprosium (Dy)					eV				Salavati- Niasari, 2020)
Molybdenum oxide (Mo ₃ O)	Transition metal	Ficus palmata leaves	-	Spherical	-	Decreased	Decreased	Solar cell and other photovoltaic cells	(Shaheen et al., 2020)
Nickel (Ni)	Transition metal	Brassica rapa leaves	-	Spherical	-	Decreased	-	Antibacterial activity and seed germination	(Khan et al., 2021)
Polydopamine	Polymer	Aloe vera leaves	218 nm	Rod and needle	-	Increased from 171	-	Wound healing	(Tavakoli, Kharaziha and

						nm to 218			Nemati, 2021)
						nm			
Ag	Transition metal	Ocimum Tenuiflorum seed	15 - 22 nm	Hexagonal and spherical	2.9 eV	Decreased from 35 nm to 18.5 nm	Decreased from 3.08 eV to 2.9 eV	Photocatalytic degradation and antibacterial activity	(Panchal et al., 2020)
Ag rGO	Transition metal Non-metal	Stigmaphyllon ovatum leaves	28.83 nm	Spherical	2.75 eV	-	Decreased from 3.15 eV to 2.75 eV	Photocatalytic degradation	(Elemike et al., 2019)
SMA-AMT Copolymer	Polymer	Piper nigrum	-	Flakes	2.43 eV	-	Decreased from 3.3 eV to 2.43	Supercapacitor	(Chakraborty, Amal Raj and Mary, 2020)

eV									
Trimesoyl 1,3,5-trimethyl malonate ester (TTDMM)	Polymer	Psidium guajava leaves	17.76 nm	Irregular shapes	-	Decreased from 20 nm to 17.76 nm	-	Antibacterial, antioxidant and anticancer activities	(Gupta, Das and Singh, 2019)
Zinc hexacyanoferrate	Metal	Azadirachta indica	100 nm	Cube and sheet	2.2 eV	Increased	Decreased from 3.3 eV to 2.2 eV	Photocatalytic degradation	(Rani and Shanker, 2018)

In addition, Khan et al. (2018b) had introduced the surface modification of ZnO nanoparticles using metallic Cu by the means of green route. In the work, the presence of Cu as dopants had resulted in the decrement of band gap energy from 3.378 eV to 3.30 eV, enhancement of crystalline structure and increment of particle surface area of ZnO nanoparticles. These properties were beneficial to the application of ZnO nanoparticles as photocatalyst in the wastewater treatment due to the increment of active sites available for the radical generation. Besides, the surface modification brought to the improvement in the biological activities of ZnO nanoparticles such as bactericidal, fungicidal and anticancer activities.

Muthukumar et al. (2019) had also proposed the doping of Fe on ZnO nanoparticles via green synthesis by using *Azadirachta indica* leaves as bio-reductant. The synthesized Fe-doped ZnO nanoparticles was then coated in the electrode of microbial electrochemical cells. Fe dopants were selected because of its excellent electric properties which was desired to improve the performance of the bio-electrochemical application. In addition, Fe-doped ZnO nanoparticles exhibited hydrophilicity property making it a promising coating material of electrode for the development of bio-electric devices. The research also showed an obvious improvement in the power generation which had been achieved by the coating of Fe-doped ZnO nanoparticles on the electrodes of the microbial fuel cell.

Krishnaswamy et al. (2019) had suggested the doping of Mn on the green synthesized ZnO nanoparticles to modulate its optoelectronic properties.

It is noteworthy that a reduction in particle size from 100 nm to 50 nm was observed in Mn-doped ZnO nanoparticles as compared to undoped ZnO nanoparticles. This was mainly attributed to the deceleration of nucleation and growth rates of particles induced by the deposition of Mn in the host ZnO lattice. The optical studies revealed that Mn doping enhanced the absorption of visible light, decreased the band gap energy from 3.14 eV to 3.01 eV and lowered down the chance of electron-hole pair recombination as compared to pristine ZnO nanoparticles. These facts enhanced the potent of ZnO nanoparticles in the applications of optical device and photocatalytic system.

Besides, Umaralikhan and Jaffar (2017) had successfully synthesized ZnO nanoparticles doped with Mg through green synthesis method by using plant extract. The findings revealed that diffusion of Mg into the lattice of ZnO nanoparticles would also induce particle size reduction from 42 nm to 33 nm by restraining the growth of particles. By the means of photoluminescence studies, the defect level of ZnO nanoparticles were found lower by the doping of Mg. Hence, cationic doping could potentially improve the application of ZnO nanoparticles in optoelectronic device.

Furthermore, rare earth metal samarium (Sm) had been utilized by Kumar et al. (2019a) as dopant ions in order to improve the optoelectronic property of green synthesized ZnO nanoparticles. Band gap narrowing was observed varying from 3.40 eV to 3.24 eV with the increasing concentration of Sm dopants from 0.1 mol% to 5 mol%. The results indicated that the doping of Sm led to the broadening of UV-Vis absorption and acceleration of charge

transfer. In addition, the rare earth metal could act as e^- trap that increased the lifetime of electron-hole pairs. The presence of Sm had also improved the conductivity of ZnO nanoparticles which made it to be a suitable material in the application of electrical device.

2.8.2 Polymer Coating

Other than metal doping, polymer is also a favourable candidate applied to tune the properties of ZnO nanoparticles. This in turn enhances the performance of ZnO nanoparticles in a particular application. In the study reported by Chakraborty, Amal Raj and Mary (2020), ZnO/co-polymer nanocomposites had been synthesized successfully by using *Piper nigrum* as biosources while the polymers involved in the incorporation were styrene maleic anhydride (SMA) and 2-amino-5-mercapto-1,3,4-thiadiazole (AMT). In term of optical property, modification using SMA-AMT copolymer could quench the band gap energy of ZnO nanoparticles to 1.95 eV. A reduction in the charge transfer resistance from 8100 Ω to 4900 Ω and an increment in the charge carrier concentration from 5.52×10^{18} to 2.4×10^{19} were observed after the incorporation of the co-polymer. These changes enabled ZnO nanoparticles to have enhanced electrical conductivity as supercapacitor. In addition, the high biocompatibility of ZnO/SMA-AMT nanocomposites made a great achievement in the development of biocapacitor which could be implanted into human body as energy-storage devices.

Besides, the modification of green synthesized ZnO nanoparticles using

polydopamine (PDA) had been proposed by Tavakoli, Kharaziha and Nemati (2021) to optimize the application of ZnO nanoparticles as an antibacterial agent for wound healing. The findings revealed that ZnO nanoparticles coated with PDA could speed up the blood clotting process as compared to bare ZnO nanoparticles. Besides, PDA coating on the green synthesized ZnO nanoparticles improved its biocompatibility even at high concentrations. This in turn enhanced the potential of ZnO nanoparticles in wound healing application. In addition, Krishnaswamy et al. (2019) had proposed the modification of green synthesized ZnO nanoparticles with Mn and sodium iodide-polypyrrole (NaI-PPy) polymer. The findings revealed a significant decrement in the band gap energy of Mn doped ZnO nanoparticles from 2.37 eV to 1.95 eV through the incorporation of NaI-PPy polymer. The synergistic effect of Mn doped ZnO nanoparticles and NaI-PPy also brought to the improved separation efficiency of electron-hole pairs. These properties were beneficial to the application of green synthesized ZnO nanoparticles in hybrid solar cell.

Gupta, Das and Singh (2019) had synthesized ZnO nanoparticles through green synthesis process using *Psidium guajava* leaf extract and modified the nanoparticles using trimesoyl 1,3,5-trimethyl malonate ester (TTDMM). This dendrimer was deemed as a promising material to alter the properties of ZnO nanoparticles such as reduction in band gap energy from 3.65 eV to 3.54 eV without any structural change. The morphological study revealed TTDMM-ZnO nanocomposites had smaller particle size than pure ZnO nanoparticles. Thus, the functional surface area was increased leading to the enhancement in the antioxidant, antibacterial and anticancer activities. In other

words, the synthesis of TTDMM-ZnO nanocomposites provided an important breakthrough in developing anti-cancer nanodrug.

In recent years, there has been an increasing amount of literature reported on the modification of green synthesized ZnO nanoparticles with natural biopolymer such as chitosan and cellulose. As discussed by Preethi et al. (2020), chitosan extracted from shrimp shell could enhance the applications of green synthesized ZnO nanoparticles in environmental and biological fields due to its biodegradability and biocompatibility. Hemmati et al. (2020) had reported an improvement in the antibacterial activity of green synthesized ZnO nanoparticles modified with chitosan as compared to the pure sample. According to Nahi, Radhakrishnan and Beena (2020), the incorporation of cellulose could improve the light absorption of green synthesized ZnO nanoparticles and hence enhance the photocatalytic activity in the degradation of organic substances.

2.8.3 Others

Besides metals and polymers, reduced graphene oxide (rGO) is a promising material to be used in the modification of green synthesized ZnO nanoparticles. Chaudhary et al. (2020) had suggested the doping of rGO on ZnO nanoparticles synthesized using *Sesbania bispinosa*. The presence of rGO as non-metallic dopants was found to enhance the photocatalytic activity of ZnO nanoparticles in the degradation of organic dye. Similar observation was obtained by Lee et al. (2020) implying the positive effect of rGO doping on the performance of Fe-

ZnO nanoparticles as catalyst. This was highly related to the excellent conductivity property of rGO resulting in better efficiency of charge carrier separation. Elemike et al. (2019) had compared the performance of undoped and rGO-Ag co-doped ZnO nanoparticles as photocatalyst in the removal of MB. This was attributed to the reduction in band gap energy of ZnO nanoparticles from 3.15 eV to 2.75 eV induced by the incorporation of rGO and Ag dopants. Besides, the photoluminescence study had discovered an increment the lifetime of electron-hole pairs in the presence of rGO and Ag on the ZnO nanoparticles which was a crucial property to advance the photocatalytic performance of ZnO nanoparticles.

CHAPTER 3

METHODOLOGY

Figure 3.1 shows the flowchart of overall research work in this study. The research was divided into 4 main parts according to the objectives. First of all, the pre-treatment of plant source was conducted prior to the preparation of plant extract. The obtained plant extract was then used in the green synthesis of ZnO nanoparticles. In addition, various characterization techniques were carried out to determine the contents of plant extract. The characterization results could develop better understanding in the mechanism of green synthesis. The optical, chemical and physical properties of the synthesized ZnO nanoparticles were also obtained through different equipment-based characterization techniques. This step was important because the characteristics of ZnO nanoparticles were well-related to the performance as sonocatalysts. This followed by the evaluation of operating parameters such as catalyst dosage, solution pH and ultrasonic power to comprehend their effect on the sonocatalytic degradation of organic dyes. In addition, the optimization of sonocatalytic reaction was conducted by the means of RSM.

Next, the stability of ZnO nanoparticles was one of the key factors to be commercially applied as sonocatalyst. Thus, reusability test was conducted to investigate the sonocatalytic performance of the reused ZnO nanoparticles. Besides, the characterization of the regenerated ZnO samples was included in

this part to develop an in-depth reusability study. Subsequently, the radical scavenging test was carried out to determine the involvement of free radicals in the sonocatalytic dye degradation. In addition, the kinetic of sonocatalytic dye degradation was identified by fitting the experimental data into different kinetic models. This section also involved thermodynamic study which was an important step to understand the nature of the sonocatalytic reaction.

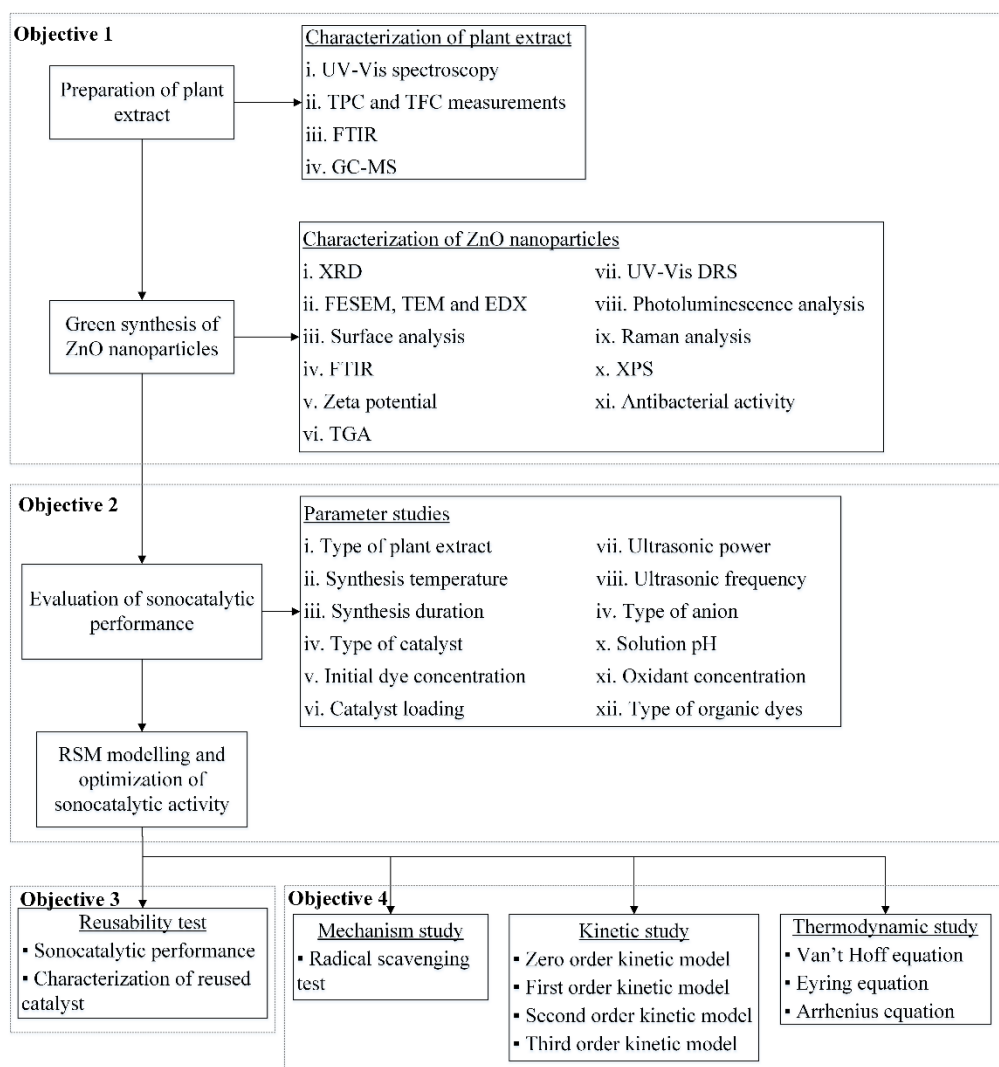


Figure 3.1: Flowchart for Research Overview.

3.1 Chemicals and Materials

The usage of chemical and material was tabulated in **Table 3.1**. All the chemicals were used as received without further purification. The chemical and material list includes the information of brand and purity as well as the respective purpose of usage in this work. For instance, zinc nitrate hexahydrate with 98% purity was purchased from Sigma-Aldrich. It was used as Zn source for the synthesis of ZnO nanoparticles.

Table 3.1: List of Chemicals and Materials.

Chemical/Material	Brand	Purity	Purpose
Zinc nitrate hexahydrate	Sigma-Aldrich	98%	Zn precursor
ZnO	Merck	≥ 99%	Control sample
Silver sulfate	Merck	≥ 95%	Ag precursor
Iron nitrate nonahydrate	Merck	≥ 98%	Fe precursor
NaOH	Merck	≥ 99%	i. Reducing agent for chemical synthesis of ZnO ii. pH adjustment
Hydrochloric acid	Sigma-Aldrich	37%	pH adjustment
<i>Clitoria ternatea</i> Linn	-	-	Plant source
Black tea waste	-	-	Plant source
Hibiscus leaves	-	-	Plant source
Palm leaves	-	-	Plant source

Sodium chloride	Merck	$\geq 99.5\%$	<ul style="list-style-type: none"> i. Electrolyte for zeta potential measurement ii. Anion source for sonocatalytic reaction
DMSO	Sigma-Aldrich	99.9%	Solvent for antibacterial study
<i>E. coli</i>	ATCC	-	Model bacteria for antibacterial study
Ethanol	Merck	$\geq 99.5\%$	<ul style="list-style-type: none"> i. Surface cleaning ii. Bactericidal prior to antibacterial study
Quercetin	Sigma-Aldrich	95%	Standard solution for total flavonoid content (TFC) measurement
Gallic acid	Merck	$\geq 98\%$	Standard solution for total phenolic content (TPC) measurement
Methanol (MetOH)	Merck	$\geq 99.9\%$	<ul style="list-style-type: none"> i. Solvent for TFC measurement ii. Scavenger for sulfate radicals
Sodium carbonate	Merck	$\geq 99.9\%$	<ul style="list-style-type: none"> i. pH adjustment for TPC measurement ii. Anion source for sonocatalytic reaction
Aluminium trichloride	Merck	$\geq 99.9\%$	Reagent for TFC measurement

Folin-Ciocalteu's phenol reagent	Merck	-	Reagent for TPC measurement
Sodium bicarbonate	Merck	≥ 99.7%	Anion source for sonocatalytic reaction
Sodium acetate	Merck	≥ 99%	Anion source for sonocatalytic reaction
MG	Friendemann Schmidt	≥ 99%	Model pollutant for sonocatalytic reaction
CR	R&M Chemicals	40%	Model pollutant for sonocatalytic reaction
RB	Sigma Aldrich	≥ 95%	Model pollutant for sonocatalytic reaction
MB	R&M Chemicals	≥ 82%	Model pollutant for sonocatalytic reaction
MO	R&M Chemicals	≥ 85%	Model pollutant for sonocatalytic reaction
Sodium persulfate	Merck	≥ 98%	Oxidant for sonocatalytic reaction
Digestion solution for COD analysis	Hach	-	Reagent for COD measurement
Total organic carbon (TOC) reagent set	Hach	-	Reagent for TOC measurement
Benzoquinone (BQ)	Merck	≥ 98%	Scavenger for superoxide radicals ($\bullet\text{O}_2^-$)

Isobutanol (IBA)	Merck	$\geq 99.5\%$	Scavenger for hydroxyl radicals ($\bullet\text{OH}$)
Ethylenediaminetetracetic acid disodium (EDTA-2Na)	Duksan	$\geq 99\%$	Scavenger for h^+

3.2 Instruments and Equipment

The instruments and equipment used in this research are listed in **Table 3.2** which included their brand, model and purpose of use. Majority of the instruments and equipment were available in Universiti Tunku Abdul Rahman (UTAR), Sungai Long campus. Both field-emission scanning electron microscope and gas chromatography-mass spectrometer were used in UTAR, Kampar campus. The instruments such as UV-Vis diffuse reflectance, photoluminescence and Raman spectrophotometers were provided by Universiti Malaya (UM) while both transmission electron microscope and X-ray photoemission spectrometer were applied at SIRIM Industrial Research.

Table 3.2: List of Instruments and Equipment Applied throughout the Research.

Instrument/Equipment	Brand/Model	Purpose
Hotplate stirrer	IKA RCT Basic	To heat the solution for plant extraction and ZnO synthesis
Analytical balance	Kern ACJ 220-4M	To determine the weight of substances throughout experiments
Oven	Memmert UNE400	i. To dry plant samples and reused Ag-ZnO ii. To heat the precursor solution for synthesis of ZnO iii. To incubate the <i>E. coli</i>
Furnace	Carbolite Gero RHF 15/8	To calcine ZnO samples
pH meter	Sartorius PB-10	To measure solution pH
Autoclave	Hirayama HICLAVE HVE-50	To sterilize the apparatus and materials before antibacterial test
Ultrasonic cleaner	Elma Transsonic series TI-H-5	To generate ultrasound irradiation for sonocatalytic reaction
Digital reactor block	Hach DRB200	To conduct digestion for COD and TOC measurements
Spectrophotometer	Hach DR3900	To measure COD and TOC of dye solution

Centrifuge machine		Sartorius Sigma 3-18K	To recover Ag-ZnO from treated dye solution
X-ray diffractometer		Shimadzu XRD-6000	To determine the phase information and crystallinity of ZnO nanoparticles.
Scanning electron microscope		Hitachi S-3400N	To observe the antibacterial activity of ZnO nanoparticles.
Field-emission scanning electron microscope		JEOL JSM-7610F	To observe the surface morphology of ZnO nanoparticles.
Transmission electron microscope		JEOL JEM-2100F	To obtain the morphological information of ZnO nanoparticles.
Energy dispersive X-ray spectrophotometer		Hitachi S-3400N	To determine the elemental composition of ZnO nanoparticles.
Adsorption analyzer		Micromeritics 3Flex	To measure the surface area and porosity of ZnO nanoparticles.
Fourier-transform infrared spectrophotometer		Nicolet IS10	To obtain the information of functional groups present on plant extract, ZnO nanoparticles and MG.
Zetasizer		Malvern Zetasizer Nano ZSP	To measure the zeta potential of ZnO nanoparticles.

Thermal analyzer	Perkin Elmer STA 8000	To study the thermal stability of ZnO nanoparticles.
UV-Vis diffuse reflectance spectrophotometer	Perkin Elmer Lambda 35	To obtain the band gap energy of ZnO nanoparticles.
Photoluminescence spectrophotometer	Renishaw inVia Raman Microscope	To compare the separation efficiency of charge carriers of pure and doped ZnO nanoparticles.
Raman spectrophotometer	Renishaw inVia Raman Microscope	To determine the chemical structure and crystallinity of ZnO samples
Freeze dryer	LaboGene CoolSafe	To dry the plant extract prior to FTIR analysis
Inductively coupled plasma-optical emission spectrometer	Perkin Elmer Optima 7000	To determine the leaching of metal after sonocatalytic degradation of dye
X-ray Photoemission Spectrometer	Omicron Multiprobe	To study the electronic state of elements present on the surface of ZnO sample.
Gas chromatography-mass	Shimadzu GCMS-QP2010 Plus	To identify and quantify the phytochemicals present in plant extract

spectrometer

UV-Vis spectrophotometer

Agilent Cary 100

- i. To measure dye concentration
 - ii. To determine the optical properties of plant extract
 - iii. To measure TPC and TFC of plant extracts
-

3.3 Synthesis of ZnO Nanoparticles

3.3.1 Preparation of Plant Extract

Plant extracts were prepared in accordance with the work reported by Karnan and Selvakumar (2016). In this part, plant extracts were obtained by using 4 different plants including *Clitoria ternatea* Linn, black tea waste, hibiscus leaves and palm leaves. The first step of plant extract preparation was the washing of plant to eliminate any contaminant followed by the drying process. Next, 3.0 g of dried plant was added into a conical flask which was filled with 150 mL of distilled water. The liquid medium consisting of dried plant was then refluxed at 120°C for 6 h until a dark color solution was obtained. Filtration of the extract was subsequently carried out using Whatman (No. 40) filter paper after cooling down to room temperature. Prior to the use in the experiment, the filtrate was kept as plant extract inside a refrigerator.

3.3.2 Green Synthesis of Pure and Metal Doped ZnO Nanoparticles

ZnO nanoparticles were synthesized through green route based on the literature reported by Geetha, Nagabhushana and Shivananjaiiah (2016) and Khan et al. (2019) with some modifications. Firstly, 5.0 g of ZnNO₃ was first added into a Teflon vessel containing 50 mL of plant extract. The vessel was then closed tightly and autoclaved at 70 °C for 5 h. The resulting mixture was calcined in a carbide furnace at 400 °C for 2 h with the heating rate of 10 °C/min in air. The powdered form of green synthesized ZnO was grounded using mortar

and pestle. ZnO samples produced using *Clitoria ternatea* Linn, black tea waste, hibiscus leaves and palm leaves were identified as ZnO-C, ZnO-B, ZnO-H and ZnO-P. In this part, ZnO-C exhibited the highest sonocatalytic performance in the degradation of MG. Hence, *Clitoria ternatea* Linn was selected to prepare plant extract for subsequent experiments.

Next, the effect of autoclave temperature was investigated at 50 °C, 70 °C, 90 °C, 110 °C and 130 °C for a duration of 5 h in which ZnO samples were designated as ZnO- γ where γ indicated the value of autoclave temperature. Besides, the effect of autoclave duration was performed at 1 h, 3 h, 5 h and 7 h for an autoclave temperature of 70 °C and the samples were labelled as ZnO- η where η represented the autoclave duration. Hereafter, the green synthesized pure ZnO nanoparticles with the best sonocatalytic efficiency was labelled as Bio-ZnO.

The steps of green synthesis were repeated for the preparation of Fe-ZnO and Ag-ZnO in which iron nitrate and silver sulphate were added to the mixture of ZnNO₃ and plant extract, respectively, before the autoclave process. Besides, chemically synthesized ZnO (Che-ZnO) was also produced by replacing the plant extract with NaOH. In this study, both Che-ZnO and commercial ZnO (Com-ZnO) were used as control samples.

3.4 Characterization of Plant Extract

UV-Vis spectroscopy of plant extract was performed using Agilent Cary

100. A quartz cuvette filled with 4 mL of plant extract was placed in the spectrophotometer and the scanning was conducted over the range of wavelength from 200 to 800 nm. UV-Vis analysis was also repeated for the resulting solution obtained during green synthesis of Ag-ZnO. Both the UV-Vis spectra of the fresh plant extract and the synthesized Ag-ZnO were compared to determine the involvement of bioactive molecules during green synthesis process (Molina et al., 2019).

TPC of plant extract before and after synthesis was determined using Folin–Ciocalteu method as reported by Mbopi et al. (2021) and Sarikhani et al. (2021) Firstly, 0.5 mL of diluted sample was mixed with 2.5 mL of 10 %v/v Folin–Ciocalteu reagent in a centrifuge tube. After 5 mins, 2 mL of 7.5 %w/v sodium carbonate was added into the mixture. The tube was shake upside down for few times to allow well-mixing of the contents. The mixture was then incubated for 1 h prior to the measurement of absorbance at 760 nm using a UV-Vis spectrophotometer. TPC value was recorded in mg of gallic acid equivalent per gram of dry extract (mg/g GAE).

In accordance with Yadavalli et al. (2018), Dowd method was adopted to identify TFC of plant extract. An aliquot of 2.5 mL of diluted sample was firstly mixed with 2.5 mL of 2 %w/v aluminium trichloride in MetOH. Next, the solution was left at room temperature for half an hour prior to the UV-Vis spectroscopy. TFC value was then obtained in mg of quercetin equivalent per gram of dry extract (mg/g QE) through measurement of absorbance at 420 nm.

The functional groups of biomolecules present in plant extract was studied through FTIR using Nicolet IS10. In this case, the intensity of the characteristic peaks for biomolecules would be minimized by the water content which was the major content in plant extract. Therefore, freeze drying of the plant extract was carried out using Labogene CoolSafe to eliminate the moisture content. FTIR spectra of plant extract was obtained within the scanning wavenumbers ranging from 4000 cm^{-1} to 400 cm^{-1} .

Gas chromatography-mass spectrometry (GC-MS) analysis was performed to identify and quantify the bioactive compounds present in plant extract. In this study, Shimadzu GCMS-QP2010 Plus was applied to conduct GC-MS test which was equipped with HP-5MS capillary column. The temperature of column increased from $50\text{ }^{\circ}\text{C}$ to $300\text{ }^{\circ}\text{C}$ at a rate of $10\text{ }^{\circ}\text{C}/\text{min}$ while the injection temperature was set at $130\text{ }^{\circ}\text{C}$. Helium was purged as a carrier gas at the flowrate of $1\text{ mL}/\text{min}$. Mass spectrum was recorded in the m/z range from 50 to 100 with 70 eV of ionization energy. Prior to the analysis, Plant extract was treated with dichloromethane as solvent.

3.5 Characterization of ZnO Nanoparticles

3.5.1 X-ray Diffraction (XRD)

The phase information and crystallinity of the synthesized ZnO samples were analyzed through XRD by using Shimadzu XRD-6000 with Cu-K α radiation which at the wavelength of 1.5406 \AA . Prior to XRD analysis, ZnO

sample was loaded in a sample holder and pressed firmly into a compact form using a piece of glass. The diffraction pattern of ZnO was then recorded within the range of diffraction angle between 5° and 80° with a scanning speed of 2° per min. The crystallite size of all ZnO samples was evaluated using Scherrer equation as shown in **Equation 3.1** (Rathnasamy, Thangasamy and Thangamuthu, 2017):

$$D = \frac{K\lambda}{FWHM \cos \theta} \quad (3.1)$$

Where, D is the crystallite size of sample, K is the shape factor, λ is the wavelength of X-ray spectrum, $FWHM$ is the full width at half maximum of peak and θ is the diffraction angle. Besides, the lattice constants a and c of the ZnO samples can be calculated using **Equation 3.2** where d is the spacing distance between planes while h , k and l are Miller indices (Bagha, Naffakh-Moosavy and Mersagh, 2021).

$$\frac{1}{d^2} = \frac{4h^2 + hk + k^2}{3a^2} + \frac{l^2}{c^2} \quad (3.2)$$

The lattice constants could be then applied to calculate the bond length, L of ZnO via **Equation 3.3** (Fifere et al., 2018):

$$L = \sqrt{\frac{a^2}{3} + c^2 \left(\frac{1}{4} - \frac{a^2}{c^2} \right)^2} \quad (3.3)$$

3.5.2 Field Emission Scanning Electron Spectroscopy (FESEM), Transmission Electron Spectroscopy (TEM) and Energy Dispersive X-ray Spectroscopy (EDX)

The elemental composition of the samples was analyzed through EDX by the means of Hitachi S-3400N. Prior to EDX analysis, ZnO powder was attached to a sample holder using conductive double-sided carbon tape. The same step was repeated for preparation of FESEM sample. In this part, gold sputter coating was performed to enhance the conductivity of electron during FESEM imaging which resulted in the images with better quality. FESEM image was then captured at $\times 50k$ magnification using JEOL JSM-7610F under 4.0 kV of accelerating voltage. In addition, TEM was also carried out by the means of JEOL JEM-2100F to obtain the morphological and crystallographic information of the synthesized samples. The particle size of ZnO sample could be measured based on the image captured through TEM. Prior to TEM analysis, ZnO nanoparticles were firstly dispersed in ethanol. Next, a few drops of the solution containing ZnO sample was placed on a carbon coated copper grid for TEM investigation.

3.5.3 Surface Analysis

An adsorption analyzer, Micromeritics 3Flex was used to collect the physical information of ZnO nanoparticles including porosity and specific surface area. Prior to the analysis, ZnO sample was degassed at 150 °C for 8 h using nitrogen gas. The purpose of degassing was to eliminate the contaminant

adsorbed on the surface of sample which might affect the accuracy of results. In this part, nitrogen gas was also used as analysis gas due to its inert nature and well-known molecular size (0.36 nm).

3.5.4 FTIR

The functional groups present in the prepared ZnO samples were identified through FTIR analysis utilizing a Nicolet IS10 system. In this part, the first step was the cleaning of attenuated total reflectance (ATR) crystal using ethanol. It was then followed by the collection of background spectrum. Next, the sample was placed on the ATR crystal and the sample presser was lowered down until the sample was held in tight proximity to the ATR crystal. The FTIR spectra were collected within the range of wavenumber between 4000 cm^{-1} and 400 cm^{-1} . The functional groups present in the sample were determined with respect to the wavenumbers of the characteristic peak.

3.5.5 Zeta Potential

The zeta potential of ZnO samples was measured using a zetasizer (Malvern Zetasizer Nano ZSP) at the range of pH value between 2 and 12. Firstly, 0.001 M NaCl solution was prepared as electrolyte in the measurement of zeta potential. Next, 0.01 g of ZnO nanoparticles were dispersed in 200 mL of NaCl solution. The pH of solution was then varied using 0.1 M of NaOH and 0.1 M of hydrochloric acid. Thereafter, the solution was injected into a folded capillary zeta cell and the zeta potential of the samples were read using the

zetazizer. A plot of zeta potential versus pH was constructed and zero-point charge (pH_{zpc}) of the sample was denoted as the pH value where the surface net charge of the sample was zero.

3.5.6 Thermogravimetric Analysis (TGA)

Analysis on the thermal stability of the catalysts was performed on the ZnO powder via TGA using a Perkin Elmer thermal analyzer STA 8000. 15 mg of ZnO sample was weighed and loaded in an empty crucible pan. The crucible pan was then placed on the balance of the thermal analyser. The thermal stability of ZnO nanoparticles was investigated in the range of temperature from 30 °C to 1000 °C with the heating rate of 10 °C/min.

3.5.7 UV-Vis Diffuse Reflectance Spectroscopy (UV-Vis DRS)

The spectra of UV-Vis DRS were recorded to obtain the band gap energies of ZnO samples using Perkin Elmer Lambda 35 with barium sulphate as reference. The optical reflectance curve was obtained in the range of wavelength between 300 nm and 800 nm. The band gap energy, E_g of sample was evaluated through Tauc relation as shown in **Equation 3.4** (Ahmad, 2019).

$$\alpha hv = (hv - E_g)^{1/2} \quad (3.4)$$

where α is the optical absorption coefficient and hv is the photon energy represented by Planck's constant ($h = 6.63 \times 10^{-34}$ J s) and frequency of light, ν .

The frequency of light was calculated using **Equation 3.5**.

$$\nu = \frac{c}{\lambda} \quad (3.5)$$

where c is the speed of light (3×10^8 m/s) and λ is the wavelength of light. Besides, the reflectance values, R were inserted into Kubelka–Munk relation as shown in **Equation 3.6** to obtain the values of α (Siva et al., 2020).

$$\alpha = F(R) = \frac{(1 - R)^2}{2R} \quad (3.6)$$

A graph of $(\alpha h\nu)^2$ against $h\nu$ was eventually constructed and the direct band gap energy of ZnO sample was obtained by extrapolating the linear part of the plot to the x-axis of graph at which $(\alpha h\nu)^2$ was equal to zero value.

3.5.8 Photoluminescence Spectroscopy (PL)

The separation efficiency of electron-hole pair of ZnO nanoparticles was determined through photoluminescence spectroscopy (PL) by using a Raman microscope (Renishaw inVia Raman Microscope) with an excitation wavelength of 325 nm. In PL analysis, the photon energy would be absorbed by the e^- present on the surface of ZnO nanoparticles. The photo-excited e^- would then relocate to a higher energy level. Photon energy would be released while the e^- returns to the lower electronic state. Hence, the observation of high photoluminescence intensity indicated the high recombination rate of electron-

hole pair.

3.5.9 Raman Analysis

Raman analysis was performed by the means of a Renishaw inVia Raman spectrometer with a laser of 532 nm wavelength. Raman spectra was recorded at the range of wavenumber between 100 and 800 cm^{-1} . Com-ZnO was used as control to study the Raman spectrum light and chemical bonds present in ZnO nanoparticles provided the crystal structure information of the samples.

3.5.10 X-ray Photoemission Spectroscopy (XPS)

XPS analysis was conducted in this study in order to determine the chemical structure and oxidation state of elements present Ag-ZnO. By the means of Omicron Multiprobe spectrometer, Al $K\alpha$ with 1480 eV of binding energy was used as X-ray irradiation source to record the XPS spectrum of sample. The calibration reference of XPS analysis was C 1s which exhibited characteristic peak at 284.6 eV.

3.5.11 Antibacterial Activity

Before conducting the antibacterial test, all the glassware, culture medium, nutrient agar and saline solution were sterilized by autoclaving at 120 °C for 15 mins. The antibacterial activity test of prepared samples was carried out by disc diffusion method against *E. coli* as proposed elsewhere (Kasi

and Seo, 2019). Firstly, 100 μL of fresh broth culture was swabbed evenly throughout the prepared nutrient agar plate using a sterile L-shaped glass rod. 10 mg of Com-ZnO was suspended in 1 mL of DMSO. Next, a filter paper disc with 4 mm diameter was impregnated with the DMSO solution containing Com-ZnO nanoparticles and placed on the surface of agar plate. After that, the plate was placed upside down in an oven at 37 °C for 24 h incubation. The size of the zone of inhibition was observed and measured after overnight incubation. The filter disc was then removed from the agar plate and observed by the means of SEM using Hitachi S-3400N. The steps were repeated for Che-ZnO, Bio-ZnO, Ag-ZnO and Fe-ZnO. Besides, a control plate was prepared by impregnating the filter paper disc with the DMSO solution without any ZnO sample.

3.6 Evaluation of Sonocatalytic Performance of ZnO Nanoparticles

The catalytic activity of the synthesized ZnO nanoparticles was investigated through the degradation of MG under ultrasound irradiation. The sonocatalytic performance evaluation was carried out using an Elma Transsonic series TI-H-5 ultrasonic bath with the operating settings at 45 kHz and 80 W of power. **Figure 3.2** presents the schematic diagram of experimental setup for sonocatalytic degradation of dye solution. In a typical catalytic dye degradation experiment, a specified amount of ZnO nanoparticles was dispersed as catalyst in dye solution followed by the addition of sodium persulfate as oxidant. The ultrasonic bath was then covered with a lid to block the transmission of light from surrounding to the reacting solution. The ultrasonic bath switched on immediately and every 5 mL aliquot of dye was collected at regular time

intervals in which the reaction was lasting for 60 mins. The sample was filtrated to separate the catalysts before subjected to liquid sample analysis. A single-beam UV-vis spectrophotometer (Agilent Cary 100) was used to monitor the catalytic performance of ZnO nanoparticles in dye degradation by measuring the concentration of dye samples collected at a maximum absorbance wavelength of 617 nm. The degradation efficiency of dye was evaluated using **Equation 3.7** where C_o is the initial dye concentration and C_t is dye concentration at time t .

$$\text{Degradation efficiency} = \frac{C_o - C_t}{C_o} \times 100\% \quad (3.7)$$

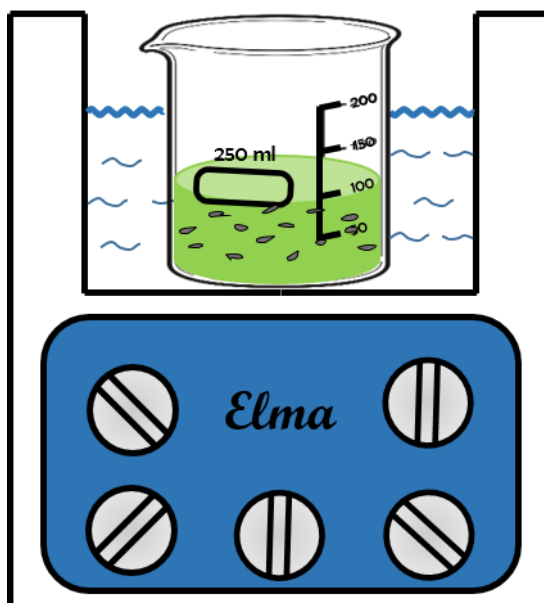


Figure 3.2: Schematic Diagram of Sonocatalytic Reaction.

In this study, the dye solution was also exposed to the ultrasound irradiation in the absence of both catalyst and oxidant in order to study the effect of sonolysis on the degradation of aqueous dye solution. Besides, the effect of

initial dye concentration on the degradation of dye was observed by varying the initial concentration of MG at 500 mg/L, 1000 mg/L, 1500 mg/L, 2000 mg/L and 2500 mg/L with the constant catalyst loading (0.5 g/L), ultrasonic power (40 W). The experiment on the influence of catalyst loading was then conducted by adjusting the amount of catalyst loading at 0.1 g/L, 0.25 g/L, 0.5 g/L, 1.0 g/L, 1.5 g/L and 2.0 g/L. The ultrasonic power was also altered in the range between 20 W and 100 W to examine its impact on the sonocatalytic degradation. In addition, the frequency of ultrasound irradiation was varied at 25 kHz and 45 kHz to understand its effect on the sonocatalytic degradation of dye.

Besides, 250 mg/L of sodium bicarbonate was added as the source of bicarbonate anions (HCO_3^-) into the reaction mixture to study the sonocatalytic degradation of dye solution in the presence of inorganic anions. The effect of other anions such as acetate anions (CH_3COO^-), carbonate anions (CO_3^{2-}) and chloride anions (Cl^-) were studied by adding sodium acetate, sodium carbonate and sodium chloride, respectively at the constant concentration of 250 mg/L. The parameter study was then followed by the effect of solution pH on the sonocatalytic degradation of dye. The solution pH was varied in the range from pH 2 to pH 10 by adding 0.1 M of hydrochloric acid or 0.1 M of NaOH. Furthermore, the amount of sodium persulfate as an oxidant of the sonocatalytic reaction was adjusted in between 0 mM and 5.0 mM to investigate its impact on the sonocatalytic degradation of dye. In addition, MG dye was replaced by MB, RB, MO and CR to study the effect of various organic dye on the sonocatalytic performance of ZnO samples. The maximum absorbance wavelengths of MB, RB, MO and CR were set at 665 nm, 555 nm, 464 nm and 500 nm, respectively.

3.7 RSM Modelling and Optimization

In this study, RSM was applied to determine the optimal operating condition of the MG degradation with the minimum experiment runs. By the means of RSM, time saving can be achieved as compared to one-factor-at-a-time approach as the number of experiment sets was reduced significantly. Central composite design (CCD) was applied for the experimental optimization as CCD model established well-fitting on a quadratic surface. In addition, CCD model was employed to evaluate the individual impact of process factors on the dye degradation efficiency and their interactions between each other. Design Expert Version 11 Software was used to develop the experimental matrix of CCD model. The number of experiment runs needed, N was calculated using **Equation 3.8** where k is the number of experimental variables and C_p is the number of central points.

$$N = 2^k + 2k + C_p \quad (3.8)$$

By using CCD model, 3 experimental parameters including catalyst loading, initial dye concentration, ultrasound power and oxidant concentration were selected as independent variables for the process optimization. These factors were coded as -1 and +1 to represent the low level and high level, respectively. **Table 3.3** shows the codes and levels of factors selected for optimization study.

Table 3.3: Experimental Factors with Their Unit, Code and Level.

Factors	Unit	Code	Levels	
			-1	+1
Catalyst loading	g/L	A	0.75	1.50
Initial dye concentration	mg/L	B	500	1250
Ultrasound power	W	C	40	80
Oxidant concentration	mM	D	0.75	1.75

After collecting the experimental data, a second-order polynomial modelling as shown in **Equation 3.9** was applied to express the model performance where the response of this experiment is dye degradation efficiency, β_o is the constant coefficient, β_i , β_{ii} and β_{ij} are interaction coefficients of linear, quadratic and second-order terms, x_i and x_j are independent variables and ε is the error.

$$Response = \beta_o + \sum_{i=1}^k \beta_i x_i + \sum_{i=1}^k \beta_{ii} x_i^2 + \sum_{i=1}^{k-1} \sum_{j=1}^k \beta_{ij} x_i x_j + \varepsilon \quad (3.9)$$

The statistical significance of the model at 95% confidence level was then evaluated using the analysis of variance (ANOVA) technique. F-test was applied to determine adequacy of the developed model in the prediction of a variation in experimental data without exceeding the confidence limit. In addition, the

regression coefficient (R^2) and the lack of fit (LOF) were important to analyse the feasibility of the resulting model. On the point of view, a strong R^2 value and less significant LOF were desired to determine the validity of the designed model. In addition, three dimensional response surface plots were generated to identify the impact of each factor and the interactive between parameters.

Besides, model validation was conducted by selecting 5 sets of model to compare their actual and estimated response. The percentage error, $PE\%$ between the experimental value, E and estimated value, T was evaluated using **Equation 3.10**.

$$PE\% = \frac{|E - T|}{T} \times 100\% \quad (3.10)$$

The optimum condition for the sonocatalytic degradation of MG dye was determined using the results obtained from RSM. The treated MG solution were measured using double beam UV-Vis spectrophotometer to study the decomposition of MG molecules under ultrasound irradiation. In addition, COD analysis was conducted with the aid of test kits available commercially to confirm the mineralization of dye in the presence of Ag-ZnO nanoparticles under ultrasonic irradiation in which the COD level was measured using a colorimeter (Hach DR 3900).

3.8 Reusability Test of Ag-ZnO Nanoparticles

The reusability of Ag-ZnO was investigated by recovering the catalyst from the treated solution through centrifugation. The obtained Ag-ZnO sample was then washed at least three times using distilled water. Next, the catalyst was dried at 80 °C overnight in an oven. After completion of the recovery process, the sonocatalytic performance of the reused Ag-ZnO was investigated by studying the degradation efficiency of MG under similar optimum condition. In this part, the steps were repeated to observe the stability of catalyst for up to 10 catalytic cycles. Besides, the characterization of reused Ag-ZnO was performed through XRD, FTIR, TGA, EDX and surface analysis. The results of sonocatalytic reaction and characterization of recovered samples were then compared with the fresh Ag-ZnO to justify the reusability of the sonocatalyst. In addition, the robustness of Ag-ZnO was determined through inductively coupled plasma-optical emission spectroscopy (ICP-OES) by measuring the amount of metal ions leached into the sonocatalytic-treated solution. ICP-OES was conducted using Perkin Elmer Optima 7000.

3.9 Mechanism Study of Sonocatalytic Degradation of MG

Furthermore, radical scavenging test was conducted to identify the radicals present in the reaction system which were responsible in the degradation of MG dye. In this experiment, chemical scavenger was added into MG dye solution at a constant 1/500 molar ratio of MG to scavenger to quench particular radicals (Kaur et al., 2019). During chemical scavenging test, BQ,

MetOH, IBA and EDTA-2Na were used as chemical scavengers for $\bullet\text{O}_2^-$, sulphate radicals, $\bullet\text{OH}$ and h^+ , respectively.

3.10 Kinetic Study

The evaluation of reaction kinetic was conducted to determine the potential rate controlling steps. The information was useful in the design of commercial-scale system. In this research, the kinetic of sonocatalytic degradation of MG was investigated by four kinetic models including zero order, first order, second order and third order kinetic models. The experimental data were fitted into the linear plot of each kinetic model as listed in **Table 3.4** (Kumar et al., 2020). The reaction rate constant is labelled as k in the kinetic models.

Table 3.4: Kinetic Models Adopted to Evaluate Sonocatalytic Degradation of MG.

Model	Equation	Linear form	Plot
Zero order	$r = -\frac{dC}{dt} = k_0$	$C_o - C_t = k_0 t$	$(C_o - C_t) \text{ vs } t$
First order	$r = -\frac{dC}{dt} = k_1 C$	$\ln\left(\frac{C_o}{C_t}\right) = k_1 t$	$\ln\left(\frac{C_o}{C_t}\right) \text{ vs } t$
Second order	$r = -\frac{dC}{dt} = k_2 C^2$	$\frac{1}{C_t} - \frac{1}{C_o} = k_2 t$	$\left(\frac{1}{C_t} - \frac{1}{C_o}\right) \text{ vs } t$
Third order	$r = -\frac{dC}{dt} = k_3 C^3$	$\frac{1}{C_t^2} - \frac{1}{C_o^2} = k_3 t$	$\left(\frac{1}{C_t^2} - \frac{1}{C_o^2}\right) \text{ vs } t$

Half-life of reaction ($t_{1/2}$) is the time required to reduce the concentration of reaction by half relative to its initial concentration which can be evaluated using the following equations (Ahmad et al., 2020a):

Zero order kinetic model:

$$t_{1/2} = \frac{C_o}{2k_0} \quad (3.11)$$

First order kinetic model:

$$t_{1/2} = \frac{\ln 2}{k_1} \quad (3.12)$$

Second order kinetic model:

$$t_{1/2} = \frac{1}{k_2 C_o} \quad (3.13)$$

Third order kinetic model:

$$t_{1/2} = \frac{3}{k_3 C_o^2} \quad (3.14)$$

3.11 Thermodynamic Study

In this section, Van't Hoff equation was applied to evaluate the influence of temperature on the equilibrium condition and obtain the values of standard enthalpy (ΔH°) and standard entropy (ΔS°) as shown in **Equation 3.15** (Sharma et al., 2022):

$$\ln K_e = \frac{\Delta S^\circ}{R} - \frac{\Delta H^\circ}{RT} \quad (3.15)$$

where R is gas constant ($8.314 \text{ J mol}^{-1} \text{ K}^{-1}$) and T is temperature (K). The parameter, K_e is the apparent equilibrium constant which can be evaluated using **Equation 3.16** where C_e are dye concentration at equilibrium condition (Samuel, Shang and Niu, 2022).

$$K_e = \frac{C_o - C_e}{C_e} \quad (3.16)$$

The thermodynamic parameters obtained from Van't Hoff equation were then adopted to calculate the standard Gibbs energy (ΔG°) via **Equation 3.17** which was the spontaneity indicator of the reaction.

$$\Delta G^\circ = \Delta H^\circ - T\Delta S^\circ \quad (3.17)$$

In addition, Eyring equation was employed to understand the variance of reaction rate constant with temperature. In addition, it provides the activated thermodynamic parameters at the transition state including enthalpy of activation (ΔH^\ddagger) and entropy of activation (ΔS^\ddagger). **Equation 3.18** shows the Eyring equation which depicts the temperature dependence of the reaction rate constant (Saleh and Taufik, 2019):

$$k = \frac{k_b T}{h} e^{-\frac{\Delta G^\ddagger}{RT}} \quad (3.18)$$

where k_b is Boltzmann constant ($1.380 \times 10^{-23} \text{ J K}^{-1}$) and h is Planck's constant

(6.626×10^{-34} J s). The value of activated Gibbs energy (ΔG^\ddagger) can be expressed in terms of activation parameters as shown in Equation 3.19.

$$\Delta G^\ddagger = \Delta H^\ddagger - T\Delta S^\ddagger \quad (3.19)$$

Together with **Equation 3.19**, Eyring equation could be derived into the linear equation as shown in **Equation 3.20** which describes the linear relationship between $\ln \frac{k}{T}$ and $\frac{1}{T}$ (Owija, Kosa and Abdel Salam, 2021).

$$\ln \frac{k}{T} = -\frac{\Delta H^\ddagger}{RT} + \ln \frac{k_b}{h} + \frac{\Delta S^\ddagger}{R} \quad (3.20)$$

Arrhenius equation was applied to calculate the activation energy, E_a of sonocatalytic degradation of MG. **Equation 3.21** and **Equation 3.22** show the original Arrhenius equation and its linearized form, respectively (Rezaei and Nezamzadeh-Ejhiha, 2020):

$$k = Ae^{-\frac{E_a}{RT}} \quad (3.21)$$

$$\ln k = \ln A - \frac{E_a}{RT} \quad (3.22)$$

where k is the reaction rate constant and A is the Arrhenius constant. The value of E_a could also be evaluated using **Equation 3.23** which was derived from both Eyring and Arrhenius equations (Esania et al., 2022):

$$E_a = \Delta H^\ddagger + RT \quad (3.23)$$

CHAPTER 4

RESULTS AND DISCUSSION

4.1 Characterization of ZnO

4.1.1 XRD

Figure 4.1 shows XRD spectra of the synthesized ZnO nanoparticles obtained in the range of 2θ from 5° to 80° . The diffractogram with high intensity and narrow peaks indicated that the ZnO samples present in high crystallinity. The characteristic peaks observed in the spectra of all the samples confirmed the formation of ZnO nanoparticles with hexagonal wurtzite crystal structure as identified in JCPDS card no: 36-1451 (Mabhouti et al., 2021). The diffraction peaks recorded at $2\theta = 31.8^\circ, 34.4^\circ, 36.3^\circ, 47.6^\circ, 56.6^\circ, 62.9^\circ, 66.4^\circ, 68.0^\circ$ and 69.1° are assigned to the planes (100), (002), (101), (102), (110), (103), (200), (112) and (201), respectively (Jayachandran, Aswathy and Nair, 2021).

As compared to Com-ZnO and Che-ZnO, it is noteworthy that there is no extra peak observed in the XRD spectrum of Bio-ZnO. The findings confirmed that ZnO nanoparticles with high purity were obtained successfully through green synthesis by using *Clitoria ternatea* Linn. The additional peaks observed in Ag-ZnO at $2\theta = 38.1^\circ, 44.3^\circ, 64.4^\circ$ and 77.3° were attributed to the

planes (111), (200), (220) and (311) of pure metallic Ag, respectively, which is in line with JCPDS card no: 04-0783 (Yaseri Nasab and Bahiraei, 2020). These extra peaks proved the presence of face-centered cubic Ag on Ag-ZnO. However, the hexagonal phase of ZnO lattice was the main structure of Ag-ZnO attributed to its high intensity of diffraction peaks as compared to the peaks of metallic Ag. Besides, a little shift of peak positions to larger theta values were noticed in the XRD spectrum of Fe-ZnO. The results confirmed the successful incorporation of Fe ions into ZnO lattice without altering the hexagonal wurtzite structure of ZnO nanoparticles. The findings was in good agreement with the work reported by Chang, Chang and Wu (2020) in which the position of major peaks of ZnO nanoparticles experienced slightly shift due to the Al doping in Zn site.

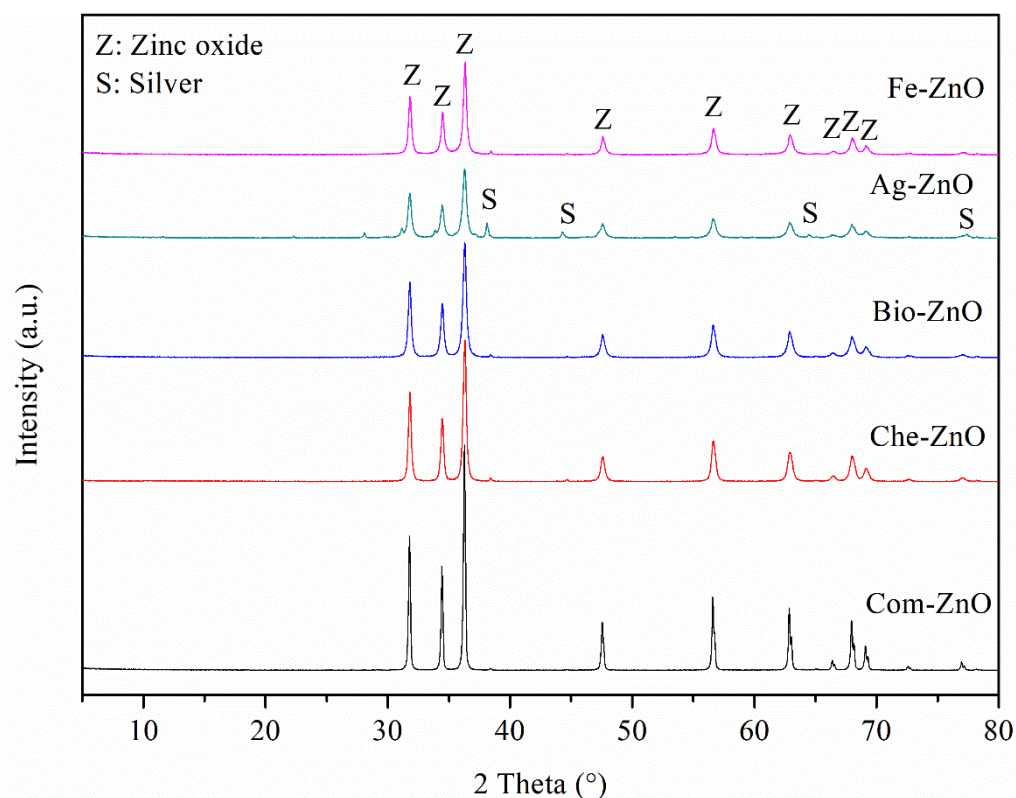


Figure 4.1: XRD Patterns of Com-ZnO, Che-ZnO, Bio-ZnO, Ag-ZnO and Fe-ZnO.

The lattice constants a and c of the ZnO samples are listed in **Table 4.1**. The lattice constants a and c were found to be almost constant for all the ZnO samples at the values of 3.25 Å and 5.21 Å, respectively. The values of lattice parameters were found in consistent with the standard values ($a = b = 3.249$ Å, $c = 5.206$ Å) (Roguai and Djelloul, 2021). It is noteworthy that the lattice parameters of Ag-ZnO were slightly larger than undoped ZnO while the lattice constants and Zn-O bond length of Fe-ZnO were smaller as compared to that of undoped ZnO. The results were attributed to the difference of ionic radii between the host and dopant ions. As the ionic radius of Ag^+ ion (1.22 Å) is larger than Zn^{2+} ion (0.74 Å), the substitution of Zn^{2+} ions by Ag^+ ions in the lattice brings to the increments in the lattice parameters (Boulahlib et al., 2021; Dhananjaya et al., 2021). The findings were in line with the work reported by Rohith et al. (2018) where partial substitution took place in the Ag doping of ZnO. In the case of Ag doping, the presence of Ag dopant was preferred in the substitutional sites of ZnO than interstitial sites due to the large ionic radius of Ag dopant (Mangala Nagasundari et al., 2021). In contrast to the case of Ag-ZnO, the lattice parameters of Fe-ZnO were smaller than undoped ZnO because Fe^{3+} ions have smaller ionic radius (0.67 Å) than Zn^{2+} ions (Mohsin et al., 2021). The c/a ratio was estimated to be 1.602 for all the ZnO samples in which this value was close to the standard c/a ratio of wurtzite structure (1.633) (Roguai and Djelloul, 2021). The findings indicated that the hexagonal structure of ZnO nanoparticles was preserved upon green synthesis and doping (Fifere et al., 2018).

Table 4.1: XRD Parameter Values of ZnO Samples.

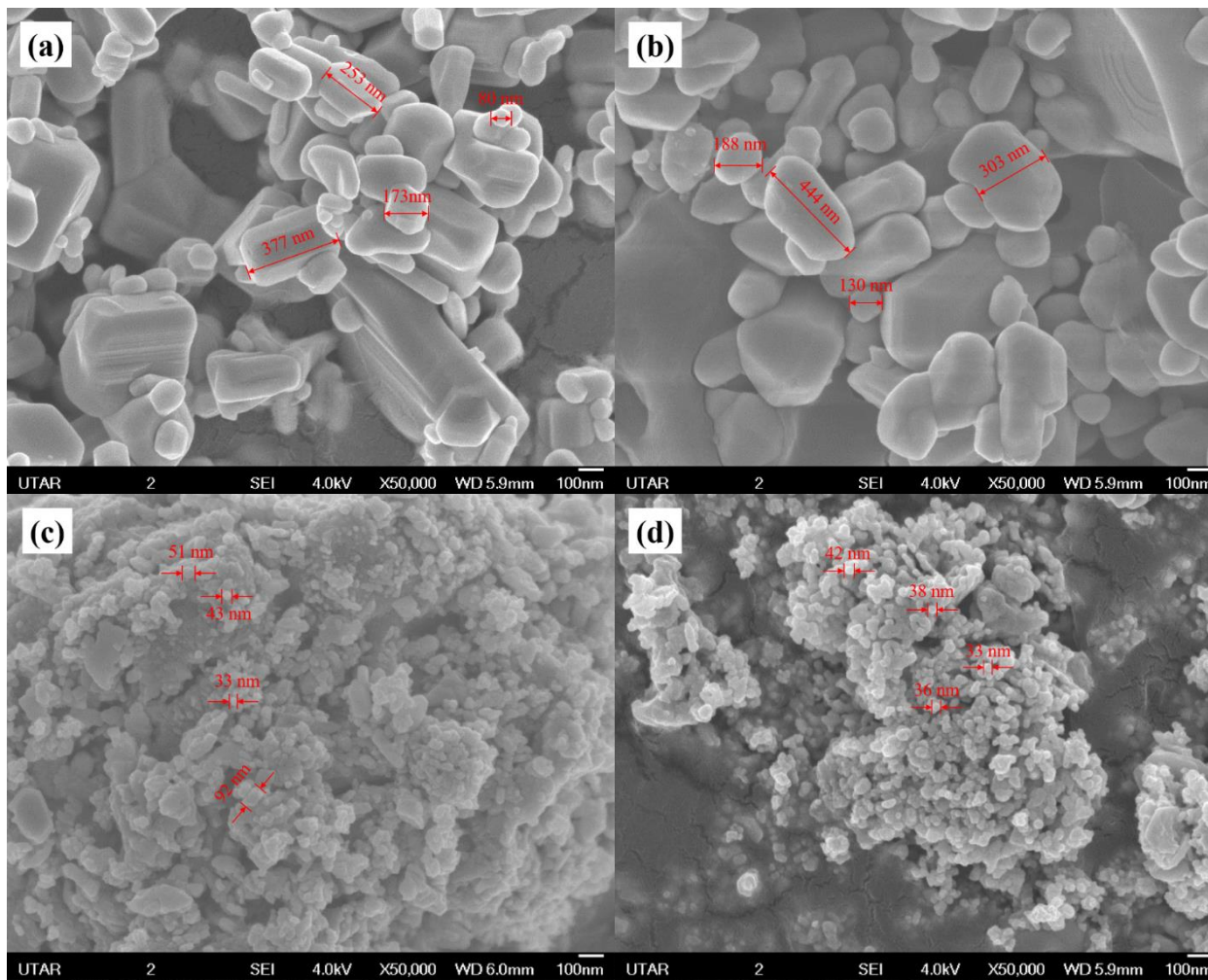
Sample	Crystallite size (nm)	Lattice parameters			L (nm)
		a = b (nm)	c (nm)	c/a	
Com-ZnO	50	0.3251	0.5207	1.602	0.1978
Che-ZnO	30	0.3249	0.5206	1.602	0.1977
Bio-ZnO	28	0.3249	0.5205	1.602	0.1978
Ag-ZnO	23	0.3250	0.5206	1.602	0.1978
Fe-ZnO	29	0.3247	0.5201	1.602	0.1976

As tabulated in **Table 4.1**, the average crystallite size of Com-ZnO, Che-ZnO, Bio-ZnO, Ag-ZnO and Fe-ZnO calculated using Scherrer's equation were 50 nm, 30 nm, 28 nm, 23 nm and 29 nm, respectively. The crystallite size of Bio-ZnO was smaller than Com-ZnO and Che-ZnO due to the presence of capping agent in plant extract which could control the grain growth. The results was found to be in accordance with Abdullah, Abu Bakar and Abu Bakar (2021) and Kumar et al. (2019) indicating green synthesis could fabricate ZnO nanoparticles with smaller crystallite size as compared to chemical approach. Besides, the crystallite size of ZnO nanoparticles also decreased with Ag incorporation due to the restraint of grain growth. Similar results were reported by Bagha, Naffakh-Moosavy and Mersagh (2021) and Yousefi et al. (2020) in which segregation of the ZnO grain boundary was induced by Ag doping. Therefore, Ag doping inhibited the grain growth and decreased the crystallite size.

4.1.2 FESEM, TEM and EDX

Figure 4.2 shows the surface morphologies of ZnO samples observed using FESEM and TEM. The FESEM images showed that the particle size of ZnO samples was fall in the range of 33 nm and 444 nm which was larger than the estimated crystallite size (25 – 50 nm). This was mainly caused by the increment of surface energy during the calcination process under high temperature. This would then lead to the sintering effect which promoted the aggregation of crystals and growth of particle (Aydoğan et al., 2017; Zhang et al., 2022d).

The FESEM images also confirmed that Com-ZnO and Che-ZnO present in cylindrical shape while Bio-ZnO exhibited spherical shape. Besides, the particle size of Com-ZnO was estimated to be in the range of 80 nm and 377 nm, while Che-ZnO had irregular particle size ranging from 130 nm to 444 nm. It is worth noting that Bio-ZnO exhibited the smallest particle size (33 nm – 92 nm) as compared to Com-ZnO and Che-ZnO. Particle agglomeration was observed in Bio-ZnO nanoparticles because particles with smaller size possessed higher surface energy (Safardoust-Hojaghan et al., 2021). Therefore, higher potential of agglomeration was resulted.



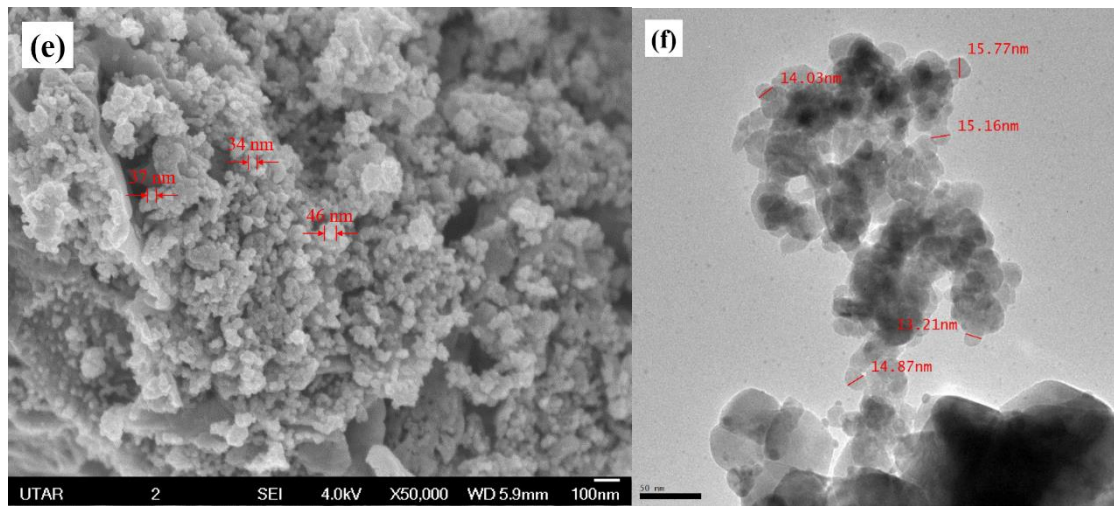


Figure 4.2: FESEM Images of (a) Com-ZnO, (b) Che-ZnO, (c) Bio-ZnO, (d) Ag-ZnO and (e) Fe-ZnO Captured at Magnification x50 000 and (f) TEM Image of Ag-ZnO Obtained at Magnification x43 000.

FESEM results also remarked that both Ag and Fe doping remained the particle shape of ZnO nanoparticles with smaller particle size. The incorporation of metal as dopant in the lattice of ZnO might restrict the crystal growth leading to the decrement in particle size (Srimathi et al., 2020). Khan et al. (2020) and Subbiah, Muthukumaran and Raja (2020) also observed the reduction in ZnO particle size due to the doping of metals such as Cu and magnesium (Mg). Smaller particle size was one of the desired properties to design a catalyst. This was because particles with higher surface-to-volume ratio provided greater surface area available for the adsorption of reactants and hence led to the higher sonocatalytic performance (Lam et al., 2021). TEM image of Ag-ZnO illustrated in **Figure 4.2(f)** showed that the sample presented in spherical shape with homogeneous particle size ranging between 13.21 and 15.77 nm. The darker spots were attributed to the presence of Ag dopant on the surface of ZnO which was consistent with the literature reported by Liu et al. (2019) and Vaiano et al. (2018).

Table 4.2 lists the elemental information of ZnO samples. The samples were mainly consisted of Zn and O elements and nearly 1 to 1 atomic ratio of Zn to O was detected. EDX analysis was in line with the findings of XRD analysis that confirmed the successful synthesis of ZnO nanoparticles using *Clitoria ternatea* Linn plant via green synthesis which was an environmentally friendly approach. In addition, the content of Ag detected in Ag-ZnO was found to be 4.3 wt% while the weight percentage of Fe present in Fe-ZnO was 4.8 wt%. The findings indicated that Ag and Fe were incorporated successfully in the matrix of ZnO nanoparticles with the weight percentage close to the desired

value (5 wt%). The deviation of actual Ag content in Ag-ZnO from the targeted value was due to the leaching of silver during the synthesis process (Narjis et al., 2020). Besides, the presence of other elements in the sample such as carbon (C), nitrogen (N) and sulphur (S) would also result in the difference between actual and desired dopant content. Negligible amount of C detected in Com-ZnO and Che-ZnO was originated from the carbon conductive tape used in EDX analysis (Aldeen, Ahmed Mohamed and Maaza, 2022). High amount of C and N present in Bio-ZnO, Ag-ZnO and Fe-ZnO due to the involvement of phytochemicals such as polyphenolic compounds and amino acid from *Clitoria ternatea* Linn plant in the green synthesis process. Alrajhi et al. (2021) also reported the presence of C and N contents in the green synthesized ZnO samples which was contributed by the biomolecules of *salvia officinalis* extract. Besides, high amount of sulphur was detected in Ag-ZnO due to the residue of silver sulphate which was used as dopant precursor during synthesis process.

Table 4.2: EDX Results of ZnO Samples.

Sample	Wt%							At%						
	Zn	O	Ag	Fe	C	N	S	Zn	O	Ag	Fe	C	N	S
Com-ZnO	87.3	12.2	0.0	0.0	0.5	0.0	0.0	62.6	35.6	0.0	0.0	1.8	0.0	0.0
Che-ZnO	64.9	31.6	0.0	0.0	3.4	0.0	0.0	30.5	60.8	0.0	0.0	8.7	0.0	0.0
Bio-ZnO	81.9	15.6	0.0	0.0	1.8	0.7	0.0	51.6	40.2	0.0	0.0	6.3	1.9	0.0
Ag-ZnO	74.2	16.0	4.3	0.0	4.1	0.6	0.8	47.3	41.5	1.6	0.0	6.7	1.8	1.1
Fe-ZnO	76.8	14.9	0.0	4.8	2.6	1.0	0.0	47.4	37.5	0.0	3.5	8.8	2.8	0.0

4.1.3 Surface Analysis

Figure 4.3 (a) - (e) displays the nitrogen adsorption-desorption isotherms of various ZnO samples. According to IUPAC classification, all the isotherm curves were of Type IV with H3 hysteresis loop, elucidating that ZnO nanoparticles exhibited slit-like shaped mesoporous structure (Dmochowska et al., 2020). As shown in the isotherms, the adsorbed volume of nitrogen increased at low relative pressure due to the formation of monolayer on the surface of ZnO nanoparticles. It was then followed by the formation of multilayers at higher relative pressure giving rise to the continuous increment in the adsorbed volume of nitrogen. A hysteresis loop was noticed at the isotherm of all the samples which confirmed that nitrogen desorbed at lower relative pressure as compared to the adsorption of nitrogen. This phenomenon occurred due to the capillary condensation of mesopores which caused a delay in the desorption of nitrogen gas (Siddique, Fayaz and Saeed, 2021). Therefore, the hysteresis loop indicated that all the ZnO samples were mesoporous materials. Mesoporous structure is one of the desired properties of a catalyst which provides higher surface area for the adsorption of reactant and ensures the reactants can enter the pores of catalyst and adsorb onto the active sites located at the interior of catalyst.

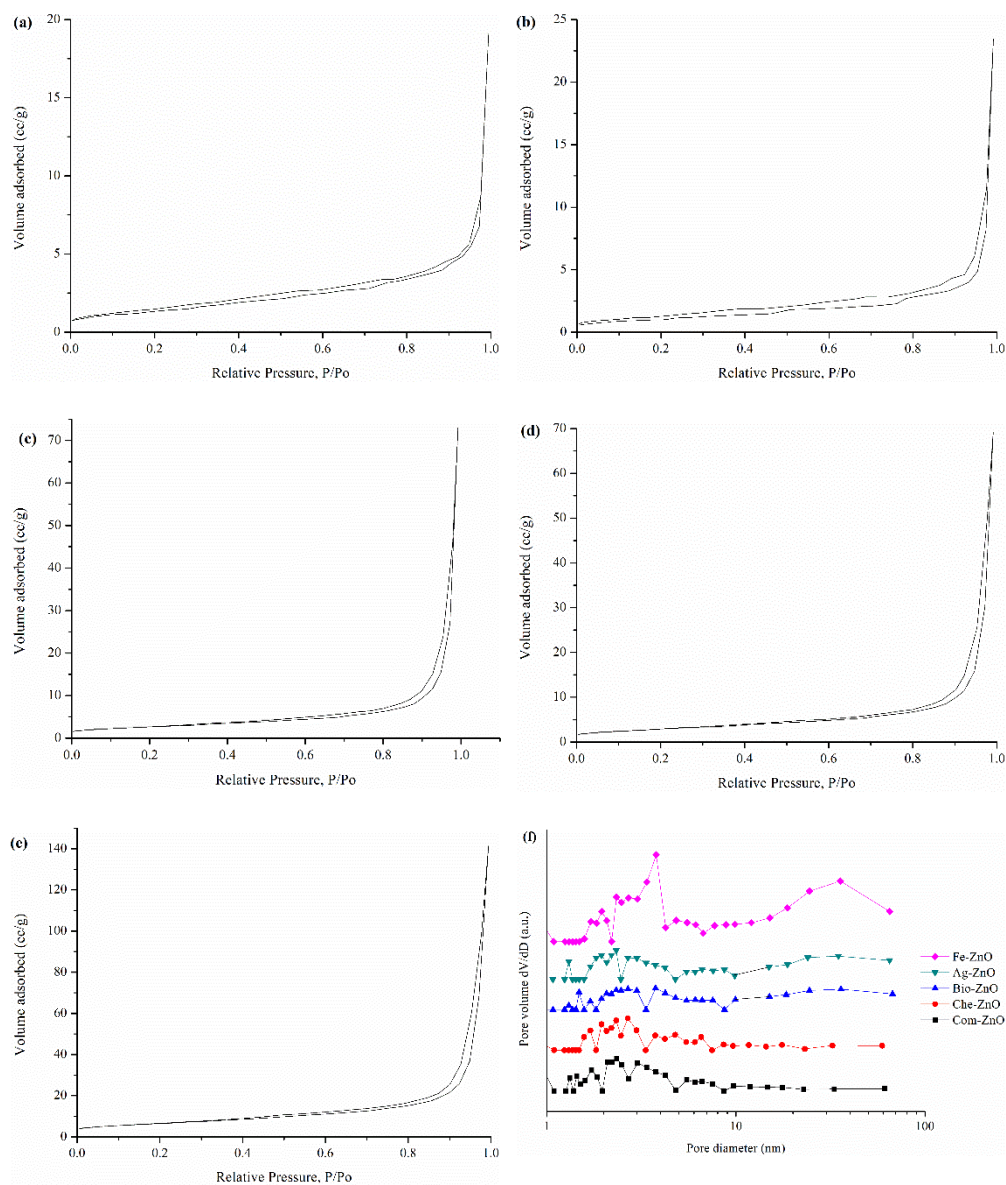


Figure 4.3: Nitrogen Adsorption-desorption Isotherms of (a) Com-ZnO, (b) Che-ZnO, (c) Bio-ZnO, (d) Ag-ZnO and (e) Fe-ZnO, and (f) BJH Pore Distribution Plots of ZnO Samples.

Figure 4.3 also shows that the volume of nitrogen adsorbed on Bio-ZnO was the highest as compared to Com-ZnO and Che-ZnO. Besides, ZnO nanoparticles doped with Ag and Fe showed relatively higher nitrogen uptake than the undoped ZnO sample indicating that metal doping could enhance the adsorption property of catalyst. **Figure 4.3(f)** presents the pore distribution

curves of ZnO samples evaluated using Barrett-Joyner-Halenda (BJH) model. The plots indicated that all the ZnO samples exhibited wide pore size distribution in the range of 2 nm to 10 nm. In other words, the samples were dominated by mesoporous structure which was in line with the Type IV adsorption isotherm.

Table 4.3: BET Surface Area and Pore Volume of ZnO Samples.

Sample (m ² /g)	Surface area (m ² /g)	Pore volume (cm ³ /g)
Com-ZnO	4.9	0.0140
Che-ZnO	3.9	0.0187
Bio-ZnO	9.3	0.0713
Ag-ZnO	10.3	0.0781
Fe-ZnO	23.2	0.1541

Based on results presented in **Table 4.3**, Bio-ZnO demonstrated the highest values of specific surface area and pore volume as compared to Com-ZnO and Che-ZnO. High specific surface area and high porosity of catalyst will theoretically enhance the catalytic performance by promoting more active surface for the subsequent oxidation reaction (Mohamed Isa et al., 2021; Uribe-López et al., 2021). The doping of Ag and Fe elements exhibited positive effect both the specific surface area and pore volume of ZnO nanoparticles. These findings were in line with the results obtained in FESEM that dopants could reduce the particle size and inhibit particle agglomeration and hence led to a higher specific surface area. This was because the dimensions of particle correlates well to the ratio of surface-to-volume in which a smaller particle size

with higher porosity exhibited higher specific surface area (Manasa et al., 2021). Besides, crystal lattice disorder induced by the difference in ionic radius of Zn^{2+} and dopant ions might enhance the surface roughness of particles (Oliveira et al., 2019). Therefore, ZnO nanoparticles with metal doping had higher specific surface area than undoped ZnO powder.

4.1.4 FTIR

Figure 4.4 illustrates FTIR analysis of the ZnO nanoparticles in the range of wavenumber from 400 to 4000 cm^{-1} . According to the results obtained, a broad absorption band was observed in all the samples between 400 cm^{-1} and 610 cm^{-1} . As discussed by Shreema et al. (2021) and Jayachandran, Aswathy and Nair (2021), the region was associated with the vibration of metal-oxygen bond implying the successful formation of ZnO nanoparticles. In Ag-ZnO, there was an extra small peak found at 619 cm^{-1} . This was elucidated by the stretching of C-S bond which was originated from the Ag precursor during the fabrication of Ag-ZnO (Alharthi et al., 2021).

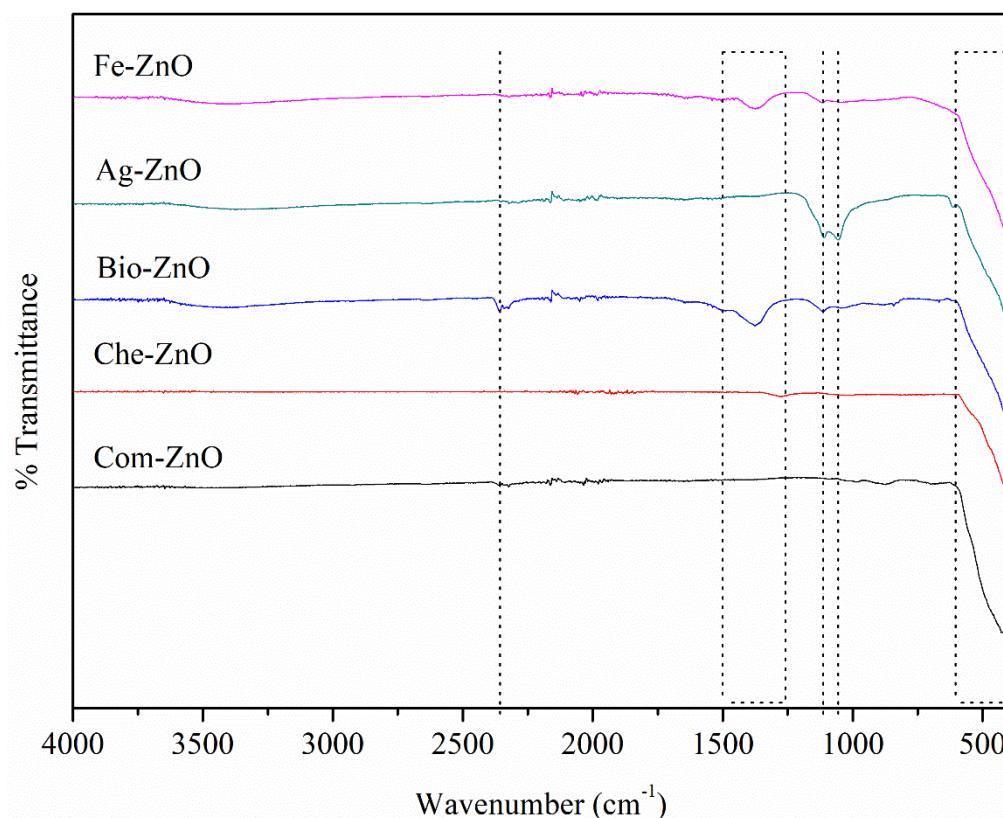


Figure 4.4: FTIR Spectra of Com-ZnO, Che-ZnO, Bio-ZnO, Ag-ZnO and Fe-ZnO.

The FTIR spectra of ZnO samples synthesized using *Clitoria ternatea* Linn plant exhibited several additional characteristic peaks as compared to the Com-ZnO and Che-ZnO. The absorption peak appeared at 1045 cm^{-1} was assigned to C–O stretching of carboxylic acid, alcohol and ester while the peak observed at 1120 cm^{-1} was resulted from the stretching of C–O–C bond (Park et al., 2021; Umamaheswari et al., 2021; Vasantharaj et al., 2021). The intensities of these 2 characteristic peaks exhibited the strongest intensity in Ag-ZnO. This was owing to the stretching of S–O bond attributed by the sulphate group of silver precursor (Bhaduri et al., 2013). Besides, the broad band at 1380 cm^{-1} was associated with the C–N stretching vibration of aromatic amine (Shreema et al., 2021; Vasantharaj et al., 2021). The peak at 2363 cm^{-1} indicated the presence of

nitrile group with triple bond from protein (Pillai et al., 2020). The extra peaks proved the presence of phytochemicals with functional groups including alcohol, carboxylic acid, ester and amine in the green synthesis of ZnO nanoparticles. The biomolecules present such as phenolic compounds and protein could be deprotonated and act as reducing and capping agents by reducing Zn ions into ZnO nanoparticles and controlling the growth of particle (Umamaheswari et al., 2021). For instance, carbonyl group originated from protein and amino acid of plant extract could reduce Zn ions and inhibit the particle agglomeration during the formation of ZnO nanoparticles (Dhandapani et al., 2020).

4.1.5 Zeta Potential

Figure 4.5 shows the measured zeta potentials as a function of pH for various types of synthesized ZnO samples. All ZnO samples exhibited negative correlation in the majority of solution pH. The zeta potential values of all the samples decreased with the increasing pH value from 2 to 12. It was concluded that positively charged hydrogen ions (H^+) were present in excess in acidic medium. Hence, the attachment of H^+ ions onto the surface of ZnO samples tend to give positively surface charge. Zeta potential values decreased with increasing pH value as the availability of H^+ ions reduced. In alkaline solution, negative charges built up at the sample surface due to the adsorption of hydroxyl ions (OH^-) (Krishnakumar and Elansezhian, 2021). Therefore, an increment in the pH value might lead to a decrement of zeta potential value.

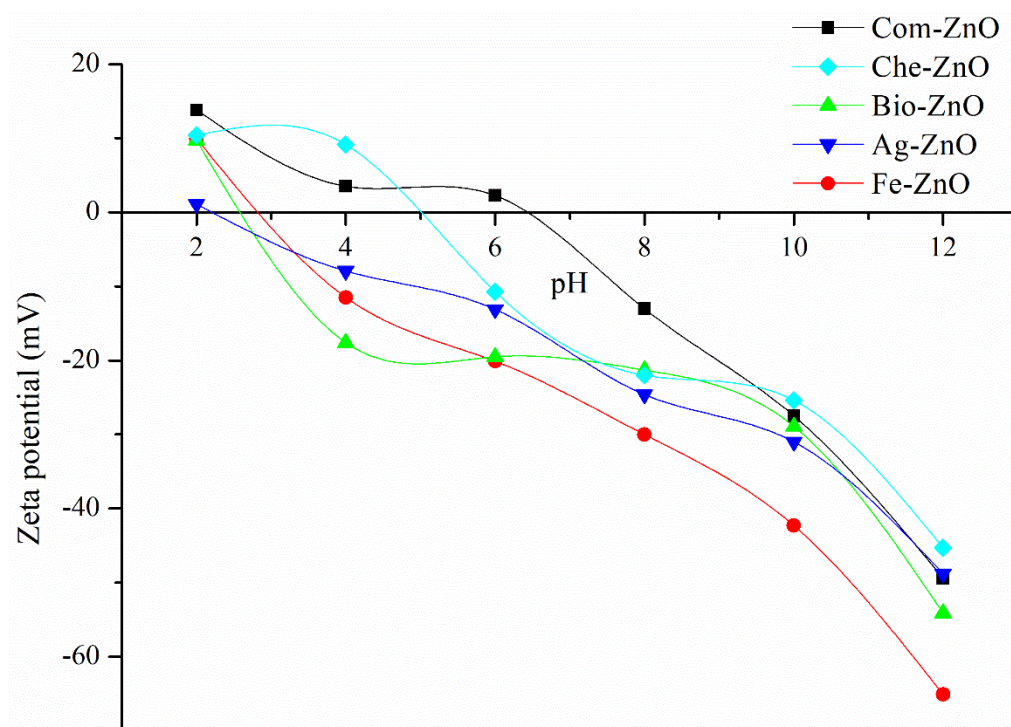


Figure 4.5: Zeta Potential of ZnO Samples.

Based on the results shown in **Figure 4.5**, it is noteworthy that Bio-ZnO nanoparticles exhibited higher magnitude of zeta potential than Com-ZnO indicating higher stability of Bio-ZnO samples. This was attributed to the presence of biomolecules as capping agent which inhibited the particle agglomeration and enhanced the stability of particle (Arumugam et al., 2021). ZnO samples fabricated via green synthesis exhibited negative zeta potential under most of the pH values. The negative values of zeta potential was owing to the anionic components of phenolic and flavonoid compounds attached on the surface of ZnO nanoparticles which act as both reducing and stabilizing agents during green synthesis (Vorobyova et al., 2021).

The value of pH_{zpc} is one of the important parameters that determines the surface charge of solid ZnO nanoparticles which is related to the adsorption

capacity of reactants on catalyst surface (Abdullah, Abu Bakar and Abu Bakar, 2021). The pH_{zpc} of Com-ZnO, Che-ZnO, Bio-ZnO, Ag-ZnO and Fe-ZnO were found to be at pH values of 6.4, 5.0, 2.6, 2.2 and 2.8, respectively. This demonstrated that the ZnO particles was positively charged in the solution with pH values lower than pH_{zpc} due to the surface protonation and hence exhibited high affinity with negatively charged reactant. On the other hand, positively-charged reactant would be attracted electrostatically to ZnO nanoparticles at pH values higher than pH_{zpc} easily owing to the presence of OH^- attached on the particle surface (Badawy et al., 2021).

4.1.6 TGA

Figure 4.6 shows the TGA curves of the synthesized ZnO nanoparticles which evaluate the thermal stability and present the thermal degradation pattern of the samples. All the ZnO samples exhibited total weight loss less than 5% over the temperature ranging from 30 °C to 1000 °C. The excellent thermal stability of ZnO nanoparticles indicated that ZnO was a promising material to be used as an efficient catalyst (Bahadoran et al., 2021). The thermal decomposition of ZnO nanoparticles was detected at 70 – 220 °C temperature range due to the moisture removal in which the evaporation of water molecules occurred (Rezaei, Rezaei and Sayadi, 2021). There was no significant weight loss for Com-ZnO and Che-ZnO at higher temperature.

Besides, ZnO samples obtained through green synthesis experienced the second stage of weight loss when the temperature increased beyond 220 °C. The

weight loss occurred owing to the removal of organic residues remaining during the synthesis process such as phenolic compounds and amino acids as detected through FTIR analysis. Similar results were also reported by Ananda Murthy et al. (2021) and Makofane, Motaung and Hintsho-Mbita (2021) which had fabricated CuO and zinc ferrite through green synthesis respectively. In addition, a drastic weight loss was detected in Ag-ZnO over the temperature range of 800 °C to 1000 °C due to the decomposition of residual silver sulfate remaining in the synthesis of Ag-ZnO powder. Nevertheless, **Figure 4.6** shows that metal doping could enhance the thermal stability of ZnO nanoparticles as the weight loss of metal doped ZnO nanoparticles was lower than the pristine ZnO sample.

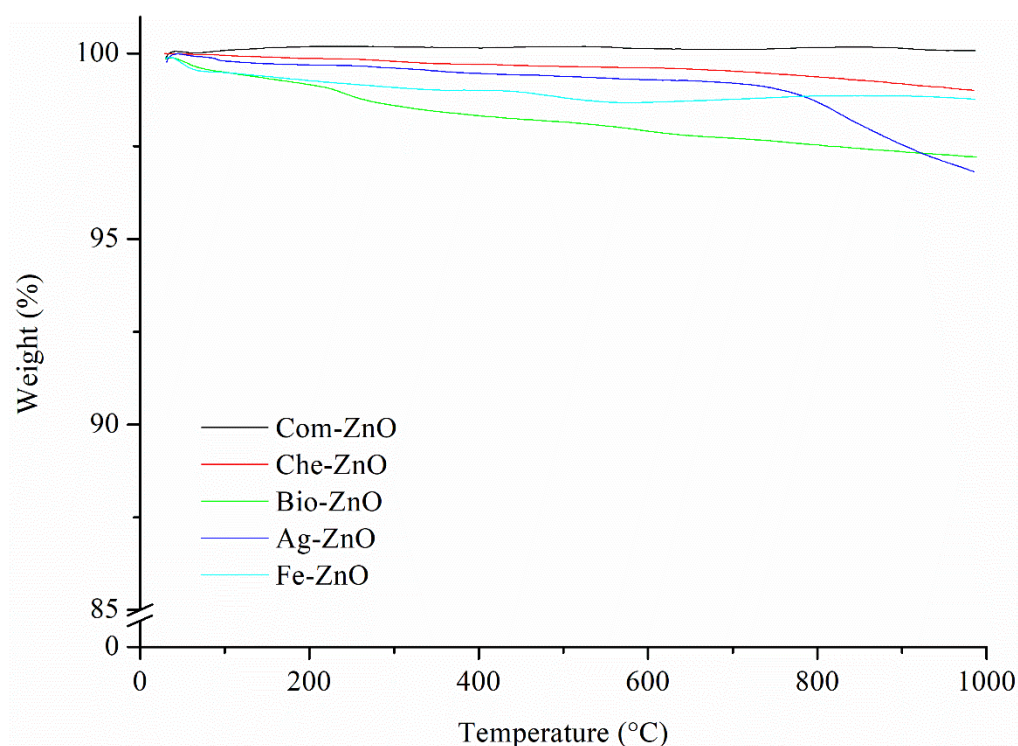


Figure 4.6: TGA Plots of ZnO Nanoparticles.

4.1.7 UV-Vis DRS

The band gap energies of ZnO samples were evaluated using Tauc plot as illustrated in **Figure 4.7**. The band gap energies of Com-ZnO, Che-ZnO, Bio-ZnO, Ag-ZnO and Fe-ZnO were estimated to be 3.22 eV, 3.18 eV, 3.14 eV, 3.10 eV and 3.02 eV respectively. The band gap energies of undoped ZnO samples were reasonable results to the literature reviewed value which was 3.2 eV (Dodoo-Arhin et al., 2021). The band gap energy of Bio-ZnO was found to be lower than Com-ZnO. The reduction in band gap energy could be related to the lattice disorder induced by the involvement of phytochemical compounds in the plant extract during the green synthesis of ZnO nanoparticles. This would result in the lowering of CB and up-lifting of VB positions (Khan et al., 2019b). Hence, the band gap energy of Bio-ZnO was observed to be lower than that of Com-ZnO.

Besides, band gap narrowing of ZnO nanoparticles was detected with the metal doping. The redshift of band gap occurred due to the replacement of cations by the metal dopants. In addition, metal dopant could act as e^- sink which trapped the e^- excited from CB. Therefore, additional energy levels and oxygen vacancies were developed bringing to the reduction in the band gap energy (Roguai and Djelloul, 2021). The findings was in good agreement with Dhir (2021) in which gadolinium doping created new energy levels in zinc sulphide nanoparticles leading to band gap narrowing. Lee et al. (2021) and Islam et al. (2021b) also supported that metal doping could reduce the band gap energy of catalyst due to the diffusion of impurities into the host lattice and

substitution of the host cation by the dopants. This would result in the transition of excited e^- from the dopant cations to the CB of the host and hence lead to the redshift of the absorption edge.

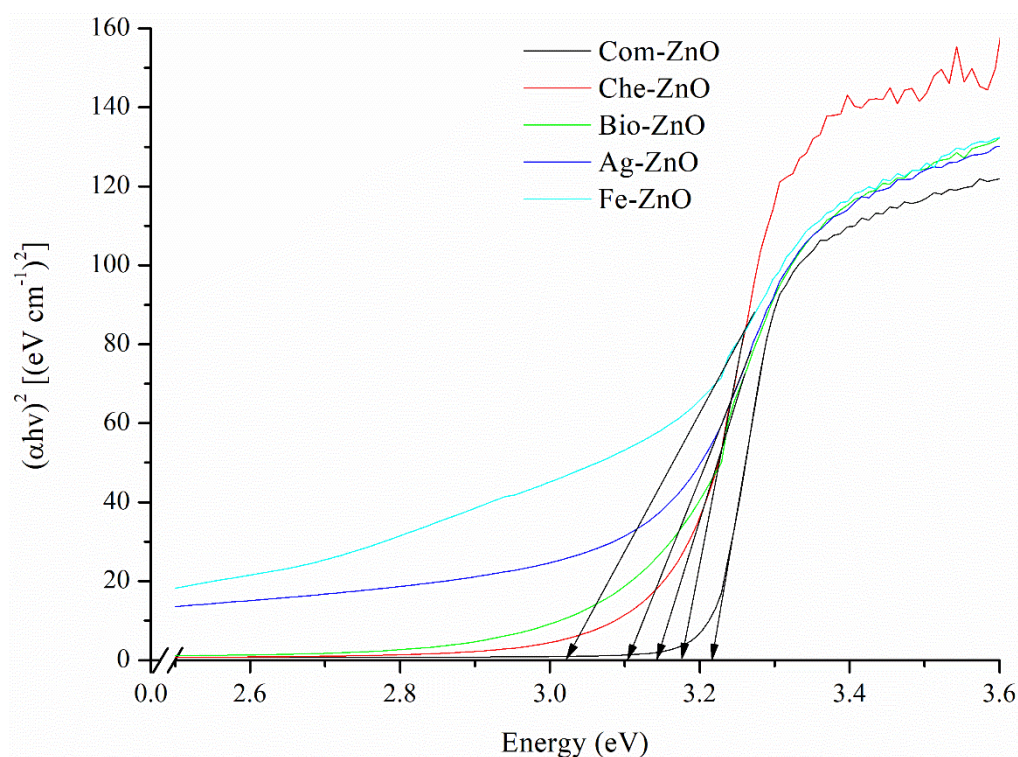


Figure 4.7: Tauc Plots of ZnO Nanoparticles.

4.1.8 Photoluminescence Analysis

The photoluminescence behavior of ZnO samples is a significant parameter used to evaluate the separation efficiency of electron-hole pair of a catalyst as photoluminescence study confirms the energy states of impurities and defects present in semiconductor (Gupta, Hassan and Barick, 2021). Hence, photoluminescence spectra of ZnO samples are shown in **Figure 4.8**. The spectrum of Com-ZnO exhibited a small peak at 390 nm which was in the UV

range. According to Seshadri (2021), the emission band observed in UV region was categorized as near-band-edge emission owing to the recombination of free exciton between VB and CB of the semiconductor. All the samples showed broad orange-red band between 600 and 750 nm. The visible emission observed was owing to the impurities and structural defects of ZnO nanoparticles such as oxygen and zinc vacancies in ZnO nanoparticles (Kumar et al., 2017; Ngom et al., 2021). In other words, the emission observed in the visible region indicated the transfer of e^- between the defect centres and ZnO nanoparticles. For instance, red emission implied the recombination of electron-hole pair from CB of ZnO nanoparticles to oxygen interstitial (Wang, Shieu and Shih, 2021).

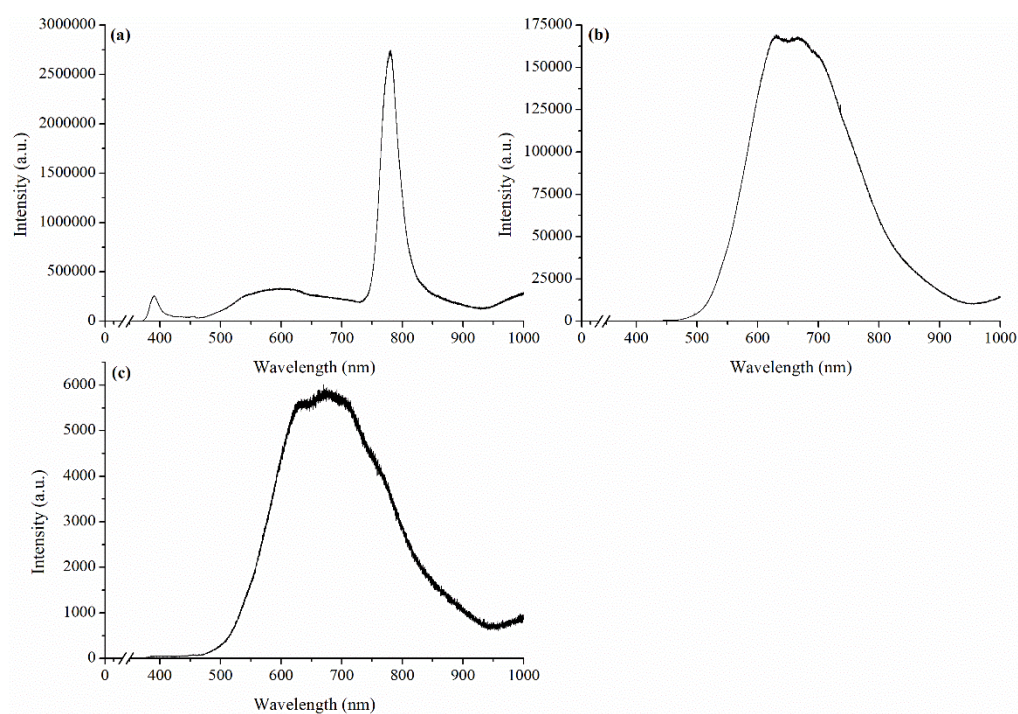


Figure 4.8: Photoluminescence Spectra of (a) Com-ZnO, (b) Bio-ZnO and (c) Ag-ZnO.

It is noteworthy that Bio-ZnO exhibited lower emission intensity than Com-ZnO indicating that the charge carriers of green synthesized ZnO

nanoparticles had longer lifetime as compared to that of chemically synthesized ZnO samples (Park et al., 2021). In addition, the peak intensity decreased further with Ag doping due to the generation of intrinsic defects. The results was in-line with the literature reported by Akbar Jan et al. (2021) in which the photoluminescence intensity decreased with metal doping. The fermi levels of ZnO nanoparticles and Ag dopants were adjusted to new position while Ag ions were incorporated into the lattice of ZnO nanoparticles. The movement of e^- from VB of ZnO nanoparticles to Ag dopant was preferred since the fermi level of Ag was located at lower energy state as compared to the CB of ZnO nanoparticles. Besides, the e^- in metallic Ag could be excited and migrated to the CB of ZnO nanoparticles. Both the energy and e^- transfers led to the decline in defect emission (Al-Gharibi et al., 2021). Therefore, ZnO nanoparticles doped with Ag ions exhibited lower photoluminescence intensity than the undoped ZnO nanoparticles. Furthermore, the results also confirm that Ag doping could act as e^- trap and hence decelerate the recombination rate of electron-hole pair. The longer lifetime of charge carriers would be able to enhance the catalytic performance of semiconductor (Wang, Shieu and Shih, 2021).

4.1.9 Raman Analysis

Figure 4.9 shows the Raman spectra of Com-ZnO and Ag-ZnO. The space group of ZnO with hexagonal wurtzite structure is classified as $C_{6v}4$ ($P6_3mc$) which exhibits two formula units per primitive cell. Based on the group theory, the optical phonon modes of a highly crystalline wurtzite ZnO detected

at the Γ point of Brillouin zone can be expressed as shown in **Equation 4.1** (Vergara-Llanos et al., 2021):

$$\Gamma_{opt} = A_1 + 2B_1 + E_1 + 2E_2 \quad (4.1)$$

Among the optical phonon modes, A_1 and E_1 are polar modes which can be categorized into longitudinal optical (LO) and transverse optical (TO) modes depending on the pathway of incident light. LO phonon component is identified when the incident radiation is parallel to c-axis while TO phonon mode is observed when the incident radiation is at an angle of 90° to c-axis (Aboorvakani, Kennady Vethanathan and Madhu, 2020). A_1 and E_1 components are infrared and Raman active while E_2 is Raman active only which is known as non-polar mode that consists of low frequency (E_{2L}) and high frequency (E_{2H}). B_1 mode is classified as silent mode (Mazhdi and Tafreshi, 2020).

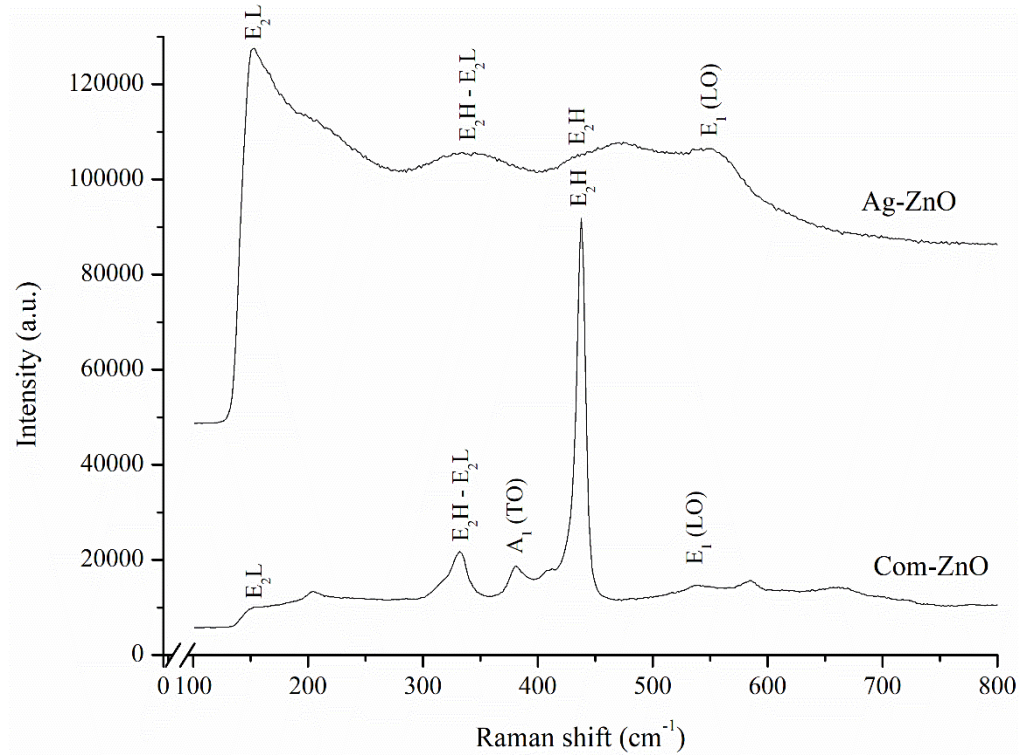


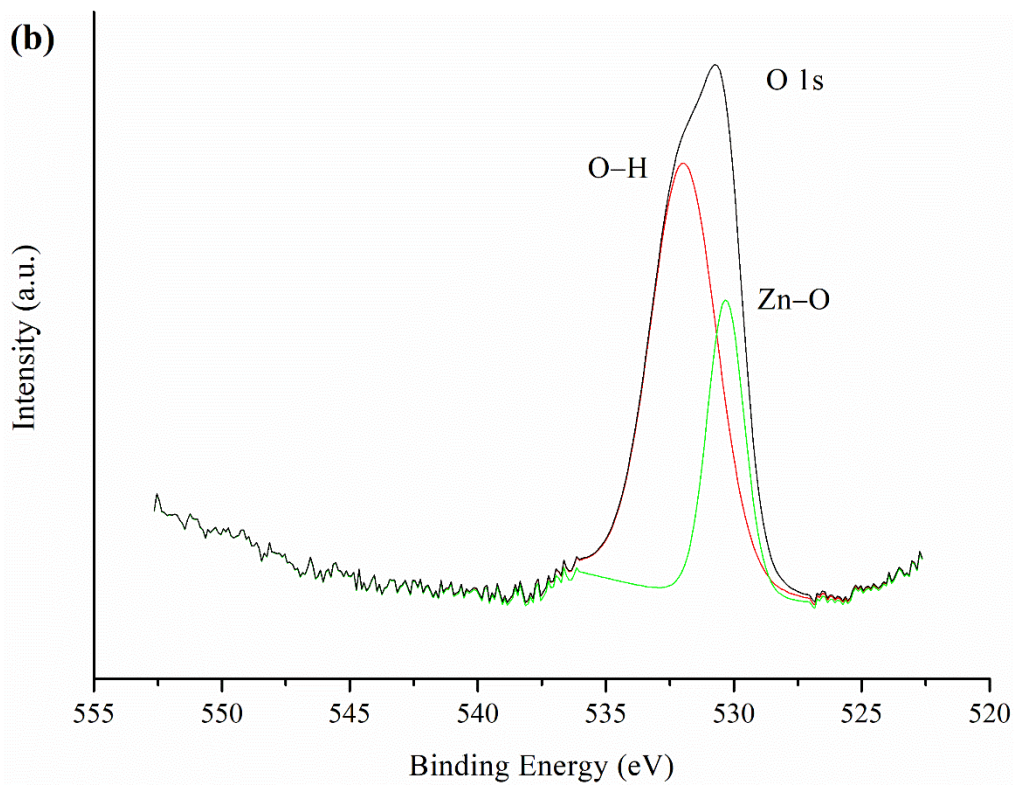
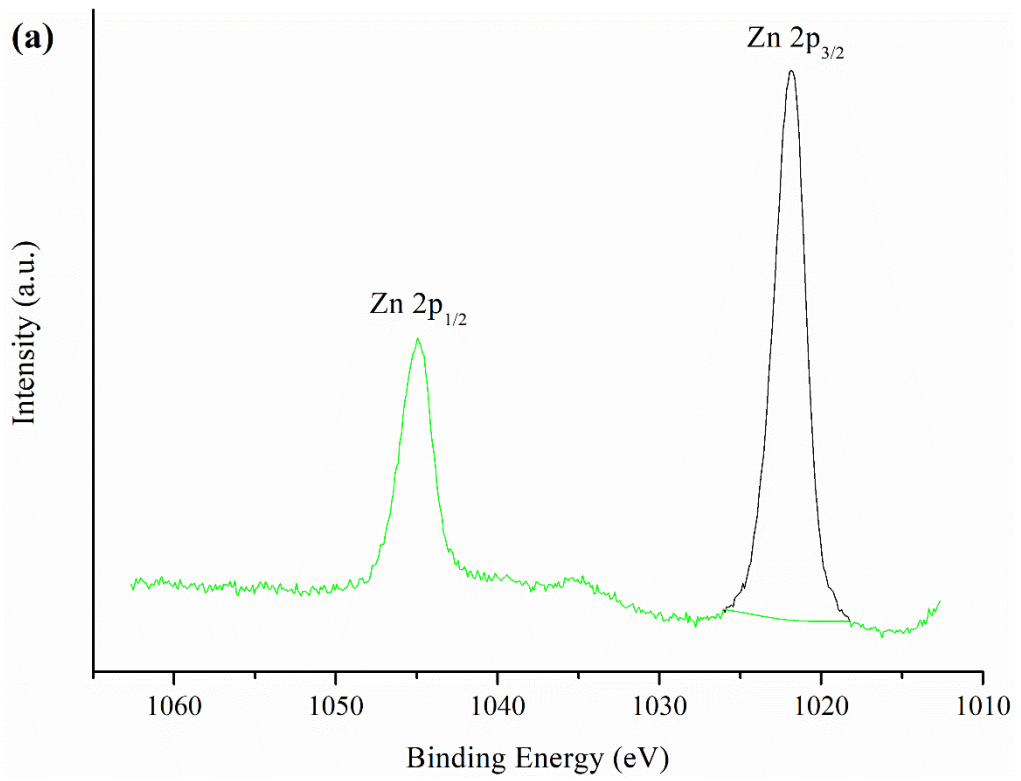
Figure 4.9: Raman Spectra of Com-ZnO and Ag-ZnO.

In **Figure 4.9**, the characteristic peaks observed at 152cm^{-1} , 335 cm^{-1} , 380 cm^{-1} , 438 cm^{-1} and 545 cm^{-1} were attributed to E_2L , multi-phonon vibration mode of E_2H-E_2L , $A_1(TO)$, E_2H and $E_1(LO)$, respectively (Islam et al., 2021a; Karthick et al., 2021). Both the E_2L and E_2H components represented the vibration of zinc oxygen atoms in the lattice of ZnO, respectively (Ramalingam and Hwang, 2020). Hence, the existence of these 2 peaks remarked the formation of wurtzite hexagonal ZnO nanoparticles. A significant decrement in the intensity of E_2H component were observed in Ag-ZnO sample as compared to Com-ZnO. The observation was consistent with the work done by Pandiyan et al. (2019) which proposed the doping of Ag and Au into ZnO lattice. The findings implied the distortion of crystal translational symmetry caused by the incorporation of Ag dopant (Padmavathy and Sankar, 2020). Furthermore, an

additional broad band was detected at 475 cm^{-1} in the Raman spectrum of Ag-ZnO due to the interfacial surface phonon mode of Ag-O (Keshari and Singh, 2020). The results proved the successful of Ag doping into ZnO nanoparticles which was in line with XRD results.

4.1.10 XPS

Figure 4.10 illustrates XPS curves of element present in Ag-ZnO including Zn 2p, O 1s and Ag 3d in accordance to C 1s at 284.6 eV as calibration reference. In **Figure 4.10(a)**, the characteristic peaks observed at 1044.9 eV and 1021.8 eV were owing to Zn $2p_{1/2}$ and Zn $2p_{3/2}$ respectively. The findings confirmed that the oxidation state of Zn present in Ag-ZnO was +2 with 23.1 eV of orbital splitting (Stanley et al., 2021). The profile of O 1s shown in **Figure 4.10(b)** confirms two Gaussian peaks at 531.9 eV and 530.3 eV indicating that Ag-ZnO exhibited two types of oxygen group. Oxygen anions (O^-) binding to Zn^{2+} in the lattice of ZnO was represented by the characteristic peak with lower binding energy while the peak with higher binding energy was attributed to hydroxyl oxygen adsorbed on the surface of Ag-ZnO (Ahmad et al., 2022a). The separation efficiency of charge carriers could be enhanced by these oxygen groups which inhibited the recombination of electron-hole pair (Chen et al., 2022).



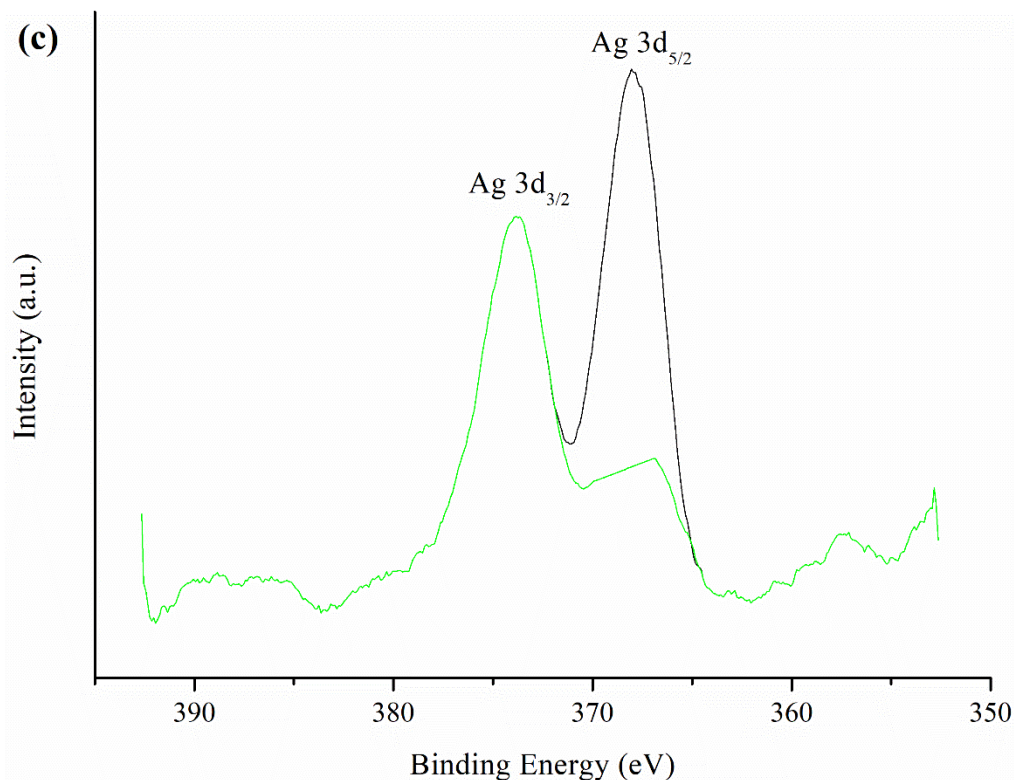


Figure 4.10: High Resolution Elemental Spectra of (a) Zn 2p, (b) O1s and (c) Ag 3d in Ag-ZnO.

According to **Figure 4.10(c)**, the graph clearly showed that Ag 3d exhibited two energy states of spin orbit ($J = 5/2$ and $3/2$). The peaks recorded at 373.7 eV and 367.9 eV corresponded to Ag $3d_{3/2}$ and Ag $3d_{5/2}$, respectively (Arumai Selvan et al., 2021). Together with 5.8 eV of energy differences, the results verified the metallic state of Ag in Ag-ZnO (Tarwal et al., 2021). In other words, Ag present in Ag-ZnO was not oxidized into other states such as AgO and Ag₂O.

4.1.11 Antibacterial Activity

Antibacterial property is an advanced feature of ZnO as sonocatalyst in the remediation of wastewater. The presence of ZnO in pathogen-containing

effluent can also act as bactericidal in addition to the removal of organic pollutants. This can in turn minimize the usage of commercial disinfectant such as ozone and chlorine in wastewater treatment which may lead to the generation of harmful by-products such as trihalomethanes and haloketones (Mohammed and Kareem, 2019; García-Espinoza et al., 2021). **Figure 4.11** shows the antibacterial activity of control, Com-ZnO, Che-ZnO, Bio-ZnO, Ag-ZnO and Fe-ZnO against *E. coli*. Zones of inhibition were observed and correlated with the antibacterial activity of the analyzed samples. There was no zone of inhibition found on the control plate indicating no antibacterial effect was observed. There were zones of inhibition observed with diameters of 7.43 mm, 7.37 mm, 7.62 mm, 8.13 mm and 8.10 mm surrounded the filter paper disc impregnated with Com-ZnO, Che-ZnO, Bio-ZnO, Ag-ZnO and Fe-ZnO, respectively. The findings marked the general antibacterial activity of ZnO against *E. coli*.

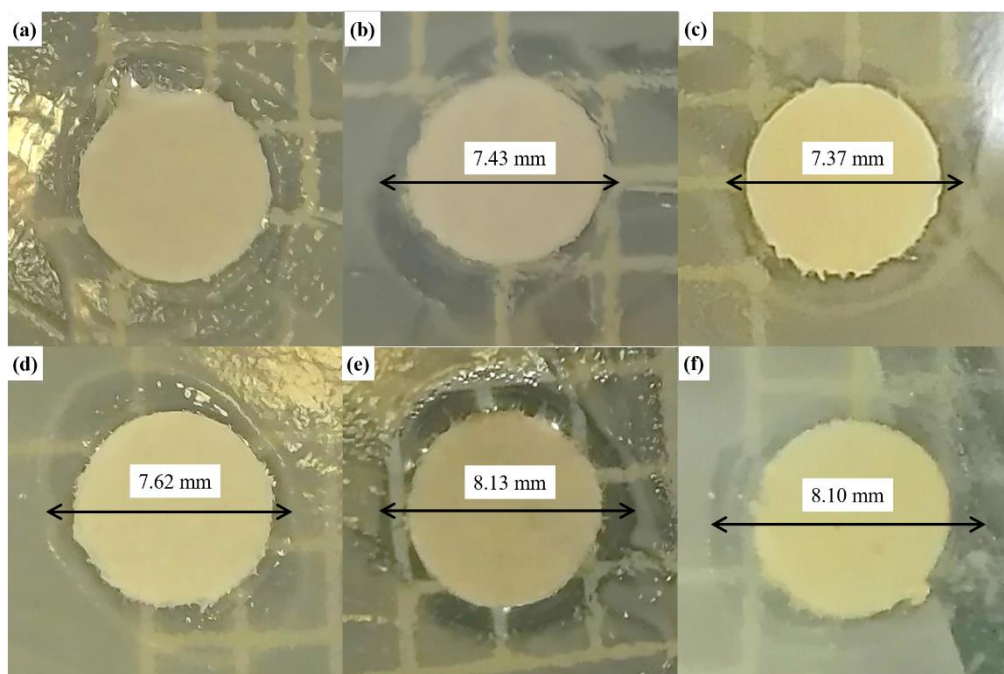


Figure 4.11: Antibacterial Activities over (a) Control, (b) Com-ZnO, (c) Che-ZnO, (d) Bio-ZnO, (e) Ag-ZnO and (f) Fe-ZnO towards *E. coli*.

Figure 4.12 displays the evaluation of antibacterial activity by the means of SEM. Based on **Figure 4.12(a)**, the colony of untreated *E. coli* grew in a group with smooth surfaces and typical rod shapes. The SEM image also clearly showed the biocidal effect of Ag-ZnO against *E. coli*. In **Figure 4.12(b)**, the damage of bacterial cell membrane was noticed which induced the change in the structure and morphology of *E. coli*. The results were in good agreement with Naskar, Lee and Kim (2020) which proposed that the antibacterial activity of metal doped ZnO nanoparticles could cause the fatality of *E. coli* through membrane disruption.

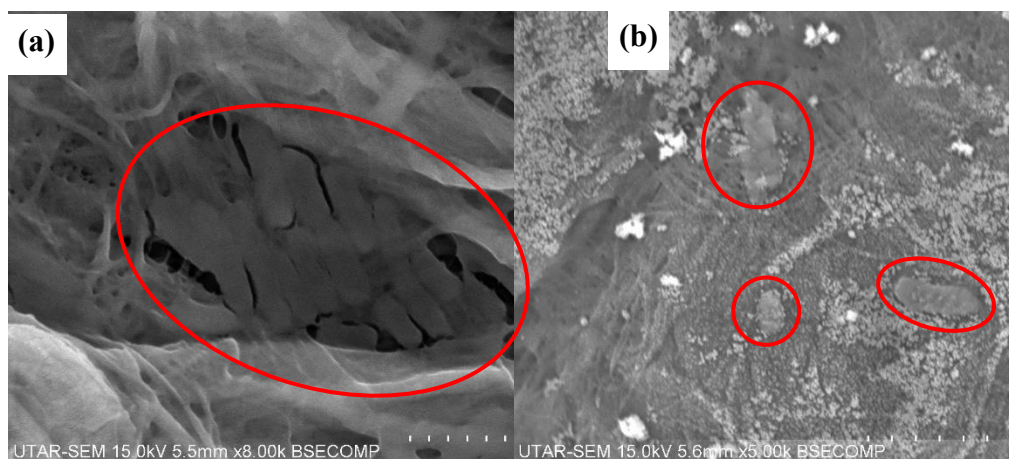


Figure 4.12: Study of Antibacterial Activity over (a) Control and (b) Ag-ZnO against *E. Coli* under SEM.

Although the exact antibacterial mechanism performed by nanoparticles is not well established, the possible mechanism for the antibacterial activity was reported. **Figure 4.13** illustrates the proposed mechanism of antibacterial activity in the presence of ZnO nanoparticles. At the beginning, the mechanism of antibacterial activity was initiated by the rupture of cell membrane due to the electrostatic interaction generated between ZnO nanoparticles and *E. coli*. At the immediate vicinity of the disc boundary, the positively charged metal ions were liberated and interacted with the negative charge carried by the cell membrane (Selvinsimpson et al., 2021). Hence, the functionality of the cell membrane was disturbed and the cell permeability was upset (Mirza et al., 2019). The disruption of *E. coli* cell membrane by Ag-ZnO could be clearly observed in **Figure 4.12** which show the structural wrinkling and cell shrinkage. Meanwhile, this would induce the leakage of cell content which was essential for the growth and survival of bacteria (Sathish et al., 2021). In addition, electron-hole pairs formed on the ZnO particles due to the absorption of photons would lead to the hydrolysis of water and oxygen molecules into ROS such as

$\bullet\text{OH}$ and $(\bullet\text{O}_2^-)$ (Lam et al., 2021). The generation of these radicals resulted in the formation of toxic hydrogen peroxide. Next, the hydrogen peroxide molecules might penetrate into the cells leading to the impairment of DNA and protein denaturation (Gnanamozhi et al., 2020). Consequently, the bacteria cells were unable to grow and replicate normally, giving rise to cell death. This was due to the fact that DNA and protein are the essential molecules of cell, DNA plays a vital role as a genetic information carrier while protein is responsible for carrying out the major cell functions based on the information received from DNA. Hence, the presence of ZnO nanoparticles was able to exhibit antimicrobial effect against *E. coli* that was mainly associated with the generation of ROS (Fouladi-Fard et al., 2022).

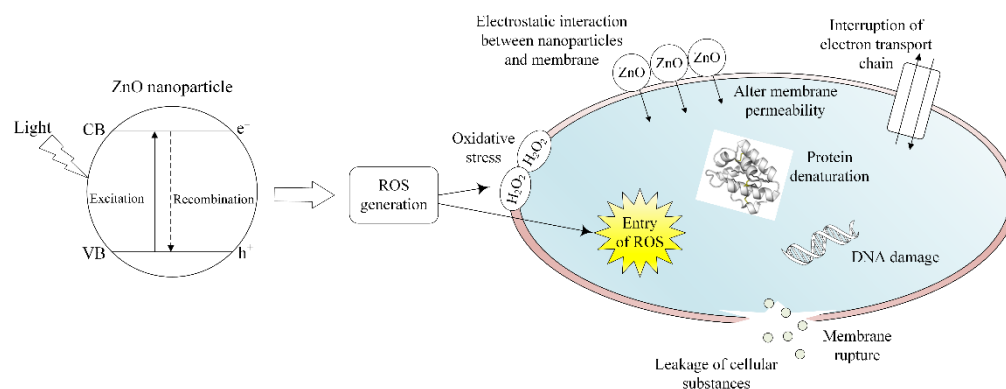


Figure 4.13. Plausible Mechanism of Antibacterial Activity in the Presence of ZnO Nanoparticles on the Bacterial Cell Membrane.

Among the Com-ZnO, Che-ZnO and Bio-ZnO catalysts, Bio-ZnO sample was found to result in the largest zone of inhibition. This was attributed to the phytochemicals with antimicrobial potential that presented in *Clitoria ternatea* Linn such as amino acid and phenolic compounds as detected in FTIR study (Siti Azima, Noriham and Manshoor, 2017). It was also interesting to note

that metal doped samples exhibited stronger antibacterial effects against *E. coli* than pure ZnO as the diameter of the zone of inhibition was found to be larger than that in pure ZnO. The findings could be related fairly well to the band gap narrowing through the introduction of metal ions into the ZnO lattice structure. The positively charged dopant ions might trap the excited e^- from the CB of particles and inhibited the recombination of electron-hole pairs more effectively (Ahmad et al., 2022b). This in turn resulted in higher ROS production by the metal doped ZnO and hydrogen peroxide generation. In addition, the smaller particle size and larger surface area of Ag-ZnO and Fe-ZnO were the key reasons leading to the enhancement of ROS formation and stronger antibacterial effect as compared to pure ZnO. The results were consistent with those reported by Chennimalai et al. (2021) and Kasi and Seo (2019) who suggested that the improvement of antibacterial activity was due to lower band gap energy, smaller particle size and larger surface area of the catalyst. Hence, the antibacterial activity also proved that Ag-ZnO was the superior sample in the generation of charge carriers and free radicals.

In addition to the improvement of ROS production, silver nanoparticle itself was a well-known antibacterial agent which could attach to the cell membrane of bacteria. This would in turn inhibit the movement of substances across the cell membrane (Ghosh et al., 2023). Silver nanoparticles could also penetrate through the cell membrane to interfere the metabolism of bacteria (Salleh et al., 2020). Silver nanoparticles could exhibit antibacterial activity by interrupting the replication of bacterial DNA which would impair the growth of bacterial cell (Shantkriti et al., 2023). Therefore, the combination of ZnO

nanoparticles and silver dopant could enhance the antibacterial effect which was favorable to the environmental application.

4.2 Characterization of Plant Extracts

4.2.1 UV-Vis Spectroscopy

Figure 4.14 presents the UV-Vis spectra of *Clitoria ternatea* Linn extract and Ag-ZnO nanoparticles. Both peaks appeared at 266 nm and 354 nm were associated with the presence of flavonoids and phenolic compounds in the *Clitoria ternatea* Linn extract (Luna-Sánchez et al., 2019; Molina et al., 2019). These two peaks were also observed in the UV-Vis spectrum of Ag-ZnO. The findings were in a good agreement with the results obtained in FTIR analysis which confirmed the presence of the bioactive molecules in the extract and involvement of biomolecules in the synthesis of ZnO nanoparticles. According to Thomas, Mary Vithiya and Augustine Arul Prasad (2019), the presence of hydroxyl groups in plant extract was responsible in the green synthesis process as reductant owing to the electronegative behaviour of oxygen atom. The hydroxyl groups of flavonoids present in the *Clitoria ternatea* Linn extract are attached to the metal salt and reduced it to ZnO nanoparticles.

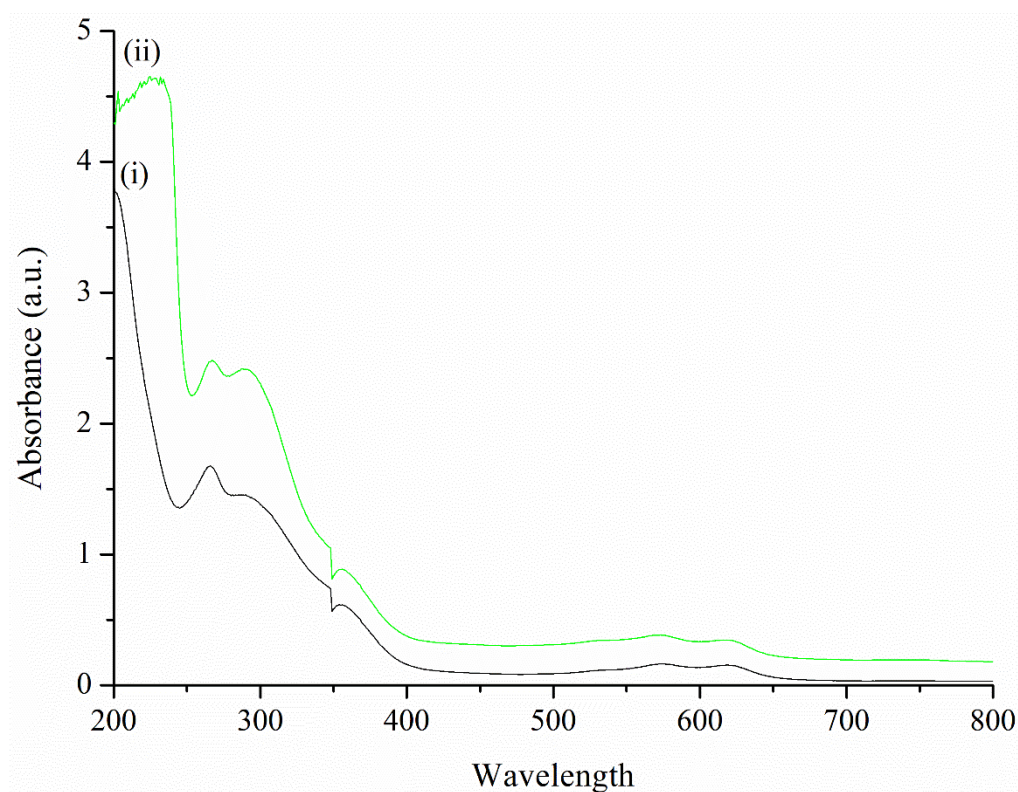


Figure 4.14: UV-Vis Spectra of (i) *Clitoria ternatea* Linn Extract and (ii) Ag-ZnO Nanoparticles.

4.2.2 TPC and TFC analysis

Table 4.4 displays TPC and TFC of plant extracts prepared in this study. As shown in **Table 4.4**, *Clitoria ternatea* Linn flower extract exhibited the highest TPC (21.7 ± 1.3 mg/g GAE) and TFC (values) followed by oil palm leaves extract, black tea waste extract and hibiscus leaves extracts. *Clitoria ternatea* Linn flower was enriched with phenolic and flavonoid components such as anthocyanin, kaempferol, quercetin and rutin (Ghuzali et al., 2021) while oil palm leaves extract mainly contained epigallocatechin gallate, epicatechin and catechin (Jaffri et al., 2011). As reported by Rajapaksha and Shimizu (2022), the phenolic and flavonoid compounds present in black tea waste extract were mainly theasinensin-gallate, kaempferol, theaflavin and

apigenin. The examples of phytochemicals present in hibiscus leaves extract included ferulic acid, caffeic acid, catechol and kaempferol (Pillai and Mini, 2016; Lingesh et al., 2019). All these bioactive molecules consisted of abundant amount of OH functional groups which exhibited strong reducing power and were able to stabilize the nanoparticles obtained from green synthesis process (Tan Sian Hui Abdullah et al., 2021). It is noteworthy that TPC and TFC values of plant extract decreased after synthesis of ZnO nanoparticles. The findings confirmed the involvement of phenolic and flavonoid compounds as natural reducing and capping agents in the green synthesis of ZnO nanoparticles (Kumari and Meena, 2020).

Table 4.4: TPC and TFC of Plant Extract.

Extract sample	TPC (mg/g GAE)	TFC (mg/g QE)
<u>Fresh</u>		
Black tea waste	13.5 ± 0.4	14.0 ± 1.5
Clitoria ternatea Linn flower	21.7 ± 1.3	24.5 ± 2.0
Hibiscus leaves	9.0 ± 1.1	11.6 ± 1.8
Palm leaves	16.3 ± 1.1	17.2 ± 1.3
<u>Post-synthesis</u>		
Black tea waste	7.3 ± 0.3	8.9 ± 1.0
Clitoria ternatea Linn flower	13.7 ± 0.9	10.0 ± 2.8
Hibiscus leaves	5.1 ± 0.9	6.8 ± 1.6
Palm leaves	9.5 ± 1.2	9.3 ± 0.5

4.2.3 FTIR

Figure 4.15 shows the FTIR analysis of *Clitoria ternatea* Linn extract, uncalcined Ag-ZnO and calcined Ag-ZnO. Both the plant extract and uncalcined Ag-ZnO exhibited a characteristic peak in the range of 3600 to 3000 cm^{-1} which was assigned to the O-H stretching owing to water molecules and phenolic compounds while the band observed at 1609 cm^{-1} was related to the C=O bond of ketones (Tabrizi Hafez Moghaddas et al., 2019; Thomas, Mary Vithiya and Augustine Arul Prasad, 2019). The presence of a broad peak in the range of 1550 to 1200 cm^{-1} was identified as the characteristic peaks of C=C and C-O contributed from aromatic compounds. These peaks depicted the presence of polyphenolic compounds such as flavonoids and alkaloids in the plant extract (Jemilugba et al., 2019). The peak presented in the range of 1200 and 900 cm^{-1} was referred to functional groups of C=O and C=N originated from the carboxylic acids of flavonoids and phenolic compounds (Rambabu et al., 2021). The characteristic peak of plant extract observed at 2360 cm^{-1} was attributed to the C-H bond of aldehyde compound (Ezhuthupurakkal et al., 2017; Dangi et al., 2020).

By comparing the FTIR spectra of plant extract and uncalcined Ag-ZnO nanoparticles, the peak of plant extract at 3281 cm^{-1} shifted slightly after undergoing green synthesis indicating the breakage of hydrogen bonding in OH functional group. In addition, a little displacement of peak at 1609 cm^{-1} was detected in FTIR pattern of uncalcined Ag-ZnO nanoparticles as compared to *Clitoria ternatea* Linn extract. The change in characteristic peaks position

implied that the deprotonated phenolic compound and ketone group played the role in the reduction of metal ions (Banu et al., 2021; Melkamu and Bitew, 2021). Moraes et al. (2021) also revealed the shifts of OH and C=O characteristics peaks in FTIR spectrum of Ag nanoparticles which inferred the role of biomolecules present in plant extract as reducing and stabilizing agents. According to Liu et al. (2022a), the shift of characteristic peaks in the synthesized metallic samples was owing to the deprotonation of hydroxyl group and change of aromatic ring skeleton. Hence, the involvement of phytochemicals in the formation of ZnO nanoparticles was confirmed in this study. The findings were in line with TPC and TFC analysis results which verified the presence of phenolic compounds in plant extract and their participation in green synthesis of ZnO nanoparticles. The peaks of organic impurities were found to disappear after calcination of Ag-ZnO due to the removal of organic residues at high temperature (Hamadneh et al., 2022).

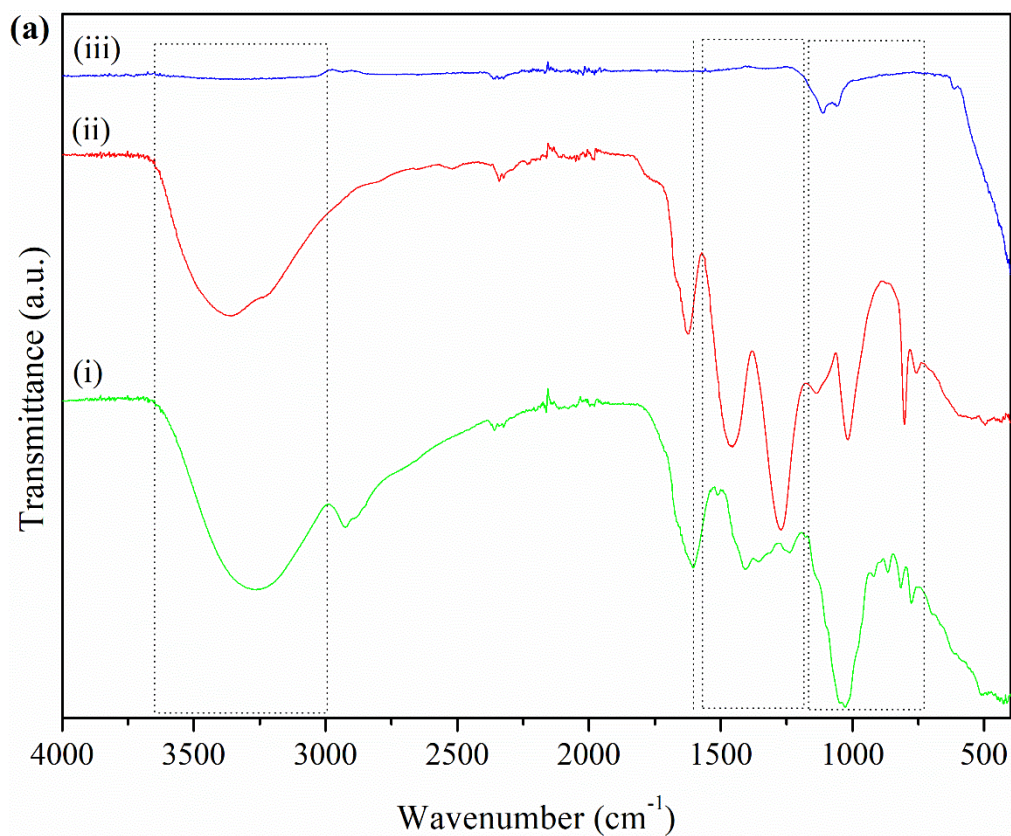


Figure 4.15: FTIR Spectra of (i) *Clitoria ternatea* Linn Extract, (ii) Uncalcined Ag-ZnO and (iii) Calcined Ag-ZnO nanoparticles.

4.2.4 GC-MS

Figure 4.16 presents GC-MS curve of *Clitoria ternatea* Linn extract while the identification of possible phytochemical compounds are listed in **Table 4.5**. According to GC-MS results, the biomolecules mainly consisted of functional groups such as benzene ring, alcohol, alkene, ketone and carboxylic acid. This was consistent with the results obtained in FTIR analysis. These functional groups with high reducing power played important roles in the green synthesis of ZnO nanoparticles. For instance, bioactive molecules with ketone and hydroxyl groups were readily oxidized into carboxylic acid leading to the reduction of metal ion (Puthukkara P, Jose T and S, 2022). In addition, GC-MS data confirmed that 1-Heneicosanol with OH bond exhibited the highest

quantity (31.9%) in the plant extract followed by Di-n-octyl phthalate (16.3%) which consisted of benzene ring and carboxylic acid. Velsankar et al. (2021) proposed that phthalate was a potential bio-reducing agent in the green synthesis of metal oxide. The outcomes also showed that another major component present in the *Clitoria ternatea Linn* extract was 7,9-Di-tert-butyl-1-oxaspiro(4,5)deca-6,9-diene-2,8-dione (13.7%) which was categorized in flavonoid group. The finding was tally with the measurement of TFC which showed high TFC value in the plant extract.

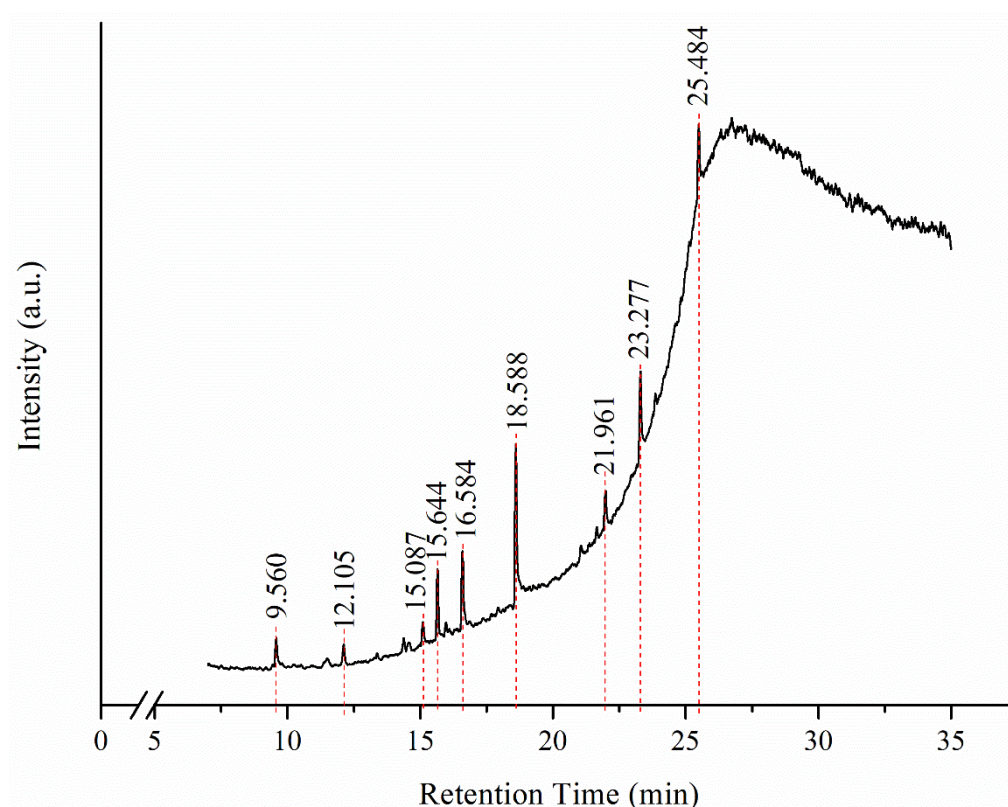


Figure 4.16: GC-MS Spectrum of *Clitoria ternatea Linn* extract.

Table 4.5: Identification of Biomolecules Present in *Clitoria ternatea* Linn extract through GC-MS.

No.	Retention Time (min)	Area (%)	Identification	Molecular Formula	Molecular Weight (g/mol)	Functional Group
1	9.56	0.99	5-Hydroxymethylfurfural	C ₆ H ₆ O ₃	126	C=O, OH
2	12.105	4.07	3-Debenzoyl-tetrahydrocarpesterol	C ₃₀ H ₅₄ O ₃	462	OH
3	15.087	4.74	17-Pentatriacontene	C ₃₅ H ₇₀	490	C=C
4	15.644	13.69	7,9-Di-tert-butyl-1-oxaspiro(4,5)deca-6,9-diene-2,8-dione	C ₁₇ H ₂₄ O ₃	276	C=O, Benzene
5	16.584	12.86	Dibutylphthalate	C ₁₆ H ₂₂ O ₄	278	Benzene, - COO
6	18.588	31.94	1-Heneicosanol	C ₂₁ H ₄₄ O	312	OH
7	21.961	4.92	Hexanedioic acid, mono(2-ethylhexyl)ester	C ₁₄ H ₂₆ O ₄	258	-COO, - COOH

8	23.277	16.25	Di-n-octyl phthalate	$C_{24}H_{38}O_4$	390	Benzene, - COO
9	25.484	10.53	(2R,3R,4aR,5S,8aS)-2-Hydroxy-4a,5-dimethyl-3-(prop-1-en-2-yl)octahydronaphthalen-1(2H)-one	$C_{15}H_{24}O_2$	236	C=O, OH, C=C

4.2.5 Possible Mechanism of Green Synthesis of ZnO

In this study, the phytochemicals such as flavonoid and phenolic compounds detected in various plant extracts were the main components involved in the green synthesis of ZnO nanoparticles as reducing and stabilizing agents. The excellent antioxidant property of biomolecules explained their good reducing power in green synthesis process (Xiao et al., 2020). Basically, the functional groups of bioactive component such as hydroxyl and carboxyl groups played important roles in the reduction of metal ions (Liu et al., 2021a). This could be further elucidated by the plausible mechanism of green synthesis as shown in **Figure 4.17**.

During the synthesis process, zinc nitrate hexahydrate solution would undergo ionic dissociation to produce Zn^{2+} ions while deprotonation of biomolecules would occur in the reaction solution (Aboelmaati et al., 2021; dos Santos et al., 2021). Next, Zn complex was formed through the formation of bond between Zn^{2+} ions and the deprotonated biomolecules (Sana et al., 2023). In this stage, the chelating effect of phytochemicals could enhance the dispersion and stability of the synthesized nanoparticles by inhibiting uncontrollable growth of Zn nuclei (Ananda Murthy et al., 2021). FTIR results obtained confirmed the attachment of deprotonated hydroxyl groups on the synthesized ZnO nanoparticles. The finding elucidated the involvement of biomolecules in the green synthesis process. The deprotonated bioactive components would reduce Zn^{2+} ions into zero valent Zn by donating π -electrons (Ahamed et al., 2022). It was then followed by the growth of Zn nuclei leading

to the formation of nanostructure. The last step would be oxidation to form ZnO nanoparticles through direct decomposition at an elevated temperature (Sidik et al., 2020).

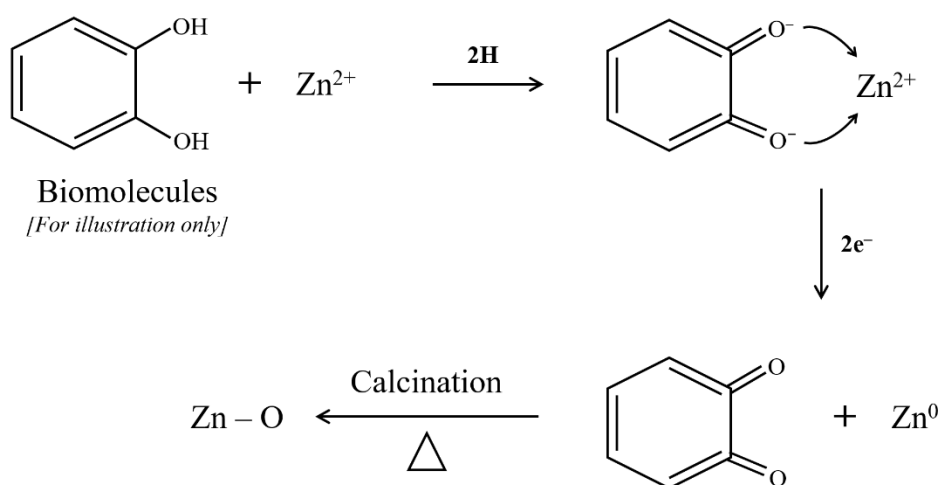


Figure 4.17: Plausible Mechanism of Green Synthesis to Obtain ZnO Nanoparticles.

4.3 Evaluation of Sonocatalytic Performance of ZnO

4.3.1 Type of Plant

Figure 4.18 presents the effect of different plant extracts on the sonocatalytic performance of the synthesized ZnO samples. The sonocatalytic degradation of MG was found to be highest in the presence of ZnO-C (56.18%) followed by ZnO-P (35.2%), ZnO-B (23.58%) and ZnO-H (18.31%). The variation of sonocatalytic activity could be related to the results of TPC and TFC

measurements as discussed in **Section 4.2.2**. The findings confirmed that *Clitoria ternatea* Linn plant exhibited the highest contents of polyphenol and flavonoid which played important roles as reducing and capping agents in the green synthesis of ZnO (Mousa et al., 2022). As mentioned previously, the chelating effect of biomolecules could control the growth of particle during the synthesis of ZnO nanoparticles. Therefore, it was expected that ZnO-C exhibited the smallest particle size with the largest specific surface area among the samples. This was further proved by the surface analysis which showed that ZnO-C exhibited the largest surface area (9.273 m²/g) as compared to ZnO-P (4.622 m²/g), ZnO-B (1.408 m²/g) and ZnO-H (0.930 m²/g). Owing to the largest specific surface area, ZnO-C could provide the highest availability of active sites which would in turn enhanced the sonocatalytic degradation efficiency of MG (Keshu et al., 2021). Hence, ZnO-C was selected as the sonocatalyst for the subsequent experiments.

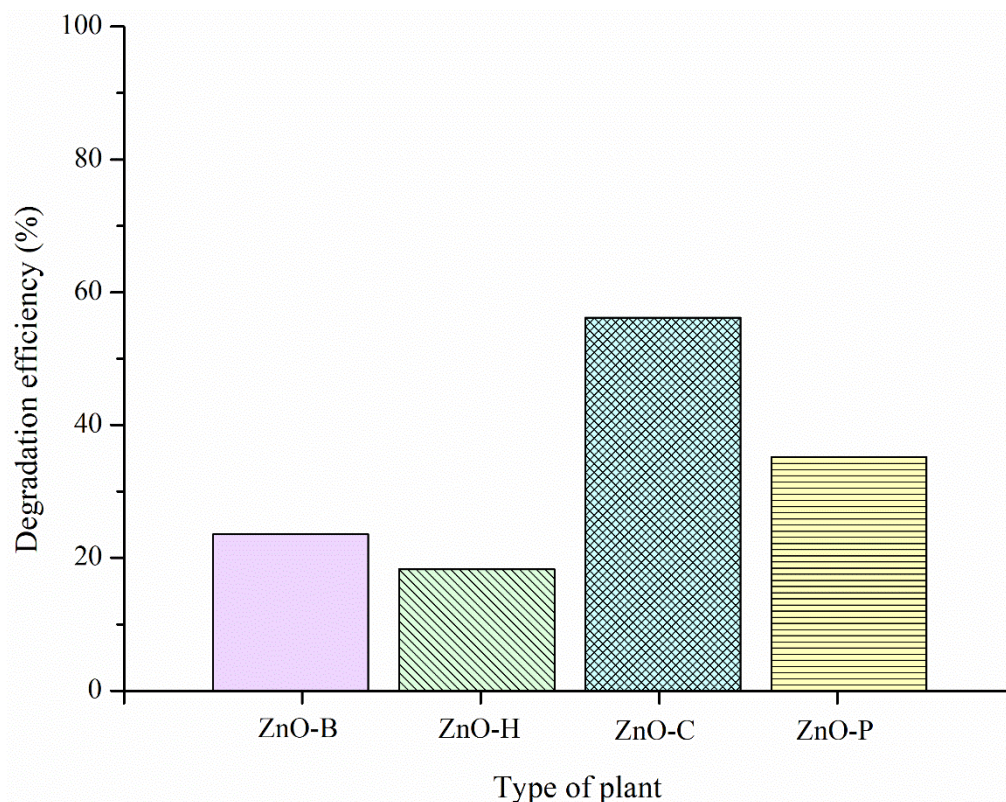


Figure 4.18: Effect of Various Plant Extract on the Sonocatalytic Performance of ZnO Nanoparticles in the Degradation of MG (Catalyst Loading: 0.5 g/L; Initial Dye Concentration: 500 mg/L; Ultrasonic Power: 40 W; Solution pH: 3; Irradiation Time: 60 mins).

4.3.2 Synthesis Temperature of ZnO

Figure 4.19 illustrates the effect of synthesis temperature of ZnO on the sonocatalytic performance in the degradation of MG. As shown in **Figure 4.19**, the degradation efficiency of MG increases with the increasing synthesis temperature from 30 °C to 70 °C. This was due to the increment in surface area at higher synthesis temperature as observed by Sahoo, Biswas and Nayak (2017). Li et al. (2016) revealed that the mesoporous structure of particles could be enhanced by increasing the synthesis temperature. However, a reduction in the degradation efficiency was observed while increasing the synthesis further to

110 °C. According to Torres-Gómez et al. (2019), the frequency of collisions between particles increased at higher synthesis temperature. This would promote the aggregation of particle and hence obtain the product with larger particle size . In addition, the mesoporous structure of ZnO nanoparticles would be destroyed as the synthesis temperature increased beyond the optimum temperature (Chen, Wang and Xiang, 2018). Subsequently, a decrement in the surface area available for reaction led to the reduction in the sonocatalytic degradation efficiency of MG. Hence, the optimum synthesis temperature (70 °C) was chosen for the subsequent parameter studies.

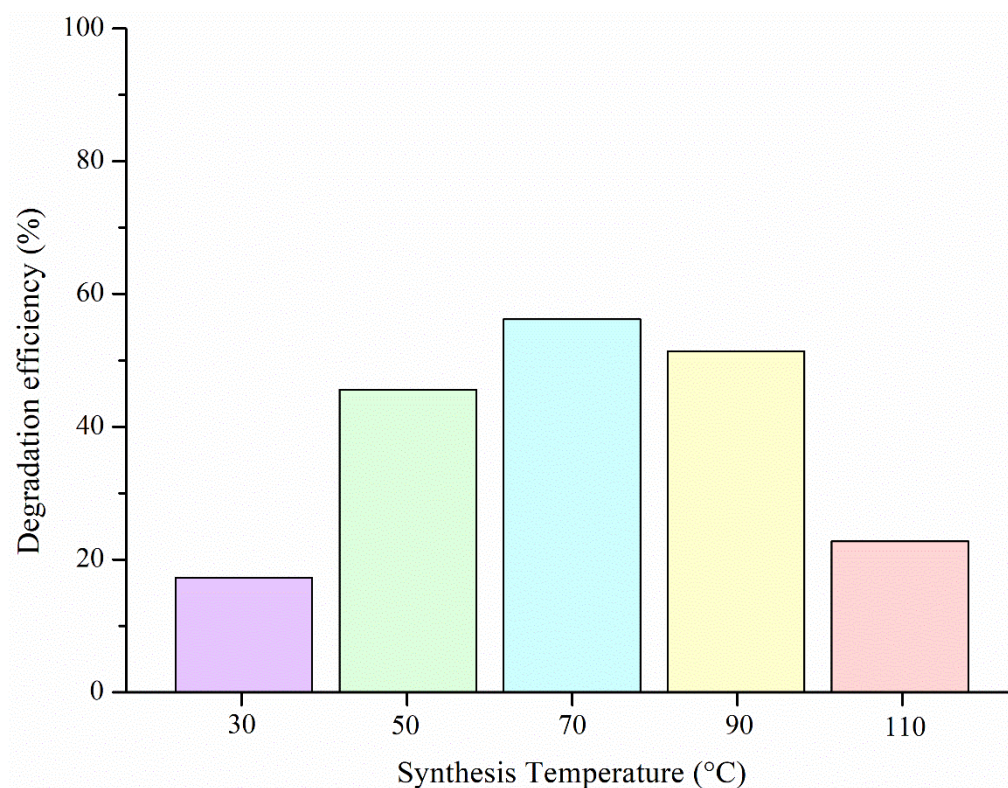


Figure 4.19: Effect of Synthesis Temperature on the Sonocatalytic Performance of ZnO Nanoparticles in the Degradation of MG (Catalyst Loading: 0.5 g/L; Initial Dye Concentration: 500 mg/L; Ultrasonic Power: 40 W; Solution pH: 3; Irradiation Time: 60 mins).

4.3.3 Synthesis Duration of ZnO

Figure 4.20 presents the effect of synthesis duration on the sonocatalytic degradation of MG. The degradation efficiency of MG increased slightly with the increasing synthesis duration from 1 h to 3 h but a decrement in the degradation efficiency of MG was recorded as the synthesis duration increased further to 7 h. According to Kan et al. (2017), prolonged heating duration would alter the crystallite structure and reduced the surface area of product. The results was further supported by Bárdos et al. (2019) which showed that product with bigger particle size was obtained at longer synthesis duration leading to the reduction in total surface area. Therefore, prolonged heat treatment was not suitable to obtain ZnO nanoparticles as sonocatalysts. Since the increment of degradation efficiency was insignificant while increasing synthesis duration from 1 h to 3 h, the heating duration was set to be 1 h in order to obtain ZnO nanoparticles with high sonocatalytic performance without compromising energy saving.

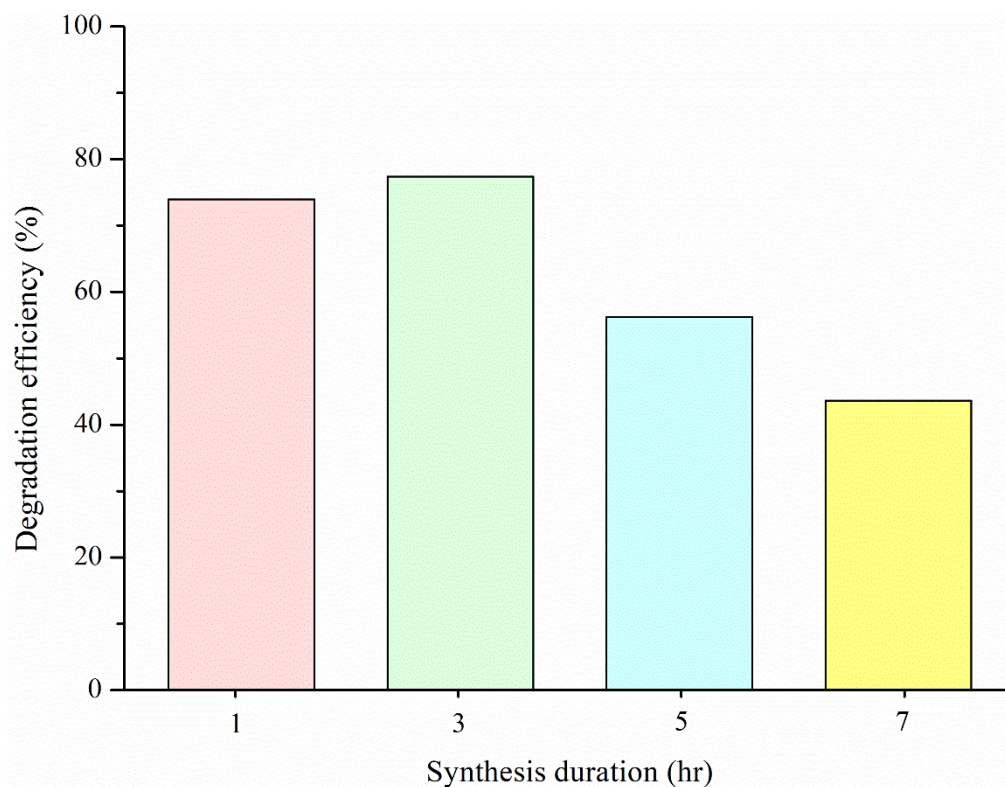


Figure 4.20: Effect of Synthesis Duration on the Sonocatalytic Performance of ZnO Nanoparticles in the Degradation of MG (Catalyst Loading: 0.5 g/L; Initial Dye Concentration: 500 mg/L; Ultrasonic Power: 40 W; Solution pH: 3; Irradiation Time: 60 mins).

4.3.4 Type of Catalyst

Figure 4.21 shows the influence of ZnO samples on the degradation efficiency of MG through sonocatalysis process. Sonolysis was conducted under ultrasound irradiation without adding any solid particle as catalyst. The degradation efficiency of MG was merely 8.75 % under ultrasonic irradiation alone indicating the low degradation ability of sonolysis process. Similar results were observed by Liu et al. (2021c) and Karaca et al. (2021). The application of ultrasound irradiation during sonolysis process induced acoustic phenomenon which involved the formation, expansion and collapse of microbubbles in the reaction medium (Eghbali et al., 2019). The generation of localized hot spot due

to the explosion of bubble might pyrolyzed water molecules into $\bullet\text{OH}$ and hydrogen radicals ($\bullet\text{H}$) (Ziylan-Yavas et al., 2021). The free radicals with high oxidizing power would then degrade the organic dye molecules into simpler products. However, sonolysis alone was unfavourable method to degrade organic substances due to the requirement of longer reaction time and higher energy (Gholami et al., 2019b).

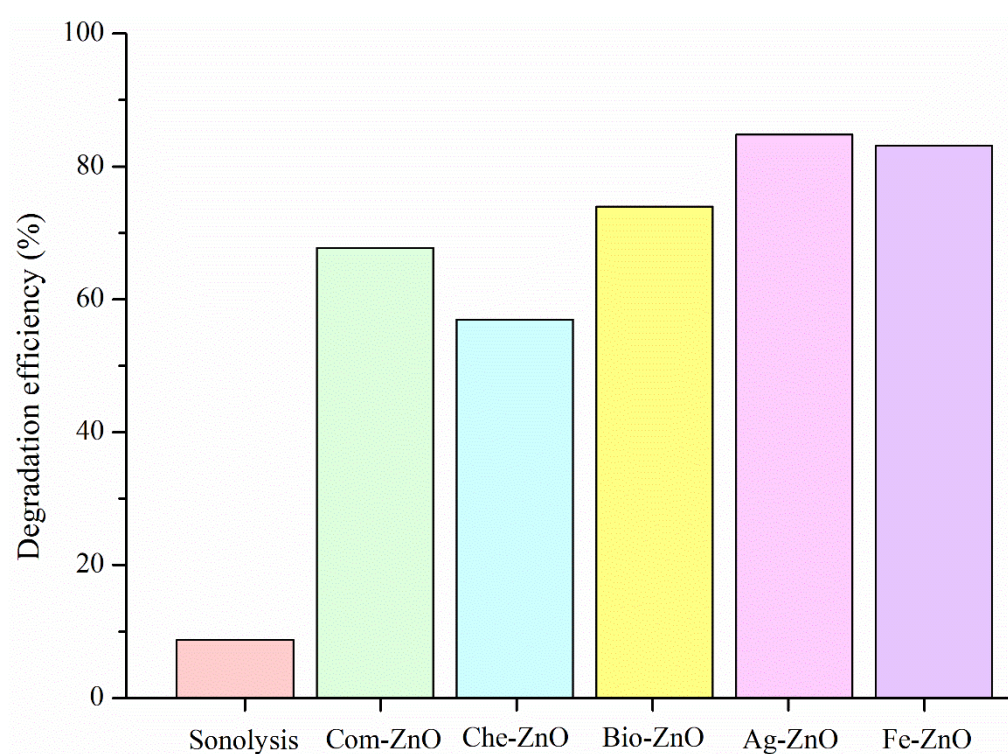


Figure 4.21: Sonocatalytic Degradation of MG using Different Catalyst (Catalyst Loading: 0.5 g/L; Initial Dye Concentration: 500 mg/L; Ultrasonic Power: 40 W; Irradiation Time: 60 mins).

The presence of solid catalyst was proposed to enhance the degradation efficiency of organic pollutants under ultrasound irradiation (Sadeghi Rad et al., 2021). A significant improvement in the degradation efficiency of MG was observed in the presence of ZnO nanoparticles as sonocatalyst. This was because heterogeneous catalyst provided more nucleation sites for the

generation of microbubbles leading to the increment in the yield of free radicals (Bose et al., 2021). Besides, the collapse of bubble could release energy in the form of sonoluminescence (Su et al., 2021). The release of photon energy higher than the band gap energy of ZnO samples would excite and transfer the surface e^- from VB to CB leading to the generation of electron-hole pairs (Thokchom, 2020). The charge carriers generated could react with water and oxygen molecules to form $\bullet\text{OH}$ and $\bullet\text{O}_2^-$ (Wang et al., 2021). The free radicals with high oxidizing power would eventually degrade organic pollutants into simpler products.

As shown in **Figure 4.21**, Bio-ZnO exhibited the highest sonocatalytic performance in the degradation efficiency of MG as compared to Com-ZnO and Che-ZnO. The findings remarked that green synthesis was a promising alternative to produce ZnO nanoparticles with good sonocatalytic performance. The findings also confirmed improvement in the degradation efficiency of MG in the presence of metal doped ZnO nanoparticles as compared to pure ZnO samples. This could be related well to the decrement in the particle size of ZnO nanoparticles observed in FESEM due to Ag and Fe doping. In other words, Ag-ZnO and Fe-ZnO exhibited larger surface area for the adsorption of dye molecules as compared to pristine ZnO nanoparticles. The oxidative removal ability is usually directly proportional to the adsorption capability (Nas, 2021; Wang et al., 2021). The amount of dye molecules adsorbed on the catalyst surface is useful to enhance the sonocatalytic degradation efficiency as the sonocatalytic degradation process occurs at the catalyst surface (Hayati et al., 2020).

Heterogeneous adsorption-sonocatalytic reaction is usually initialized by the mass transfer of dye molecules from bulk liquid to the catalyst surface leading to the pore diffusion and adsorption of reactants on the surface of catalyst. It is then followed by the surface oxidation reaction between the organic dyes and reactive oxygen species such as $\bullet\text{OH}$ and h^+ (Karaca et al., 2021). Next, the products resulted from the oxidation will desorb from the catalyst surface. Simultaneously, the free radicals generated will react with the other adsorbed dye molecules or escape from catalyst surface into bulk solution to oxidize dye molecules (de Andrade, Augusti and de Lima, 2021). Therefore, the strength of adsorption capacity is one of the important parameter which can highly affect the rate of surface reaction occurred during a heterogenous sonocatalysis degradation of organic dyes (Kakavandi et al., 2019; Mirzaei et al., 2019).

Besides, the removal efficiencies of MG through adsorption were found lower in the presence of Com-ZnO and Che-ZnO as compared to the green synthesized ZnO samples (Bio-ZnO, Ag-ZnO and Fe-ZnO). This was due to the cationic nature of MG and the prepared solution pH of MG was measured at value of 3.1 which was lower than the pH_{zpc} of Com-ZnO and Che-ZnO. At the condition of pH values below pH_{zpc} , the surface of ZnO nanoparticles was protonated and positively charge due to the excessive amount of H^+ ions present in the solution. In other words, the presence of OH^- ions would contribute to the negative surface charge of ZnO samples at pH values above pH_{zpc} (Moosavi et al., 2020). Therefore, the positively charged Com-ZnO would repel the

cationic dye molecules from occupying the active sites of ZnO samples (Ahmad et al., 2021). In contrast, the adsorption of MG was favourable in the presence of green synthesized ZnO nanoparticles. This was because the solution pH was higher than the pH_{zpc} of green synthesized ZnO nanoparticles. It was anticipated that there was a force of electrostatic attraction appeared between the cationic dye molecules and negatively charged ZnO nanoparticles (Munyai et al., 2021). In this case, Ag-ZnO showed the best dye removal efficiency through the adsorption process due to the most negatively charged behaviour and the highest specific surface area available for the attachment of MG molecules.

In addition, Ag-ZnO and Fe-ZnO performed the highest sonocatalytic activity in the dye degradation of MG as compared to the pristine ZnO samples. This was attributed to the band gap narrowing effect through the doping of Ag and Fe into ZnO lattice as observed using UV-Vis DRS. According to Reddy et al. (2020), the reduction in band gap was related to the presence of impurity energy levels between the CB and the VB in the metal-doped substance. The improvement in the degradation efficiency of MG in the Ag-ZnO was also owing to the longer lifetime of charge carriers generated as observed in PL analysis. The presence of metal dopant as e^- sink could delay the recombination of charge carriers leading to the enhancement in the generation of radicals (Padmanaban et al., 2021). Hence, Ag-ZnO was selected among all the ZnO samples for the subsequent experiments.

4.3.5 Initial Dye Concentration

The effect of initial dye concentration on the sonocatalytic degradation of MG was illustrated as shown in **Figure 4.22**. A noticeable decrement in the degradation efficiency from 62.19 % to 14.55 % was observed with the increasing initial dye concentration from 500 mg/L to 2500 mg/L. Similar trend which showed the negative effect of initial dye concentration on the degradation efficiency was observed by Siadatnasab et al. (2020) and Jamal Sisi et al. (2020). The amount of dye molecules present in the reaction medium increased at higher initial dye concentration. However, catalyst loading remained constant while increasing initial dye concentration leading to the active sites of catalyst accessible for the adsorption of dye molecules were insufficient (Ahmadi et al., 2020b; Karaca et al., 2021). In addition, the active sites covered by the excessive dye molecules would hardly absorb energy generated from acoustic cavitation (Ghulamchi and Aber, 2020). Also, the chance for the absorption of ultrasonic wave by dye molecules rather than catalyst increased with increasing the amount of dye molecules (Yang et al., 2021). Therefore, the generation of electron-hole pair was restricted in the liquid medium with higher initial dye concentration. The limited number of free radicals produced was insufficient to degrade the high amount of dye molecules.

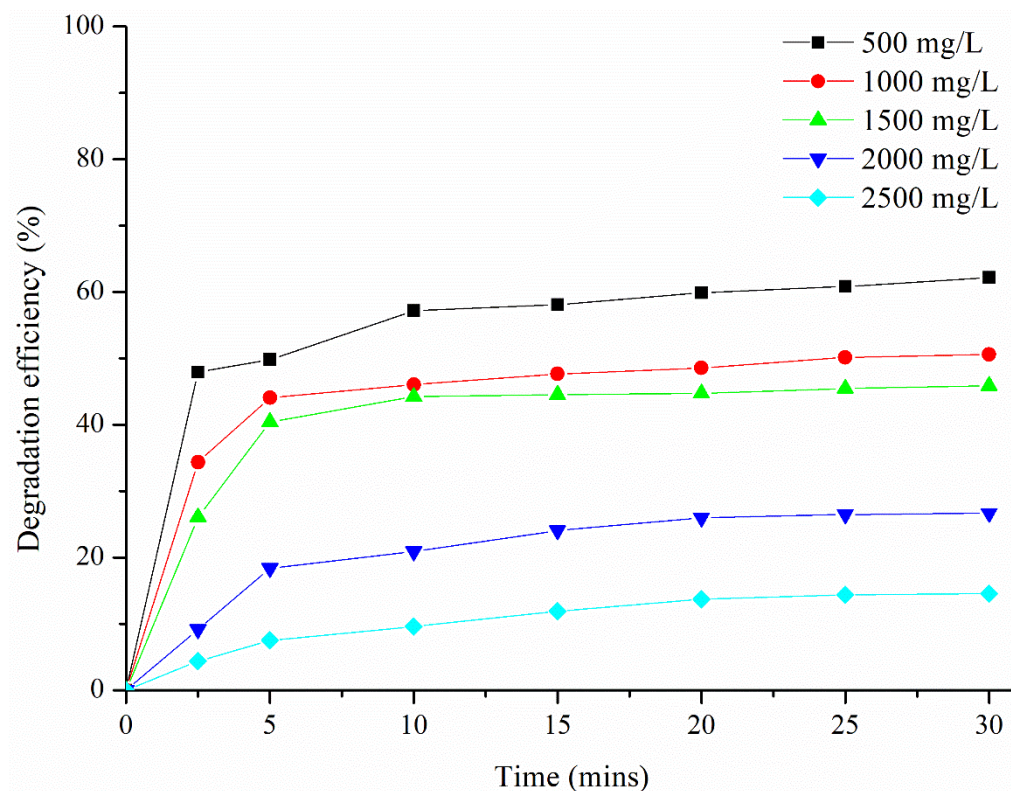


Figure 4.22: Effect of Initial Dye Concentration on the Sonocatalytic Degradation of MG (Catalyst Loading: 0.5 g/L; Ultrasonic Power: 40 W; Solution pH: 3; Irradiation Time: 30 mins).

4.3.6 Catalyst Loading

Figure 4.23 depicts the relationship between catalyst loading and degradation efficiency of MG under ultrasound irradiation. The findings clearly show a significant improvement in degradation efficiency of MG as the catalyst dosage increased from 0.1 g/L to 1.0 g/L. The positive effect of catalyst dosage on the sonocatalytic degradation of MG could be explained by the increment of surface area available for adsorption at higher catalyst dosage (Behura, Sakthivel and Das, 2021). Besides, the availability of active sites increased with increasing catalyst dosage leading to greater number of radicals generated for dye degradation (Hayati et al., 2020; Yang et al., 2021). Together with increasing

catalyst dosage, more nucleation sites were available for the formation of microbubbles (Kakavandi et al., 2019). In other words, the massive amount of solid particles enhanced acoustic cavitation activity bringing to the improvement in rate of charge carrier generation (Khairy, Naguib and Mohamed, 2020). Hence, the sonocatalytic degradation of MG was accelerated due to the increment in the generation of free radicals.

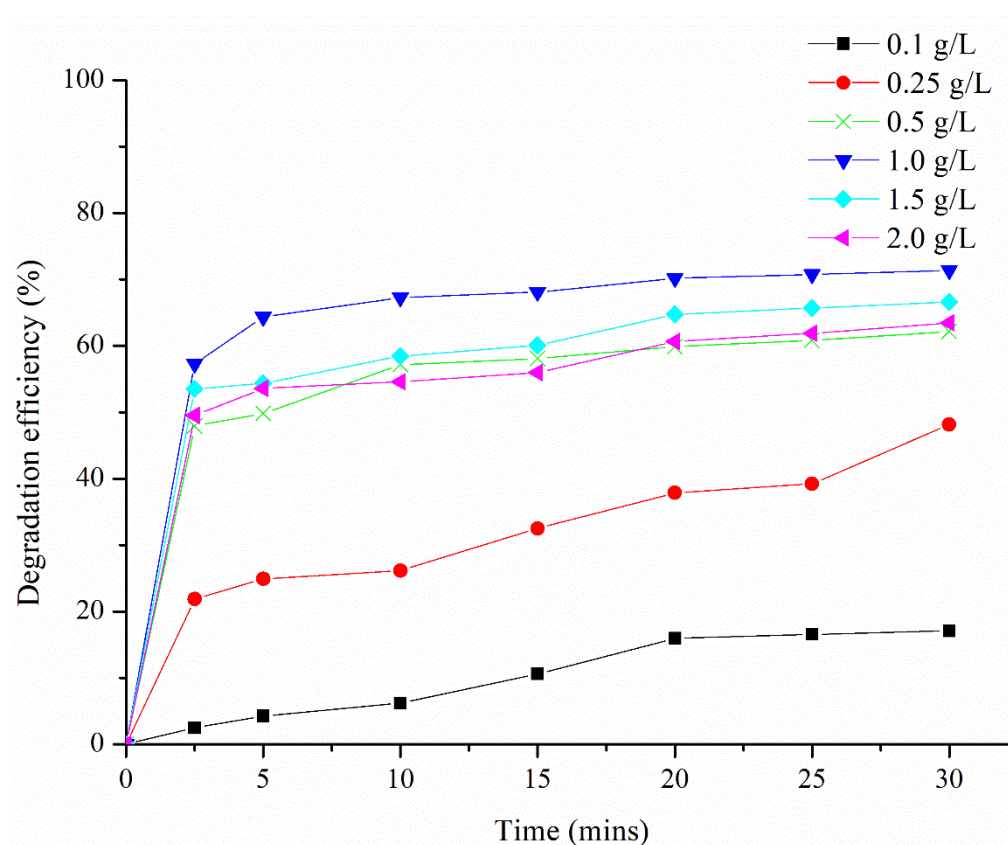


Figure 4.23: Effect of Catalyst Loading on the Sonocatalytic Degradation of MG (Initial Dye Concentration: 500 mg/L; Ultrasonic Power: 40 W; Solution pH: 3; Irradiation Time: 30 mins).

As the catalyst dosage increased beyond 1.0 g/L, a decrement in the degradation efficiency of MG through sonocatalysis was observed. This was attributed to the screening effect with the increasing solution turbidity at higher catalyst dosage which blocked the ultrasound dispersion (Sadeghi Rad et al.,

2021; Talukdar et al., 2021). As the ultrasound transmittance was inhibited by the massive amount of catalyst, the formation of microbubbles under ultrasound irradiation decreased leading to the reduction in free radicals generation (Ayare and Gogate, 2019; Jamal Sisi et al., 2020). In addition, the chance of particle aggregation increased at higher catalyst loadings. This would in turn decrease the surface area accessible for dye degradation and hence reduce the degradation efficiency of MG (Khataee et al., 2020; Fan et al., 2022a). It was known that ultrasound irradiation could enhance the dispersion of catalyst in solution. However, the catalyst dispersion would be restricted at certain amount of catalyst dosage because the energy of ultrasound irradiation applied was not sufficient to deagglomerate the sonocatalysts (Isari et al., 2020). Therefore, the optimum value of catalyst loading in this case was 1.0 g/L.

4.3.7 Ultrasonic Power

Figure 4.24 illustrates the impact of ultrasonic power on the degradation efficiency of MG. A positive effect of ultrasonic power was observed on the sonocatalytic degradation of MG. This could be explained by the increment in the energy dissipation into the system with the increasing ultrasonic power applied. This would subsequently increase the amount of cavitation bubbles formed (Xu et al., 2021). The improvement in the acoustic cavitation was one of the important factors to enhance the degradation efficiency of MG through sonocatalysis due to higher generation of free radicals through water pyrolysis (Siadatnasab et al., 2020). Together with the increment in the collapse of cavitation bubbles, the emission of sonoluminescence was enhanced to activate

ZnO nanoparticles and hence created more free radicals through the formation of electron-hole pairs (Gholami et al., 2020; He et al., 2021a).

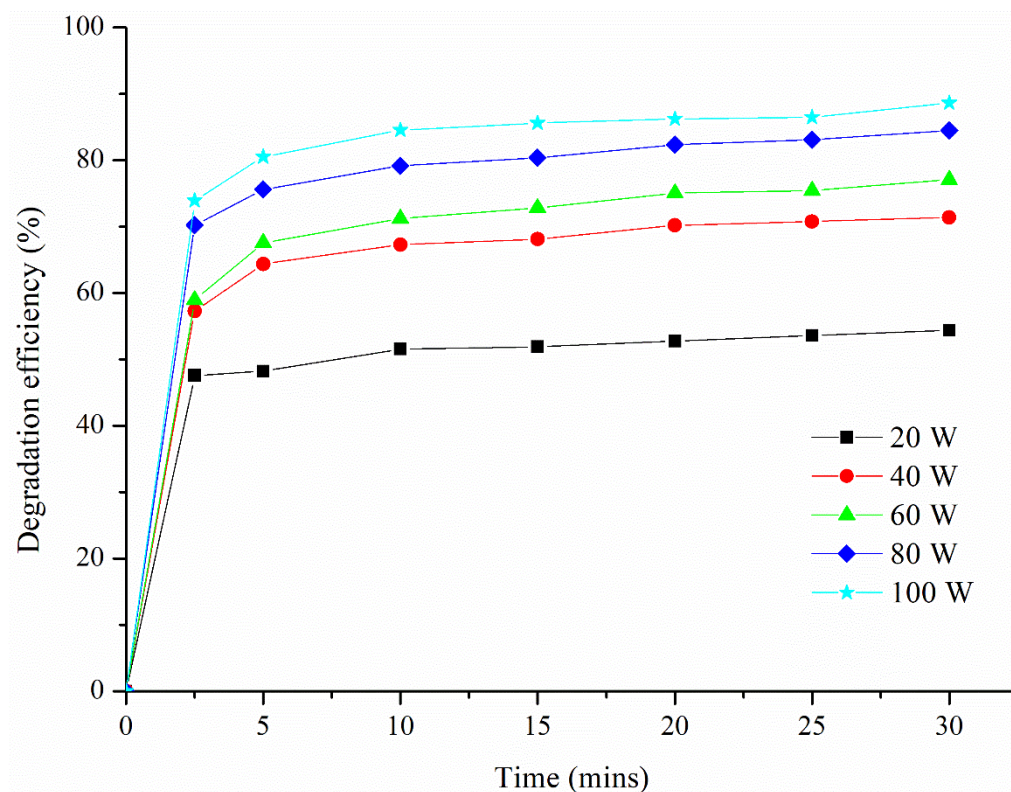


Figure 4.24: Effect of Ultrasonic Power on the Sonocatalytic Degradation of MG (Catalyst Dosage: 1.0 g/L; Initial Dye Concentration: 500 mg/L; Solution pH: 3; Irradiation Time: 30 mins).

Besides, higher solution turbulence was formed under higher intensity of ultrasound irradiation (Cheng et al., 2021). This would in turn lead to enhanced mass transfer of reactants and catalyst that improved the sonocatalytic activity in the degradation of MG (Sadeghi Rad et al., 2022). In addition, higher ultrasonic power promoted the de-aggregation of Ag-ZnO as sonocatalyst in the reaction solution. Hence, the sonocatalytic degradation of MG was higher with greater surface area of catalyst available (Darbandi et al., 2022). Continuous cleaning of catalyst surface could also be enhanced at higher ultrasonic power

leading to the creation of more new accessible active sites for dye degradation (Moradi et al., 2020). Therefore, the increment in the ultrasound power could result in higher degradation efficiency of MG. In this part, an ultrasonic power of 80 W was chosen for the subsequent experiments since insignificant effect was noticed while further increasing the ultrasonic power from 80 W to 100 W. The selection of suitable ultrasonic power was made based on the high dye degradation efficiency with the minimum electricity usage (Karaca et al., 2021).

4.3.8 Ultrasonic Frequency

Figure 4.25 illustrates the effect of ultrasonic frequency on the degradation efficiency of MG. The findings confirmed that degradation efficiency of MG increased with increasing ultrasound frequency. As energy is directly proportional to frequency, the energy dissipation into the reaction medium is higher at higher ultrasonic frequency. Therefore, more cavitation bubbles were formed under the condition of higher ultrasonic frequency leading to the increment in the formation of free radicals (Ding et al., 2021). According to Dhar, Teja and Vinu (2020), the resonant size of cavitation bubble was negatively correlated to the ultrasonic frequency. The collapse time of microbubbles with smaller resonant size was shorter at higher ultrasonic frequency. Hence, the frequency of acoustic cavitation event increased to trigger water pyrolysis and generation of charge carriers under high ultrasonic frequency. Subsequently, higher number of free radicals were created to enhance the sonocatalytic activity.

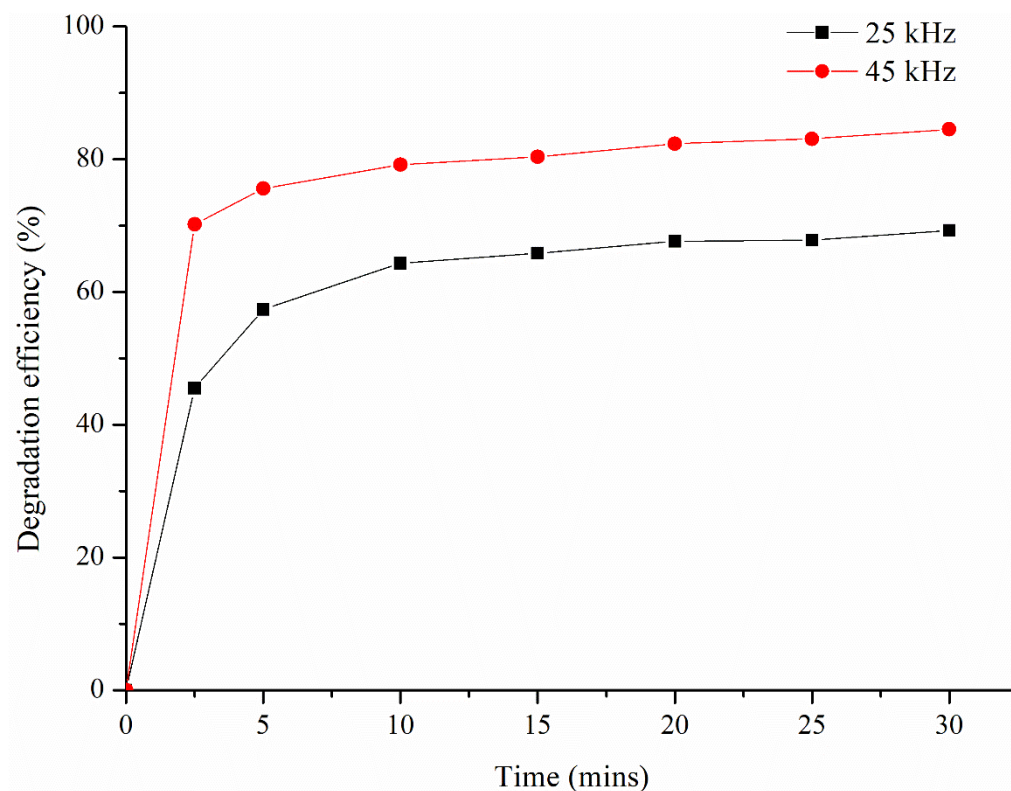


Figure 4.25: Effect of Ultrasonic Frequency on the Sonocatalytic Degradation of MG (Catalyst Loading: 1.0 g/L; Initial Dye Concentration: 500 mg/L; Ultrasonic Power: 80 W; Solution pH: 3; Irradiation Time: 30 mins).

In addition, higher ultrasonic frequency could accelerate the mass transfer of reactant and catalyst as well as enhance the catalyst surface cleaning (Nas, 2021). Together with the better dispersion of sonocatalyst under higher ultrasonic frequency, there was greater chance for the adsorption of reactants onto catalyst surface due to the greater surface area of catalyst available and improvement in the mass transfer (Reheman et al., 2019). Therefore, the sonocatalytic degradation efficiency was higher at higher ultrasonic frequency.

4.3.9 Type of Anion

Figure 4.26 presents the influence of anions on the degradation efficiency of MG through sonocatalysis. Based on Figure 4.26, it was worth noting that all the anions exhibited inhibition effect on the sonocatalytic activity. The presence of anions caused the competition between organic dye molecules during pore filling and adsorption on catalyst surface (Moradi et al., 2020). Hence, the decline in the degradation efficiency of MG was noticed consequently.

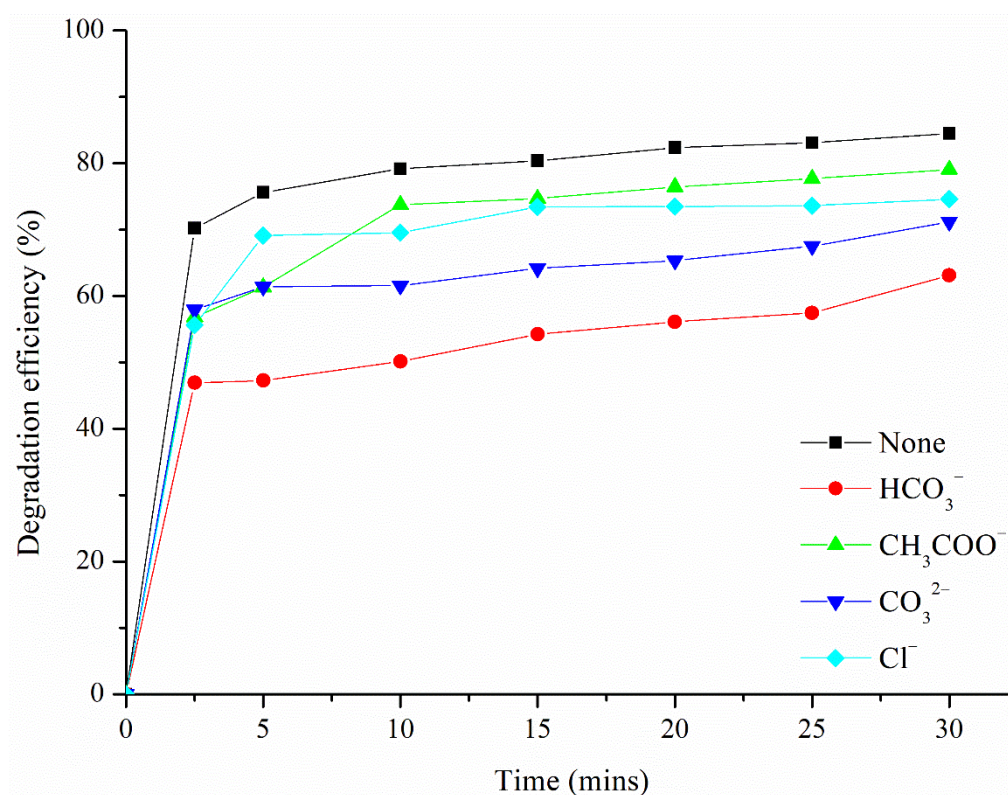


Figure 4.26: Effect of Anions on the Degradation Efficiency of MG (Catalyst Loading: 1.0 g/L; Initial Dye Concentration: 500 mg/L; Ultrasonic Power: 80 W; Solution pH: 3; Irradiation Time: 30 mins).

Anions would also compete with organic reactants for free radicals such

as $\bullet\text{OH}$ and $\bullet\text{O}_2^-$ to form other oxygen reactive species with lower oxidizing power (Kakavandi et al., 2019). As shown in **Equation 4.2**, the inhibitory effect of CO_3^{2-} on the sonocatalytic degradation of MG could be explained by the reaction with $\bullet\text{OH}$ to form carbonate radicals ($\text{CO}_3^-\bullet$) and hydroxide ions (OH^-) in which $\text{CO}_3^-\bullet$ had lower oxidation potential ($E^\circ = 1.60 \text{ V}$) than $\bullet\text{OH}$ ($E^\circ = 2.8 \text{ V}$) (Gayathri, Yesodharan and Yesodharan, 2019).



Besides, $\bullet\text{OH}$ would be consumed by HCO_3^- to generate $\bullet\text{CO}_3^{2-}$ with less oxidizing power as presented in **Equation 4.3** (Wang et al., 2022).



In addition, the presence of Cl^- would suppress the generation of $\bullet\text{OH}$ through the reaction with the h^+ located in the VB of catalyst as shown in **Equation 4.4**.



The presence of Cl^- might also result in the scavenge of $\bullet\text{OH}$ and formation of chlorine radicals ($\bullet\text{Cl}$) with lower oxidizing power ($E^\circ = 2.41 \text{ V}$) as compared to $\bullet\text{OH}$ (Ma et al., 2018; Moradi et al., 2021a).



The findings showed that Cl^- exhibited less inhibition effect on the sonocatalytic degradation of MG as compared to CO_3^- and HCO_3^- . This could be elucidated by the higher oxidation potential of $\bullet\text{Cl}$ ($E^\circ = 2.41 \text{ V}$) than $\bullet\text{CO}_3^-$ ($E^\circ = 1.60 \text{ V}$). Other than that, sonocatalytic degradation efficiency of MG decreased in the presence of CH_3COO^- owing to its competition with water and MG molecules for h^+ and $\bullet\text{OH}$, respectively as presented in **Equations 4.6 and 4.7**.



Therefore, the sonocatalytic activity was quenched in the presence of anions due to the consumption of reactive oxygen species through ineffective way.

The increment of solution turbidity was also one of the factors that reduced the degradation efficiency of MG in the presence of anions. The dispersion of ultrasound wave would be restricted by the anions leading to less generation of charge carriers and free radicals (Kakavandi et al., 2019). In summary, the sonocatalytic degradation efficiency of MG could be affected slightly by the presence of anions attributed to the stated reasons. The results implied that Ag-ZnO was suitable to be applied as sonocatalyst in the treatment of real wastewater which might contain various type of anions.

4.3.10 Solution pH

Figure 4.27 shows the effect of solution pH on the degradation efficiency of MG through sonocatalysis process. The optimum pH value was determined as pH 3 which exhibited the highest sonocatalytic degradation efficiency of 84.49 %. The result was in a good agreement with the literature reported by Mohanty et al. (2022). This was owing to the electrostatic attraction between MG molecules and Ag-ZnO which enhanced the adsorption of reactants onto the active sites of catalyst. The surface of Ag-ZnO was negatively charged at pH value greater than pH_{zpc} (2.2) while MG molecules present in cationic nature at pH value lower than pK_a (6.9) (Munyai et al., 2021). Hence, the adsorption capacity was enhanced at pH 3 leading to the excellent sonocatalytic degradation of MG. The findings confirmed that the degradation efficiency of MG reduced with the increasing of pH from 3 to 6. This could be attributed to the fact that MG existed in zwitterion form at pH value closer to pK_a leading to the aggregation of MG molecules (Arumugam et al., 2019; Khawaja et al., 2021). This would in turn inhibited the diffusion of MG into the pore of Ag-ZnO and resulted in the poor sonocatalytic degradation efficiency.

Besides, the degradation efficiency of MG decreased as decreasing solution pH from pH 3 to pH 2. This was because the surface of Ag-ZnO was protonated by H^+ ions at pH value less than pH_{zpc} which repelled the cationic MG dye from adsorption (Li et al., 2021c). The electrostatic repulsion between Ag-ZnO and MG was also resulted in the case at pH 8. Both the sonocatalyst and reactants were negatively charged as the solution pH was greater than both

pH_{zpc} of Ag-ZnO and pK_a of MG (Hayati et al., 2020). Therefore, the inefficient adsorption of MG caused the reduction in the sonocatalytic activity. It was worth noting that the results obtained at pH 10 was exceptional from the trend which showed decrement in the degradation efficiency with increasing solution pH values from 3 to 8. This was mainly attributed to the hydrolysis of MG by OH^- under high alkaline condition. The hydrolysis of MG would bring to the alteration in structure and stability of MG molecules (Sarojini et al., 2022).

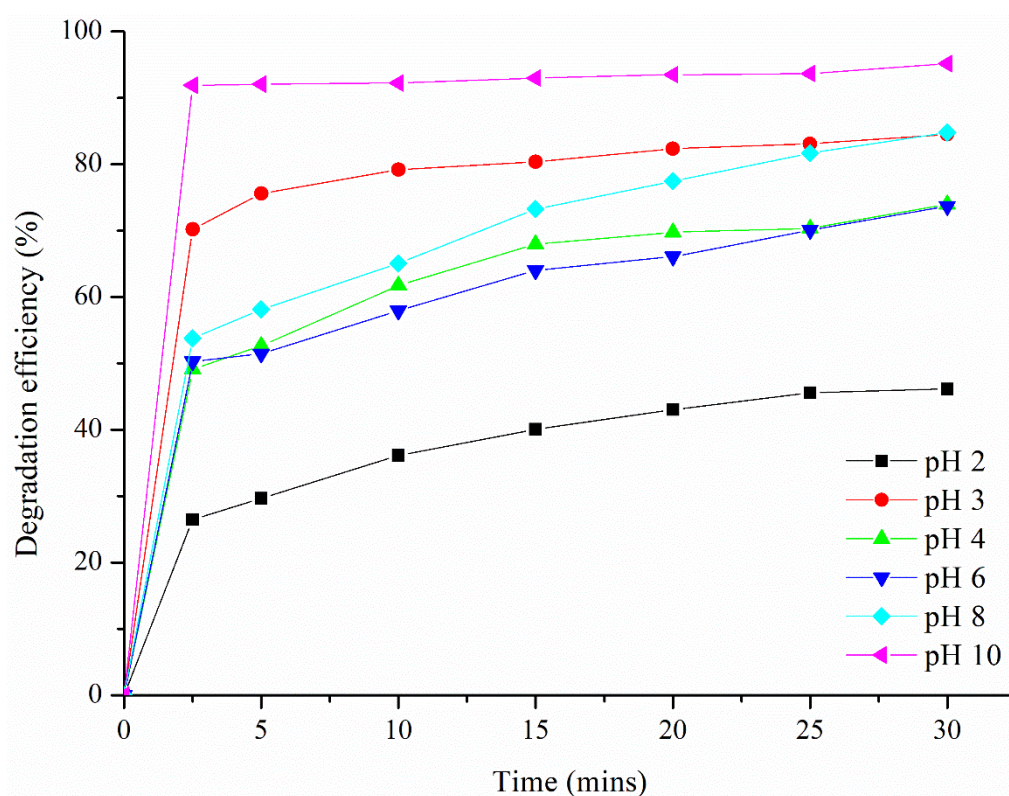


Figure 4.27: Effect of Solution pH on the Sonocatalytic Degradation of MG (Catalyst Loading: 1.0 g/L; Initial Dye Concentration: 500 mg/L; Ultrasonic Power: 80 W; Irradiation Time: 30 mins).

4.3.11 Oxidant Concentration

Figure 4.28 illustrates the impact of sodium persulfate concentration in the degradation of MG under ultrasound irradiation. Persulfate ions ($S_2O_8^{2-}$) is a potential oxidant which can further enhance the sonocatalytic activity by producing sulfate radicals ($SO_4^{\cdot-}$). Besides, $S_2O_8^{\cdot-}$ is environmentally friendly to be applied in the treatment of wastewater. As shown in **Figure 4.28**, the degradation efficiency of MG increased with the increasing concentration of sodium persulfate from 0 mM to 2.0 mM. Sodium persulfate could be activated under ultrasound irradiation leading to the generation of $SO_4^{\cdot-}$ with high oxidizing power ($E^\circ = 2.5 - 3.1$ V) (Gayathri, Yesodharan and Yesodharan, 2019). The sono-generated $SO_4^{\cdot-}$ could also trigger the formation of $\cdot OH$ through the reaction with water molecules (Vidya Lekshmi, Yesodharan and Yesodharan, 2018). Hence, the degradation of MG was accelerated at higher amount of free radicals available for reaction. In addition, high sodium persulfate concentration provided higher chance of contact between free radicals and reactants (Ahmadi et al., 2020a; Bose et al., 2021). However, there was no significant change in degradation efficiency of MG observed while further increasing the sodium persulfate concentration from 2.0 mM to 5.0 mM. At higher concentration of sodium persulfate, the deactivation of $SO_4^{\cdot-}$ happened due to the competition of $SO_4^{\cdot-}$ between the degradation of MG and side reactions (Zhong et al., 2020). $SO_4^{\cdot-}$ present in excess would induce self-quenching effect through the reaction with $SO_4^{\cdot-}$ itself to produce $S_2O_8^{\cdot-}$ which exhibited lower oxidation potential ($E^\circ = 2.1$ V) than $S_2O_8^{\cdot-}$ (Ghanbari and Moradi, 2017; Gayathri, Yesodharan and Yesodharan, 2019; Dang et al., 2021).

In addition, $\text{SO}_4^{\cdot-}$ would react with $\text{S}_2\text{O}_8^{2-}$ to produce $\text{S}_2\text{O}_8^{\cdot-}$ leading to the decrement amount of $\text{SO}_4^{\cdot-}$. Therefore, the increment in the degradation efficiency of MG was insignificant at the concentration of sodium persulfate beyond the optimum value (2.0 mM).

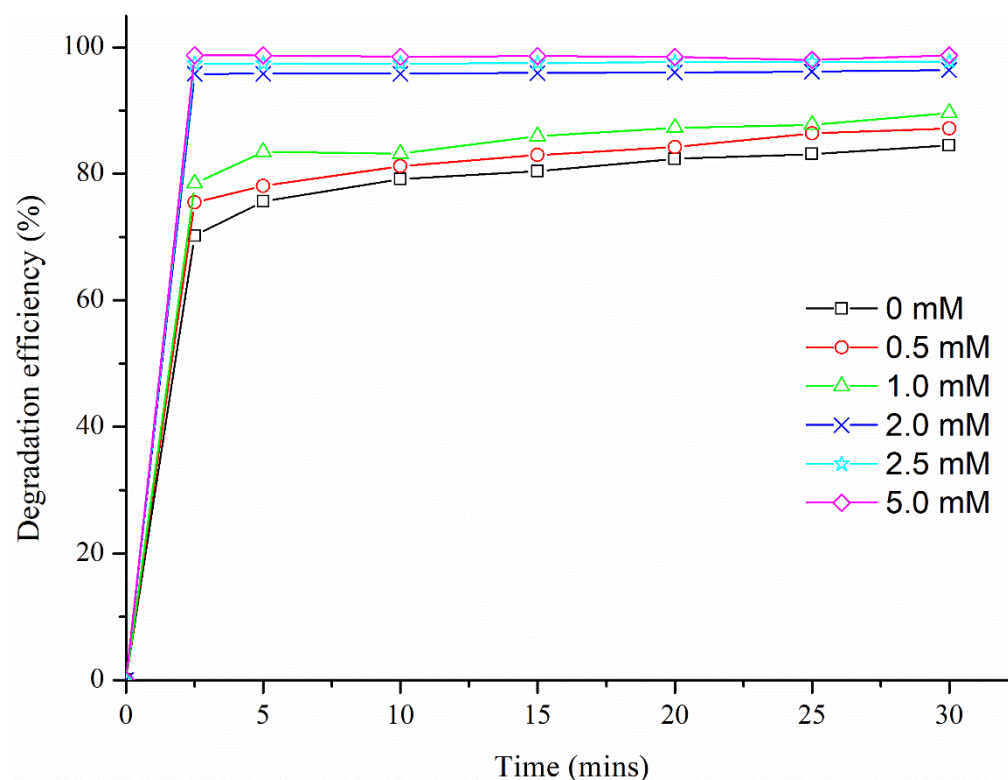


Figure 4.28: Effect of Sodium Persulfate Concentration in the Sonocatalytic Degradation of MG (Catalyst Loading: 1.0 g/L; Initial Dye Concentration: 500 mg/L; Ultrasonic Power: 80 W; Solution pH: 3; Irradiation Time: 30 mins).

4.3.12 Type of Organic Dyes

Figure 4.29 shows the sonocatalytic performance of Ag-ZnO in the presence of various organic dyes. The results confirmed that Ag-ZnO exhibited the best sonocatalytic activity in the degradation of MG (97.70 %), followed by MB (84.04 %), MO (36.36 %), RB (15.02 %) and CR (6.08 %). The cationic

dyes (MG and MB) showed better degradation efficiency than the anionic dyes (MO and CR) in the presence of Ag-ZnO as sonocatalyst. This could be attributed to the relatively simpler molecular structure of MG and MB as listed in **Table 4.6** (Long et al., 2021). Hence, MG and MB could be degraded more easily in the sonocatalytic process. Besides, the zeta potential values of Ag-ZnO illustrated in **Figure 4.5** showed that the surface of Ag-ZnO was mostly negatively charged in wide range of solution pH. The pKa value of MG was 6.9 indicating that the surface of MG were positively charged in the solution with pH value below 6.9 (Eskandari et al., 2023). The electrostatic attraction facilitated the attachment of the positively charged dye onto the active sites of Ag-ZnO (Tiwari, Sonwani and Singh, 2022). Therefore, greatest amount of MG could be degraded ultrasonically in the presence of Ag-ZnO as sonocatalyst.

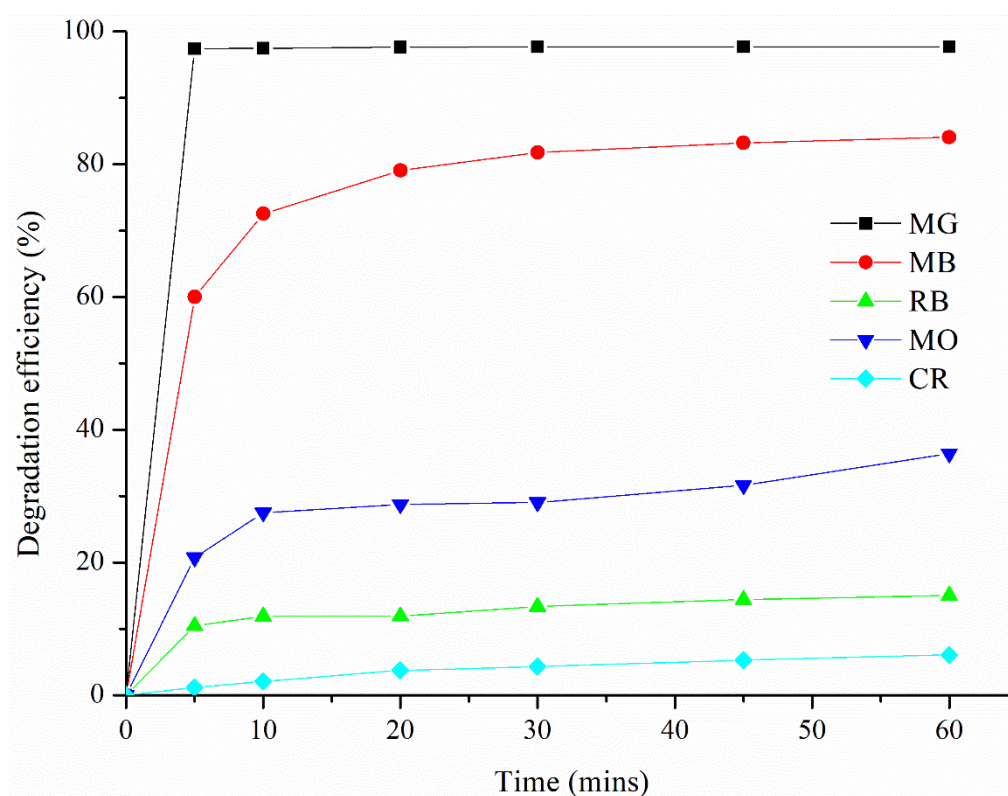
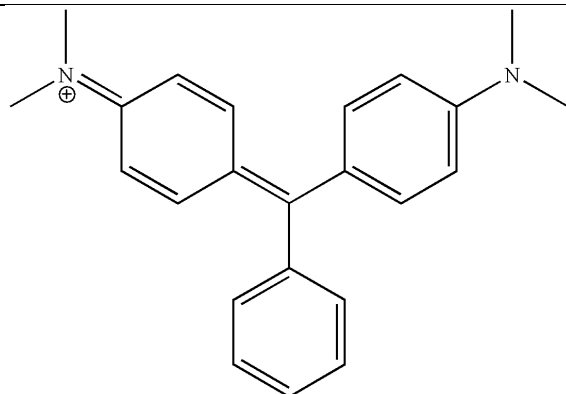
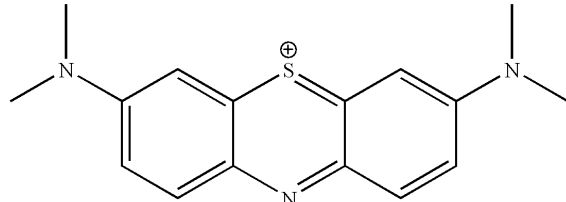
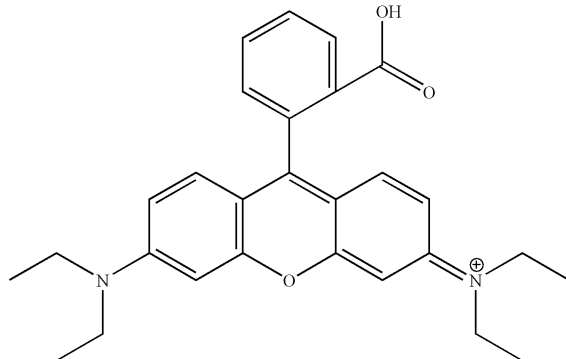
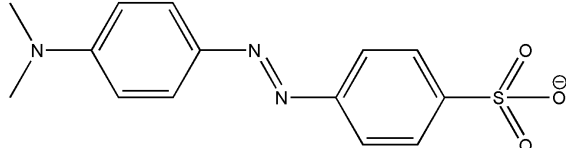
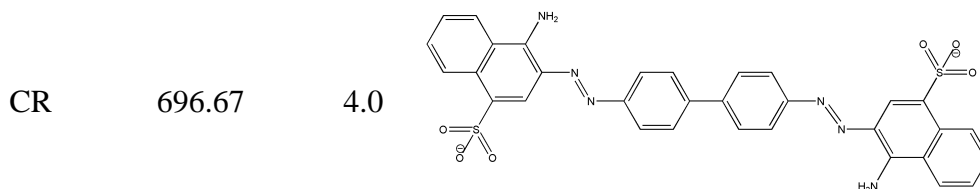


Figure 4.29: The Sonocatalytic Activity of Ag-ZnO in the Presence of Different Organic Dyes (Catalyst Loading: 1.0 g/L; Initial Dye

Concentration: 500 mg/L; Ultrasonic Power: 80 W; Sodium Persulfate Concentration: 2.0 mM; Irradiation Time: 60 mins).

Table 4.6: Molecular Weight and Molecular Structure of Organic Dyes.

Organic dyes	Molecular weight (g/mol)	pKa	Molecular structure
MG	364.91	6.9	
MB	319.85	3.8	
RB	479.02	3.2	
MO	327.33	3.5	



It is noteworthy that the degradation efficiency of cationic RB was lower as compared to MO. The findings could be related to more negative zeta potential of RB (-30 mV) than MO (-15 mV) at pH 4 (Chandrabose et al., 2021). Hence, the electrostatic repulsion force between RB and Ag-ZnO was greater than MO leading to lower degradation efficiency. Jin et al. (2020) also suggested that the degradation efficiency of RB was lower than MO due to its lower affinity towards catalyst induced by the electrostatic interaction. In addition, the molecular structure of RB was relatively bigger than MO as presented in **Table 4.6**. Therefore, a complicated degradation process was required to decompose RB leading to lower degradation efficiency of RB than MO (Chairungsri et al., 2022).

In this study, the degradation efficiency of CR was the lowest among the organic dyes. This could be attributed to its anionic nature which inhibited its adsorption to the sonocatalyst. Besides, CR exhibited the largest molecular structure which would give rise to the steric effect. This would in turn hinder the interaction between CR and the radicals and hence reduce the degradation efficiency remarkably (Aragaw and Alene, 2022). Other than that, CR consisted of azo groups (R-N=N-R') which were very stable and hard to be destroyed (Wang et al., 2020b). A high energy of about 9420 kJ/mol was needed in order to break the bond in azo dyes (Xu et al., 2020). Therefore, the sonocatalytic

performance of Ag-ZnO was the lowest in the degradation of CR as compared to other dyes.

4.4 RSM Modelling and Optimization of Sonocatalytic MG Degradation Efficiency

Table 4.7 reports the ANOVA results for the experimental data collected from the study of RSM while **Equation 4.8** express the empirical model equation in terms of coded factors obtained via regression analysis.

$$\begin{aligned} \text{Degradation efficiency}(\%) = & 61.47 + 3.11A - 13.58B + \\ & 1.71C + 10.62D + 1.65AB + 1.34AC - 1.15AD + 2.88BC - \\ & 1.46BD - 0.7075CD \end{aligned} \quad (4.8)$$

The CCD model was statistically significant due to the F-value of 45.68 corresponding with the p-value < 0.0001. The results indicated that F-value could occur due to noise with merely 0.01% of chance. However, the terms C, AB, AC, AD, BD and CD were insignificant since their corresponding p-value was larger than 0.05. Hence, backward elimination method was applied to remove the insignificant terms and simplify the model equation.

Table 4.7: ANOVA Results for Sonocatalytic Degradation Efficiency of MG Dye.

Source	Sum of Squares	Freedom Degrees	Mean Square	F-value	p-value	
Model	7701.29	10	770.13	45.68	0.0001	< significant
A-Catalyst loading	232.38	1	232.38	13.78	0.0015	
B-Initial dye concentration	4424.91	1	4424.91	262.45	0.0001	<
C-Ultrasonic power	70.04	1	70.04	4.15	0.0557	
D-Oxidant concentration	2705.98	1	2705.98	160.50	0.0001	<
AB	43.30	1	43.30	2.57	0.1255	
AC	28.78	1	28.78	1.71	0.2069	
AD	21.25	1	21.25	1.26	0.2755	
BC	132.71	1	132.71	7.87	0.0113	
BD	33.93	1	33.93	2.01	0.1722	
CD	8.01	1	8.01	0.4750	0.4990	
Residual	320.34	19	16.86			
LOF	163.15	14	11.65	0.3707	0.9344	not significant
Pure Error	157.18	5	31.44			
Cor Total	8021.62	29				

$R^2 = 0.9601$; Adequate precision = 24.5996

Table 4.8 shows the ANOVA results for the sonocatalytic degradation of MG after backward elimination with the newly developed model as shown in **Equation 4.9**.

$$\text{Degradation efficiency (\%)} = 61.47 + 3.11A - 13.58B + 10.62D + 2.88BC \quad (4.9)$$

The p-value of the modified model was found to be lower than 0.0001 indicating that the model remained statistically significant after backward elimination. In addition, the model with a small LOF F-value of 0.5860 indicated that the model mismatch was insignificant. There was an 82.08% chance that a LOF F-value could occur due to noise. The adequate precision of this model was evaluated at a value 32.2527 which was larger than 4, indicated the adequacy of the model in the prediction of experimental response with a high ratio of signal to noise. In this case, all the terms A, B, D and BC were the significant model terms with p-values smaller than 0.05.

Table 4.8: ANOVA Results for Sonocatalytic Degradation Efficiency of MG Dye after Backward Elimination.

Source	Sum of Squares	Freedom Degrees	Mean Square	F-value	p-value	
Model	7495.97	4	1873.99	89.13	< 0.0001	significant
A-Catalyst loading	232.38	1	232.38	11.05	0.0027	
B-Initial dye concentration	4424.91	1	4424.91	210.45	< 0.0001	
D-Oxidant concentration	2705.98	1	2705.98	128.70	< 0.0001	
BC	132.71	1	132.71	6.31	0.0188	
Residual	525.65	25	21.03			
LOF	368.47	20	18.42	0.5860	0.8208	not significant
Pure Error	157.18	5	31.44			
Cor Total	8021.62	29				

$R^2 = 0.9345$; Adequate precision = 32.2527

Table 4.9 presents the CCD design of the experiment together with the predicted and actual values of degradation efficiency. The results showed that

the degradation efficiency obtained in this study was in the range of 28.24% to 89.49%. The predicted values were evaluated using **Equation 4.9**. **Figure 4.30** illustrates the plot of predicted and actual outcomes of the response in this study. The findings showed that the experimental data were fitted well with the designed model. The statistical analysis confirmed that this model exhibited a R^2 value of 0.9345, indicated a high correlation between the predicted and actual values of MG degradation efficiency. Hence, the model was highly adaptable in the prediction of the degradation efficiency by varying the variables in the studied range.

Table 4.9: Designed Matrix of CCD Together with the Predicted and Experimental Results.

Run	Catalyst Loading (g/L)	Initial dye concentration (mg/L)	Ultrasonic power (W)	Oxidant concentration (mM)	Degradation efficiency (%)	
					Actual Value	Predicted Value
1	0.75	1250	40	1.75	53.14	52.52
2	0.75	500	80	1.75	86.16	79.67
3	0.75	1250	40	0.75	28.24	31.28
4	1.5	500	40	1.75	89.49	91.66
5	0.75	1250	80	1.75	51.68	58.28
6	1.125	875	60	0.25	41.21	40.23
7	0.375	875	60	1.25	59.46	55.25
8	0.75	500	40	1.75	88.33	85.43
9	1.125	875	60	2.25	82.52	82.71
10	0.75	500	80	0.75	58.46	58.44
11	1.5	1250	40	1.75	56.21	58.74
12	1.125	875	60	1.25	59.95	61.47
13	1.125	125	60	1.25	86.04	88.63
14	1.5	1250	80	1.75	70.44	64.50
15	1.5	500	80	1.75	88.21	85.90
16	1.125	875	20	1.25	56.58	61.47
17	1.125	875	60	1.25	65	61.47

18	1.5	500	40	0.75	69.71	70.42
19	0.75	500	40	0.75	59.81	64.20
20	1.125	875	60	1.25	50.38	61.47
21	1.125	875	60	1.25	61.8	61.47
22	1.5	1250	40	0.75	37.64	37.50
23	0.75	1250	80	0.75	37.47	37.04
24	1.875	875	60	1.25	62.54	67.69
25	1.5	500	80	0.75	66.45	64.66
26	1.125	875	60	1.25	65.19	61.47
27	1.125	1625	60	1.25	32.17	34.31
28	1.125	875	60	1.25	64.02	61.47
29	1.125	875	100	1.25	62.1	61.47
30	1.5	1250	80	0.75	53.66	43.26

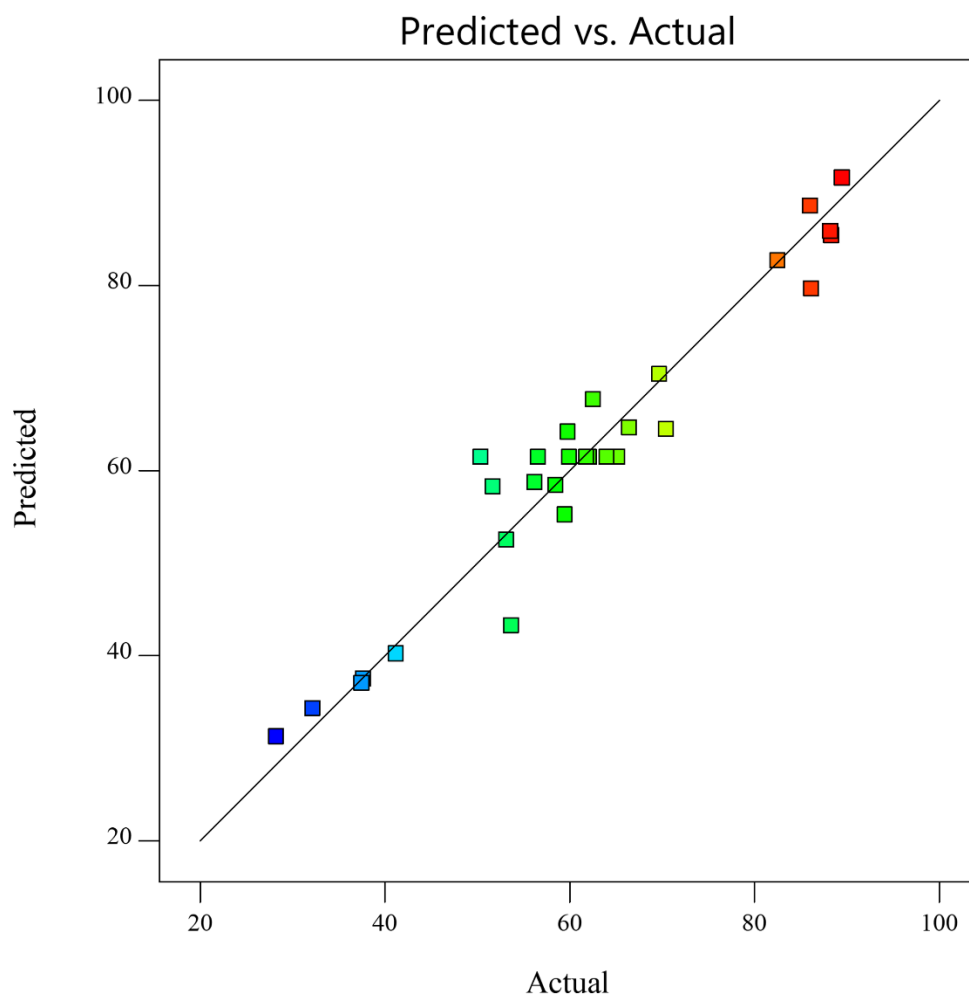


Figure 4.30: The Relationship between Predicted and Experimental Data of Sonocatalytic Degradation Efficiency.

4.4.1 Effect of Experimental Variables on the Degradation Efficiency

Figure 4.31(a) represents the effect of catalyst loading and initial dye concentration on the degradation efficiency of MG at constant ultrasonic power of 60 W and oxidant concentration of 1.25 mM. The 3D surface plot shows that the degradation efficiency of MG increased slightly as increasing catalyst loading. This was owing to more effective active sites available for the generation of more active oxidizing species such as $\bullet\text{OH}$ and $\text{SO}_4^{\bullet-}$ (Ruíz-Baltazar, 2021). In addition, a greater amount of catalyst loading increased the

surface area available for the adsorption of pollutants and hence improved the degradation efficiency (Rahimi et al., 2019). However, the sonocatalytic degradation efficiency was quenched significantly by the increasing initial dye concentration. By comparing Run 13 and 27, the degradation efficiency of MG decreased from 86.04% to 32.17% with the increasing of initial dye concentration from 125 mg/L to 1625 mg/L. The comparison confirmed that initial dye concentration was one of the significant factors in this model. The decrement in the degradation efficiency with the increasing initial dye concentration was attributed to the less effective heat and energy absorption with the increasing amount of dye molecules adsorbed on the catalyst surface (Mehrizad et al., 2019). Hence, the better degradation efficiency of MG can be attained at higher catalyst loading and lower initial dye concentration.

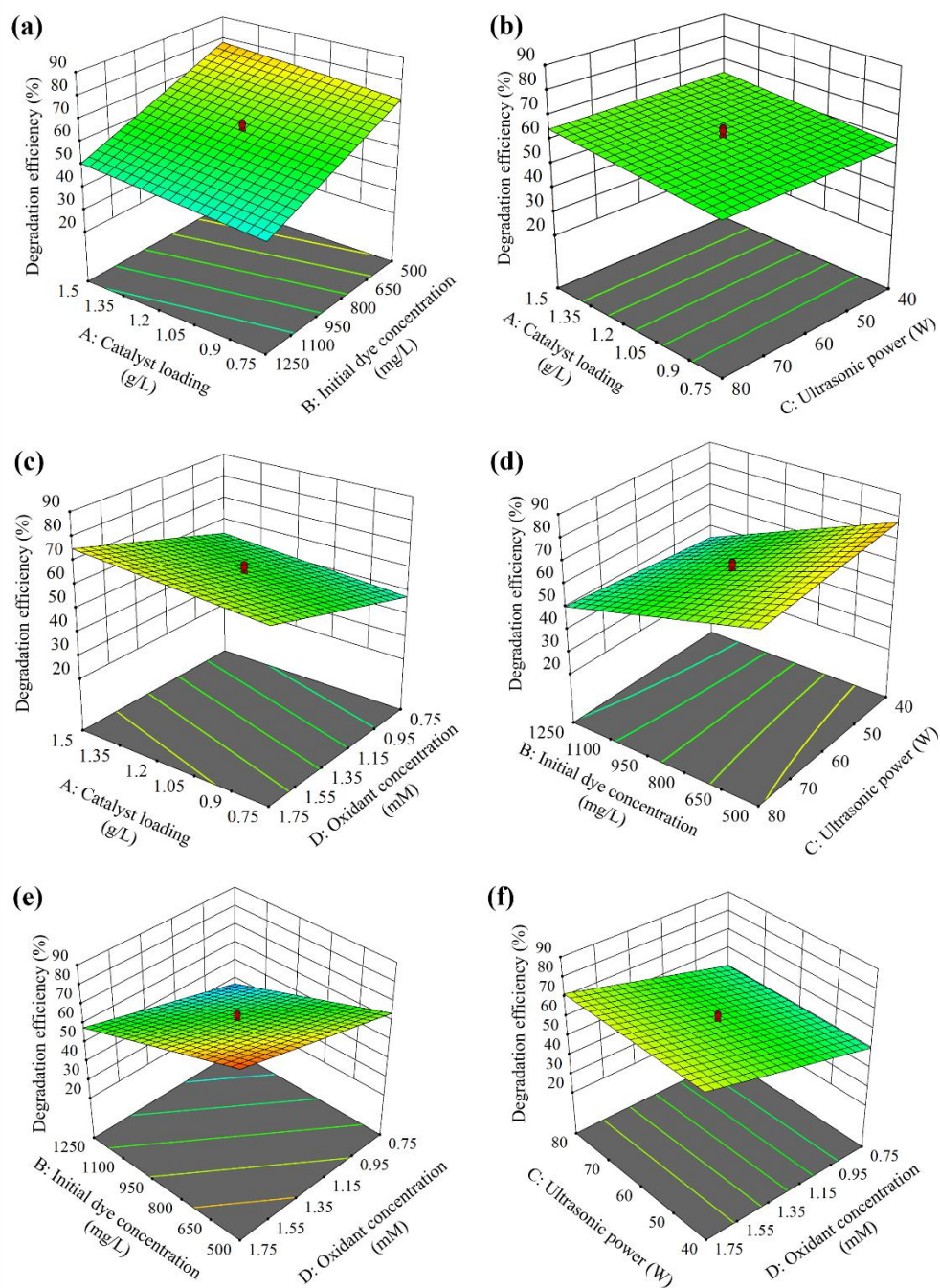


Figure 4.31: Interactive Effects of (a) Catalyst Loading and Initial Dye Concentration, (b) Catalyst Loading and Ultrasonic Power, (c) Catalyst Loading and Oxidant Concentration, (d) Initial Dye Concentration and Ultrasonic Power, (e) Initial Dye Concentration and Oxidant Concentration and (f) Ultrasonic Power and Oxidant Concentration.

Figure 4.31(b) illustrates the effect of catalyst loading and ultrasonic power on the sonocatalytic degradation efficiency at a constant oxidant

concentration of 1.25 mM and initial dye concentration of 875 mg/L. The findings showed that the degradation efficiency of MG dye increased slightly with increasing catalyst dosage and ultrasonic power. According to Xu et al. (2019), an increment in the ultrasonic power resulted in strengthened acoustic power and higher acoustic amplitude. This led to the formation of more microbubbles with higher potential energy in the aqueous reacting medium. Accompanied by the increasing catalyst loading, the generation of acoustic bubbles was further enhanced due to more nucleation sites present in the system (Dinesh and Chakma, 2019). Hence, higher photon energy was induced under higher ultrasonic power with higher catalyst loading. This would in turn lead to more generation of ROS species which was responsible for the degradation of organic dye. In addition, the microjet speed of cavitation bubbles was generated in the liquid medium. Higher ultrasonic power could improve the mass transfer rate of reactants and products. The continuously cleaning effect applied on the surface of sonocatalyst by the ultrasound wave was also enhanced by increasing the ultrasonic power (Hassan and Elhadidy, 2019). The total surface active sites for the possible reactions could also be increased by increasing the catalyst loading (Ayanda et al., 2021). This would then lead to the improvement of sonocatalytic MG degradation efficiency.

Figure 4.31(c) shows a three-dimensional surface plot representing the interactive effect of catalyst loading and oxidant concentration on the response of sonocatalytic degradation efficiency at a constant initial dye concentration of 875 mg/L and ultrasonic power of 60 W. It was found that there was an increasing trend on the degradation efficiency of MG dye with both the

increasing catalyst loading and oxidant concentration. This was because the activation of $S_2O_8^{2-}$ was performed through an electron transfer mechanism. Together with higher catalyst loading, more charge carriers could be generated for the activation of $S_2O_8^{2-}$ which enhanced the formation of free radicals (Chu et al., 2021). A higher amount of catalyst loading also provided a higher surface area of the active site the production of more radicals from water and oxygen molecules under ultrasound irradiation. In this case, oxidant concentration had a greater positive effect than catalyst loading on the outcome of degradation efficiency. This was because a higher amount of sodium persulfate present in the degradation could produce a greater amount of $S_2O_8^{2-}$. In addition, a greater amount of $S_2O_8^{2-}$ increased the lifetime of electron-hole pairs formed on the surface of the catalyst by inhibiting their recombination rate (Jegadeesan et al., 2019). This was able to improve the degradation efficiency of MG dye to an appreciable extent by the greater amount of reactive radicals with strong oxidizing power. Therefore, the designed model confirmed that the sonocatalytic dye decomposition could be improved by the combination of high catalyst loading and high oxidant concentration.

Figure 4.31(d) presents the influence of initial dye concentration and ultrasonic power at a constant catalyst loading of 1.125 g/L and oxidant concentration of 1.25 mM. These two parameters showed a significant interactive effect on the degradation efficiency of MG dye with a p-value of 0.0113. The effect of ultrasonic power could be observed through the comparison between Run 16 and 29. The sonocatalytic degradation efficiency increased slightly from 56.58% to 62.10% at constant initial dye concentration

of 875 mg/L with the increasing ultrasonic power from 20 W to 100 W. The outcome showed that ultrasonic power affected the degradation efficiency of MG insignificantly at constant initial dye concentration. However, the interactive effect of initial dye concentration and ultrasonic power was conducted by comparing Run 5 and 8. Together with the decreasing initial dye concentration from 1250 mg/L to 500 mg/L and increasing ultrasonic power from 40 W to 80 W, the degradation efficiency of MG increased from 53.14% to 86.16%. The results implied that the interaction between ultrasonic power and initial dye concentration affected the developed model remarkably.

As shown in **Figure 4.31(d)**, the findings depicted that the degradation efficiency of MG decreased with increasing initial dye concentration. This was due to the limited number of radicals available for dye degradation at higher initial dye concentration (Ahmadi et al., 2020b). From this point of view, the performance of the sonocatalytic decomposition could be enhanced by increasing the ultrasonic power because the shock wave with higher intensity could be induced under greater ultrasonic power condition, leading to more generation of active oxidizing species (Mehrizad et al., 2019). Besides, the increment in ultrasonic power could dissipate higher energy into the reaction solution. Hence, more cavitation effect could be induced and the thickness of liquid film would be diminished leading to the improvement in the mass transfer between the surface of Ag-ZnO and liquid medium (Gujar and Gogate, 2021). Therefore, the degradation of MG could be enhanced by increasing the ultrasonic power and decreasing initial dye concentration.

Figure 4.31(e) shows the effect of oxidant concentration and initial dye concentration on the performance of sonocatalytic degradation at a constant catalyst loading of 1.125 g/L and ultrasonic power of 60 W. According to the results of the study, the degradation efficiency of MG is inversely correlated to the initial dye concentration. As discussed by Chu et al. (2021), the adsorption of dye molecules on the catalyst surface might decrease the surface area available for the generation of radicals at higher initial dye concentration. Anyhow, the degradation efficiency of MG could be improved at higher oxidant concentrations due to the greater amount of radicals available to decompose the organic dye compounds (Ahmadi et al., 2020b). Hence, the combination of lower initial dye concentration and higher oxidant concentration could improve the performance of sonocatalytic degradation.

Figure 4.31(f) depicts the interactive effect of oxidant concentration and ultrasonic power on the degradation efficiency at a constant catalyst loading of 1.125 g/L and initial dye concentration of 875 mg/L. According to **Figure 4.31(f)**, the highest degradation efficiency could be achieved by maximizing both the oxidant concentration and ultrasonic power. This was because the $S_2O_8^{2-}$ could be activated directly under ultrasonic irradiation to form $SO_4^{\cdot-}$. The generated $SO_4^{\cdot-}$ triggered the yield of other radicals by breaking down the water molecules into $\bullet OH$ and hence resulted in the oxidation of organic dye (Mukhopadhyay et al., 2021). The sound wave intensity increased with increasing ultrasonic power. This brought to the increment in the energy and quality of bubble cavitation which induced high pressure gradient in the liquid medium (Shen et al., 2019). As a result, more conversion of $S_2O_8^{2-}$ could occur

which enhanced the yield radicals. Eventually, the degradation efficiency of MG dye was improved with the increasing oxidant concentration under high ultrasonic power.

4.4.2 Model Validation and Optimization

According to the results obtained from the RSM modelling, the optimum condition for the degradation efficiency of MG dye could be determined through the optimization of the studied experimental variables. **Table 4.10** lists the first five solutions of optimum condition generated by Design Expert software. In this part, model validation was carried out to confirm the feasibility of the predicted model as shown in **Equation 4.9**. The experimental values of degradation efficiency exhibited a high accuracy with error percentage lower than 5 % as compared to the predicted values. The results again proved that the model could be applied convincingly in the prediction and optimization of MG dye degradation efficiency.

Table 4.10: Comparative Results of Experimental and Predicted Values for Model Validation.

Run	Catalyst loading (g/L)	Initial dye concentration (mg/L)	Ultrasonic power (W)	Oxidant concentration (mM)	Experimental values	Predicted values	Percentage error (%)
1	1.5	500	80	1.75	89.43	85.90	4.11
2	0.75	500	40	1.75	89.21	85.43	4.43
3	1.19	543	61	1.69	86.22	83.27	3.55
4	1.41	512	76	1.64	86.61	82.97	4.39
5	1.17	557	56	1.63	84.02	81.91	2.58

In this part, the set of optimum condition with 0.75 g/L catalyst loading, 500 mg/L initial dye concentration, 40 W ultrasonic power and 1.75 mM oxidant concentration was selected for the subsequent experiments. It is noteworthy that the degradation efficiency of MG obtained through RSM study (89.21 %) was slightly lower than the one obtained through one-factor-at-a-time method (97.7 %). However, the operating parameters including catalyst dosage, oxidant concentration and ultrasound power were minimized via RSM as compared to the latter. This could in turn reduce the energy consumption and the usage of catalyst and oxidant in a more efficient way without compromising the degradation efficiency of MG significantly.

Figure 4.32 presents the change of UV-Vis spectra of MG dye under the optimum condition of sonocatalytic degradation. As shown in **Figure 4.32**, the presence of acid function of oxalate species, aromatic rings and chromophore in the MG dye were confirmed by the characterization peaks at 316 nm, 425 nm and 617 nm, respectively (Guenfoud, Mokhtari and Akrou, 2014). It is noteworthy that the maximum absorbance peak at 617 nm showed a dramatic decrease implying that the structure of chromophore was destroyed which resulted in the nearly invisible solution after undergoing the sonocatalytic degradation (Huang et al., 2021). Besides, a decreasing trend was observed at the peaks with wavelengths of 316 nm and 425 nm were owing to the cleavage of central carbon and breakage of aromatic rings, respectively (Ju et al., 2009). In addition, the new peak observed at 251 nm was owing to the formation of single-benzene derivatives during the degradation of MG molecules (Peng et al., 2021). Both the decrement of MG original peaks and the presence of new peaks

indicated that MG compounds were degraded during the sonocatalytic process. The findings were in good agreement with Yulizar, Apriandanu and Ashna (2020) which observed the photocatalytic degradation of MG using a UV-Vis spectrophotometer.

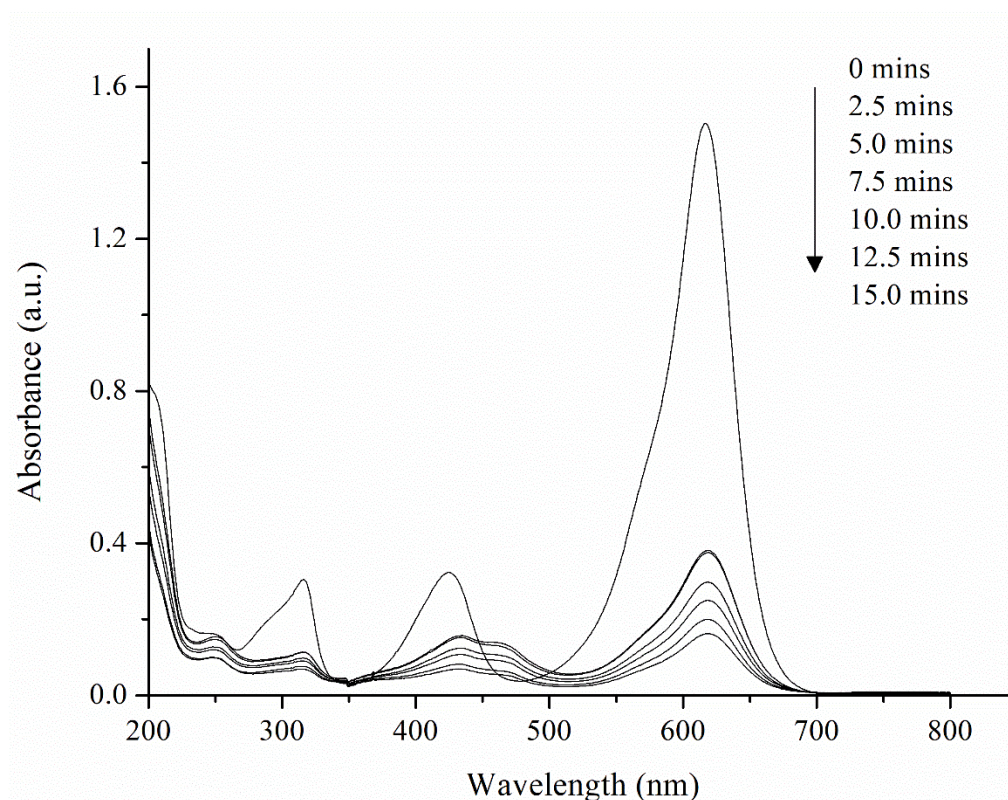


Figure 4.32: Absorption Spectra of MG in the Sonocatalytic Degradation of MG under the Optimized Condition (Initial Dye Concentration: 500 mg/L, Catalyst Loading: 0.75 g/L, Concentration of Oxidant: 1.75 mM, Ultrasonic Power: 40 W).

In this study, TOC and COD measurements were carried out to investigate the sonocatalytic degradation of MG. The value of TOC depicts the total amount of carbon present in the sample while COD measurement determines the amount of oxidizable organic matters. **Figure 4.33** illustrates the COD and TOC removal efficiencies in the optimized sonocatalytic degradation of MG. The COD and TOC removal efficiencies were found to be 80.34% and

75.24%, respectively after 90 mins of sonocatalytic degradation process under the optimum operating condition. The decrements of both the COD and TOC values confirmed the mineralization of MG molecules into simple products in the presence of Ag-ZnO as catalyst and sodium persulfate as oxidant under ultrasound irradiation. It is noteworthy that TOC removal was less than COD reduction attributed to the stable intermediate products generated during the degradation of MG. Jaafarzadeh et al. (2018) commented that the remaining TOC was owing to the stable organic compounds and intermediates formed during the degradation of organic substances which could be further oxidized into simpler products.

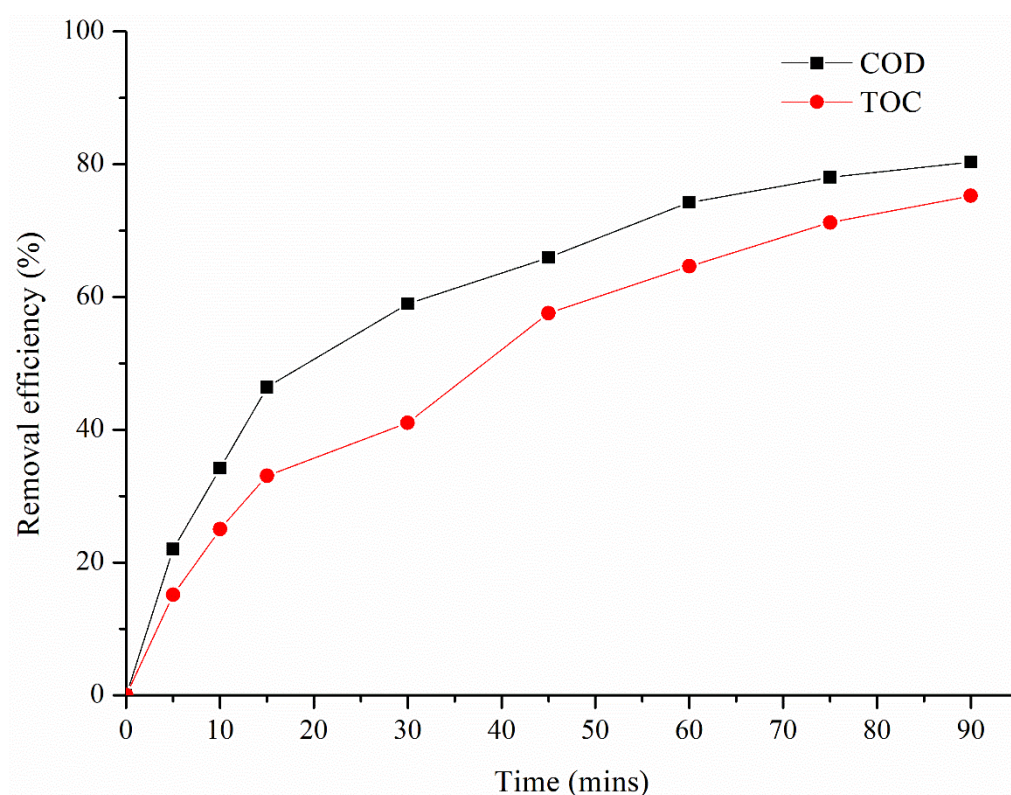


Figure 4.33: COD and TOC Removal Efficiencies in the Sonocatalytic Degradation of MG under Optimum Condition (Initial Dye Concentration: 500 mg/L, Catalyst Loading: 0.75 g/L, Concentration of Oxidant: 1.75 mM, Ultrasonic Power: 40 W).

Carbon oxidation state (COS) and average oxidation state (AOS) were evaluated using **Equation 4.10** and **Equation 4.11**, respectively (Hayati et al., 2020):

$$COS = 4 - 1.5 \left(\frac{COD}{TOC_0} \right) \quad (4.10)$$

$$AOS = 4 - 1.5 \left(\frac{COD}{TOC} \right) \quad (4.11)$$

where TOC_0 is the initial TOC value of MG. An increment in COS value from +1.07 to +3.43 was observed while AOS increased from +1.07 to +2.39 after undergoing sonocatalytic degradation of MG. The improvement in both the parameters indicated the successful formation of oxidized products through sonocatalytic degradation of MG (Isari et al., 2020). In addition, the findings also confirmed the enhancement in biodegradability of the samples after ultrasound-assisted treatment (Moradi et al., 2020).

Table 4.11 compares the ultrasound-assisted removal of MG between present work and previous study. It is noteworthy that the work reported by Hasan et al. (2020) could achieve MG removal efficiency up to 99.05 % using chitosan-ascorbic acid@NiFe₂O₄. However, the degradation of MG was carried out under lower initial dye concentration, higher power consumption, higher catalyst dosage and longer reaction time as compared to current work. Besides, Zhang et al. (2021b) suggested that MG removal through adsorption could attain 99.0 % efficiency within 30 mins. However, adsorption process would generate secondary waste which required further treatment since MG molecules were

only transferred to another phase without being decomposed through adsorption (Lum et al., 2020). This would in turn lead to the necessity of post-treatment which might consume more time and energy to eliminate MG completely from the environment. The findings confirmed that the amount of MG degraded under optimum condition in current work was the greatest among the reported works with the lowest energy consumption and shortest reaction time. This remarks the feasibility of green synthesis to produce Ag-ZnO nanoparticles as one of the potential candidates to be sonocatalyst in the degradation of organic dye.

Table 4.11: Comparative Data on the Removal of MG.

Removal technique	Energy source	Catalyst	Catalyst dosage (g/L)	Initial concentration (mg/L)	dye	Reaction time (mins)	Degradation efficiency (%)	Reference
Sonocatalysis	40 ultrasound	W Ag-ZnO	0.75	500		15	89.21	Present work
Sonocatalysis	300 ultrasound	W NiGa ₂ O ₄ /CeO ₂	1.0	10		60	96.2	(Wang et al., 2020a)
Sonocatalysis	Ultrasound	Zeolite imidazole framework-8	0.05	25		90	95.0	(Khoshnamvand et al., 2019)
Ultrasonic-electrochemical	300 ultrasound	W Ruthenium-iridium plated titanium electrode	-	100		60	94.92	(Ren et al., 2021)

Sonophotocatalysis	127	W	Chitosan-Ascorbic ultrasound	Acid@NiFe ₂ O ₄	1.0	70	90	99.05	(Hasan et al., 2020)
				Spinel Ferrite					
Sono-assisted adsorption	-			Magnesium ferrite	0.5	50	15	90.0	(Das, Debnath and Debnath, 2021)
Adsorption	-			ZIF-8@Fe/Ni	1.0	50	30	99.0	(Zhang et al., 2021b)
Photocatalysis	300	W		Cu ₂ CdSnS ₄	0.5	80	120	90.29	(Xu et al., 2022)
				Xenon lamp					
Photocatalysis	500	W	Al-Li@Th tungsten lamp	LDH- CNT	0.1	40	45	98.05	(Manea et al., 2022)

4.5 Reusability Test

The reusability potential of a catalyst is crucial to confirm the feasibility in real scale application. The results of ICP-OES analysis showed that only 0.04 mg/L of Ag and 0.08 mg/L of Zn leached into the treated solution after sonocatalytic reaction. The leaching concentration of both of Ag and Zn falls below the limit of industrial effluent set by Department of Environment (DOE), Malaysia in which the allowable of Zn and Ag in the discharge of industrial effluent are 2.0 m/L and 0.1 mg/L, respectively. The insignificant leaching of metal ions elucidated Ag-ZnO is a suitable material to be applied in sonocatalytic treatment of dye-containing wastewater due to its high stability and durability. The stability of Ag-ZnO was also evaluated up to 10 cycles of sonocatalytic degradation of MG. **Figure 4.34** illustrates the reusability test of Ag-ZnO in the degradation of MG. A gradual decrement in the degradation efficiency of MG was observed while recycling Ag-ZnO for 10 times. This was owing to the occupancy of active sites by MG molecules and intermediate products remaining from the previous run (Wang et al., 2020a). Hence, the number of active sites available for the subsequent degradation of MG reduced leading to the reduction in the sonocatalytic activity of recycled Ag-ZnO. The degradation efficiency of MG could retain up to 75 % even after undergoing 5 cycles of sonocatalytic reaction. The findings remarked the outstanding stability of Ag-ZnO as sonocatalyst in the degradation of Ag-ZnO.

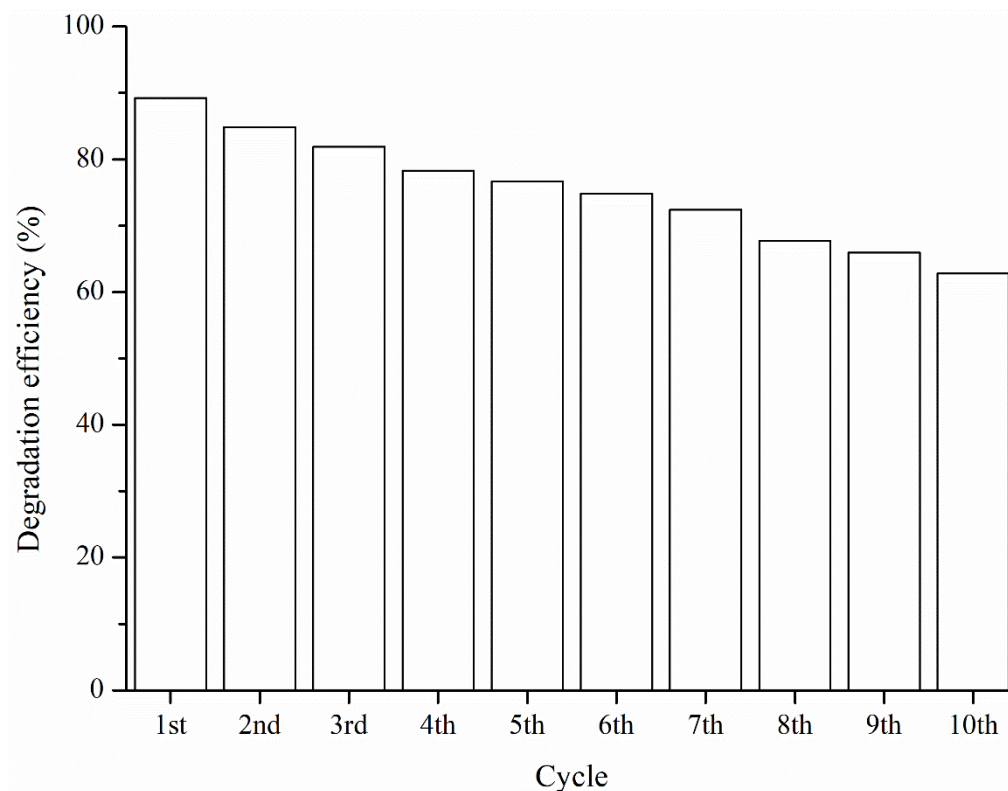


Figure 4.34: Reusability Study of Ag-ZnO in the Sonocatalytic Degradation of MG under Optimum Condition (Initial Dye Concentration: 500 mg/L, Catalyst Loading: 0.75 g/L, Concentration of Oxidant: 1.75 mM, Ultrasonic Power: 40 W).

Figure 4.35 presents the XRD patterns of fresh Ag-ZnO and reused Ag-ZnO. There was no obvious alteration observed in characteristic peaks of Ag-ZnO after being reused in the sonocatalytic degradation of MG. The characteristic peaks matched well to the peaks of wurtzite hexagonal ZnO and pure metallic Ag as per identified in JCPDS card no: 36-1451 and JCPDS card no: 04-0783, respectively (Zhang et al., 2022a; Mustafa, Barzinjy and Hamad, 2023). Therefore, the XRD confirmed the presence of wurtzite hexagonal ZnO incorporated with Ag dopant. Based on **Figure 4.35**, the peak intensities of Ag-ZnO decreased slightly after undergoing the sonocatalytic degradation of MG as compared to the fresh sample. This could be owing to the

attachment of MG molecules or intermediate products on the surface of Ag-ZnO after reaction (Swamy, Mohana and Yashas, 2022). However, the position of characteristic peaks did not experience significant variation after sonocatalytic degradation of MG. The findings reflected the stable structural framework and robustness of Ag-ZnO which was hardly influenced by the cavitation effect under ultrasound irradiation.

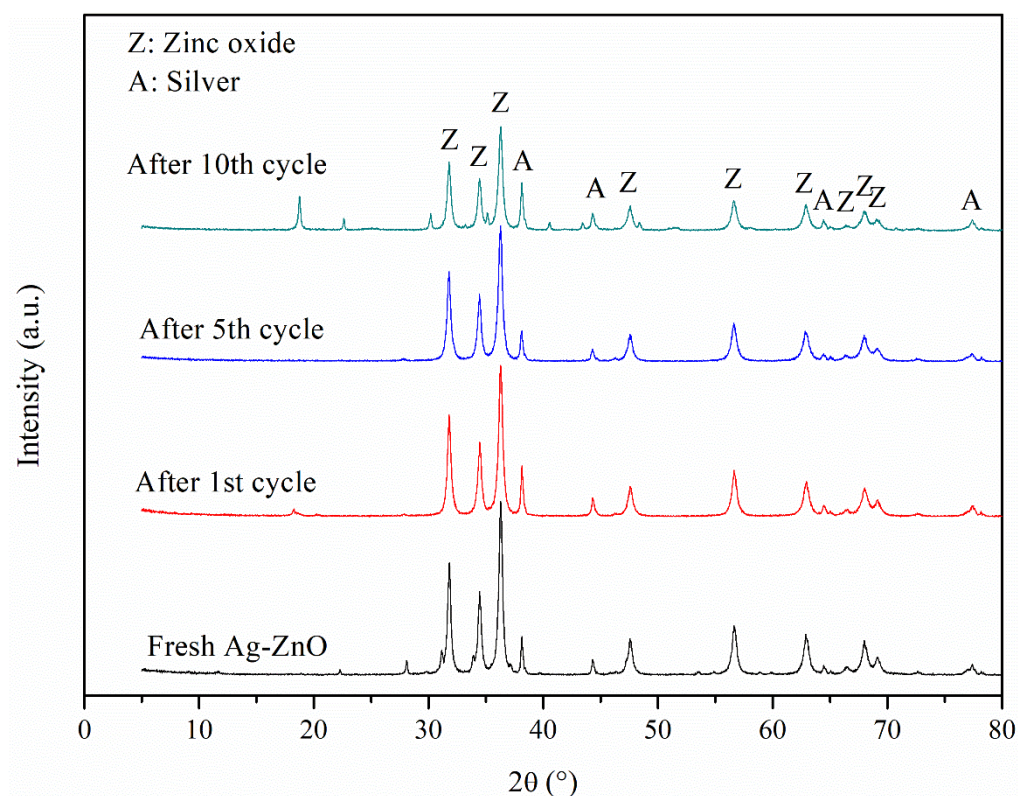


Figure 4.35: XRD Spectra of Fresh and Recycled Ag-ZnO.

Figure 4.36 illustrates the FTIR spectra of MG molecules, fresh Ag-ZnO and recycled Ag-ZnO. By comparing the FTIR spectrum of recycled Ag-ZnO with fresh Ag-ZnO, the position of characteristic peaks for Ag-ZnO remained unchanged indicating the stability in the functional groups after undergoing sonocatalytic degradation of MG. However, the peak intensities at

1045 cm^{-1} and 1120 cm^{-1} were found decreasing in the reused ZnO. This could be owing to the contaminants present in the recycled Ag-ZnO and loss of functional groups caused by the shock wave of ultrasound (Hayati et al., 2020). The FTIR spectrum of MG exhibited characteristic peaks at 1577 cm^{-1} , 1153 cm^{-1} and 2900 cm^{-1} corresponding to the C=C stretching of benzene rings, C-N stretching vibration of the aromatic amines and C-H stretching of asymmetric methyl group, respectively (Zhang et al., 2021a). It is noteworthy that these peaks were absent in the FTIR spectra of reused Ag-ZnO as shown in **Figure 4.36**. The findings indicated that the successful bond-breaking of MG functional groups in the sonocatalytic degradation of MG. In the FTIR pattern of MG molecules, the peaks appeared in the range of 850 cm^{-1} and 670 cm^{-1} were assigned to the aromatic structure present in MG molecules (Sutar et al., 2019). The disappearance and shift of peaks in this range were detected in the recycled Ag-ZnO after 5th and 10th cycles of reaction as compared to MG molecules. The observation implied the decomposition of aromatic structure during sonocatalytic process which was in line with the results of UV-Vis absorption as illustrated in **Figure 4.32**. Thus, the absence and modification of MG functional groups observed on the recycled Ag-ZnO after sonocatalytic degradation proved that the removal of MG molecules was performed through degradation under ultrasonic irradiation instead of adsorption only.

In addition, the broad peaks present at 3378 cm^{-1} and 1600 cm^{-1} in the spectra of reused samples were attributed to the stretching and bending of amine groups, respectively, implying the attachment of intermediate products on Ag-ZnO after sonocatalytic degradation (Liu et al., 2022b). FTIR spectra of reused

Ag-ZnO also showed additional peaks in between 1750 cm^{-1} and 750 cm^{-1} which were assigned to the footprints of MG residue and oxidized intermediates remaining on the surface of Ag-ZnO after sonocatalytic degradation. It is worth noting that the intensities of extra peak increased with the increasing number of experimental runs indicating the accumulation of impurities on Ag-ZnO during the recycle process. Hence, the reduction in the degradation efficiency of MG using reused Ag-ZnO could be elucidated by the attachment of the contaminants which reduced the active sites accessible to the further degradation of MG.

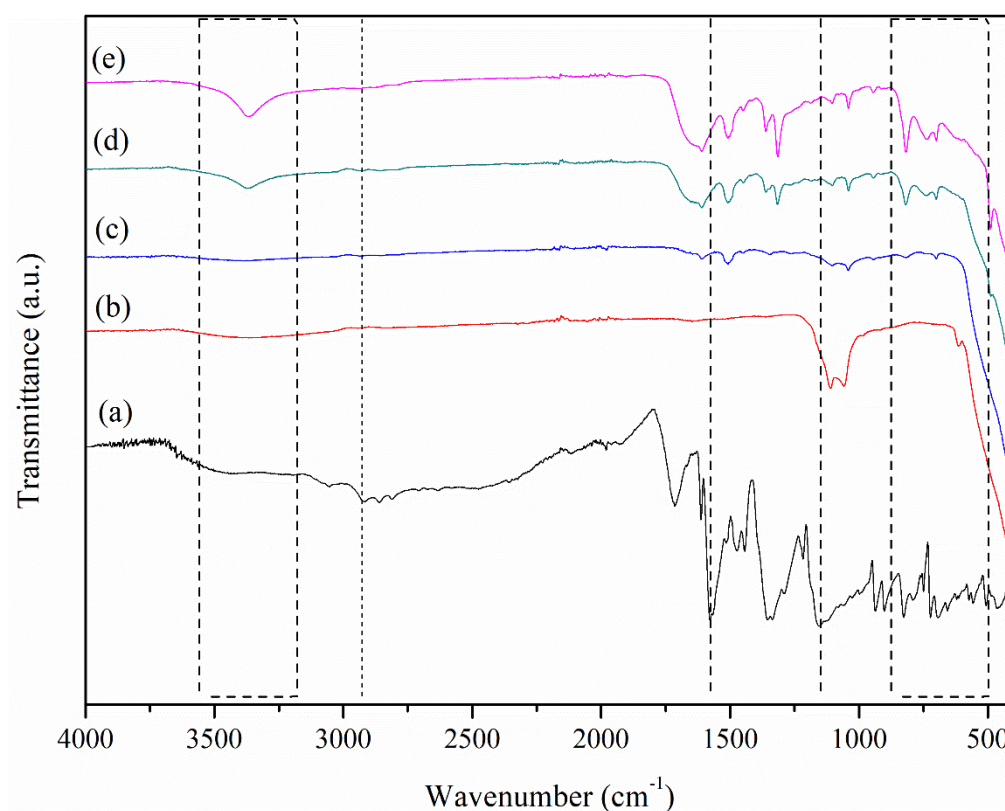


Figure 4.36: FTIR Spectra of (a) MG Molecules, (b) Fresh Ag-ZnO, (c) Recycled Ag-ZnO after 1st Cycle, (d) 5th Cycle and (e) 10th Cycle of Sonocatalytic Reaction.

Figure 4.37 represents the TGA curves of fresh and reused Ag-ZnO after sonocatalytic degradation of MG. There was negligible weight loss of about 1%

observed in all samples at the first 120 °C indicating that Ag-ZnO was thermally stable. It is noteworthy that the total weight loss of recycled Ag-ZnO after 1st run of sonocatalytic reaction was same as the fresh Ag-ZnO which was 3.2%. The findings showed that the thermal stability of Ag-ZnO was preserved after undergoing sonocatalytic process. As illustrated in **Figure 4.37**, the recycled Ag-ZnO after 5th and 10th cycles of sonocatalytic degradation of MG experienced notable weight loss with the increasing temperature beyond 120 °C. The major weight loss could be attributed to the decomposition of organic dye and the intermediate products remaining on Ag-ZnO after sonocatalytic degradation as detected in UV-Vis absorption and FTIR analysis. The recycled Ag-ZnO after 5th and 10th runs of experiments exhibited 5.2% and 17.8% of total weight loss respectively. As compared to the fresh Ag-ZnO, about 2.0% and 14.6% of the residual mass in the recycled Ag-ZnO samples were owing to the organic products of sonocatalytic reaction after 5th and 10th cycles, respectively. In addition, it is noteworthy that the weight of the samples remained almost constant at the temperature higher than 550 °C and high residual mass (> 80%) was retained in the recycled Ag-ZnO. The findings confirmed the excellent thermal stability of Ag-ZnO after sonocatalytic degradation of MG.

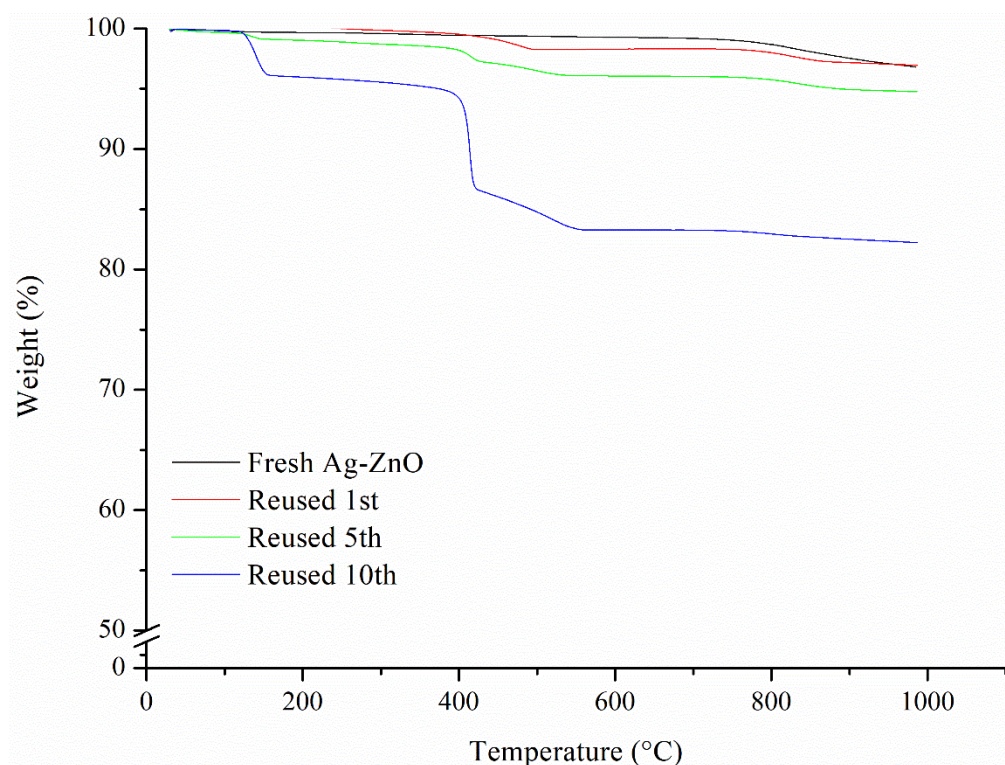


Figure 4.37: TGA Curves of Fresh Ag-ZnO and Recycled Ag-ZnO Samples.

Table 4.12 listed the elemental composition of fresh and reused Ag-ZnO. The content of major elements (Zn, Ag and O) remained almost the same in the recycled samples as compared to the fresh Ag-ZnO. This results obtained from EDX analysis proved the stability of elemental composition in Ag-ZnO. Wang et al. (2021) and Liu et al. (2021c) also reported on the high stability of catalyst through the examination of unaffected elemental composition by sonocatalytic process as compared to the freshly synthesized sample. Herein, an increment in the contents of C and N were detected in the reused Ag-ZnO. The finding was in consistent with FTIR and TGA results which confirmed the accumulation of organic dye molecules and by-products generated in the previous runs of experiment. The reusability study had confirmed the heavy-duty behavior and satisfactory stability of Ag-ZnO under reaction composition despite the

cavitation effect.

Table 4.12: Elemental Composition of Fresh and Reused Ag-ZnO.

Ag-ZnO Sample	Wt%					At%				
	C	N	O	Zn	Ag	C	N	O	Zn	Ag
Fresh	4.1	0.6	16.1	74.9	4.3	13.3	1.7	39.0	44.4	1.5
After 1st cycle	6.7	0.7	17.3	71.3	4.0	19.8	1.8	38.4	38.7	1.3
After 5th cycle	6.8	0.9	14.5	73.4	4.3	21.0	2.4	33.6	41.5	1.5
After 10th cycle	13.0	1.4	15.3	66.7	3.6	33.9	3.1	29.9	32.0	1.1

Figure 4.38 presents the pore distribution of fresh and reused Ag-ZnO after undergoing sonocatalytic degradation of MG. The results signify that the pore volume of Ag-ZnO was not affected significantly by ultrasonic irradiation which explained the stable structure of Ag-ZnO. However, it is worth noting that reused Ag-ZnO after 10th catalytic cycle showed an intense peak observed at pore diameter of 5.26 nm in the plot. This was attributed to the constriction of pore by the remaining MG molecules or intermediate products as detected in FTIR and EDX analysis. Hence, Ag-ZnO nanoparticles experienced reduction in pore size after sonocatalytic degradation of MG.

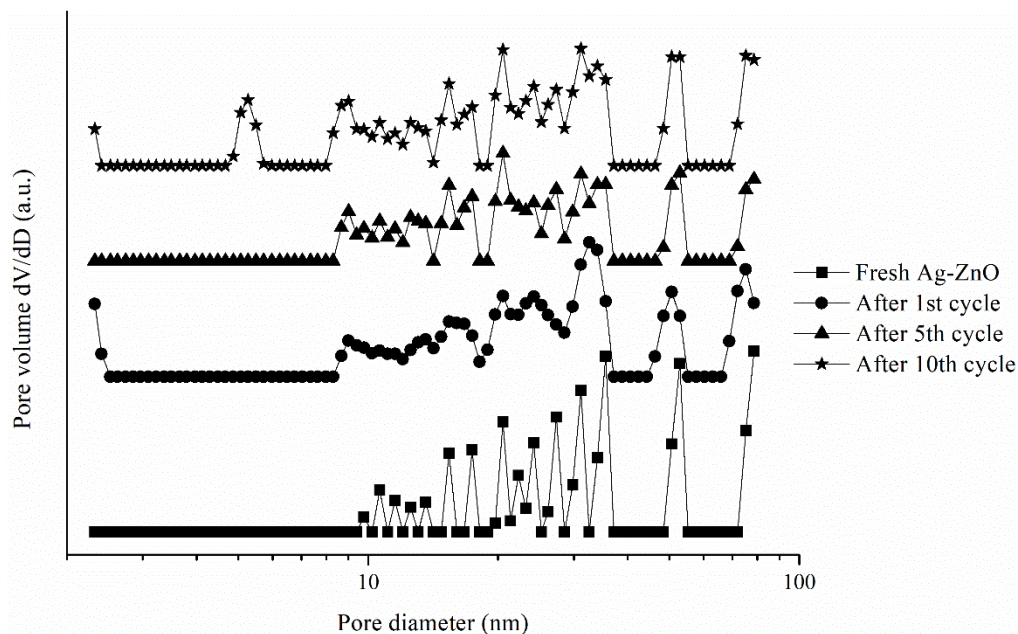


Figure 4.38: Pore Distribution for the Fresh and Reused Ag-ZnO.

4.6 Mechanism Studies of Sonocatalysis

Figure 4.39 illustrates the effect of scavenger addition on the sonocatalytic degradation efficiency of MG dye. It is noteworthy that the degradation efficiencies of MG dye were quenched from 89.21% to 86.41%, 64.27%, 55.47% and 65.33% in the presence of BQ, MetOH, IBA and $K_2Cr_2O_7$, respectively. The decrement in the degradation efficiency of MG with the addition of BQ, MetOH, IBA and EDTA-2Na confirmed the presence of $\bullet O_2^-$, $SO_4^{\bullet -}$, $\bullet OH$ and h^+ during the sonocatalytic degradation of MG dye, respectively.

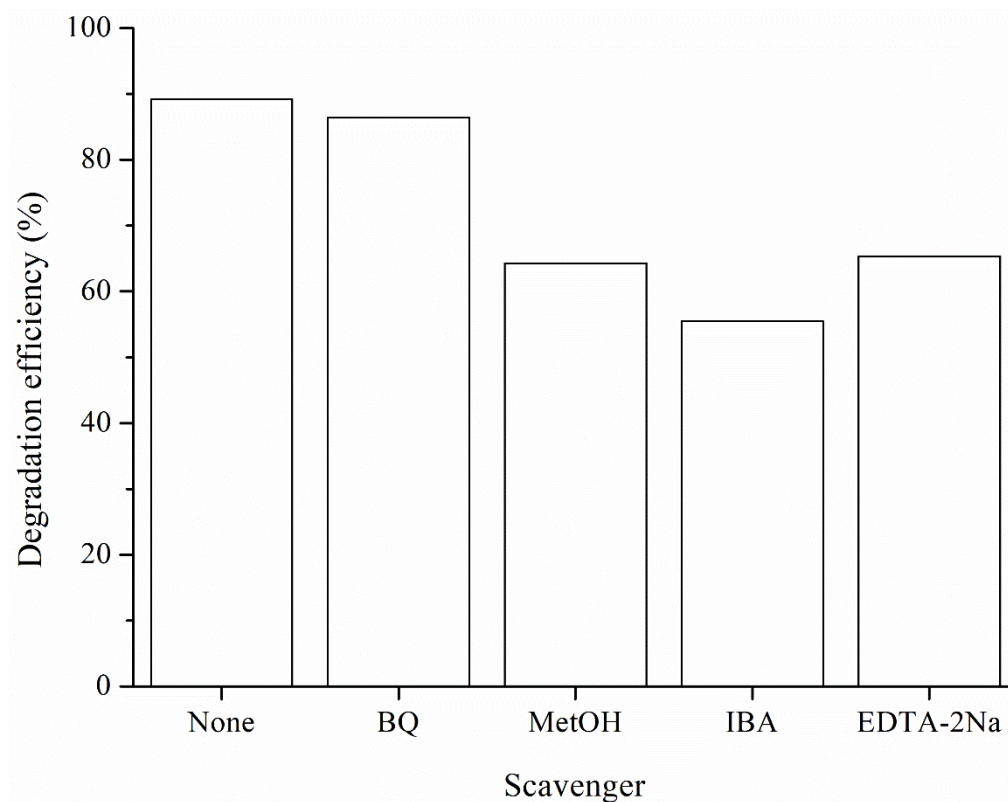
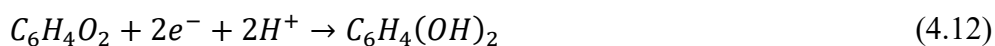
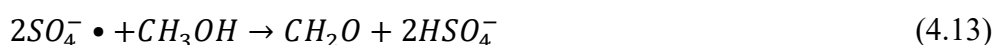


Figure 4.39: Effect of Chemical Scavengers on the Sonocatalytic Degradation of MG Dye in the Presence of Ag-ZnO as Catalyst and Sodium Persulfate as Oxidant.

Basically, the scavenging effect could be elucidated by the competitive reaction of the added chemical with ROS. The introduction of BQ into the reaction medium would compete for e^- with O_2 to form hydroquinone (H_2Q) as shown in **Equation 4.12**. The reaction between BQ and e^- was more favourable owing to its higher reaction rate constant ($k_{BQ/e^-} = 3.9 \times 10^{10} \text{ M}^{-1} \text{ s}^{-1}$) than the reaction of O_2/e^- ($k_{O_2/e^-} = 2.3 \times 10^{10}$) (Fónagy, Szabó-Bárdos and Horváth, 2021). This would in turn suppress the generation of $\bullet O_2^-$ and hence the decline in the sonocatalytic degradation of MG after addition of BQ could be explained by the quenching of $\bullet O_2^-$.



Both $SO_4^{\cdot-}$ and $\cdot OH$ could react with MetOH added into the reaction solution. However, the reaction between $SO_4^{\cdot-}$ and MetOH was preferable to the reaction with $\cdot OH$ due to its higher reaction rate constant ($k_{SO_4^{\cdot-}/MetOH} = 1.2 - 2.8 \times 10^9 \text{ M}^{-1} \text{ s}^{-1}$) than the latter ($k_{\cdot OH/MetOH} = 1.6 - 7.7 \times 10^7 \text{ M}^{-1} \text{ s}^{-1}$) (Alnaggar et al., 2022). Therefore, MetOH was applied as a scavenging agent for $SO_4^{\cdot-}$ in this study. During the reaction between $SO_4^{\cdot-}$ and MetOH, hydrogen abstraction would occur to form formaldehyde as listed in **Equation 4.13** (Sühnholz, Kopinke and Mackenzie, 2020; Xia et al., 2020).



IBA could as a $\cdot OH$ scavenger in the sonocatalytic degradation of MG attributed to high reaction rate constant ($k_{\cdot OH/IBA} = 3.8 - 7.6 \times 10^8 \text{ M}^{-1} \text{ s}^{-1}$) (Li et al., 2021b). IBA would compete with MG molecules for $\cdot OH$ to form ketone product through the reactions as shown in **Equations 4.14** and **4.15** (Collin, 2019).



In addition, EDTA-2Na was a good candidate to scavenge the activity of h^+ in the sonocatalytic degradation of MG due to its good reactivity with h^+ (El Hakim, Chave and Nikitenko, 2021). According to He et al. (2021b), the

positively charged h^+ could oxidize the organic ligand of EDTA-2Na into degradation products such as ethylene glycol, oxalic acid and carbon dioxide.

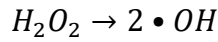
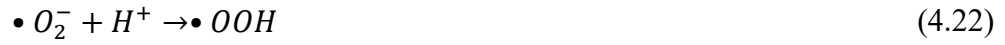
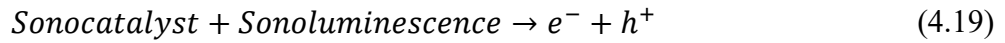
The radical scavenging test showed that the degradation efficiency of MG was affected insignificantly by the addition of BQ indicating that $\bullet O_2^-$ was the minor active species in this sonocatalytic process. The findings also confirmed that $\bullet OH$ was the dominant active species in the sonocatalytic oxidation of MG dye as the degradation efficiency was suppressed the most in the presence of IBA. The presence of IBA in the reaction medium would trap $\bullet OH$ and reduced the availability of main active species, $\bullet OH$ in sonocatalytic degradation of MG. The result was in line with the addition of EDTA-2Na. The quenching of degradation efficiency in the presence of EDTA-2Na was attributed to the consumption of h^+ which would in turn interrupt the formation of $\bullet OH$. Therefore, the sonocatalytic degradation of MG was inhibited apparently in the scavenging test which also confirmed the important role of h^+ to generate $\bullet OH$. Lv et al. (2020) reported similar results indicating that $\bullet OH$ was a prominent oxidizing species involved in the degradation of organic compounds through the advanced oxidation process.

The degradation of organic dye under ultrasound irradiation can be divided into two main processes which are sonolysis and sonocatalysis. In sonolysis process, the acoustic cavitation effect occurs including the formation, growth and collapse of microbubbles in the aqueous solution. Basically, the cavitation nuclei of bubbles are originated from the gas molecules or vapor which fill up the void space of liquid (Gholami et al., 2019b). The bubbles will

then expand into bigger size under the alternate compression-rarefaction cycles of ultrasound waves (Hayati et al., 2020). The microbubbles with extremely short lifetime of about 25 μs will eventually attain its critical size and implode with the emission of energy (Her, Park and Yoon, 2011; Gholami et al., 2019b). The collapse of bubbles lead to the generation of hotspot with critical pressure of 1,000 atm and temperature of 5,000 K (Ahmadi et al., 2020b). This results in the pyrolysis of water and oxygen molecules into $\bullet\text{OH}$, $\bullet\text{O}_2^-$ and $\bullet\text{H}$ as illustrated in **Equation 4.16** to **Equation 4.18** (Hassan and Elhadidy, 2019):



In the sonocatalysis process, the presence of heterogeneous catalyst can enhance the formation of radicals by providing more nucleation sites for the acoustic bubbles (He et al., 2021a). Besides, photons irradiation can be induced in the sonicated solution in the form of sonoluminescence which is able to excite surface e^- of nanoparticles from the VB to the CB (Sravandas and Alexander, 2021). The separation ability of electron-hole pair and the lifetime of charge carriers are the important factors that affect the sonocatalytic degradation efficiency (Ayodhya and Veerabhadram, 2020). The formation of the charge carriers followed by the conversion of the water and oxygen molecules into various types of radical as presented in the following equations (Xu et al., 2019):



Accompanied with Ag doping, the sonocatalytic degradation efficiency of MG in the presence of ZnO nanoparticles was improved due to the prolonged lifetime of charge carriers as confirmed through photoluminescence analysis. The transition of excited e^{-} would occur favourably from the CB of ZnO nanoparticles to the metallic Ag owing to the lower level of Fermi energy of Ag-ZnO than the CB of ZnO (Jalili-Jahani et al., 2021). Moreover, Schottky barrier established at the interface of Ag-ZnO could prevent the backflow of e^{-} from Ag to ZnO (Ning et al., 2021). At the Schottky barrier, band bending occurred leading to the formation of e^{-} depletion layer (Jalili-Jahani et al., 2021). Hence, the recombination of electron-hole pair in ZnO could be hindered drastically.

In addition, surface plasmon resonance (SPR) could occur in the metallic Ag which would further enhance the energy absorption efficiency of Ag-ZnO under the range of visible light. According to the absorption spectra shown in **Figure 4.40**, it is clear that Ag-ZnO exhibited better energy absorption in the visible region than Bio-ZnO and the broad peak at 500 nm confirmed SPR absorption of the Ag-ZnO heterostructure (Abdel Messih et al., 2019). Truong

et al. (2021) and Seong et al. (2019) also proposed that SPR absorption of Ag could enhance the absorption of visible energy leading to the increment in the generation of charge carriers. This would in turn enhance the sonocatalytic performance of Ag-ZnO because SPR might induce the excitation of e^- in Ag dopant as a results of energy absorption. The rapid oscillation of the excited e^- in the noble metal would promote e^- transition to the CB of ZnO at the heterojunction of Ag-ZnO (Munawar et al., 2020). Together with the plasmonic effect, the presence of metallic Ag as e^- capture could enhance the separation efficiency of electron-hole pair and increase the concentration of charge carriers which were important elements in the sonocatalytic reaction. Therefore, Ag was indeed a promising candidate to modify and improve the sonocatalytic performance of ZnO nanoparticles.

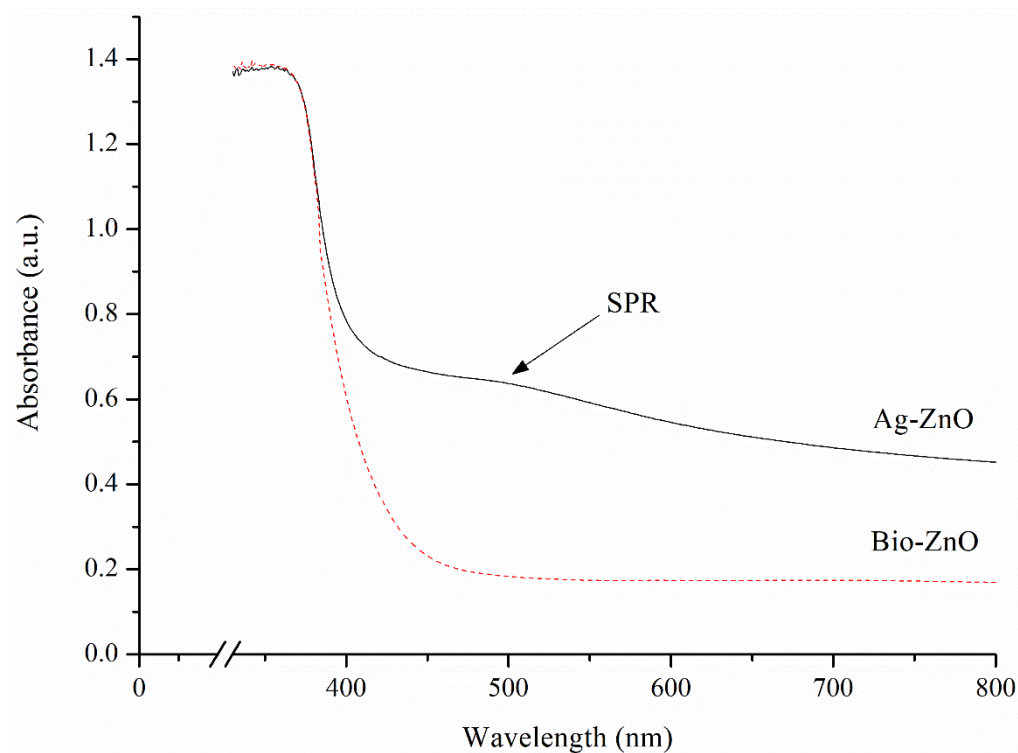
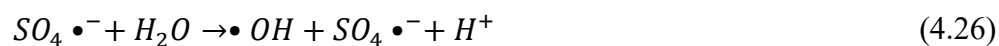


Figure 4.40: Absorption Spectra of Bio-ZnO and Ag-ZnO.

In addition, thermocatalytic process can also be resulted from the acoustic cavitation during ultrasonic irradiation. Pyrolysis of water molecules and formation of electron-hole pair of catalyst can be further enhanced by thermal energy resulted from the immense local temperature of bubble collapse (Mehrizad et al., 2019). The presence of persulfate can improve the generation of free radicals through self-decomposition and water pyrolysis under ultrasound irradiation as shown in **Equation 4.25** and **Equation 4.26**, respectively (Ahmadi et al., 2020b):



All these free radicals generated eventually play significant roles in the degradation of organic dye. According to the UV-Vis spectra presented in **Figure 4.32** the free radicals with high oxidizing power will attack the central carbon and break the aromatic rings. In addition, the mechanism will also be extended to the breakage of C=C and C=N bonds of chromophore, leading to the decolourization of organic dye. In the final stage of sonocatalytic degradation, the organic pollutant will be degraded into carbon dioxide and water molecules ideally.

4.7 Kinetic and Thermodynamic Studies

4.7.1 Reaction Kinetic Study

Figure 4.41 displays the kinetic models used to evaluate the sonocatalytic degradation while **Table 4.13** tabulates the parameters of kinetic models obtained from the graph. Based on the results of kinetic study, the experimental data obtained from sonocatalytic degradation of MG showed the best compliance with second order kinetic model due to the highest R^2 value obtained (0.953). The findings showed that the rate of sonocatalytic reaction was dependent on the reactant concentration raised to the second power (Vallero, 2019). Therefore, the reaction rate of sonocatalytic degradation was proportional to the square of dye concentration remaining in the solution. The results also showed that the reaction rate decreased with increasing time which was owing to the reduction in the remaining concentration of MG over time. Besides, the rate constant of second order kinetic model could be obtained from

the slope of linear plot as illustrated in **Figure 4.41(c)**. The sonocatalytic degradation of MG occurred with a rate constant of $0.001 \text{ L mg}^{-1} \text{ min}^{-1}$.

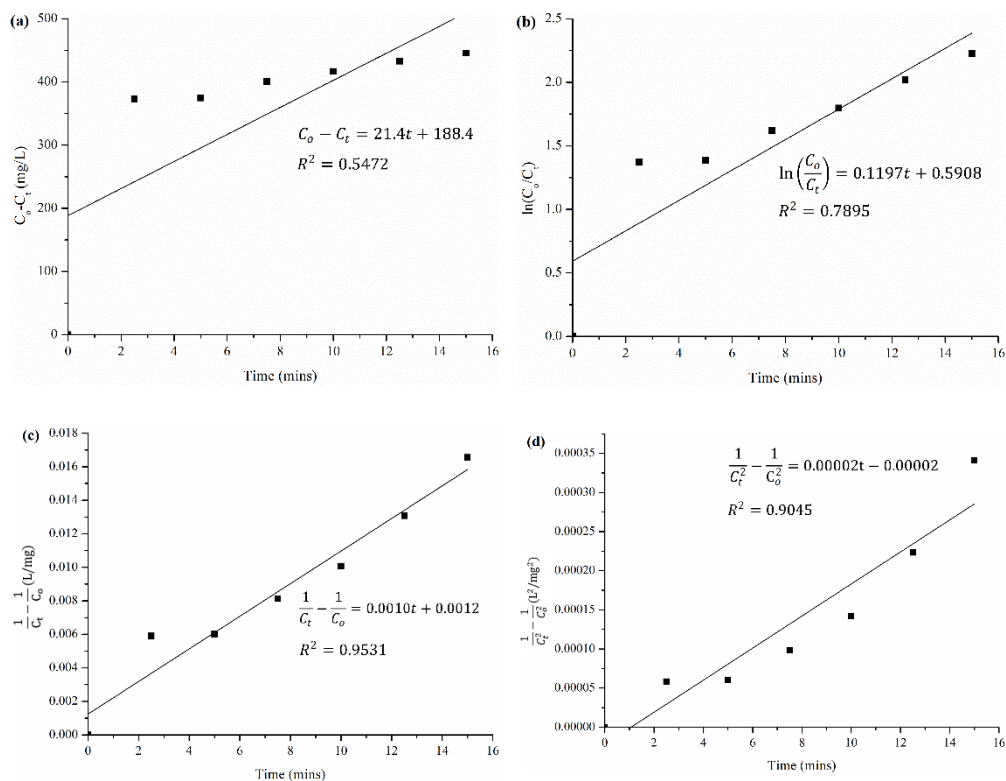


Figure 4.41: (a) Zero order, (b) First Order, (c) Second Order and (d) Third Order Kinetic Models for the Sonocatalytic Degradation of MG.

Table 4.13: Kinetic Modelling for Sonocatalytic Degradation of MG.

Kinetic model	Reaction rate constant	R^2	$t_{1/2}$ (mins)
Zero order	$k_0 = 21.4 \text{ mg L}^{-1} \text{ min}^{-1}$	0.547	11.68
First order	$k_1 = 0.120 \text{ min}^{-1}$	0.790	5.79
Second order	$k_2 = 0.001 \text{ L mg}^{-1} \text{ min}^{-1}$	0.953	2.0
Third order	$k_3 = 0.00002 \text{ L mg}^{-2} \text{ min}^{-2}$	0.905	0.6

Zero order kinetic model depicted that a reaction happened at a constant rate without being affected by the concentration of reactant (Wu et al., 2022). In this study, R^2 value of zero order kinetic model was found to be 0.54 which was unsatisfactory to describe the sonocatalytic degradation of MG. In other words, the reaction rate of sonocatalytic degradation of MG was dependent on the concentration of reactant. First order kinetic model disclosed that the rate of reaction was directly proportional to reactant concentration. The moderate R^2 value (0.790) implied that first order kinetic model was less inaccurate to illustrate the kinetic of sonocatalytic degradation of MG. In addition, third order kinetic model was also less suitable to fit the experimental results as compared to second kinetic order model due to its lower R^2 value (0.905) than the latter (0.953). Hence, the reaction rate of sonocatalytic degradation of MG was proportional to the second power of reactant concentration instead of third power.

Reaction kinetic model could be applied to estimate the time taken at which MG molecules would be degraded to a desired concentration. In this study, the values of $t_{1/2}$ with respect each reaction kinetic model are calculated using **Equations 3.11 – 3.14** and tabulated **Table 4.12**. The values $t_{1/2}$ for zero order, first order, second order and third order kinetic models were found to be 11.7 mins, 5.8 mins, 2.0 mins and 0.6 mins respectively. According to **Figure 4.42**, the experimental value of $t_{1/2}$ was estimated to be 1.7 mins which was the closest to the value evaluated in second order kinetic model. Thus, it could be concluded that the sonocatalytic degradation of MG using Ag-ZnO obeyed the

second order kinetic model.

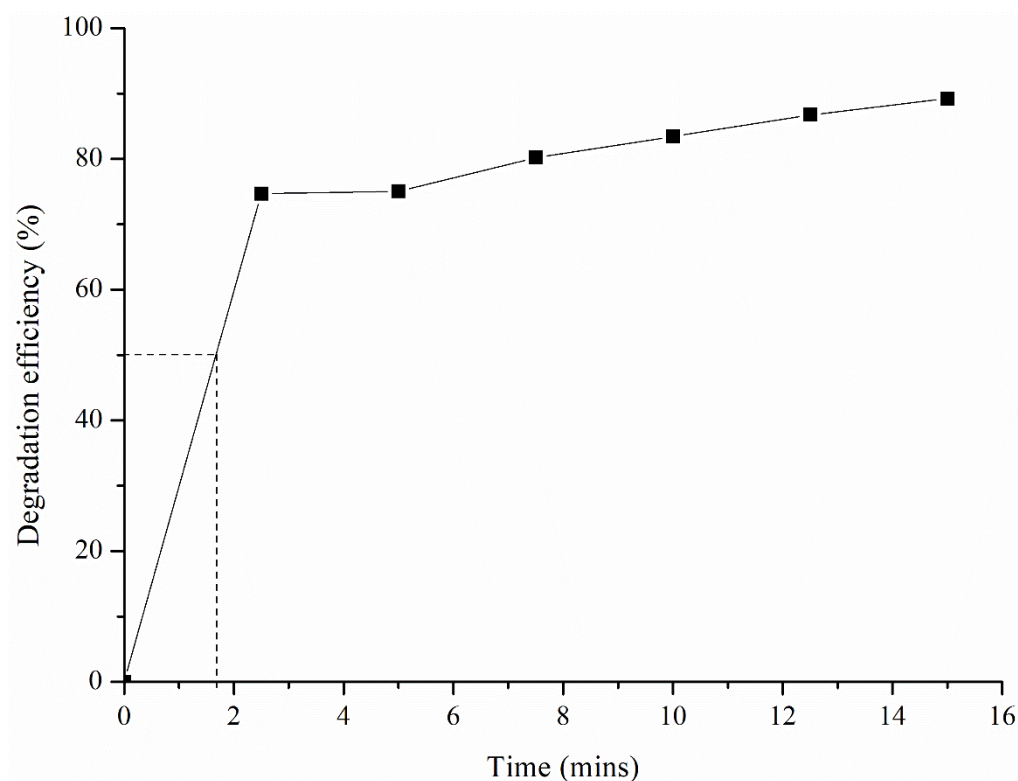


Figure 4.42: Sonocatalytic Degradation of MG under Optimum Condition (Initial Dye Concentration: 500 mg/L, Catalyst Loading: 0.75 g/L, Concentration of Oxidant: 1.75 mM, Ultrasonic Power: 40 W).

4.7.2 Thermodynamic Study

Figure 4.43(a) displays Van't Hoff plot of sonocatalytic degradation of MG. Van't Hoff plot confirmed the linear relationship between $\ln K_e$ and $1/T$ with R^2 value equals to 0.955. The values of ΔH° and ΔS° were evaluated from the slope and y-intercept of the plot, respectively. The negative slope of Van't Hoff plot gave positive value ΔH° (+20.52 kJ mol⁻¹) as tabulated in **Table 4.14** indicating that the reaction was endothermic (Sharma et al., 2022). In this study, ΔS° was estimated to be +86.44 J mol⁻¹ K⁻¹. The positive value of ΔS° explained

the order of system decreased at the interface of MG dye solution and Ag-ZnO (El-Sawy et al., 2021). According to Das et al. (2017) and Abraham et al. (2018), the positive ΔS° values for the sonocatalytic degradation of dye indicating the increased randomness at the interface of solid and solution. During sonocatalytic degradation of MG, the water molecules adsorbed on the surface Ag-ZnO was forced to be displaced by MG molecules leading to the increment in the degree of randomness at the interface of solution and catalyst (Emara et al., 2021; Tang and Zaini, 2021). Hence, positive ΔS° value reflected good interaction between MG molecules and Ag-ZnO (Saghir and Xiao, 2021). According to **Table 4.14**, ΔG° was found to be negative at all studied solution temperature. The findings confirmed that sonocatalytic degradation of MG using Ag-ZnO was a thermodynamically spontaneous process (Liu et al., 2021b). In addition, it is worth noting that **Figure 4.43(b)** showed the positive effect of temperature on the negative magnitude of ΔG° . This implied the affinity of reaction was enhanced at higher reaction temperature (Owija, Kosa and Abdel Salam, 2021).

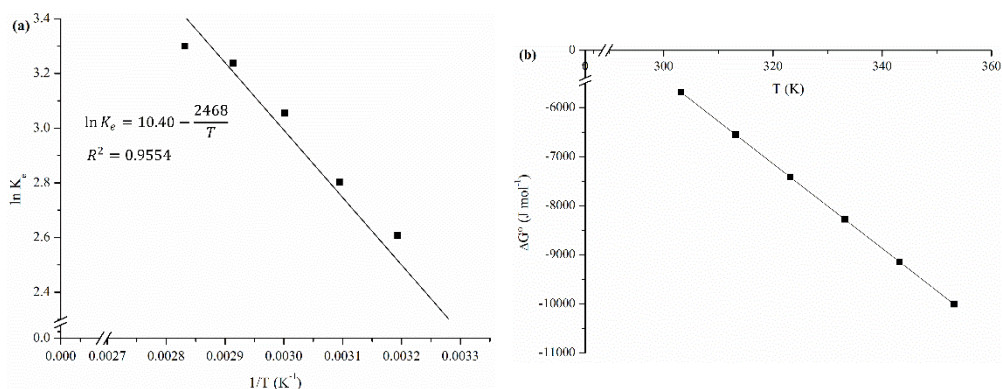


Figure 4.43: (a) Van't Hoff Plot of Sonocatalytic Degradation of MG and (b) Standard Gibbs Energy at Various Temperature.

Table 4.14: Thermodynamic parameters for the sonocatalytic degradation of MG.

Parameters	Value
<u>Van't Hoff equation</u>	
R^2	0.955
ΔH°	20.52 kJ mol ⁻¹
ΔS°	86.44 J mol ⁻¹ K ⁻¹
ΔG°	-5.69 kJ mol ⁻¹ – -10.01 kJ mol ⁻¹
<u>Eyring equation</u>	
R^2	0.995
ΔH^\ddagger	21.72 kJ mol ⁻¹
ΔS^\ddagger	-280.1 J mol ⁻¹
ΔG^\ddagger	106.6 kJ mol ⁻¹ – 120.6 kJ mol ⁻¹
<u>Arrhenius equation</u>	
R^2	0.996
E_a	24.43 kJ mol ⁻¹
Arrhenius constant, A	15.82 min ⁻¹

Figure 4.44 shows the graph of $\ln (k/T)$ against $1/T$ which obeyed the Eyring equation as shown in **Equation 3.20**. A linear graph with high R^2 value (0.995) was obtained indicating that the experimental results were fitted well into Eyring equation. The activation parameters calculated from the gradient and y-intercept of Eyring plot are summarized in **Table 4.14**. The negative value of ΔS^\ddagger (-280.1 J mol⁻¹) implied that the intermediate formed at the transition state was more ordered than the reactants. In other words, sonocatalytic degradation of MG involved the formation of activated complex with weak

bond through an associative reaction leading to the rapid degradation of MG under ultrasound irradiation (Thanh Tu et al., 2018; Rezaei and Nezamzadeh-Ejhiha, 2020). Both the positive ΔH^\ddagger and ΔG^\ddagger values explained the endothermic nature of sonocatalytic degradation of MG. The finding was in a good agreement with Van't Hoff model which confirmed that energy was required for the reaction to take place (Owija, Kosa and Abdel Salam, 2021).

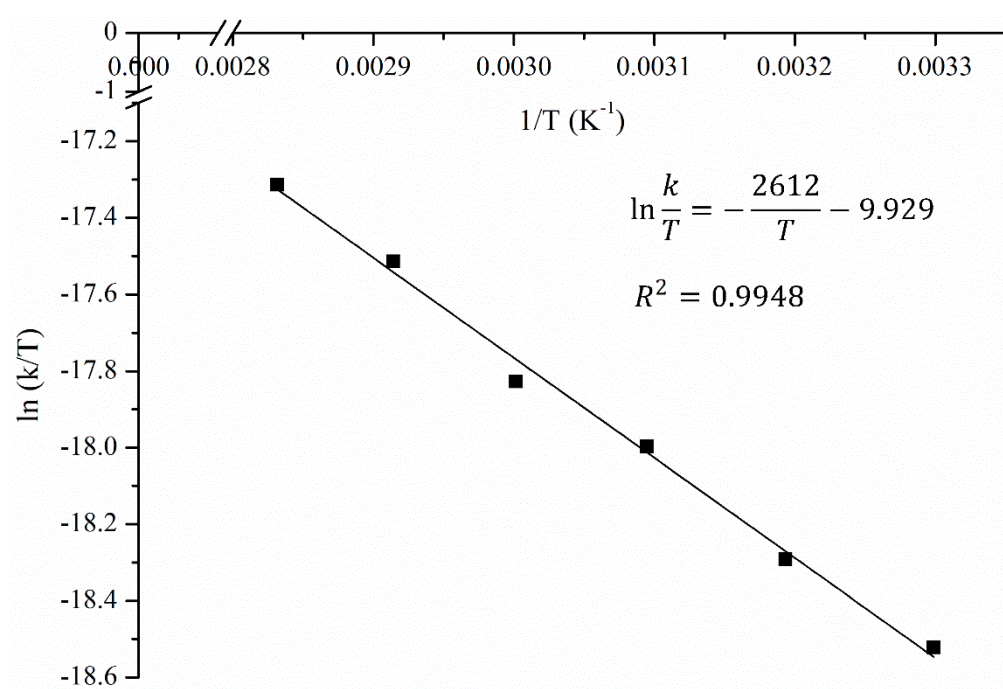


Figure 4.44. Eyring Plot for Sonocatalytic Degradation of MG.

Figure 4.45 illustrates Arrhenius plot of sonocatalytic degradation of MG. The negative linear relationship between $\ln k$ and $1/T$ confirmed that the rate of reaction was enhanced with the increasing temperature. In other words, sonocatalytic degradation of MG was accelerated at higher temperature (Qiu et al., 2021). It could be related to the increment in the kinetic energy with the increasing temperature leading to the promotion in the rate of sonocatalytic

degradation of MG (Zubair et al., 2020). According to the slope and y-intercept of Arrhenius plot, E_a and constant A were estimated to be +24.43 kJ mol⁻¹ and 15.82 min⁻¹, respectively. Together with the parameters obtained from Arrhenius equation, the rate of sonocatalytic degradation of MG could be derived from second order kinetic model and expressed in **Equation 4.27**:

$$r = 15.82e^{-\frac{24.43}{RT}}C_0^2 \quad (4.27)$$

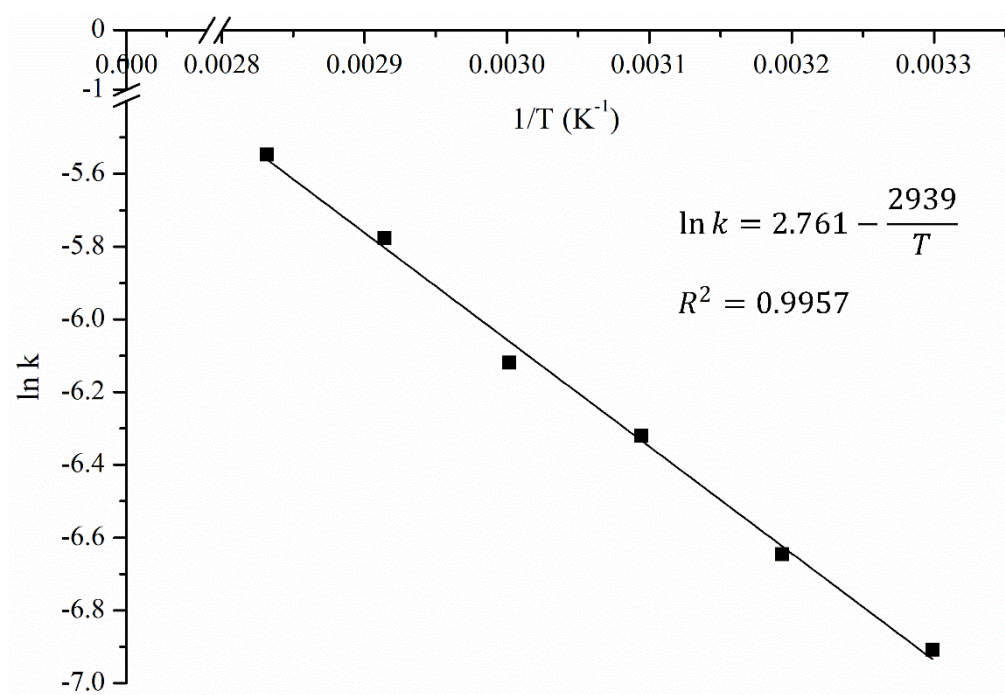


Figure 4.45. Arrhenius Plot for Sonocatalytic Degradation of MG.

In this study, the value of E_a lower than 29 kJ/mol indicated that sonocatalytic degradation of MG was mainly controlled by diffusion process instead of intrinsic chemical reaction (Saleh and Taufik, 2019; Yentür and Dükkancı, 2021). It is worth noting that the value of E_a obtained in this study was lower than the one reported in the work by Meriem, Souad and Lakhdar

(2020) with a value of $90.51 \text{ kJ mol}^{-1}$ which used Cu as catalyst to degrade MG dye through Fenton-like process. The findings confirmed that sonocatalysis was favoured in the degradation of MG rather than Fenton-like process because the latter required higher energy consumption. This could be related to the advantages of ultrasound irradiation which enhanced mass transfer, dispersion of catalyst and continuous cleaning of catalyst surface during degradation of organic substances (Du et al., 2022). Hence, high sonocatalytic degradation efficiency of MG could be achieved at lower energy consumption under ultrasound irradiation. Besides, the E_a value reported by Abbas (2020) to remove MG through adsorption using activated carbon as adsorbent was $58.52 \text{ kJ mol}^{-1}$. The lower value of E_a value evaluated in this study showed that sonocatalytic degradation of MG molecules was preferred due to the higher efficiency and effectiveness of sonocatalytic to decompose MG molecules into simpler and less harmful products (Darbandi et al., 2022). Besides, post-treatment was required to remove the sludge generated during adsorption process leading to more energy and time consumption (Lum et al., 2020). The value of E_a was evaluated using Eyring parameters through the relation as shown in **Equation 3.23**. The average value of E_a was found to be $+24.45 \text{ kJ mol}^{-1}$ which was in line with the value obtained from Arrhenius equation and the percentage error was found to be 0.05%.

CHAPTER 5

CONCLUSIONS AND FUTURE PERSPECTIVES

5.1 Conclusions

This study confirmed that ZnO nanoparticles were successfully fabricated through a facile green synthesis approach using plant extract. The findings signified the involvement of phytoactive compounds, such as phenolic compounds and flavonoids, contributed by plant extract as reductants and stabilizers in the green synthesis of ZnO sonocatalysts. The mechanism of green synthesis elucidated that the bioactive molecules firstly reduced Zn^{2+} ions to zero valent Zn and followed by the formation of ZnO through calcination. The green synthesized ZnO samples with particle sizes between 33 to 92 nm was found to be of hexagonal wurtzite crystal structure. Besides, green synthesized ZnO nanoparticles exhibited narrower band gap energy, higher thermal stability and mesoporous structure, larger specific surface area and pore volume in comparison to chemical synthesized ZnO. The green synthesized ZnO samples with these superior properties exhibited the best degradation efficiency as compared to the chemically synthesized ZnO and commercial ZnO. These properties could be further enhanced with the presence of Ag and Fe as dopants. Through the study of sonocatalytic activity, the ideal synthesis parameters of ZnO nanoparticles were found to be 70 °C of synthesis temperature and 1 h of synthesis duration using *Clitoria ternatea* Linn plant. Among all the analyzed

samples, 5wt% Ag-ZnO was found to be the best catalyst in the sonocatalytic degradation of organic dye.

The sonocatalytic degradation efficiency of dye could be attained up to 89.21% within 15 mins by using the green synthesized Ag-ZnO under the optimized operating condition (*i.e.* catalyst loading: 0.75 g/L; initial dye concentration: 500 mg/L; ultrasonic power: 40 W; persulfate concentration: 1.75 mM). A modified second-order equation was obtained through the RSM to evaluate the sonocatalytic degradation efficiency of MG dye. The ANOVA results indicated that the constructed central composite model which was statistically significant with $p\text{-value} < 0.0001$ could predict sonocatalytic degradation efficiency with high accuracy in the studied range of experimental variables. This model exhibited high adequacy of 32.2527 and a high coefficient of determination of 0.935.

By the means of reusability test, about 75% of sonocatalytic degradation efficiency of dye could be achieved in the presence of the green synthesized Ag-ZnO at the 5th cycle of catalytic reaction. The findings of characterization confirmed that Ag-ZnO exhibited stable crystal structure, thermal and chemical properties indicating its high potential to be commercialized. In this study, the sonocatalytic degradation of organic dye in the presence of green synthesized Ag-ZnO obeyed the second-order kinetic model with $0.0010 \text{ L mg}^{-1} \text{ min}^{-1}$ of reaction rate constant. By the means of thermodynamic study, the sonocatalytic degradation of dye was found to be an endothermic, spontaneous reaction with $+24.43 \text{ kJ/mol}$ of E_a .

5.2 Future Perspectives

The excellent sonocatalytic performance of the green synthesized Ag-ZnO achieved in this study is a great breakthrough in the development of wastewater treatment which is able to remove organic dyes effectively. However, there is still a gap remaining to reach the commercial application. For instance, further study is required to be conducted in the degradation of other organic pollutants such as pharmaceutical waste and pesticides to confirm the range of application and effectiveness of the sonocatalytic reaction. In addition, it is crucial to elucidate in-depth study on the techniques of green synthesis such as phytochemical extraction, cultivation and storage so that improved knowledge can be explored and applied to maximize the yield of phytochemicals and lengthen the lifetime of biomolecules. Besides, the design of an effective automated reactor for the large quantity yield of nanomaterials is also one of the challenges that needs to be studied prior to the scale-up production.

In addition, it is imperative to study the potential hazards which may be arisen throughout the green synthesis process such as handling, storage and disposal stages. Besides, the consequence attributed to the release of the green synthesized Ag-ZnO nanoparticles into environment is still unknown and unpredictable. Therefore, it is important to conduct toxicological assessment and evaluate safety profile on the nano-scaled products to foster the commercialization of green synthetic method. During toxicity test, real wastewater parameters such as pH, salinity and water temperature should be

taken into considerations because these variables are also important parameters in water remediation which will affect the toxicity of Ag-ZnO nanoparticles.

The application of the green synthesized Ag-ZnO nanoparticles as sonocatalyst can be studied in the degradation of other organic pollutants such as pharmaceutical and agricultural wastes to determine its feasibility in the removal of high variety of organic contaminants. In addition, ROS is the main element which drives the sonocatalytic degradation of organic substances. However, the quantification of ROS generated during sonocatalytic reaction is difficult to perform due to its extremely short lifetime. It is important to quantify active radicals in-situ in order to design the commercial system more accurately and precisely. This research can also be extended to a pilot scale study with the real wastewater condition prior to the industrial application. Furthermore, interdisciplinary cooperation is required with the scientists from other areas such as physics and applied engineering to design a suitable ultrasound equipment for commercialization purpose.

By tackling and exploring the incomplete information relevant to the application of green synthesized Ag-ZnO nanoparticles in sonocatalytic water remediation, the hidden potential of this green technology for the development of commercial products can be unlocked and lead to a greener future for the real-world applications.

REFERENCES

- Abbas, M., 2020. Performance of apricot stone to remove dyes from aqueous solutions – Equilibrium, kinetics, isotherms modeling and thermodynamic studies. *Materials Today: Proceedings*, 31, pp.437–443.
- Abdel Messih, M.F., Ahmed, M.A., Soltan, A. and Anis, S.S., 2019. Synthesis and characterization of novel Ag/ZnO nanoparticles for photocatalytic degradation of methylene blue under UV and solar irradiation. *Journal of Physics and Chemistry of Solids*, 135, p.109086.
- Abdelhakim, H.K., El-Sayed, E.R. and Rashidi, F.B., 2020. Biosynthesis of zinc oxide nanoparticles with antimicrobial, anticancer, antioxidant and photocatalytic activities by the endophytic *Alternaria tenuissima*. *Journal of Applied Microbiology*, 128(6), pp.1634–1646.
- Abdi, J., Sisi, A.J., Hadipoor, M. and Khataee, A., 2022. State of the art on the ultrasonic-assisted removal of environmental pollutants using metal-organic frameworks. *Journal of Hazardous Materials*, 424, p.127558.
- Abdullah, F.H., Abu Bakar, N.H.H. and Abu Bakar, M., 2021. Comparative study of chemically synthesized and low temperature bio-inspired *Musa acuminata* peel extract mediated zinc oxide nanoparticles for enhanced visible-photocatalytic degradation of organic contaminants in wastewater treatment. *Journal of Hazardous Materials*, 406, p.124779.
- Abdurahman, M.H., Abdullah, A.Z. and Shoparwe, N.F., 2021. A comprehensive review on sonocatalytic, photocatalytic, and sonophotocatalytic processes for the degradation of antibiotics in water: Synergistic mechanism and degradation pathway. *Chemical Engineering Journal*, 413, p.127412.
- Aboelmaati, M.G., Abdel Gaber, S.A., Soliman, W.E., Elkhatib, W.F., Abdelhameed, A.M., Sahyon, H.A. and El-Kemary, M., 2021. Biogenic and biocompatible silver nanoparticles for an apoptotic anti-ovarian activity and as polydopamine-functionalized antibiotic carrier for an augmented antibiofilm activity. *Colloids and Surfaces B: Biointerfaces*, 206, p.111935.
- Aboorvakani, R., Kennady Vethanathan, S.J. and Madhu, K.U., 2020. Influence of Zn concentration on zinc oxide nanoparticles and their anti-corrosion property. *Journal of Alloys and Compounds*, 834, p.155078.
- Abraham, R., Mathew, S., Kurian, S., Saravanakumar, M.P., Mary Ealias, A. and George, G., 2018. Facile synthesis, growth process, characterisation of a nanourchin-structured α -MnO₂ and their application on ultrasonic-assisted adsorptive removal of cationic dyes: A half-life and half-capacity concentration approach. *Ultrasonics Sonochemistry*, 49, pp.175–189.

Acar, M.K., Altun, T. and Gubbuk, I.H., 2022. Synthesis and characterization of silver doped magnetic clay nanocomposite for environmental applications through effective RhB degradation. *International Journal of Environmental Science and Technology*.

Adam, R.E., Pozina, G., Willander, M. and Nur, O., 2018. Synthesis of ZnO nanoparticles by co-precipitation method for solar driven photodegradation of Congo red dye at different pH. *Photonics and Nanostructures - Fundamentals and Applications*, 32, pp.11–18.

Ahamed, M., Javed Akhtar, M., Majeed Khan, M.A. and Alhadlaq, H.A., 2022. Facile green synthesis of ZnO-RGO nanocomposites with enhanced anticancer efficacy. *Methods*, 199, pp.28–36.

Ahmad, A., Razali, M.H., Mamat, M., Kassim, K. and Amin, K.A.M., 2020a. Physiochemical properties of TiO₂ nanoparticle loaded APTES-functionalized MWCNTs composites and their photocatalytic activity with kinetic study. *Arabian Journal of Chemistry*, 13(1), pp.2785–2794.

Ahmad, A.A., Ahmad, M.A., Yahaya, N.K.E.M. and Karim, J., 2021. Adsorption of malachite green by activated carbon derived from gasified Hevea brasiliensis root. *Arabian Journal of Chemistry*, 14(4), p.103104.

Ahmad, H., Tajdidzadeh, M., Thambiratnam, K. and Yasin, M., 2018. Hydrothermally synthesized zinc oxide nanoparticle based photodetector for blue spectrum detection. *Optik*, 172, pp.35–42.

Ahmad, I., 2019. Inexpensive and quick photocatalytic activity of rare earth (Er, Yb) co-doped ZnO nanoparticles for degradation of methyl orange dye. *Separation and Purification Technology*, 227, p.115726.

Ahmad, M., Qureshi, M.T., Rehman, W., Alotaibi, N.H., Gul, A., Abdel Hameed, R.S., Elaimi, M. Al, Abd el-kader, M.F.H., Nawaz, M. and Ullah, R., 2022a. Enhanced photocatalytic degradation of RhB dye from aqueous solution by biogenic catalyst Ag@ZnO. *Journal of Alloys and Compounds*, 895, p.162636.

Ahmad, M., Rehman, W., Khan, M.M., Qureshi, M.T., Gul, A., Haq, S., Ullah, R., Rab, A. and Mena, F., 2020b. Phytogenic fabrication of ZnO and gold decorated ZnO nanoparticles for photocatalytic degradation of Rhodamine B. *Journal of Environmental Chemical Engineering*, p.104725.

Ahmad, M.P., Rao, A.V., Babu, K.S. and Rao, G.N., 2020c. Effect of hydrogen annealing on structure and dielectric properties of zinc oxide nanoparticles. *Materials Chemistry and Physics*, 243, p.122226.

Ahmad, S., Aadil, M., Ejaz, S.R., Akhtar, M.U., Noor, H., Haider, S., Alsafari, I.A. and Yasmin, G., 2022b. Sol-gel synthesis of nanostructured ZnO/SrZnO₂ with boosted antibacterial and photocatalytic activity. *Ceramics International*, 48(2), pp.2394–2405.

Ahmadi, E., Shokri, B., Mesdaghinia, A., Nabizadeh, R., Reza Khani, M.,

Yousefzadeh, S., Salehi, M. and Yaghmaeian, K., 2020a. Synergistic effects of α -Fe₂O₃-TiO₂ and Na₂S₂O₈ on the performance of a non-thermal plasma reactor as a novel catalytic oxidation process for dimethyl phthalate degradation. *Separation and Purification Technology*, 250, p.117185.

Ahmadi, S., Rahdar, A., Adaobi Igwegbe, C., SobhanMortazavi-Derazkola, Marek Banach, A., Rahdar, S., Kumar Singh, A., Rodriguez-Couto, S. and Kyzas, G.Z., 2020b. Praseodymium-doped cadmium tungstate (CdWO₄) nanoparticles for dye degradation with sonocatalytic process. *Polyhedron*, 190, p.114792.

Akash, S., Ahalya, N. and Dhamodhar, P., 2020. Green synthesis, characterization and antimicrobial activity of zinc oxide nanoparticles on clinical isolates of streptococcus pyogenes. *Asian Journal of Chemistry*, 32(4), pp.907–911.

Akbar, A. and Anal, A.K., 2014. Zinc oxide nanoparticles loaded active packaging, a challenge study against Salmonella typhimurium and Staphylococcus aureus in ready-to-eat poultry meat. *Food Control*, 38, pp.88–95.

Akbar Jan, F., Wajidullah, Ullah, R., Ullah, N., Salman and Usman, M., 2021. Exploring the environmental and potential therapeutic applications of Myrtus communis L. assisted synthesized zinc oxide (ZnO) and iron doped zinc oxide (Fe-ZnO) nanoparticles. *Journal of Saudi Chemical Society*, 25(7), p.101278.

Akbarian, M., Mahjoub, S., Elahi, S.M., Zabihi, E. and Tashakkorian, H., 2020. Green synthesis, formulation and biological evaluation of a novel ZnO nanocarrier loaded with paclitaxel as drug delivery system on MCF-7 cell line. *Colloids and Surfaces B: Biointerfaces*, 186, p.110686.

Al-Gharibi, M.A., Kyaw, H.H., Al-Sabahi, J.N., Zar Myint, M.T., Al-Sharji, Z.A. and Al-Abri, M.Z., 2021. Silver nanoparticles decorated zinc oxide nanorods supported catalyst for photocatalytic degradation of paracetamol. *Materials Science in Semiconductor Processing*, 134, p.105994.

Al-Tohamy, R., Ali, S.S., Li, F., Okasha, K.M., Mahmoud, Y.A.-G., Elsamahy, T., Jiao, H., Fu, Y. and Sun, J., 2022. A critical review on the treatment of dye-containing wastewater: Ecotoxicological and health concerns of textile dyes and possible remediation approaches for environmental safety. *Ecotoxicology and Environmental Safety*, 231, p.113160.

Aldeen, T.S., Ahmed Mohamed, H.E. and Maaza, M., 2022. ZnO nanoparticles prepared via a green synthesis approach: Physical properties, photocatalytic and antibacterial activity. *Journal of Physics and Chemistry of Solids*, 160, p.110313.

Alenezi, M.R., 2018. Hierarchical zinc oxide nanorings with superior sensing properties. *Materials Science and Engineering: B*, 236–237, pp.132–138.

Alharthi, M.N., Ismail, I., Bellucci, S. and Salam, M.A., 2021. Green synthesis of zinc oxide nanoparticles by Ziziphus jujuba leaves extract: Environmental

application, kinetic and thermodynamic studies. *Journal of Physics and Chemistry of Solids*, p.110237.

Alnaggar, G., Hezam, A., Bajiri, M.A., Drmash, Q.A. and Ananda, S., 2022. Sulfate radicals induced from peroxymonosulfate on electrochemically synthesized TiO₂-MoO₃ heterostructure with Ti-O-Mo bond charge transfer pathway for potential organic pollutant removal under solar light irradiation. *Chemosphere*, p.134562.

Alp, E., Araz, E.C., Buluç, A.F., Güner, Y., Değer, Y., Eşgin, H., Dermenci, K.B., Kazmanlı, M.K., Turan, S. and Genç, A., 2018. Mesoporous nanocrystalline ZnO microspheres by ethylene glycol mediated thermal decomposition. *Advanced Powder Technology*, 29(12), pp.3455–3461.

Alrajhi, A.H., Ahmed, N.M., Al Shafouri, M., Almessiere, M.A. and ahmed Mohammed Al-Ghamdi, A., 2021. Green synthesis of zinc oxide nanoparticles using salvia officials extract. *Materials Science in Semiconductor Processing*, 125, p.105641.

Alves, M.M., Andrade, S.M., Grenho, L., Fernandes, M.H., Santos, C. and Montemor, M.F., 2019. Influence of apple phytochemicals in ZnO nanoparticles formation, photoluminescence and biocompatibility for biomedical applications. *Materials Science and Engineering: C*, 101, pp.76–87.

Amirthavalli, C., Manikandan, A. and Prince, A.A.M., 2018. Effect of zinc precursor ratio on morphology and luminescent properties of ZnO nanoparticles synthesized in CTAB medium. *Ceramics International*, 44(13), pp.15290–15297.

Ananda Murthy, H.C., Zeleke, T.D., Tan, K.B., Ghotekar, S., Alam, M.W., Balachandran, R., Chan, K.-Y., Sanaulla, P.F., Anil Kumar, M.R. and Ravikumar, C.R., 2021. Enhanced multifunctionality of CuO nanoparticles synthesized using aqueous leaf extract of Vernonia amygdalina plant. *Results in Chemistry*, 3, p.100141.

de Andrade, F. V, Augusti, R. and de Lima, G.M., 2021. Ultrasound for the remediation of contaminated waters with persistent organic pollutants: A short review. *Ultrasonics Sonochemistry*, 78, p.105719.

Annathurai, S., Chidambaram, S., Rathinam, M. and Venkatesan, G.K.D.P., 2019. Ga doping improved electrical properties in p-Si/n-ZnO heterojunction diodes. *Journal of Materials Science: Materials in Electronics*, 30(6), pp.5923–5928.

Ansari, M.A., Murali, M., Gowtham, H.G., Kalegowda, N., Amruthesh, K.N., Prasad, D., Alzohairy, M.A., Almatroudi, A., Alomary, M.N., Udayashankar, A.C., Singh, S.B., Lakshmeesha, T.R., Niranjana, S.R., Asiri, S.M.M. and Ashwini, B.S., 2020. Cinnamomum verum bark extract mediated green synthesis of ZnO nanoparticles and their antibacterial potentiality. *Biomolecules*, 10(2).

Antuñano, N., Cambra, J.F. and Arias, P.L., 2017. Development of a combined solid and liquid wastes treatment integrated into a high purity ZnO hydrometallurgical production process from Waelz oxide. *Hydrometallurgy*, 173, pp.250–257.

Ao, W., Li, J., Yang, H., Zeng, X. and Ma, X., 2006. Mechanochemical synthesis of zinc oxide nanocrystalline. *Powder Technology*, 168(3), pp.148–151.

Aragaw, T.A. and Alene, A.N., 2022. A comparative study of acidic, basic, and reactive dyes adsorption from aqueous solution onto kaolin adsorbent: Effect of operating parameters, isotherms, kinetics, and thermodynamics. *Emerging Contaminants*, 8, pp.59–74.

Artifon, W., Cesca, K., de Andrade, C.J., Ulson de Souza, A.A. and de Oliveira, D., 2021. Dyestuffs from textile industry wastewaters: Trends and gaps in the use of biofloculants. *Process Biochemistry*, 111, pp.181–190.

Artifon, W., Mazur, L.P., de Souza, A.A.U. and de Oliveira, D., 2022. Production of biofloculants from spent brewer's yeast and its application in the treatment of effluents with textile dyes. *Journal of Water Process Engineering*, 49, p.102997.

Arumai Selvan, D.S., keerthi, M., Murugesan, S., Shobana, S., Lakshmi, B., Veena, V. and Rahiman, A.K., 2021. In vitro cytotoxicity efficacy of phytosynthesized Ag/ZnO nanocomposites using *Murraya koenigii* and *Zingiber officinale* extracts. *Materials Chemistry and Physics*, 272, p.124903.

Arumugam, M., Manikandan, D.B., Dhandapani, E., Sridhar, A., Balakrishnan, K., Markandan, M. and Ramasamy, T., 2021. Green synthesis of zinc oxide nanoparticles (ZnO NPs) using *Syzygium cumini*: Potential multifaceted applications on antioxidants, cytotoxic and as nanonutrient for the growth of *Sesamum indicum*. *Environmental Technology & Innovation*, 23, p.101653.

Arumugam, T.K., Krishnamoorthy, P., Rajagopalan, N.R., Nanthini, S. and Vasudevan, D., 2019. Removal of malachite green from aqueous solutions using a modified chitosan composite. *International Journal of Biological Macromolecules*, 128, pp.655–664.

Ayanda, O.S., Aremu, O.H., Akintayo, C.O., Sodeinde, K.O., Igboama, W.N., Oseghe, E.O. and Nelana, S.M., 2021. Sonocatalytic degradation of amoxicillin from aquaculture effluent by zinc oxide nanoparticles. *Environmental Nanotechnology, Monitoring & Management*, 16, p.100513.

Ayare, S.D. and Gogate, P.R., 2019. Sonocatalytic treatment of phosphonate containing industrial wastewater intensified using combined oxidation approaches. *Ultrasonics Sonochemistry*, 51, pp.69–76.

Aydoğan, Ş., Grilli, M.L., Yilmaz, M., Çaldıran, Z. and Kaçuş, H., 2017. A facile growth of spray based ZnO films and device performance investigation for Schottky diodes: Determination of interface state density distribution. *Journal of Alloys and Compounds*, 708, pp.55–66.

Ayodhya, D. and Veerabhadram, G., 2020. Green synthesis of garlic extract stabilized Ag@CeO₂ composites for photocatalytic and sonocatalytic degradation of mixed dyes and antimicrobial studies. *Journal of Molecular Structure*, 1205, p.127611.

Azizi, S., Shahri, M.M. and Mohamad, R., 2017. Green synthesis of zinc oxide nanoparticles for enhanced adsorption of lead ions from aqueous solutions: Equilibrium, kinetic and thermodynamic studies. *Molecules*, 22(6).

Babu, A.T. and Antony, R., 2019. Green synthesis of silver doped nano metal oxides of zinc & copper for antibacterial properties, adsorption, catalytic hydrogenation & photodegradation of aromatics. *Journal of Environmental Chemical Engineering*, 7(1), p.102840.

Badawy, A.A., Ghanem, A.F., Yassin, M.A., Youssef, A.M. and Abdel Rehim, M.H., 2021. Utilization and characterization of cellulose nanocrystals decorated with silver and zinc oxide nanoparticles for removal of lead ion from wastewater. *Environmental Nanotechnology, Monitoring & Management*, 16, p.100501.

Bagha, G., Naffakh-Moosavy, H. and Mersagh, M.R., 2021. The effect of reduced graphene oxide sheet on the optical and electrical characteristics of Ni-doped and Ag-doped ZnO ETLs in planar perovskite solar cells. *Journal of Alloys and Compounds*, 870, p.159658.

Bahadoran, A., Liu, Q., Liu, B., Gu, J., Zhang, D., Fakhri, A. and Kumar Gupta, V., 2021. Preparation of Sn/Fe nanoparticles for Cr (III) detection in presence of leucine, photocatalytic and antibacterial activities. *Spectrochimica Acta Part A: Molecular and Biomolecular Spectroscopy*, 253, p.119592.

Baniasadi, M., Vakilchap, F., Bahaloo-Horeh, N., Mousavi, S.M. and Farnaud, S., 2019. Advances in bioleaching as a sustainable method for metal recovery from e-waste: A review. *Journal of Industrial and Engineering Chemistry*, 76, pp.75–90.

Banu, R., Ramakrishna, D., Reddy, G.B., Veerabhadram, G. and Mangatayaru, K.G., 2021. Facile one-pot microwave-assisted green synthesis of silver nanoparticles using Bael gum: Potential application as catalyst in the reduction of organic dyes. *Materials Today: Proceedings*, 43, pp.2265–2273.

Bárdos, E., Király, A.K., Pap, Z., Baia, L., Garg, S. and Hernádi, K., 2019. The effect of the synthesis temperature and duration on the morphology and photocatalytic activity of BiOX (X = Cl, Br, I) materials. *Applied Surface Science*, 479, pp.745–756.

Barsainya, M. and Singh, D.P., 2018. Green Synthesis of Zinc Oxide Nanoparticles by *Pseudomonas aeruginosa* and their Broad-Spectrum Antimicrobial Effects. *Journal of Pure & Applied Microbiology*, 12(4), pp.2123–2134.

Behera, M., Nayak, J., Banerjee, S., Chakraborty, S. and Tripathy, S.K., 2021. A review on the treatment of textile industry waste effluents towards the

development of efficient mitigation strategy: An integrated system design approach. *Journal of Environmental Chemical Engineering*, 9(4), p.105277.

Behura, R., Sakthivel, R. and Das, N., 2021. Synthesis of cobalt ferrite nanoparticles from waste iron ore tailings and spent lithium ion batteries for photo/sono-catalytic degradation of Congo red. *Powder Technology*, 386, pp.519–527.

Belay, A., Bekele, B. and Reddy, A.R.C., 2019. Effects of temperature and polyvinyl alcohol concentrations in the synthesis of zinc oxide nanoparticles. *Digest Journal of Nanomaterials & Biostructures (DJNB)*, 14(1), pp.51–60.

Belwal, T., Ezzat, S.M., Rastrelli, L., Bhatt, I.D., Daglia, M., Baldi, A., Devkota, H.P., Orhan, I.E., Patra, J.K., Das, G., Anandharamakrishnan, C., Gomez-Gomez, L., Nabavi, S.F., Nabavi, S.M. and Atanasov, A.G., 2018. A critical analysis of extraction techniques used for botanicals: Trends, priorities, industrial uses and optimization strategies. *TrAC Trends in Analytical Chemistry*, 100, pp.82–102.

El Bendary, M.M., Radwan, E.K. and El-Shahat, M.F., 2021. Valorization of secondary resources into silica-based adsorbents: Preparation, characterization and application in dye removal from wastewater. *Environmental Nanotechnology, Monitoring & Management*, 15, p.100455.

Benkhaya, S., Lgaz, H., Alrashdi, A.A., M'rabet, S., El Bachiri, A., Assouag, M., Chung, I.-M. and El Harfi, A., 2021a. Upgrading the performances of polysulfone/polyetherimide ultrafiltration composite membranes for dyes removal: Experimental and molecular dynamics studies. *Journal of Molecular Liquids*, 331, p.115743.

Benkhaya, S., Lgaz, H., Chraïbi, S., Alrashdi, A.A., Rafik, M., Lee, H.-S. and El Harfi, A., 2021b. Polysulfone/Polyetherimide Ultrafiltration composite membranes constructed on a three-component Nylon-fiberglass-Nylon support for azo dyes removal: Experimental and molecular dynamics simulations. *Colloids and Surfaces A: Physicochemical and Engineering Aspects*, 625, p.126941.

Benkhaya, S., M'rabet, S. and El Harfi, A., 2020. A review on classifications, recent synthesis and applications of textile dyes. *Inorganic Chemistry Communications*, 115, p.107891.

Bhattacharya, P., Banerjee, S., Mukherjee, D., Deb, N. and Swarnakar, S., 2020. Application of green synthesized ZnO nanoparticle coated ceramic ultrafiltration membrane for remediation of pharmaceutical components from synthetic water: Reusability assay of treated water on seed germination. *Journal of Environmental Chemical Engineering*, 8(3).

Bijanzad, K., Tadjarodi, A. and Akhavan, O., 2015. Photocatalytic activity of mesoporous microbricks of ZnO nanoparticles prepared by the thermal decomposition of bis(2-aminonicotinato) zinc (II). *Chinese Journal of Catalysis*, 36(5), pp.742–749.

- Bose, S., Kumar Tripathy, B., Debnath, A. and Kumar, M., 2021. Boosted sono-oxidative catalytic degradation of Brilliant green dye by magnetic MgFe_2O_4 catalyst: Degradation mechanism, assessment of bio-toxicity and cost analysis. *Ultrasonics Sonochemistry*, 75, p.105592.
- Boulahlib, S., Dib, K., Özacar, M. and Bessekhoud, Y., 2021. Optical, dielectric, and transport properties of Ag-doped ZnO prepared by Aloe Vera assisted method. *Optical Materials*, 113, p.110889.
- Caesario, B.A.D., Ali, M.D.R., Puspitasari, D., Arnanda, H.K., Ni'mah, H., Kurniawansyah, F. and Ningrum, E.O., 2022. Cellulose-Based beads for cationic dye removal in continuous adsorption. *Materials Today: Proceedings*, 63, pp.S354–S358.
- Čech Barabaszová, K., Hundáková, M., Mackovčáková, M. and Pazdziora, E., 2018. Three methods for antibacterial ZnO nanoparticles preparation. *Materials Today: Proceedings*, 5(Supplement 1), pp.S11–S19.
- Chairungsri, W., Subkomkaew, A., Kijjanapanich, P. and Chimupala, Y., 2022. Direct dye wastewater photocatalysis using immobilized titanium dioxide on fixed substrate. *Chemosphere*, 286, p.131762.
- Chakraborty, S., Amal Raj, M. and Mary, N.L., 2020. Biocompatible supercapacitor electrodes using green synthesised ZnO/Polymer nanocomposites for efficient energy storage applications. *Journal of Energy Storage*, 28, p.101275.
- Chandra Joshi, N. and Singh, A., 2020. Adsorptive performances and characterisations of biologically synthesised zinc oxide based nanosorbent (ZOBN). *Groundwater for Sustainable Development*, 10, p.100325.
- Chandrabose, G., Dey, A., Gaur, S.S., Pitchaimuthu, S., Jagadeesan, H., Braithwaite, N.S.J., Selvaraj, V., Kumar, V. and Krishnamurthy, S., 2021. Removal and degradation of mixed dye pollutants by integrated adsorption-photocatalysis technique using 2-D $\text{MoS}_2/\text{TiO}_2$ nanocomposite. *Chemosphere*, 279, p.130467.
- Chang, F., Wu, F., Yan, W., Jiao, M., Zheng, J., Deng, B. and Hu, X., 2019. Oxygen-rich bismuth oxychloride $\text{Bi}_{12}\text{O}_{17}\text{Cl}_2$ materials: construction, characterization, and sonocatalytic degradation performance. *Ultrasonics Sonochemistry*, 50, pp.105–113.
- Chang, T.-H., Chang, Y.-C. and Wu, S.-H., 2020. Ag nanoparticles decorated ZnO: Al nanoneedles as a high-performance surface-enhanced Raman scattering substrate. *Journal of Alloys and Compounds*, 843, p.156044.
- Chaudhary, R.G., Potbhare, A.K., Aziz, S.K.T., Umekar, M.S., Bhuyar, S.S. and Mondal, A., 2020. Phytochemically fabricated reduced graphene Oxide-ZnO NCs by *Sesbania bispinosa* for photocatalytic performances. *Materials Today: Proceedings*.

- Chemingui, H., Missaoui, T., Mzali, J.C., Smiri, M., Saidi, N., Hafiane, A., Yildiz, T., Konyar, M. and Yatmaz, H.C., 2019. Facile green synthesis of zinc oxide nanoparticles (ZnO NPs): Antibacterial and photocatalytic activities. *Materials Research Express*, 6(10).
- Chen, L., Batjikh, I., Hurh, J., Han, Y., Huo, Y., Ali, H., Li, J.F., Rupa, E.J., Ahn, J.C., Mathiyalagan, R. and Yang, D.C., 2019. Green synthesis of zinc oxide nanoparticles from root extract of *Scutellaria baicalensis* and its photocatalytic degradation activity using methylene blue. *Optik*, 184, pp.324–329.
- Chen, R., Wang, J. and Xiang, L., 2018. Facile synthesis of mesoporous ZnO sheets assembled by small nanoparticles for enhanced NO₂ sensing performance at room temperature. *Sensors and Actuators B: Chemical*, 270, pp.207–215.
- Chen, X., Zhu, L., Ma, Z., Wang, M., Zhao, R., Zou, Y. and Fan, Y., 2022. Derivatization reaction-based surface-enhanced Raman scattering for detection of methanol in transformer oil using Ag/ZnO composite nanoflower substrate. *Applied Surface Science*, 604, p.154442.
- Cheng, Z., Luo, S., Li, X., Zhang, S., Thang Nguyen, T., Guo, M. and Gao, X., 2021. Ultrasound-assisted heterogeneous Fenton-like process for methylene blue removal using magnetic MnFe₂O₄/biochar nanocomposite. *Applied Surface Science*, 566, p.150654.
- Chennimalai, M., Vijayalakshmi, V., Senthil, T.S. and Sivakumar, N., 2021. One-step green synthesis of ZnO nanoparticles using *Opuntia humifusa* fruit extract and their antibacterial activities. *Materials Today: Proceedings*, 47, pp.1842–1846.
- Chu, J.-H., Kang, J.-K., Park, S.-J. and Lee, C.-G., 2021. Enhanced sonocatalytic degradation of bisphenol A with a magnetically recoverable biochar composite using rice husk and rice bran as substrate. *Journal of Environmental Chemical Engineering*, 9(4), p.105284.
- Çolak, H., Karaköse, E. and Derin, Y., 2017. Properties of ZnO nanostructures produced by mechanochemical-solid state combustion method using different precursors. *Materials Chemistry and Physics*, 193, pp.427–437.
- Collin, F., 2019. Chemical Basis of Reactive Oxygen Species Reactivity and Involvement in Neurodegenerative Diseases. *International Journal of Molecular Sciences*, 20, p.2407.
- Da'na, E., Taha, A. and Hessien, M., 2020. Application of ZnO–NiO greenly synthesized nanocomposite adsorbent on the elimination of organic dye from aqueous solutions: Kinetics and equilibrium. *Ceramics International*.
- Dalponete Dallabona, I., Mathias, Á.L. and Jorge, R.M.M., 2021. A new green floating photocatalyst with Brazilian bentonite into TiO₂/alginate beads for dye removal. *Colloids and Surfaces A: Physicochemical and Engineering Aspects*, 627, p.127159.

Dang, V.C., Tran, D.T., Phan, A.T., Pham, N.K. and Nguyen, V.N., 2021. Synergistic effect for the degradation of tetracycline by rGO-Co₃O₄ assisted persulfate activation. *Journal of Physics and Chemistry of Solids*, 153, p.110005.

Dangi, S., Gupta, A., Gupta, D.K., Singh, S. and Parajuli, N., 2020. Green synthesis of silver nanoparticles using aqueous root extract of *Berberis asiatica* and evaluation of their antibacterial activity. *Chemical Data Collections*, 28, p.100411.

Darbandi, M., Eynollahi, M., Badri, N., Mohajer, M.F. and Li, Z.-A., 2022. NiO nanoparticles with superior sonophotocatalytic performance in organic pollutant degradation. *Journal of Alloys and Compounds*, 889, p.161706.

Das, P., Debnath, P. and Debnath, A., 2021. Enhanced sono-assisted adsorptive uptake of malachite green dye onto magnesium ferrite nanoparticles: Kinetic, isotherm and cost analysis. *Environmental Nanotechnology, Monitoring & Management*, 16, p.100506.

Das, R., Bhaumik, M., Giri, S. and Maity, A., 2017. Sonocatalytic rapid degradation of Congo red dye from aqueous solution using magnetic Fe₀/polyaniline nanofibers. *Ultrasonics Sonochemistry*, 37, pp.600–613.

Deep, A., Sharma, A.L., Mohanta, G.C., Kumar, P. and Kim, K.-H., 2016. A facile chemical route for recovery of high quality zinc oxide nanoparticles from spent alkaline batteries. *Waste Management*, 51, pp.190–195.

Delice, S., Isik, M. and Gasanly, N.M., 2019. Traps distribution in sol-gel synthesized ZnO nanoparticles. *Materials Letters*, 245, pp.103–105.

Department of Environment, Malaysia, 2021. *Environmental Quality Report 2020*. [online].

Dhananjaya, N., Ambujakshi, N.P., Raveesha, H.R., Pratibha, S. and Ravikumar, C.R., 2021. Electrochemical Sensor and luminescence applications of *Chonemorpha fragrans* leaf extract mediated ZnO/Ag nanostructures. *Applied Surface Science Advances*, 4, p.100075.

Dhandapani, K.V., Anbumani, D., Gandhi, A.D., Annamalai, P., Muthuvenkatachalam, B.S., Kavitha, P. and Ranganathan, B., 2020. Green route for the synthesis of zinc oxide nanoparticles from *Melia azedarach* leaf extract and evaluation of their antioxidant and antibacterial activities. *Biocatalysis and Agricultural Biotechnology*, 24, p.101517.

Dhar, P., Teja, V. and Vinu, R., 2020. Sonophotocatalytic degradation of lignin: Production of valuable chemicals and kinetic analysis. *Journal of Environmental Chemical Engineering*, 8(5), p.104286.

Dhara, S. and Giri, P.K., 2011. Quick single-step mechanosynthesis of ZnO nanorods and their optical characterization: milling time dependence. *Applied Nanoscience (Switzerland)*, 1(4), pp.165–171.

Dhasmana, H., Dutta, V., Kumar, A., Kumar, A., Verma, A. and Jain, V.K., 2020.

Hydrothermally synthesized zinc oxide nanoparticles for reflectance study onto Si surface. *Materials Today: Proceedings*, 32, pp.287–293.

Dhir, R., 2021. Synthesis, characterization and applications of Gadolinium doped ZnS nanoparticles as photocatalysts for the degradation of dyes (Malachite Green and Rhodamine B) and as antioxidants. *Chemical Physics Impact*, 3, p.100027.

Dimitriev, Y., Gancheva, M. and Iordanova, R., 2012. Effects of the mechanical activation of zinc carbonate hydroxide on the formation and properties of zinc oxides. *Journal of Alloys and Compounds*, 519, pp.161–166.

Dinesh, G.K. and Chakma, S., 2019. Degradation kinetic study of cholesterol lowering statin drug using sono-hybrid techniques initiated by metal-free polymeric catalyst. *Journal of the Taiwan Institute of Chemical Engineers*, 100, pp.95–104.

Ding, Z., Sun, M., Liu, W., Sun, W., Meng, X. and Zheng, Y., 2021. Ultrasonically synthesized N-TiO₂/Ti₃C₂ composites: Enhancing sonophotocatalytic activity for pollutant degradation and nitrogen fixation. *Separation and Purification Technology*, 276, p.119287.

Dmochowska, A., Czajkowska, J., Jędrzejewski, R., Stawiński, W., Migdał, P. and Fiedot-Toboła, M., 2020. Pectin based banana peel extract as a stabilizing agent in zinc oxide nanoparticles synthesis. *International Journal of Biological Macromolecules*, 165, pp.1581–1592.

Dodoo-Arhin, D., Asiedu, T., Agyei-Tuffour, B., Nyankson, E., Obada, D. and Mwabora, J.M., 2021. Photocatalytic degradation of Rhodamine dyes using zinc oxide nanoparticles. *Materials Today: Proceedings*, 38, pp.809–815.

Dominguez-Benetton, X., Varia, J.C., Pozo, G., Modin, O., Ter Heijne, A., Fransaeer, J. and Rabaey, K., 2018. Metal recovery by microbial electro-metallurgy. *Progress in Materials Science*, 94, pp.435–461.

Dou, A., 2016. A novel process for treating with low grade zinc oxide ores in hydrometallurgy. In: *TMS Annual Meeting*.

Du, B., Fan, G., Yang, S., Chen, Z., Luo, J., Yu, W., Yu, J., Wei, Q. and Lu, Y., 2022. Sonophotocatalytic degradation of 17β-estradiol by Er³⁺-CdS/MoS₂: The role and transformation of reactive oxygen species. *Journal of Cleaner Production*, 333, p.130203.

Dutta, T., Kim, K.-H., Deep, A., Szulejko, J.E., Vellingiri, K., Kumar, S., Kwon, E.E. and Yun, S.-T., 2018. Recovery of nanomaterials from battery and electronic wastes: A new paradigm of environmental waste management. *Renewable and Sustainable Energy Reviews*, 82, pp.3694–3704.

Eghbali, P., Hassani, A., Sündü, B. and Metin, Ö., 2019. Strontium titanate nanocubes assembled on mesoporous graphitic carbon nitride (SrTiO₃/mpg-C₃N₄): Preparation, characterization and catalytic performance. *Journal of*

Molecular Liquids, 290, p.111208.

El-Sawy, A.M., Abdo, M.H., Darweesh, M.A. and Salahuddin, N.A., 2021. Synthesis of modified PANI/CQDs nanocomposite by dimethylglyoxime for removal of Ni (II) from aqueous solution. *Surfaces and Interfaces*, 26, p.101392.

Elemike, E.E., Onwudiwe, D.C., Wei, L., Lou, C. and Zhao, Z., 2019. Synthesis of nanostructured ZnO, AgZnO and the composites with reduced graphene oxide (rGO-AgZnO) using leaf extract of *Stigmaphyllon ovatum*. *Journal of Environmental Chemical Engineering*, 7(3), p.103190.

Emara, M.M., Ali, S.H., Hassan, A.A., Kassem, T.S.E. and Van Patten, P.G., 2021. How does photocatalytic activity depend on adsorption, composition, and other key factors in mixed metal oxide nanocomposites? *Colloid and Interface Science Communications*, 40, p.100341.

Esania, Z., Younesi, H., Nowrouzi, M. and Karimi-Maleh, H., 2022. Characterization and assessment of the photocatalytic activity of ZnO-Fe₃O₄/TiO₂ nanocomposite based on MIL-125(Ti) synthesized by mixed solvo-hydrothermal and sol-gel methods. *Journal of Water Process Engineering*, 47, p.102750.

Eskandari, P., Amarloo, E., Zangeneh, H., Rezakazemi, M., Zamani, M.R. and Aminabhavi, T.M., 2023. Photocatalytic activity of visible-light-driven L-Proline-TiO₂/BiOBr nanostructured materials for dyes degradation: The role of generated reactive species. *Journal of Environmental Management*, 326, p.116691.

Ezhuthupurakkal, P.B., Polaki, L.R., Suyavaran, A., Subastri, A., Sujatha, V. and Thirunavukkarasu, C., 2017. Selenium nanoparticles synthesized in aqueous extract of *Allium sativum* perturbs the structural integrity of Calf thymus DNA through intercalation and groove binding. *Materials Science and Engineering: C*, 74, pp.597–608.

Fan, G., Yang, S., Du, B., Luo, J., Lin, X. and Li, X., 2022a. Sono-photo hybrid process for the synergistic degradation of levofloxacin by FeVO₄/BiVO₄: Mechanisms and kinetics. *Environmental Research*, 204, p.112032.

Fan, J., Li, W., Zhang, B., Shi, W. and Lens, P.N.L., 2022b. Unravelling the biodegradation performance and mechanisms of acid orange 7 by aerobic granular sludge at different salinity levels. *Bioresource Technology*, 357, p.127347.

Fifere, N., Airinei, A., Timpu, D., Rotaru, A., Sacarescu, L. and Ursu, L., 2018. New insights into structural and magnetic properties of Ce doped ZnO nanoparticles. *Journal of Alloys and Compounds*, 757, pp.60–69.

Fónagy, O., Szabó-Bárdos, E. and Horváth, O., 2021. 1,4-Benzoquinone and 1,4-hydroquinone based determination of electron and superoxide radical formed in heterogeneous photocatalytic systems. *Journal of Photochemistry and Photobiology A: Chemistry*, 407, p.113057.

Fouda, A., EL-Din Hassan, S., Salem, S.S. and Shaheen, T.I., 2018. In-Vitro cytotoxicity, antibacterial, and UV protection properties of the biosynthesized Zinc oxide nanoparticles for medical textile applications. *Microbial Pathogenesis*, 125, pp.252–261.

Fouladi-Fard, R., Aali, R., Mohammadi-Aghdam, S. and Mortazavi-derazkola, S., 2022. The surface modification of spherical ZnO with Ag nanoparticles: A novel agent, biogenic synthesis, catalytic and antibacterial activities. *Arabian Journal of Chemistry*, 15(3), p.103658.

Freedman, J.J., Kennedy, L.J., Kumar, R.T., Sekaran, G. and Vijaya, J.J., 2010. Studies on the structural and optical properties of zinc oxide nanobushes and Co-doped ZnO self-aggregated nanorods synthesized by simple thermal decomposition route. *Materials Research Bulletin*, 45(10), pp.1481–1486.

Gallegos, M. V, Aparicio, F., Peluso, M.A., Damonte, L.C. and Sambeth, J.E., 2018. Structural, optical and photocatalytic properties of zinc oxides obtained from spent alkaline batteries. *Materials Research Bulletin*, 103, pp.158–165.

Ganesan, S., Gollu, S.R., Alam khan, J., Kushwaha, A. and Gupta, D., 2019. Inkjet printing of zinc oxide and P3HT:ICBA in ambient conditions for inverted bulk heterojunction solar cells. *Optical Materials*, 94, pp.430–435.

Ganesan, V., Muthuramkumar, S., Hariram, M. and Vivekanandhan, S., 2020. Periconium sp. (endophytic fungi) extract mediated sol-gel synthesis of ZnO nanoparticles for antimicrobial and antioxidant applications. *Materials Science in Semiconductor Processing*, 105, p.104739.

Gao, Y., Arokia Vijaya Anand, M., Ramachandran, V., Shalini, V., Vijayalakshmi, S., Ernest, D. and Karthikkumar, V., 2019. Biofabrication of Zinc Oxide Nanoparticles from *Aspergillus niger*, Their Antioxidant, Antimicrobial and Anticancer Activity. *Journal of Cluster Science*, 30(4), pp.937–946.

Gao, Y., Xu, D., Ren, D., Zeng, K. and Wu, X., 2020. Green synthesis of zinc oxide nanoparticles using *Citrus sinensis* peel extract and application to strawberry preservation: A comparison study. *LWT*, 126.

García-Espinoza, J.D., Robles, I., Durán-Moreno, A. and Godínez, L.A., 2021. Photo-assisted electrochemical advanced oxidation processes for the disinfection of aqueous solutions: A review. *Chemosphere*, 274, p.129957.

Gayathri, P. V, Yesodharan, S. and Yesodharan, E.P., 2019. Microwave/Persulphate assisted ZnO mediated photocatalysis (MW/PS/UV/ZnO) as an efficient advanced oxidation process for the removal of RhB dye pollutant from water. *Journal of Environmental Chemical Engineering*, 7(4), p.103122.

Geetha, M.S., Nagabhushana, H. and Shivananjaiah, H.N., 2016. Green mediated synthesis and characterization of ZnO nanoparticles using *Euphorbia Jatropha latex* as reducing agent. *Journal of Science: Advanced Materials and*

Devices, 1(3), pp.301–310.

Ghalamchi, L. and Aber, S., 2020. An aminated silver orthophosphate/graphitic carbon nitride nanocomposite: An efficient visible light sonophotocatalyst. *Materials Chemistry and Physics*, 256, p.123649.

Ghanbari, F. and Moradi, M., 2017. Application of peroxymonosulfate and its activation methods for degradation of environmental organic pollutants: Review. *Chemical Engineering Journal*, 310, pp.41–62.

Gholami, P., Dinpazhoh, L., Khataee, A. and Orooji, Y., 2019a. Sonocatalytic activity of biochar-supported ZnO nanorods in degradation of gemifloxacin: Synergy study, effect of parameters and phytotoxicity evaluation. *Ultrasonics Sonochemistry*, 55, pp.44–56.

Gholami, P., Dinpazhoh, L., Khataee, A. and Orooji, Y., 2019b. Sonocatalytic activity of biochar-supported ZnO nanorods in degradation of gemifloxacin: Synergy study, effect of parameters and phytotoxicity evaluation. *Ultrasonics Sonochemistry*, 55, pp.44–56.

Gholami, P., Khataee, A., Vahid, B., Karimi, A., Golizadeh, M. and Ritala, M., 2020. Sonophotocatalytic degradation of sulfadiazine by integration of microfibrillated carboxymethyl cellulose with Zn-Cu-Mg mixed metal hydroxide/g-C₃N₄ composite. *Separation and Purification Technology*, 245, p.116866.

Ghosh, A., Kumar De, S., Mondal, S., Halder, A., Barai, M., Chandra Guchhait, K., Raul, P., Karmakar, S., Ghosh, C., Patra, A., Kumar Panda, A., Senapati, D. and Kumar Sur, U., 2023. Green synthesis of silver nanoparticles and its applications as sensor, catalyst, and antibacterial agent. *Materials Today: Proceedings*.

Ghuzali, N.A.M., Noor, M.A.A.C.M., Zakaria, F.A., Hamidon, T.S. and Husin, M.H., 2021. Study on Clitoria ternatea extracts doped sol-gel coatings for the corrosion mitigation of mild steel. *Applied Surface Science Advances*, 6, p.100177.

Gnanamozhi, P., Renganathan, V., Chen, S.-M., Pandiyan, V., Antony Arockiaraj, M., Alharbi, N.S., Kadaikunnan, S., Khaled, J.M. and Alanzi, K.F., 2020. Influence of Nickel concentration on the photocatalytic dye degradation (methylene blue and reactive red 120) and antibacterial activity of ZnO nanoparticles. *Ceramics International*, 46(11, Part A), pp.18322–18330.

Golmohammadi, M., Honarmand, M. and Ghanbari, S., 2020. A green approach to synthesis of ZnO nanoparticles using jujube fruit extract and their application in photocatalytic degradation of organic dyes. *Spectrochimica Acta - Part A: Molecular and Biomolecular Spectroscopy*, 229, p.117961.

Gomez-Gomez, B., Perez-Corona, M.T. and Madrid, Y., 2020. Using single-particle ICP-MS for unravelling the effect of type of food on the physicochemical properties and gastrointestinal stability of ZnONPs released

from packaging materials. *Analytica Chimica Acta*, 1100, pp.12–21.

Goswami, M., Adhikary, N.C. and Bhattacharjee, S., 2018. Effect of annealing temperatures on the structural and optical properties of zinc oxide nanoparticles prepared by chemical precipitation method. *Optik*, 158, pp.1006–1015.

Guenfoud, F., Mokhtari, M. and Akrouf, H., 2014. Electrochemical degradation of malachite green with BDD electrodes: Effect of electrochemical parameters. *Diamond and Related Materials*, 46, pp.8–14.

Gujar, S.K. and Gogate, P.R., 2021. Application of hybrid oxidative processes based on cavitation for the treatment of commercial dye industry effluents. *Ultrasonics Sonochemistry*, 75, p.105586.

Gul, R., Sharma, P., Kumar, R., Umar, A., Ibrahim, A.A., Alhamami, M.A.M., Jaswal, V.S., Kumar, M., Dixit, A. and Baskoutas, S., 2023. A sustainable approach to the degradation of dyes by fungal species isolated from industrial wastewaters: Performance, parametric optimization, kinetics and degradation mechanism. *Environmental Research*, 216, p.114407.

Gupta, J., Hassan, P.A. and Barick, K.C., 2021. Structural, photoluminescence, and photocatalytic properties of Mn and Eu co-doped ZnO nanoparticles. *Materials Today: Proceedings*, 42, pp.926–931.

Gupta, R., Das, N. and Singh, M., 2019. Fabrication and surface characterisation of c-ZnO loaded TTDMM dendrimer nanocomposites for biological applications. *Applied Surface Science*, 484, pp.781–796.

Gupta, V.K., 2019. Fundamentals of Natural Dyes and Its Application on Textile Substrates. In: A.K. Samanta, N.S. Awwad and H.M. Algarni, eds. Rijeka: IntechOpen.p.Ch. 2.

Hairom, N.H.H., Mohammad, A.W. and Kadhum, A.A.H., 2015. Influence of zinc oxide nanoparticles in the nanofiltration of hazardous Congo red dyes. *Chemical Engineering Journal*, 260, pp.907–915.

Hajjashrafi, S. and Motakef Kazemi, N., 2019. Preparation and evaluation of ZnO nanoparticles by thermal decomposition of MOF-5. *Heliyon*, 5(9).

El Hakim, S., Chave, T. and Nikitenko, S.I., 2021. Photocatalytic and Sonocatalytic Degradation of EDTA and Rhodamine B over Ti⁰ and Ti@TiO₂ Nanoparticles. *Catalysts*, 11(8), p.928.

Hamadneh, I., Al-Mobydeen, A., Al-Dalahmeh, Y., Albuqain, R., Alstari, S., Al-Obaidi, O.H., Albiss, B. and Al-Dujaili, A.H., 2022. Green synthesis of a YBa₂Cu₃O₇ ceramic superconductor using the fruit extract of *Juniperus phoenicea*. *Ceramics International*.

Hamouda, R.A., Yousuf, W.E., Abeer Mohammed, A.B., Darwish, D.B. and Abdeen, E.E., 2020. Comparative study between zinc oxide nanoparticles synthesized by chemical and biological methods in view of characteristics, antibacterial activity and loading on antibiotics in vitro. *Digest Journal of*

Nanomaterials and Biostructures, 15(1), pp.93–106.

Hao, N., Xu, Z., Nie, Y., Jin, C., Closson, A.B., Zhang, M. and Zhang, J.X.J., 2019. Microfluidics-enabled rational design of ZnO micro-/nanoparticles with enhanced photocatalysis, cytotoxicity, and piezoelectric properties. *Chemical Engineering Journal*, 378, p.122222.

Hasan, I., Bassi, A., Alharbi, K.H., BinSharfan, I.I., Khan, R.A. and Alslame, A., 2020. Sonophotocatalytic Degradation of Malachite Green by Nanocrystalline Chitosan-Ascorbic Acid@NiFe₂O₄ Spinel Ferrite. *Coatings*, 10(12), p.1200.

Hasanpour, M. and Hatami, M., 2020. Photocatalytic performance of aerogels for organic dyes removal from wastewaters: Review study. *Journal of Molecular Liquids*, 309, p.113094.

Hassan, A.F. and Elhadidy, H., 2019. Effect of Zr⁴⁺ doping on characteristics and sonocatalytic activity of TiO₂/carbon nanotubes composite catalyst for degradation of chlorpyrifos. *Journal of Physics and Chemistry of Solids*, 129, pp.180–187.

Hayami, R., Endo, N., Abe, T., Miyase, Y., Sagawa, T., Yamamoto, K., Gunji, T. and Tsukada, S., 2018. Zinc–diethanolamine complex: synthesis, characterization, and formation mechanism of zinc oxide via thermal decomposition. *Journal of Sol-Gel Science and Technology*, 87(3), pp.743–748.

Hayati, F., Khodabakhshi, M.R., Isari, A.A., Moradi, S. and Kakavandi, B., 2020. LED-assisted sonocatalysis of sulfathiazole and pharmaceutical wastewater using N,Fe co-doped TiO₂@SWCNT: Optimization, performance and reaction mechanism studies. *Journal of Water Process Engineering*, 38, p.101693.

He, L.-L., Zhu, Y., Qi, Q., Li, X.-Y., Bai, J.-Y., Xiang, Z. and Wang, X., 2021a. Synthesis of CaMoO₄ microspheres with enhanced sonocatalytic performance for the removal of Acid Orange 7 in the aqueous environment. *Separation and Purification Technology*, 276, p.119370.

He, S., Li, T., Zhang, L., Zhang, X., Liu, Z., Zhang, Y., Wang, J., Jia, H., Wang, T. and Zhu, L., 2021b. Highly effective photocatalytic decomplexation of Cu-EDTA by MIL-53(Fe): Highlight the important roles of Fe. *Chemical Engineering Journal*, 424, p.130515.

Hemmati, F., Salehi, R., Ghotaslou, R., Kafil, H.S., Hasani, A., Gholizadeh, P. and Rezaee, M.A., 2020. The assessment of antibiofilm activity of chitosan-zinc oxide-gentamicin nanocomposite on *Pseudomonas aeruginosa* and *Staphylococcus aureus*. *International Journal of Biological Macromolecules*, 163, pp.2248–2258.

Her, N., Park, J.-S. and Yoon, Y., 2011. Sonochemical enhancement of hydrogen peroxide production by inert glass beads and TiO₂-coated glass beads in water. *Chemical Engineering Journal*, 166(1), pp.184–190.

Huang, Q., Chen, C., Zhao, X., Bu, X., Liao, X., Fan, H., Gao, W., Hu, H., Zhang, Y. and Huang, Z., 2021. Malachite green degradation by persulfate activation with CuFe₂O₄@biochar composite: Efficiency, stability and mechanism. *Journal of Environmental Chemical Engineering*, 9(4), p.105800.

Huy, N.N., Thanh Thuy, V.T., Thang, N.H., Thuy, N.T., Quynh, L.T., Khoi, T.T. and Van Thanh, D., 2019. Facile one-step synthesis of zinc oxide nanoparticles by ultrasonic-assisted precipitation method and its application for H₂S adsorption in air. *Journal of Physics and Chemistry of Solids*, 132, pp.99–103.

Ibrahim, E.J., Thalij, K.M., Saleh, M.K. and Badawy, A.S., 2017. Biosynthesis of zinc oxide nanoparticles and assay of antibacterial activity. *American Journal of Biochemistry and Biotechnology*, 13(2), pp.63–69.

Iqbal, A., Cevik, E., Alagha, O. and Bozkurt, A., 2022. Highly robust multilayer nanosheets with ultra-efficient batch adsorption and gravity-driven filtration capability for dye removal. *Journal of Industrial and Engineering Chemistry*, 109, pp.287–295.

Isari, A.A., Mehregan, M., Mehregan, S., Hayati, F., Rezaei Kalantary, R. and Kakavandi, B., 2020. Sono-photocatalytic degradation of tetracycline and pharmaceutical wastewater using WO₃/CNT heterojunction nanocomposite under US and visible light irradiations: A novel hybrid system. *Journal of Hazardous Materials*, 390, p.122050.

Ishwarya, R., Vaseeharan, B., Kalyani, S., Banumathi, B., Govindarajan, M., Alharbi, N.S., Kadaikunnan, S., Al-anbr, M.N., Khaled, J.M. and Benelli, G., 2018. Facile green synthesis of zinc oxide nanoparticles using *Ulva lactuca* seaweed extract and evaluation of their photocatalytic, antibiofilm and insecticidal activity. *Journal of Photochemistry & Photobiology, B: Biology*, 178, pp.249–258.

Islam, A., Sharma, A., Chaturvedi, R. and Kumar Singh, P., 2021a. Synthesis and structural analysis of zinc oxide nano particle by chemical method. *Materials Today: Proceedings*, 45, pp.3670–3673.

Islam, M.R., Saiduzzaman, M., Nishat, S.S., Kabir, A. and Farhad, S.F.U., 2021b. Synthesis, characterization and visible light-responsive photocatalysis properties of Ce doped CuO nanoparticles: A combined experimental and DFT+U study. *Colloids and Surfaces A: Physicochemical and Engineering Aspects*, 617, p.126386.

Ismail, A.M., Menazea, A.A., Kabary, H.A., El-Sherbiny, A.E. and Samy, A., 2019. The influence of calcination temperature on structural and antimicrobial characteristics of zinc oxide nanoparticles synthesized by Sol–Gel method. *Journal of Molecular Structure*, 1196, pp.332–337.

Ismail, G.A. and Sakai, H., 2022. Review on effect of different type of dyes on advanced oxidation processes (AOPs) for textile color removal. *Chemosphere*, 291, p.132906.

Jaafarzadeh, N., Takdastan, A., Jorfi, S., Ghanbari, F., Ahmadi, M. and Barzegar, G., 2018. The performance study on ultrasonic/ $\text{Fe}_3\text{O}_4/\text{H}_2\text{O}_2$ for degradation of azo dye and real textile wastewater treatment. *Journal of Molecular Liquids*.

Jaffri, J.M., Mohamed, S., Ahmad, I.N., Mustapha, N.M., Manap, Y.A. and Rohimi, N., 2011. Effects of catechin-rich oil palm leaf extract on normal and hypertensive rats' kidney and liver. *Food Chemistry*, 128(2), pp.433–441.

Jalili-Jahani, N., Rabbani, F., Fatehi, A. and Musavi Haghighi, T., 2021. Rapid one-pot synthesis of Ag-decorated ZnO nanoflowers for photocatalytic degradation of tetracycline and product analysis by LC/APCI-MS and direct probe ESI-MS. *Advanced Powder Technology*, 32(8), pp.3075–3089.

Jamal Sisi, A., Fathinia, M., Khataee, A. and Orooji, Y., 2020. Systematic activation of potassium peroxydisulfate with ZIF-8 via sono-assisted catalytic process: Mechanism and ecotoxicological analysis. *Journal of Molecular Liquids*, 308, p.113018.

Jamdnagni, P., Khatri, P. and Rana, J.S., 2018. Green synthesis of zinc oxide nanoparticles using flower extract of *Nyctanthes arbor-tristis* and their antifungal activity. *Journal of King Saud University - Science*, 30(2), pp.168–175.

Jamkhande, P.G., Ghule, N.W., Bamer, A.H. and Kalaskar, M.G., 2019. Metal nanoparticles synthesis: An overview on methods of preparation, advantages and disadvantages, and applications. *Journal of Drug Delivery Science and Technology*, 53, p.101174.

Janani Archana, K., Christy Preetha, A. and Balasubramanian, K., 2022. Influence of Urbach energy in enhanced photocatalytic activity of Cu doped ZnO nanoparticles. *Optical Materials*, 127, p.112245.

Jankowski, W., Li, G., Kujawski, W. and Kujawa, J., 2022. Recent development of membranes modified with natural compounds: Preparation methods and applications in water treatment. *Separation and Purification Technology*, 302, p.122101.

Jawad, A.H., Saber, S.E.M., Abdulhameed, A.S., Reghioia, A., ALOthman, Z.A. and Wilson, L.D., 2022. Mesoporous activated carbon from mangosteen (*Garcinia mangostana*) peels by H_3PO_4 assisted microwave: Optimization, characterization, and adsorption mechanism for methylene blue dye removal. *Diamond and Related Materials*, 129, p.109389.

Jayabalan, J., Mani, G., Krishnan, N., Pernabas, J., Devadoss, J.M. and Jang, H.T., 2019. Green biogenic synthesis of zinc oxide nanoparticles using *Pseudomonas putida* culture and its In vitro antibacterial and anti-biofilm activity. *Biocatalysis and Agricultural Biotechnology*, 21, p.101327.

Jayachandran, A., Aswathy, T.R. and Nair, A.S., 2021. Green synthesis and characterization of zinc oxide nanoparticles using *Cayratia pedata* leaf extract. *Biochemistry and Biophysics Reports*, 26, p.100995.

- Jegadeesan, G.B., Amirthavarshini, S., Divya, J. and Gunarani, G.I., 2019. Catalytic peroxygen activation by biosynthesized iron nanoparticles for enhanced degradation of Congo red dye. *Advanced Powder Technology*, 30(12), pp.2890–2899.
- Jemilugba, O.T., Sakho, E.H.M., Parani, S., Mavumengwana, V. and Oluwafemi, O.S., 2019. Green synthesis of silver nanoparticles using Combretum erythrophyllum leaves and its antibacterial activities. *Colloid and Interface Science Communications*, 31, p.100191.
- Jin, C.-Z., Yang, Y., Yang, X.-A., Wang, S.-B. and Zhang, W.-B., 2020. Visible photocatalysis of Cr(VI) at g/L level in Si/N-TiO₂ nanocrystals synthesized by one-step co-hydrolysis method. *Chemical Engineering Journal*, 398, p.125641.
- Ju, Y., Yang, S., Ding, Y., Sun, C., Gu, C., He, Z., Qin, C., He, H. and Xu, B., 2009. Microwave-enhanced H₂O₂-based process for treating aqueous malachite green solutions: Intermediates and degradation mechanism. *Journal of Hazardous Materials*, 171(1), pp.123–132.
- Kakavandi, B., Bahari, N., Rezaei Kalantary, R. and Dehghani Fard, E., 2019. Enhanced sono-photocatalysis of tetracycline antibiotic using TiO₂ decorated on magnetic activated carbon (MAC@T) coupled with US and UV: A new hybrid system. *Ultrasonics Sonochemistry*, 55, pp.75–85.
- Kakhaki, Z.M., Youzbashi, A. and Naderi, N., 2015. Optical Properties of Zinc Oxide Nanoparticles Prepared by a One-Step Mechanochemical Synthesis Method. *Journal of Physical Science*, 26(2), pp.41–51.
- Kalpana, V.N., Kataru, B.A.S., Sravani, N., Vigneshwari, T., Panneerselvam, A. and Devi Rajeswari, V., 2018. Biosynthesis of zinc oxide nanoparticles using culture filtrates of *Aspergillus niger*: Antimicrobial textiles and dye degradation studies. *OpenNano*, 3, pp.48–55.
- Kamath Miyar, H., Pai, A. and Goveas, L.C., 2021. Adsorption of Malachite Green by extracellular polymeric substance of *Lysinibacillus* sp. SS1: kinetics and isotherms. *Heliyon*, 7(6), p.e07169.
- Kan, C.-C., Sumalinog, M.J.R., Rivera, K.K.P., Arazo, R.O. and de Luna, M.D.G., 2017. Ultrasound-assisted synthesis of adsorbents from groundwater treatment residuals for hexavalent chromium removal from aqueous solutions. *Groundwater for Sustainable Development*, 5, pp.253–260.
- Karaca, S., Önal, E.Ç., Açışlı, Ö. and Khataee, A., 2021. Preparation of chitosan modified montmorillonite biocomposite for sonocatalysis of dyes: Parameters and degradation mechanism. *Materials Chemistry and Physics*, 260, p.124125.
- Karnan, T. and Selvakumar, S.A.S., 2016. Biosynthesis of ZnO nanoparticles using rambutan (*Nephelium lappaceum*L.) peel extract and their photocatalytic activity on methyl orange dye. *Journal of Molecular Structure*, 1125, pp.358–365.

Karthick, K., Kathirvel, P., Marnadu, R., Chakravarty, S. and Shkir, M., 2021. Ultrafast one step direct injection flame synthesis of zinc oxide nanoparticles and fabrication of p-Si/n-ZnO photodiode and characterization. *Physica B: Condensed Matter*, 612, p.412971.

Kasi, G. and Seo, J., 2019. Influence of Mg doping on the structural, morphological, optical, thermal, and visible-light responsive antibacterial properties of ZnO nanoparticles synthesized via co-precipitation. *Materials Science and Engineering C*.

Katheresan, V., Kannedo, J. and Lau, S.Y., 2018. Efficiency of various recent wastewater dye removal methods: A review. *Journal of Environmental Chemical Engineering*, 6(4), pp.4676–4697.

Kaur, B., Kuntus, L., Tikker, P., Kattel, E., Trapido, M. and Dulova, N., 2019. Photo-induced oxidation of ceftriaxone by persulfate in the presence of iron oxides. *Science of The Total Environment*, 676, pp.165–175.

Kaur, J. and Singh, H., 2020. Fabrication and analysis of piezoelectricity in 0D, 1D and 2D Zinc Oxide nanostructures. *Ceramics International*, 46(11, Part B), pp.19401–19407.

Kaur, M., Kaur, P., Kaur, G., Dev, K., Negi, P. and Sharma, R., 2018. Structural, morphological and optical properties of Eu-N co-doped zinc oxide nanoparticles synthesized using co-precipitation technique. *Vacuum*, 155, pp.689–695.

Keshari, A.K. and Singh, M., 2020. Precession controlled synthesis and ligands assisted modulation of optical properties and Raman scattering in Ag doped ZnO nano-egg. *Physica E: Low-dimensional Systems and Nanostructures*, 123, p.114177.

Keshu, Rani, M., Yadav, J., Meenu, Chaudhary, S. and Shanker, U., 2021. An updated review on synthetic approaches of green nanomaterials and their application for removal of water pollutants: Current challenges, assessment and future perspectives. *Journal of Environmental Chemical Engineering*, 9(6), p.106763.

Khairy, M., Naguib, E.M. and Mohamed, M.M., 2020. Enhancement of Photocatalytic and Sonophotocatalytic Degradation of 4-nitrophenol by ZnO/Graphene Oxide and ZnO/Carbon Nanotube Nanocomposites. *Journal of Photochemistry and Photobiology A: Chemistry*, 396, p.112507.

Khalil, M.I., Al-Qunaibit, M.M., Al-zahem, A.M. and Labis, J.P., 2014. Synthesis and characterization of ZnO nanoparticles by thermal decomposition of a curcumin zinc complex. *Arabian Journal of Chemistry*, 7(6), pp.1178–1184.

Khan, M.A.M., Kumar, S., Alhazaa, A.N. and Al-Gawati, M.A., 2018a. Modifications in structural, morphological, optical and photocatalytic properties of ZnO:Mn nanoparticles by sol-gel protocol. *Materials Science in Semiconductor Processing*, 87, pp.134–141.

- Khan, M.F., Kundu, D., Hazra, C. and Patra, S., 2019a. A strategic approach of enzyme engineering by attribute ranking and enzyme immobilization on zinc oxide nanoparticles to attain thermostability in mesophilic *Bacillus subtilis* lipase for detergent formulation. *International Journal of Biological Macromolecules*, 136, pp.66–82.
- Khan, M.I., Fatima, N., Shakil, M., Tahir, M.B., Riaz, K.N., Rafique, M., Iqbal, T. and Mahmood, K., 2021. Investigation of in-vitro antibacterial and seed germination properties of green synthesized pure and nickel doped ZnO nanoparticles. *Physica B: Condensed Matter*, 601, p.412563.
- Khan, M.M., Harunsani, M.H., Tan, A.L., Hojamberdiev, M., Poi, Y.A. and Ahmad, N., 2020. Antibacterial Studies of ZnO and Cu-Doped ZnO Nanoparticles Synthesized Using Aqueous Leaf Extract of *Stachytarpheta jamaicensis*. *BioNanoScience*, 10(4), pp.1037–1048.
- Khan, M.M., Saadah, N.H., Khan, M.E., Harunsani, M.H., Tan, A.L. and Cho, M.H., 2019b. Potentials of *Costus woodsonii* leaf extract in producing narrow band gap ZnO nanoparticles. *Materials Science in Semiconductor Processing*, 91, pp.194–200.
- Khan, S.A., Noreen, F., Kanwal, S., Iqbal, A. and Hussain, G., 2018b. Green synthesis of ZnO and Cu-doped ZnO nanoparticles from leaf extracts of *Abutilon indicum*, *Clerodendrum infortunatum*, *Clerodendrum inerme* and investigation of their biological and photocatalytic activities. *Materials Science and Engineering: C*, 82, pp.46–59.
- Khansili, N., Rattu, G., Kumar, A. and Krishna, P.M., 2020. Development of Colorimetric Sensor with Zinc Oxide Nanoparticles for Rapid Detection of Aflatoxin B1 in Rice. *Materials Today: Proceedings*, 21, pp.1846–1855.
- Khataee, A., Karimi, A., Zarei, M. and Joo, S.W., 2020. Eu-doped ZnO nanoparticles: Sonochemical synthesis, characterization, and sonocatalytic application. *Ultrasonics Sonochemistry*, 67, p.102822.
- Khawaja, H., Zahir, E., Asghar, M.A. and Asghar, M.A., 2021. Graphene oxide decorated with cellulose and copper nanoparticle as an efficient adsorbent for the removal of malachite green. *International Journal of Biological Macromolecules*, 167, pp.23–34.
- Khor, C.M., Khan, M.M. and Harunsani, M.H., 2022. Silver Niobate-based Photocatalysts: Relevance in Dye Degradation. *Chemical Physics Impact*, p.100141.
- Khoshtamvand, N., Jafari, A., Kamarehie, B., Mohammadi, A. and Faraji, M., 2019. Removal of Malachite Green Dye from Aqueous Solutions Using Zeolitic Imidazole Framework-8. *Environmental Processes*, 6(3), pp.757–772.
- Kołodziejczak-Radzimska, A. and Jesionowski, T., 2014. Zinc Oxide-From Synthesis to Application: A Review. *Materials (1996-1944)*, 7(4), pp.2833–2881.

Kontopoulou, I., Angelopoulou, A. and Bouropoulos, N., 2016. ZnO spherical porous nanostructures obtained by thermal decomposition of zinc palmitate. *Materials Letters*, 165, pp.87–90.

Krishnakumar, V. and Elansezhian, R., 2021. Dispersion stability of zinc oxide nanoparticles in an electroless bath with various surfactants. *Materials Today: Proceedings*.

Krishnaswamy, S., Ragupathi, V., Panigrahi, P. and Nagarajan, G.S., 2019. Photoluminescence quenching of green synthesized manganese doped zinc oxide by sodium iodide doped Polypyrrole polymer. *Thin Solid Films*, 689, p.137510.

Król, A., Railean-Plugaru, V., Pomastowski, P., Złoch, M. and Buszewski, B., 2018. Mechanism study of intracellular zinc oxide nanocomposites formation. *Colloids and Surfaces A: Physicochemical and Engineering Aspects*, 553, pp.349–358.

Kumar, M.R.A., Nagaswarupa, H.P., Ravikumar, C.R., Prashantha, S.C., Nagabhushana, H. and Bhatt, A.S., 2019a. Green engineered nano MgO and ZnO doped with Sm^{3+} : Synthesis and a comparison study on their characterization, PC activity and electrochemical properties. *Journal of Physics and Chemistry of Solids*, 127, pp.127–139.

Kumar, M.R.A., Ravikumar, C.R., Nagaswarupa, H.P., Purshotam, B., Gonfa, B., Murthy, H.C.A., Sabir, F.K. and Tadesse, S., 2019b. Evaluation of bi-functional applications of ZnO nanoparticles prepared by green and chemical methods. *Journal of Environmental Chemical Engineering*, 7(6), p.103468.

Kumar, R., Barakat, M.A., Al-Mur, B.A., Alseroury, F.A. and Eniola, J.O., 2020. Photocatalytic degradation of cefoxitin sodium antibiotic using novel BN/CdAl₂O₄ composite. *Journal of Cleaner Production*, 246, p.119076.

Kumar, S., Boro, J.C., Ray, D., Mukherjee, A. and Dutta, J., 2019c. Bionanocomposite films of agar incorporated with ZnO nanoparticles as an active packaging material for shelf life extension of green grape. *Heliyon*, 5(6), p.e01867.

Kumar Sinha, A., Kumar Sasmal, A., Pal, A., Pal, D. and Pal, T., 2021. Ammonium phosphomolybdate [(NH₄)₃PMo₁₂O₄₀] an inorganic ion exchanger for environmental application for purification of dye contaminant wastewater. *Journal of Photochemistry and Photobiology A: Chemistry*, 418, p.113427.

Kumar, V., Prakash, J., Singh, J.P., Chae, K.H., Swart, C., Ntwaeaborwa, O.M., Swart, H.C. and Dutta, V., 2017. Role of silver doping on the defects related photoluminescence and antibacterial behaviour of zinc oxide nanoparticles. *Colloids and Surfaces B: Biointerfaces*.

Kumaresan, N., Ramamurthi, K., Ramesh Babu, R., Sethuraman, K. and Moorthy Babu, S., 2017. Hydrothermally grown ZnO nanoparticles for effective photocatalytic activity. *Applied Surface Science*, 418, pp.138–146.

- Kumari, P. and Meena, A., 2020. Green synthesis of gold nanoparticles from *Lawsoniainermis* and its catalytic activities following the Langmuir-Hinshelwood mechanism. *Colloids and Surfaces A: Physicochemical and Engineering Aspects*, 606, p.125447.
- Kundu, D., Hazra, C., Chatterjee, A., Chaudhari, A. and Mishra, S., 2014. Extracellular biosynthesis of zinc oxide nanoparticles using *Rhodococcus pyridinivorans* NT2: Multifunctional textile finishing, biosafety evaluation and in vitro drug delivery in colon carcinoma. *Journal of Photochemistry and Photobiology B: Biology*, 140, pp.194–204.
- Lam, S.-M., Sin, J.-C., Zeng, H., Lin, H., Li, H., Chai, Y.-Y., Choong, M.-K. and Mohamed, A.R., 2020. Green synthesis of Fe-ZnO nanoparticles with improved sunlight photocatalytic performance for polyethylene film deterioration and bacterial inactivation. *Materials Science in Semiconductor Processing*, 123, p.105574.
- Lam, S.-M., Sin, J.-C., Zeng, H., Lin, H., Li, H., Chai, Y.-Y., Choong, M.-K. and Mohamed, A.R., 2021. Green synthesis of Fe-ZnO nanoparticles with improved sunlight photocatalytic performance for polyethylene film deterioration and bacterial inactivation. *Materials Science in Semiconductor Processing*, 123, p.105574.
- Lee, H., Jang, H.S., Kim, N.Y. and Joo, J.B., 2021. Cu-doped TiO₂ hollow nanostructures for the enhanced photocatalysis under visible light conditions. *Journal of Industrial and Engineering Chemistry*, 99, pp.352–363.
- Lee, J.-H., Velmurugan, P., Ravi, A.V. and Oh, B.-T., 2020. Green and hydrothermal assembly of reduced graphene oxide (rGO)-coated ZnO and Fe hybrid nanocomposite for the removal of nitrate and phosphate. *Environmental Chemistry and Ecotoxicology*, 2, pp.141–149.
- Li, C.Y., Qi, N., Liu, Z.W., Zhou, B., Chen, Z.Q. and Wang, Z., 2016. Effect of synthesis temperature on the ordered pore structure in mesoporous silica studied by positron annihilation spectroscopy. *Applied Surface Science*, 363, pp.445–450.
- Li, J., Li, W., Gu, J., Zhong, Z., Yang, C., Hou, J., Tao, H., Du, J., Li, X., Xu, L., Wan, S., Long, H. and Wang, H., 2020. Carrier transport improvement in ZnO/MgZnO multiple-quantum-well ultraviolet light-emitting diodes by energy band modification on MgZnO barriers. *Optics Communications*, 459, p.124978.
- Li, P., Miao, R., Wang, P., Sun, F. and Li, X., 2021a. Bi-metal oxide-modified flat-sheet ceramic membranes for catalytic ozonation of organic pollutants in wastewater treatment. *Chemical Engineering Journal*, 426, p.131263.
- Li, Y., Gan, P., Jiang, R., Zhao, Z., Ye, J., Liu, W., Tong, M. and Liang, J., 2021b. Insight into the synergetic effect of photocatalysis and transition metal on sulfite activation: Different mechanisms for carbamazepine and diclofenac degradation. *Science of The Total Environment*, 787, p.147626.

- Li, Y., Wang, X., Wang, X., Xia, Y., Zhang, A., Shi, J., Gao, L., Wei, H. and Chen, W., 2021c. Z-scheme BiVO₄/g-C₃N₄ heterojunction: an efficient, stable and heterogeneous catalyst with highly enhanced photocatalytic activity towards Malachite Green assisted by H₂O₂ under visible light. *Colloids and Surfaces A: Physicochemical and Engineering Aspects*, 618, p.126445.
- Li, Z., Zhuang, T., Dong, J., Wang, L., Xia, J., Wang, H., Cui, X. and Wang, Z., 2021d. Sonochemical fabrication of inorganic nanoparticles for applications in catalysis. *Ultrasonics Sonochemistry*, 71, p.105384.
- Lin, L., Xu, M., Mu, H., Wang, W., Sun, J., He, J., Qiu, J.-W. and Luan, T., 2019. Quantitative Proteomic Analysis to Understand the Mechanisms of Zinc Oxide Nanoparticle Toxicity to *Daphnia pulex* (Crustacea: Daphniidae): Comparing with Bulk Zinc Oxide and Zinc Salt. *Environmental science & technology*, 53(9), pp.5436–5444.
- Lingesh, A., Paul, D., Naidu, V.G.M. and Satheeshkumar, N., 2019. AMPK activating and anti adipogenic potential of *Hibiscus rosa sinensis* flower in 3T3-L1 cells. *Journal of Ethnopharmacology*, 233, pp.123–130.
- Liu, D., Lin, R., Wu, H., Ji, J., Wang, D., Xue, Z., Feng, S. and Chen, X., 2022a. Green synthesis, characterization of procyanidin-mediated gold nanoparticles and its application in fluorescence detection of prazosin. *Microchemical Journal*, 173, p.107045.
- Liu, H., Li, P., Wang, Y., Wang, H., Fang, Y., Guo, Z., Huang, Y., Lin, J., Hu, L., Tang, C. and Liu, Z., 2022b. Eco-green C, O co-doped porous BN adsorbent for aqueous solution with superior adsorption efficiency and selectivity. *Chemosphere*, 288, p.132520.
- Liu, L., Chen, W.-T., Kihara, S. and Kilmartin, P.A., 2021a. Green synthesis of akaganéite (β -FeOOH) nanocomposites as peroxidase-mimics and application for discoloration of methylene blue. *Journal of Environmental Management*, 296, p.113163.
- Liu, M., Yin, W., Zhao, T.-L., Yao, Q.-Z., Fu, S.-Q. and Zhou, G.-T., 2021b. High-efficient removal of organic dyes from model wastewater using Mg(OH)₂-MnO₂ nanocomposite: Synergistic effects of adsorption, precipitation, and photodegradation. *Separation and Purification Technology*, 272, p.118901.
- Liu, S.-L., Liu, B., Xiang, Z., Xu, L., Wang, X.-F., Liu, Y. and Wang, X., 2021c. Fabrication of CaWO₄ microspheres with enhanced sonocatalytic performance for ciprofloxacin removal in aqueous solution. *Colloids and Surfaces A: Physicochemical and Engineering Aspects*, 628, p.127206.
- Liu, S., Zhu, L., Cao, W., Li, P., Zhan, Z., Chen, Z., Yuan, X. and Wang, J., 2020. Defect-related optical properties of Mg-doped ZnO nanoparticles synthesized via low temperature hydrothermal method. *Journal of Alloys and Compounds*, p.157654.
- Liu, Y., Zhang, Q., Xu, M., Yuan, H., Chen, Y., Zhang, J., Luo, K., Zhang, J. and

- You, B., 2019. Novel and efficient synthesis of Ag-ZnO nanoparticles for the sunlight-induced photocatalytic degradation. *Applied Surface Science*, 476, pp.632–640.
- Long, R., Yu, Z., Tan, Q., Feng, X., Zhu, X., Li, X. and Wang, P., 2021. Ti₃C₂ MXene/NH₂-MIL-88B(Fe): Research on the adsorption kinetics and photocatalytic performance of an efficient integrated photocatalytic adsorbent. *Applied Surface Science*, 570, p.151244.
- Lum, P.T., Foo, K.Y., Zakaria, N.A. and Palaniandy, P., 2020. Ash based nanocomposites for photocatalytic degradation of textile dye pollutants: A review. *Materials Chemistry and Physics*, 241, p.122405.
- Luna-Sánchez, J.L., Jiménez-Pérez, J.L., Carbajal-Valdez, R., Lopez-Gamboa, G., Pérez-González, M. and Correa-Pacheco, Z.N., 2019. Green synthesis of silver nanoparticles using Jalapeño Chili extract and thermal lens study of acrylic resin nanocomposites. *Thermochimica Acta*, 678, p.178314.
- Lungu, I.I., Holban, A.M., Ficai, A. and Grumezescu, A.M., 2017. Chapter 22 - Zinc Oxide Nanostructures: New Trends in Antimicrobial Therapy. In: *Nanostructures for Antimicrobial Therapy*. Elsevier Inc. pp.503–514.
- Luptáková, N., Pešlová, F. and Kliber, J., 2015. The study and microstructure analysis of zinc and zinc oxide. *Metalurgija*, 54(1), pp.43–46.
- Luque, P.A., Nava, O., Soto-Robles, C.A., Vilchis-Nestor, A.R., Garrafa-Galvez, H.E. and Castro-Beltran, A., 2018a. Effects of *Daucus carota* extract used in green synthesis of zinc oxide nanoparticles. *Journal of Materials Science: Materials in Electronics*, 29(20), pp.17638–17643.
- Luque, P.A., Soto-Robles, C.A., Nava, O., Gomez-Gutierrez, C.M., Castro-Beltran, A., Garrafa-Galvez, H.E., Vilchis-Nestor, A.R. and Olivas, A., 2018b. Green synthesis of zinc oxide nanoparticles using *Citrus sinensis* extract. *Journal of Materials Science: Materials in Electronics*, 29(12), pp.9764–9770.
- LV, S.-W., Liu, J.-M., Zhao, N., Li, C.-Y., Yang, F.-E., Wang, Z.-H. and Wang, S., 2020. MOF-derived CoFe₂O₄/Fe₂O₃ embedded in g-C₃N₄ as high-efficient Z-scheme photocatalysts for enhanced degradation of emerging organic pollutants in the presence of persulfate. *Separation and Purification Technology*, 253, p.117413.
- Ma, X., Cheng, Y., Ge, Y., Wu, H., Li, Q., Gao, N. and Deng, J., 2018. Ultrasound-enhanced nanosized zero-valent copper activation of hydrogen peroxide for the degradation of norfloxacin. *Ultrasonics Sonochemistry*, 40, pp.763–772.
- Ma, X., Yan, Y., Dai, Q., Gao, J., Liu, S. and Xia, Y., 2021. Energy-efficient pulse electrochemical oxidation of Acid Blue 9 using a Ti/SnO₂-Sb/ α,β -Polytetrafluoroethylene-Fe-PbO₂ electrode: Kinetics, mass transfer and mechanism. *Separation and Purification Technology*, 279, p.119775.

Mabhouti, K., Karamirad, M., Norouzzadeh, P., Golzan, M.M. and Naderali, R., 2021. Measurement of nickel doped zinc oxide NPs resonance frequencies and electromagnetic properties in X-Band. *Physica B: Condensed Matter*, 602, p.412532.

Madhumitha, G., Fowsiya, J., Gupta, N., Kumar, A. and Singh, M., 2019. Green synthesis, characterization and antifungal and photocatalytic activity of *Pithecellobium dulce* peel-mediated ZnO nanoparticles. *Journal of Physics and Chemistry of Solids*, 127, pp.43–51.

Mahamuni-Badiger, P.P., Patil, P.M., Badiger, M. V, Patel, P.R., Thorat- Gadgil, B.S., Pandit, A. and Bohara, R.A., 2020. Biofilm formation to inhibition: Role of zinc oxide-based nanoparticles. *Materials Science and Engineering: C*, 108, p.110319.

Mahdavi, R. and Ashraf Talesh, S.S., 2017. The effect of ultrasonic irradiation on the structure, morphology and photocatalytic performance of ZnO nanoparticles by sol-gel method. *Ultrasonics Sonochemistry*, 39(February), pp.504–510.

Mahendiran, M., Asha, A., Madhavan, J. and Victor Antony Raj, M., 2019. Structural and Optical Analysis of 1D Zinc Oxide Nanoparticles Synthesized Via Hydrothermal Method. *Materials Today: Proceedings*, 8, pp.412–418.

Mahmud, S., Johar Abdullah, M., Putrus, G., Chong, J. and Karim Mohamad, A., 2006. Nanostructure of ZnO fabricated via French Process and its correlation to electrical properties of semiconducting varistors. *Synthesis & Reactivity in Inorganic, Metal-Organic, & Nano-Metal Chemistry*, 36(2), pp.155–159.

Makofane, A., Motaung, D.E. and Hintsho-Mbita, N.C., 2021. Photocatalytic degradation of methylene blue and sulfisoxazole from water using biosynthesized zinc ferrite nanoparticles. *Ceramics International*, 47(16), pp.22615–22626.

Maleki, A., Moradi, F., Shahmoradi, B., Rezaee, R. and Lee, S.-M., 2020. The photocatalytic removal of diazinon from aqueous solutions using tungsten oxide doped zinc oxide nanoparticles immobilized on glass substrate. *Journal of Molecular Liquids*, 297, p.111918.

Mallikarjunaswamy, C., Lakshmi Ranganatha, V., Ramu, R., Udayabhanu and Nagaraju, G., 2020. Facile microwave-assisted green synthesis of ZnO nanoparticles: application to photodegradation, antibacterial and antioxidant. *Journal of Materials Science: Materials in Electronics*, 31(2), pp.1004–1021.

Manasa, D.J., Chandrashekar, K.R., Madhu Kumar, D.J., Niranjana, M. and Navada, K.M., 2021. *Mussaenda frondosa* L. mediated facile green synthesis of Copper oxide nanoparticles – Characterization, photocatalytic and their biological investigations. *Arabian Journal of Chemistry*, 14(6), p.103184.

Manea, Y.K., Khan, A.M., Wani, A.A., Saleh, M.A.S., Qashqoosh, M.T.A.,

- Shahadat, M. and Rezakazemi, M., 2022. In-grown flower like Al-Li/Th-LDH@CNT nanocomposite for enhanced photocatalytic degradation of MG dye and selective adsorption of Cr (VI). *Journal of Environmental Chemical Engineering*, 10(1), p.106848.
- Mangala Nagasundari, S., Muthu, K., Kaviyarasu, K., Farraj, D.A. Al and Alkufeidy, R.M., 2021. Current trends of Silver doped Zinc oxide nanowires photocatalytic degradation for energy and environmental application. *Surfaces and Interfaces*, 23, p.100931.
- Manik, U.P., Nande, A., Raut, S. and Dhoble, S.J., 2020. Green synthesis of silver nanoparticles using plant leaf extraction of *Artocarpus heterophyllus* and *Azadirachta indica*. *Results in Materials*, 6, p.100086.
- Marlinda, A.R., Yusoff, N., Pandikumar, A., Huang, N.M., Akbarzadeh, O., Sagadevan, S., Wahab, Y.A. and Johan, M.R., 2019. Tailoring morphological characteristics of zinc oxide using a one-step hydrothermal method for photoelectrochemical water splitting application. *International Journal of Hydrogen Energy*, 44(33), pp.17535–17543.
- Maučec, D., Šuligoj, A., Ristić, A., Dražić, G., Pintar, A. and Tušar, N.N., 2018. Titania versus zinc oxide nanoparticles on mesoporous silica supports as photocatalysts for removal of dyes from wastewater at neutral pH. *Catalysis Today*, 310(May 2017), pp.32–41.
- Mazhdi, M. and Tafreshi, M.J., 2020. The investigation of scintillation properties of gadolinium doped zinc oxide nanoparticles for nuclear radiation detection. *Nuclear Instruments and Methods in Physics Research Section A: Accelerators, Spectrometers, Detectors and Associated Equipment*, 959, p.163604.
- Mbopi, P.Y., Fozeng, H.D.S., Nguekeu, Y.M.M., Bitchagno, G.T.M., Ngantchouko, C.B.N., Awouafack, M.D., Opatz, T., Ngouela, S.A., Morita, H. and Tene, M., 2021. Chemical constituents, total phenolic content, antioxidant activity and bactericidal effect of *Dicliptera verticillate* (Acanthaceae). *South African Journal of Botany*, 142, pp.216–221.
- Mehrizad, A., Behnajady, M.A., Gharbani, P. and Sabbagh, S., 2019. Sonocatalytic degradation of Acid Red 1 by sonochemically synthesized zinc sulfide-titanium dioxide nanotubes: Optimization, kinetics and thermodynamics studies. *Journal of Cleaner Production*, 215, pp.1341–1350.
- Melkamu, W.W. and Bitew, L.T., 2021. Green synthesis of silver nanoparticles using *Hagenia abyssinica* (Bruce) J.F. Gmel plant leaf extract and their antibacterial and anti-oxidant activities. *Heliyon*, 7(11), p.e08459.
- Mendoza-Mendoza, E., Nuñez-Briones, A.G., García-Cerda, L.A., Peralta-Rodríguez, R.D. and Montes-Luna, A.J., 2018. One-step synthesis of ZnO and Ag/ZnO heterostructures and their photocatalytic activity. *Ceramics International*, 44(6), pp.6176–6180.

- Merabet, N. and Kerboua, K., 2022. Sonolytic and ultrasound-assisted techniques for hydrogen production: A review based on the role of ultrasound. *International Journal of Hydrogen Energy*, 47(41), pp.17879–17893.
- Meriem, H., Souad, D. and Lakhdar, T., 2020. Synthesis of copper with sodium ascorbate and its application in malachite green discoloration. *Journal of Environmental Chemical Engineering*, 8(5), p.104457.
- Mir, N., Rakhshanipour, M., Heidari, A., Mir, A.A. and Salavati-Niasari, M., 2015. Synthesis and characterization of ZnO nanohemispheres via solution-phase thermal decomposition and its comparison with the solid-phase approach. *Journal of Industrial and Engineering Chemistry*, 21, pp.884–888.
- Mirza, A.U., Kareem, A., Nami, S.A.A., Bhat, S.A., Mohammad, A. and Nishat, N., 2019. Malus pumila and Juglen regia plant species mediated zinc oxide nanoparticles: Synthesis, spectral characterization, antioxidant and antibacterial studies. *Microbial Pathogenesis*, 129, pp.233–241.
- Mirzaei, A., Haghghat, F., Chen, Z. and Yerushalmi, L., 2019. Sonocatalytic removal of ampicillin by Zn(OH)F: Effect of operating parameters, toxicological evaluation and by-products identification. *Journal of Hazardous Materials*, 375, pp.86–95.
- Moatamed, E.R., Hussein, A.A., El-desoky, M.M. and Khayat, Z.E.L., 2019. Comparative study of zinc oxide nanoparticles and its bulk form on liver function of Wistar rat. *Toxicology and Industrial Health*, 35(10), pp.627–637.
- Moezzi, A., McDonagh, A.M. and Cortie, M.B., 2012. Zinc oxide particles: Synthesis, properties and applications. *Chemical Engineering Journal*, 185–186, pp.1–22.
- Moghaddam, A.B., Moniri, M., Azizi, S., Ariff, A.B., Mohamad, R., Rahim, R.A., Saad, W.Z., Namvar, F. and Navaderi, M., 2017. Biosynthesis of ZnO nanoparticles by a new *Pichia kudriavzevii* yeast strain and evaluation of their antimicrobial and antioxidant activities. *Molecules*, 22(6).
- Mohamed, A.A., Fouda, A., Abdel-Rahman, M.A., Hassan, S.E.-D., El-Gamal, M.S., Salem, S.S. and Shaheen, T.I., 2019. Fungal strain impacts the shape, bioactivity and multifunctional properties of green synthesized zinc oxide nanoparticles. *Biocatalysis and Agricultural Biotechnology*, 19, p.101103.
- Mohamed, E.A., 2020. Green synthesis of copper & copper oxide nanoparticles using the extract of seedless dates. *Heliyon*, 6(1), p.e03123.
- Mohamed Isa, E.D., Shameli, K., Ch'ng, H.J., Che Jusoh, N.W. and Hazan, R., 2021. Photocatalytic degradation of selected pharmaceuticals using green fabricated zinc oxide nanoparticles. *Advanced Powder Technology*, 32(7), pp.2398–2409.
- Mohamed, R.M., McKinney, D., Kadi, M.W., Mkhallid, I.A. and Sigmund, W., 2016. Platinum/zinc oxide nanoparticles: Enhanced photocatalysts degrade

malachite green dye under visible light conditions. *Ceramics International*, 42(8), pp.9375–9381.

Mohammed, A.A. and Kareem, S.L., 2019. Adsorption of tetracycline from wastewater by using Pistachio shell coated with ZnO nanoparticles: Equilibrium, kinetic and isotherm studies. *Alexandria Engineering Journal*, 58(3), pp.917–928.

Mohanty, L., Sundar Pattanayak, D., Singhal, R., Pradhan, D. and Kumar Dash, S., 2022. Enhanced photocatalytic degradation of rhodamine B and malachite green employing BiFeO₃/g-C₃N₄ nanocomposites: An efficient visible-light photocatalyst. *Inorganic Chemistry Communications*, p.109286.

Mohsin, M., Bhatti, I.A., Ashar, A., Khan, M.W., Farooq, M.U., Khan, H., Hussain, M.T., Loomba, S., Mohiuddin, M., Zavabeti, A., Ahmad, M., Yousaf, M. and Mahmood, N., 2021. Iron-doped zinc oxide for photocatalyzed degradation of humic acid from municipal wastewater. *Applied Materials Today*, 23, p.101047.

Molina, G.A., Esparza, R., López-Miranda, J.L., Hernández-Martínez, A.R., España-Sánchez, B.L., Elizalde-Peña, E.A. and Estevez, M., 2019. Green synthesis of Ag nanoflowers using Kalanchoe Daigremontiana extract for enhanced photocatalytic and antibacterial activities. *Colloids and Surfaces B: Biointerfaces*, 180, pp.141–149.

Moon, S., Ryu, J., Hwang, J. and Lee, C.-G., 2023. Efficient removal of dyes from aqueous solutions using short-length bimodal mesoporous carbon adsorbents. *Chemosphere*, 313, p.137448.

Moosavi, A., Amooey, A.A., Mir, A.A. and Marzbali, M.H., 2020. Extraordinary adsorption of acidic fuchsine and malachite green onto cheap nano-adsorbent derived from eggshell. *Chinese Journal of Chemical Engineering*, 28(6), pp.1591–1602.

Moradi, M., Hasanvandian, F., Isari, A.A., Hayati, F., Kakavandi, B. and Setayesh, S.R., 2021a. CuO and ZnO co-anchored on g-C₃N₄ nanosheets as an affordable double Z-scheme nanocomposite for photocatalytic decontamination of amoxicillin. *Applied Catalysis B: Environmental*, 285, p.119838.

Moradi, S., Sobhghol, S.A., Hayati, F., Isari, A.A., Kakavandi, B., Bashardoust, P. and Anvaripour, B., 2020. Performance and reaction mechanism of MgO/ZnO/Graphene ternary nanocomposite in coupling with LED and ultrasound waves for the degradation of sulfamethoxazole and pharmaceutical wastewater. *Separation and Purification Technology*, 251, p.117373.

Moradi, Z., Madadkar Haghjou, M., Zarei, M., Colville, L. and Raza, A., 2021b. Synergy of production of value-added bioplastic, astaxanthin and phycobilin co-products and Direct Green 6 textile dye remediation in *Spirulina platensis*. *Chemosphere*, 280, p.130920.

Moraes, L.C., Figueiredo, R.C., Ribeiro-Andrade, R., Pontes-Silva, A. V,

Arantes, M.L., Giani, A. and Figueredo, C.C., 2021. High diversity of microalgae as a tool for the synthesis of different silver nanoparticles: A species-specific green synthesis. *Colloid and Interface Science Communications*, 42, p.100420.

Mousa, M.A., Bayoumy, W.A.A. and Khairy, M., 2013. Characterization and photo-chemical applications of nano-ZnO prepared by wet chemical and thermal decomposition methods. *Materials Research Bulletin*, 48(11), pp.4576–4582.

Mousa, S.A., Shalan, A.E., Hassan, H.H., Ebnawaled, A.A. and Khairy, S.A., 2022. Enhanced the photocatalytic degradation of titanium dioxide nanoparticles synthesized by different plant extracts for wastewater treatment. *Journal of Molecular Structure*, 1250, p.131912.

Moyo, S., Makhanya, B.P. and Zwane, P.E., 2022. Use of bacterial isolates in the treatment of textile dye wastewater: A review. *Heliyon*, 8(6), p.e09632.

Mukhopadhyay, A., Tripathy, B.K., Debnath, A. and Kumar, M., 2021. Enhanced persulfate activated sono-catalytic degradation of brilliant green dye by magnetic CaFe_2O_4 nanoparticles: Degradation pathway study, assessment of bio-toxicity and cost analysis. *Surfaces and Interfaces*, 26, p.101412.

Munawar, K., Mansoor, M.A., Olmstead, M.M., Zaharinie, T., Mohd Zubir, M.N., Haniffa, M., Basirun, W.J. and Mazhar, M., 2020. Fabrication of Ag-ZnO composite thin films for plasmonic enhanced water splitting. *Materials Chemistry and Physics*, 255, p.123220.

Munyai, S., Tetana, Z.N., Mathipa, M.M., Ntsendwana, B. and Hintsho-Mbita, N.C., 2021. Green synthesis of Cadmium Sulphide nanoparticles for the photodegradation of Malachite green dye, Sulfisoxazole and removal of bacteria. *Optik*, 247, p.167851.

Mustafa, S.M., Barzinjy, A.A. and Hamad, A.H., 2023. An environmentally friendly green synthesis of Co^{2+} and Mn^{2+} ion doped ZnO nanoparticles to improve solar cell efficiency. *Journal of Environmental Chemical Engineering*, 11(2), p.109514.

Muthukumar, H., Mohammed, S.N., Chandrasekaran, N., Sekar, A.D., Pugazhendhi, A. and Matheswaran, M., 2019. Effect of iron doped Zinc oxide nanoparticles coating in the anode on current generation in microbial electrochemical cells. *International Journal of Hydrogen Energy*, 44(4), pp.2407–2416.

Nagar, A., Kumar, A., Parveen, S., Kumar, A., Dhasmana, H., Husain, S., Verma, A. and Jain, V.K., 2020. Zinc oxide nanoflowers synthesized by sol-gel technique for field emission displays (FEDs). *Materials Today: Proceedings*, 32, pp.402–406.

Nahi, J., Radhakrishnan, A. and Beena, B., 2020. Green synthesis of zinc oxide incorporated nanocellulose with visible light photocatalytic activity and

application for the removal of antibiotic enrofloxacin from aqueous media. *Materials Today: Proceedings*.

Narjis, A., El Aakib, H., Boukendil, M., El Hasnaoui, M., Nkhaili, L., Aberkouks, A. and Outzourhit, A., 2020. Controlling the structural properties of pure and aluminum doped zinc oxide nanoparticles by annealing. *Journal of King Saud University - Science*, 32(1), pp.1074–1080.

Nas, M.S., 2021. AgFe₂O₄/MWCNT nanoparticles as novel catalyst combined adsorption-sonocatalytic for the degradation of methylene blue under ultrasonic irradiation. *Journal of Environmental Chemical Engineering*, 9(3), p.105207.

Naskar, A., Lee, S. and Kim, K., 2020. Antibacterial potential of Ni-doped zinc oxide nanostructure: comparatively more effective against Gram-negative bacteria including multi-drug resistant strains. *RSC Advances*, 10(3), pp.1232–1242.

Nasr, R.A. and Ali, E.A., 2022. Polyethersulfone/gelatin nano-membranes for the Rhodamine B dye removal and textile industry effluents treatment under cost effective condition. *Journal of Environmental Chemical Engineering*, 10(2), p.107250.

Nava, O.J., Luque, P.A., Gómez-Gutiérrez, C.M., Vilchis-Nestor, A.R., Castro-Beltrán, A., Mota-González, M.L. and Olivas, A., 2017. Influence of *Camellia sinensis* extract on Zinc Oxide nanoparticle green synthesis. *Journal of Molecular Structure*, 1134, pp.121–125.

Ngoc, P.K., Mac, T.K., Nguyen, H.T., Viet, D.T., Thanh, T.D., Van Vinh, P., Phan, B.T., Duong, A.T. and Das, R., 2022. Superior organic dye removal by CoCr₂O₄ nanoparticles: Adsorption kinetics and isotherm. *Journal of Science: Advanced Materials and Devices*, 7(2), p.100438.

Ngom, I., Ngom, B.D., Sackey, J. and Khamlich, S., 2021. Biosynthesis of zinc oxide nanoparticles using extracts of *Moringa Oleifera*: Structural & optical properties. *Materials Today: Proceedings*, 36, pp.526–533.

Nguyen, T.H., Watari, T., Vo, T.T., Hatamoto, M., Setiadi, T. and Yamaguchi, T., 2022. Enhancement of azo dye anaerobic bio-treatment performance with ferrous oxide supplement. *Journal of Environmental Chemical Engineering*, 10(5), p.108350.

Ning, X., Hao, A., Cao, Y., Lv, N. and Jia, D., 2021. Boosting piezocatalytic performance of Ag decorated ZnO by piezo-electrochemical synergistic coupling strategy. *Applied Surface Science*, 566, p.150730.

Norek, M., 2019. Approaches to enhance UV light emission in ZnO nanomaterials. *Current Applied Physics*, 19(8), pp.867–883.

Oliveira, J.A., Reis, M.O., Pires, M.S., Ruotolo, L.A.M., Ramalho, T.C., Oliveira, C.R., Lacerda, L.C.T. and Nogueira, F.G.E., 2019. Zn-doped Nb₂O₅ photocatalysts driven by visible-light: An experimental and theoretical study.

Materials Chemistry and Physics, 228, pp.160–167.

Owija, N.Y., Kosa, S.A. and Abdel Salam, M., 2021. Removal of cadmium ions from aqueous solution by zero valent iron nanoparticles: Equilibrium and thermodynamic studies. *Journal of Molecular Liquids*, 342, p.117462.

Özgür, M., Pat, S., Mohammadigharehbagh, R., Musaoğlu, C., Demirkol, U., Elmas, S., Özen, S. and Korkmaz, Ş., 2019. Al doped ZnO thin film deposition by thermionic vacuum arc. *Journal of Materials Science: Materials in Electronics*, 30(1), pp.624–630.

Özgür, Ü., Avrutin, V. and Morkoç, H., 2018. Chapter 16 - Zinc Oxide Materials and Devices Grown by Molecular Beam Epitaxy. In: M.B.T.-M.B.E. (Second E. Henini, ed. Elsevier.pp.343–375.

Padmanaban, A., Murugadoss, G., Venkatesh, N., Hazra, S., Rajesh Kumar, M., Tamilselvi, R. and Sakthivel, P., 2021. Electrochemical determination of harmful catechol and rapid decolorization of textile dyes using ceria and tin doped ZnO nanoparticles. *Journal of Environmental Chemical Engineering*, 9(5), p.105976.

Padmavathy, V. and Sankar, S., 2020. Influence of rare earth (La and Y) codoping on optical properties of ZnO:Ag nanograins. *Optik*, 220, p.165133.

Palimakaa, P., Pietrzyk, S., Stępień, M., Cieccko, K. and Nejman, I., 2018. Zinc recovery from steelmaking dust by hydrometallurgical methods. *Metals*, 8(7).

Pallela, P.N.V.K., Ruddaraju, L.K., Veerla, S.C., Matangi, R., Kollu, P., Ummey, S. and Pammi, S.V.N., 2020. Synergetic antibacterial potential, dye degrading capability and biocompatibility of *Asperagus racemosus* root assisted ZnO nanoparticles. *Materials Today Communications*, 25, p.101574.

Panchal, P., Paul, D.R., Sharma, A., Choudhary, P., Meena, P. and Nehra, S.P., 2020. Biogenic mediated Ag/ZnO nanocomposites for photocatalytic and antibacterial activities towards disinfection of water. *Journal of Colloid and Interface Science*, 563, pp.370–380.

Panda, S.K.B.C., Sen, K. and Mukhopadhyay, S., 2021. Sustainable pretreatments in textile wet processing. *Journal of Cleaner Production*, 329, p.129725.

Pandiyan, N., Murugesan, B., Arumugam, M., Sonamuthu, J., Samayanan, S. and Mahalingam, S., 2019. Ionic liquid - A greener templating agent with *Justicia adhatoda* plant extract assisted green synthesis of morphologically improved Ag-Au/ZnO nanostructure and its antibacterial and anticancer activities. *Journal of Photochemistry and Photobiology B: Biology*, 198, p.111559.

Park, J.K., Rupa, E.J., Arif, M.H., Li, J.F., Anandapadmanaban, G., Kang, J.P., Kim, M., Ahn, J.C., Akter, R., Yang, D.C. and Kang, S.C., 2021. Synthesis of zinc oxide nanoparticles from *Gynostemma pentaphyllum* extracts and

assessment of photocatalytic properties through malachite green dye decolorization under UV illumination-A green approach. *Optik*, p.166249.

Patra, J.K., Das, G., Lee, S., Kang, S.-S. and Shin, H.-S., 2018. Selected commercial plants: A review of extraction and isolation of bioactive compounds and their pharmacological market value. *Trends in Food Science & Technology*, 82, pp.89–109.

Peng, C., Chen, L., Wu, X., Wei, X., Tehrim, A., Dai, M. and Xu, S., 2021. Identification of adsorption or degradation mechanism for the removal of different ionic dyes with iron-carbon micro-electrolysis process. *Journal of Environmental Chemical Engineering*, 9(4), p.105690.

Phin, H.-Y., Ong, Y.-T. and Sin, J.-C., 2020. Effect of carbon nanotubes loading on the photocatalytic activity of zinc oxide/carbon nanotubes photocatalyst synthesized via a modified sol-gel method. *Journal of Environmental Chemical Engineering*, 8(3), p.103222.

Pillai, A.M., Sivasankarapillai, V.S., Rahdar, A., Joseph, J., Sadeghfar, F., Anuf A, R., Rajesh, K. and Kyzas, G.Z., 2020. Green synthesis and characterization of zinc oxide nanoparticles with antibacterial and antifungal activity. *Journal of Molecular Structure*, 1211, p.128107.

Pillai, S.S. and Mini, S., 2016. Polyphenols rich Hibiscus rosa sinensis Linn. petals modulate diabetic stress signalling pathways in streptozotocin-induced experimental diabetic rats. *Journal of Functional Foods*, 20, pp.31–42.

Pirsaheb, M. and Moradi, N., 2021. A systematic review of the sonophotocatalytic process for the decolorization of dyes in aqueous solution: Synergistic mechanisms, degradation pathways, and process optimization. *Journal of Water Process Engineering*, 44, p.102314.

Preethi, S., Abarna, K., Nithyasri, M., Kishore, P., Deepika, K., Ranjithkumar, R., Bhuvaneshwari, V. and Bharathi, D., 2020. Synthesis and characterization of chitosan/zinc oxide nanocomposite for antibacterial activity onto cotton fabrics and dye degradation applications. *International Journal of Biological Macromolecules*, 164, pp.2779–2787.

Purkayastha, D.D., Sarma, B. and Bhattacharjee, C.R., 2014. Surfactant controlled low-temperature thermal decomposition route to zinc oxide nanorods from zinc(II) acetylacetonate monohydrate. *Journal of Luminescence*, 154, pp.36–40.

Puthukkara P, A.R., Jose T, S. and S, D.L., 2022. Green synthesis of iron nanoparticles for malachite green removal. *Materials Today Communications*, 33, p.104759.

Qiu, P., Cheng, Z., Xue, N., Zeng, Y., Kai, X., Zhang, S., Xu, C., Liu, F. and Guo, Z., 2021. The synergistic effect in metal-free graphene oxide coupled graphitic carbon nitride/light/peroxymonosulfate system: Photothermal effect and catalyst stability. *Carbon*, 178, pp.81–91.

Quek, J.A., Sin, J.C., Lam, S.M., Mohamed, A.R. and Zeng, H.H., 2020. Bioinspired green synthesis of ZnO structures with enhanced visible light photocatalytic activity. *Journal of Materials Science: Materials in Electronics*, 31(2), pp.1144–1158.

Rahimi, B., Jafari, N., Abdolahnejad, A., Farrokhzadeh, H. and Ebrahimi, A., 2019. Application of efficient photocatalytic process using a novel BiVO₄/TiO₂-NaY zeolite composite for removal of acid orange 10 dye in aqueous solutions: Modeling by response surface methodology (RSM). *Journal of Environmental Chemical Engineering*, 7(4), p.103253.

Raj, K.P. and Sadayandi, K., 2016. Effect of temperature on structural, optical and photoluminescence studies on ZnO nanoparticles synthesized by the standard co-precipitation method. *Physica B: Condensed Matter*, 487, pp.1–7.

Rajapaksha, S. and Shimizu, N., 2022. Pilot-scale extraction of polyphenols from spent black tea by semi-continuous subcritical solvent extraction. *Food Chemistry: X*, 13, p.100200.

Ramalingam, V. and Hwang, I., 2020. Zinc oxide nanoparticles promoting the formation of myogenic differentiation into myotubes in mouse myoblast C2C12 cells. *Journal of Industrial and Engineering Chemistry*, 83, pp.315–322.

Ramanarayanan, R., Bhabhina, N.M., Dharsana, M. V, Nivedita, C. V and Sindhu, S., 2018. Green synthesis of zinc oxide nanoparticles using extract of *Averrhoa bilimbi*(L) and their photoelectrode applications. *Materials Today: Proceedings*, 5(8), pp.16472–16477.

Rambabu, K., Bharath, G., Banat, F. and Show, P.L., 2021. Green synthesis of zinc oxide nanoparticles using *Phoenix dactylifera* waste as bioreductant for effective dye degradation and antibacterial performance in wastewater treatment. *Journal of Hazardous Materials*, 402, p.123560.

Rani, M. and Shanker, U., 2018. Insight in to the degradation of bisphenol A by doped ZnO@ZnHCF nanocubes: High photocatalytic performance. *Journal of Colloid and Interface Science*, 530, pp.16–28.

Rathnasamy, R., Thangasamy, P. and Thangamuthu, R., 2017. Green synthesis of ZnO nanoparticles using *Carica papaya* leaf extracts for photocatalytic and photovoltaic applications. *Journal of Materials Science: Materials in Electronics*, 28, p.10374-10381.

Rawat, A., Soni, U., Malik, R.S. and Pandey, S.C., 2018. Facile synthesis of UV blocking nano-sized Zinc Oxide and Polymethyl-methacrylate polymer nanocomposite coating material. *Nano-Structures & Nano-Objects*, 16, pp.371–380.

Reddy, C.V., Reddy, I.N., Harish, V.V.N., Reddy, K.R., Shetti, N.P., Shim, J. and Aminabhavi, T.M., 2020. Efficient removal of toxic organic dyes and photoelectrochemical properties of iron-doped zirconia nanoparticles. *Chemosphere*, 239, p.124766.

Reheman, A., Kadeer, K., Okitsu, K., Halidan, M., Tursun, Y., Dilinuer, T. and Abulikemu, A., 2019. Facile photo-ultrasonic assisted reduction for preparation of rGO/Ag₂CO₃ nanocomposites with enhanced photocatalytic oxidation activity for tetracycline. *Ultrasonics Sonochemistry*, 51, pp.166–177.

Rehman, S., Jermy, B.R., Akhtar, S., Borgio, J.F., Abdul Azeez, S., Ravinayagam, V., Al Jindan, R., Alsalem, Z.H., Buhameid, A. and Gani, A., 2019. Isolation and characterization of a novel thermophile; *Bacillus haynesii*, applied for the green synthesis of ZnO nanoparticles. *Artificial Cells, Nanomedicine & Biotechnology*, 47(1), pp.2072–2082.

Ren, Q., Kong, C., Chen, Z., Zhou, J., Li, W., Li, D., Cui, Z., Xue, Y. and Lu, Y., 2021. Ultrasonic assisted electrochemical degradation of malachite green in wastewater. *Microchemical Journal*, 164, p.106059.

Ren, Y., Tan, Y., Cheng, Z., Liu, Y., Liu, S., Shen, Z. and Fan, M., 2022. QSAR model and mechanism research on color removal efficiency of dyeing wastewater by FeCl₃ coagulation. *Ecotoxicology and Environmental Safety*, 240, p.113693.

Rezaei, A., Rezaei, M.R. and Sayadi, M.H., 2021. Enhanced 3,5-dimethylphenol photodegradation via adsorption-photocatalysis synergy using FSTRG nanohybrid catalyst. *Journal of Molecular Liquids*, 335, p.116546.

Rezaei, M. and Nezamzadeh-Ejhiha, A., 2020. The ZnO-NiO nano-composite: A brief characterization, kinetic and thermodynamic study and study the Arrhenius model on the sulfasalazine photodegradation. *International Journal of Hydrogen Energy*, 45(46), pp.24749–24764.

Roguai, S. and Djelloul, A., 2021. Structural, microstructural and photocatalytic degradation of methylene blue of zinc oxide and Fe-doped ZnO nanoparticles prepared by simple coprecipitation method. *Solid State Communications*, 334–335, p.114362.

Rohith, N.M., Kathirvel, P., Saravanakumar, S. and Lakshmi, M., 2018. Influence of Ag doping on the structural, optical, morphological and conductivity characteristics of ZnO nanorods. *Optik*, 172, pp.940–952.

Roopan, S.M., Mathew, R.S., Mahesh, S.S., Aggarwal, K., Bhatia, N., Titus, D., Samuel, J.J., Damodharan, K.I. and Elumalai, K., 2019. Environmental friendly synthesis of zinc oxide nanoparticles and estimation of its larvicidal activity against *Aedes aegypti*. *International Journal of Environmental Science and Technology*, 16(12), pp.8053–8060.

Rueda-Salaya, L., Hernández-Ramírez, A., Hinojosa-Reyes, L., Guzmán-Mar, J.L., Villanueva-Rodríguez, M. and Sánchez-Cervantes, E., 2020. Solar photocatalytic degradation of diclofenac aqueous solution using fluorine doped zinc oxide as catalyst. *Journal of Photochemistry and Photobiology A: Chemistry*, 391, p.112364.

Ruíz-Baltazar, Á. de J., 2021. Sonochemical activation-assisted biosynthesis of

Au/Fe₃O₄ nanoparticles and sonocatalytic degradation of methyl orange. *Ultrasonics Sonochemistry*, 73, p.105521.

Sabri, N.S., Yahya, A.K. and Talari, M.K., 2012. Emission properties of Mn doped ZnO nanoparticles prepared by mechanochemical processing. *Journal of Luminescence*, 132(7), pp.1735–1739.

Sadeghi Rad, T., Ansarian, Z., Khataee, A., Vahid, B. and Doustkhah, E., 2021. N-doped graphitic carbon as a nanoporous MOF-derived nanoarchitecture for the efficient sonocatalytic degradation process. *Separation and Purification Technology*, 256, p.117811.

Sadeghi Rad, T., Khataee, A., Arefi-Oskoui, S., Sadeghi Rad, S., Orooji, Y., Gengec, E. and Kobya, M., 2022. Graphene-based ZnCr layered double hydroxide nanocomposites as bactericidal agents with high sonophotocatalytic performances for degradation of rifampicin. *Chemosphere*, 286, p.131740.

Safaei-Ghomi, J. and Ghasemzadeh, M.A., 2017. Zinc oxide nanoparticle promoted highly efficient one pot three-component synthesis of 2,3-disubstituted benzofurans. *Arabian Journal of Chemistry*, 10, pp.S1774–S1780.

Safardoust-Hojaghan, H., Salavati-Niasari, M., Amiri, O., Rashki, S. and Ashrafi, M., 2021. Green synthesis, characterization and antimicrobial activity of carbon quantum dots-decorated ZnO nanoparticles. *Ceramics International*, 47(4), pp.5187–5197.

Saghir, S. and Xiao, Z., 2021. Hierarchical mesoporous ZIF-67@LDH for efficient adsorption of aqueous Methyl Orange and Alizarine Red S. *Powder Technology*, 377, pp.453–463.

Sahoo, K., Biswas, A. and Nayak, J., 2017. Effect of synthesis temperature on the UV sensing properties of ZnO-cellulose nanocomposite powder. *Sensors and Actuators A: Physical*, 267, pp.99–105.

Salama, D.M., Osman, S.A., Abd El-Aziz, M.E., Abd Elwahed, M.S.A. and Shaaban, E.A., 2019. Effect of zinc oxide nanoparticles on the growth, genomic DNA, production and the quality of common dry bean (*Phaseolus vulgaris*). *Biocatalysis and Agricultural Biotechnology*, 18, p.101083.

Saleh, R. and Taufik, A., 2019. Degradation of methylene blue and congo-red dyes using Fenton, photo-Fenton, sono-Fenton, and sonophoto-Fenton methods in the presence of iron(II,III) oxide/zinc oxide/graphene (Fe₃O₄/ZnO/graphene) composites. *Separation and Purification Technology*, 210, pp.563–573.

Salleh, A., Naomi, R., Utami, N.D., Mohammad, A.W., Mahmoudi, E., Mustafa, N. and Fauzi, M.B., 2020. *The Potential of Silver Nanoparticles for Antiviral and Antibacterial Applications: A Mechanism of Action*. *Nanomaterials*, .

Samuel, M.S., Shang, M. and Niu, J., 2022. Photocatalytic degradation of perfluoroalkyl substances in water by using a duo-functional tri-metallic-oxide hybrid catalyst. *Chemosphere*, 293, p.133568.

Sana, S.S., Vadde, R., Kumar, R., Arla, S.K., Somala, A.R., Krishna Rao, K.S. V, Zhijun, Z., Boya, V.K.N., Mondal, K. and Mamidi, N., 2023. Eco-friendly and facile production of antibacterial zinc oxide nanoparticles from *Grewia flavescens* (*G. flavescens*) leaf extract for biomedical applications. *Journal of Drug Delivery Science and Technology*, 80, p.104186.

Sanaeimehr, Z., Javadi, I. and Namvar, F., 2018. Antiangiogenic and antiapoptotic effects of green-synthesized zinc oxide nanoparticles using *Sargassum muticum* algae extraction. *Cancer Nanotechnology*, 9.

Sankar Sana, S., Haldhar, R., Parameswaranpillai, J., Chavali, M. and Kim, S.-C., 2022. Silver nanoparticles-based composite for dye removal: A comprehensive review. *Cleaner Materials*, 6, p.100161.

dos Santos, O.A.L., de Araujo, I., Dias da Silva, F., Sales, M.N., Christoffolete, M.A. and Backx, B.P., 2021. Surface modification of textiles by green nanotechnology against pathogenic microorganisms. *Current Research in Green and Sustainable Chemistry*, 4, p.100206.

Saravanan, A., Karishma, S., Kumar, P.S., Varjani, S., Yaashikaa, P.R., Jeevanantham, S., Ramamurthy, R. and Reshma, B., 2021a. Simultaneous removal of Cu(II) and reactive green 6 dye from wastewater using immobilized mixed fungal biomass and its recovery. *Chemosphere*, 271, p.129519.

Saravanan, M., Gopinath, V., Chaurasia, M.K., Syed, A., Ameen, F. and Purushothaman, N., 2018. Green synthesis of anisotropic zinc oxide nanoparticles with antibacterial and cytofriendly properties. *Microbial Pathogenesis*, 115, pp.57–63.

Saravanan, P., Kumaran, S., Bharathi, S., Sivakumar, P., Sivakumar, P., Pugazhvendan, S.R., Aruni, W. and Renganathan, S., 2021b. Bioremediation of synthetic textile dyes using live yeast *Pichia pastoris*. *Environmental Technology & Innovation*, 22, p.101442.

Sarikhani, M., Deylam, M., Alizadeh, E., Hejazy, M., Alizadeh-Salteh, S., Moeini, H. and Firouzmandi, M., 2021. Anti-aging effects of peppermint (*Mentha piperita* L.) and Shirazi thyme (*Zataria multiflora* Boiss.) plant extracts. *Food Bioscience*, 41, p.100930.

Sarojini, G., Venkatesh Babu, S., Rajamohan, N. and Rajasimman, M., 2022. Performance evaluation of polymer-marine biomass based bionanocomposite for the adsorptive removal of malachite green from synthetic wastewater. *Environmental Research*, 204, p.112132.

Sathish, P., Dineshbabu, N., Ravichandran, K., Arun, T., Karuppasamy, P., SenthilPandian, M. and Ramasamy, P., 2021. Combustion synthesis, characterization and antibacterial properties of pristine ZnO and Ga doped ZnO nanoparticles. *Ceramics International*, 47(19), pp.27934–27941.

Saxena, P., Ruparelia, J. and Saxena, P., 2022. Comparative study of 4-dimensional DSA on electrochemical treatability of a reactive dye. *Materials*

Today: Proceedings, 57, pp.2457–2464.

Selvinsimpson, S., Gnanamozi, P., Pandiyan, V., Govindasamy, M., Habila, M.A., AlMasoud, N. and Chen, Y., 2021. Synergetic effect of Sn doped ZnO nanoparticles synthesized via ultrasonication technique and its photocatalytic and antibacterial activity. *Environmental Research*, 197, p.111115.

Seong, S., Park, I.-S., Jung, Y.C., Lee, T., Kim, S.Y., Park, J.S., Ko, J.-H. and Ahn, J., 2019. Synthesis of Ag-ZnO core-shell nanoparticles with enhanced photocatalytic activity through atomic layer deposition. *Materials & Design*, 177, p.107831.

Seshadri, V.D., 2021. Zinc oxide nanoparticles from *Cassia auriculata* flowers showed the potent antimicrobial and in vitro anticancer activity against the osteosarcoma MG-63 cells. *Saudi Journal of Biological Sciences*, 28(7), pp.4046–4054.

Shaaban, M. and El-Mahdy, A.M., 2018. Biosynthesis of Ag, Se, and ZnO nanoparticles with antimicrobial activities against resistant pathogens using waste isolate *Streptomyces enissocaesilis*. *IET Nanobiotechnology*, 12(6), pp.741–747.

Shaheen, I., Ahmad, K.S., Jaffri, S.B. and Ali, D., 2020. Biomimetic [MoO₃@ZnO] semiconducting nanocomposites: Chemo-proportional fabrication, characterization and energy storage potential exploration. *Renewable Energy*.

Shaik, A.M., David Raju, M. and Rama Sekhara Reddy, D., 2020. Green synthesis of zinc oxide nanoparticles using aqueous root extract of *Sphagneticola trilobata* Lin and investigate its role in toxic metal removal, sowing germination and fostering of plant growth. *Inorganic and Nano-Metal Chemistry*, 50(7), pp.569–579.

Shamsipur, M., Pourmortazavi, S.M., Hajimirsadeghi, S.S., Zahedi, M.M. and Rahimi-Nasrabadi, M., 2013. Facile synthesis of zinc carbonate and zinc oxide nanoparticles via direct carbonation and thermal decomposition. *Ceramics International*, 39(1), pp.819–827.

Shankar, S., Wang, L.-F. and Rhim, J.-W., 2018. Incorporation of zinc oxide nanoparticles improved the mechanical, water vapor barrier, UV-light barrier, and antibacterial properties of PLA-based nanocomposite films. *Materials Science and Engineering: C*, 93, pp.289–298.

Shantkriti, S., Pradeep, M., Unish, K., Viji Das, M., Nidhin, S., Gugan, K. and Murugan, A., 2023. Bioynthesis of silver nanoparticles using *Dunaliella salina* and its antibacterial applications. *Applied Surface Science Advances*, 13, p.100377.

Sharma, R., Raghav, S., Dhillon, A. and Kumar, D., 2022. Mechanistic insights into the antimicrobial action and detoxification of mercury by humic acid-incorporated silica and zinc nanoparticles. *Environmental Nanotechnology*,

Monitoring & Management, 17, p.100631.

Shen, X., Liu, Z., Li, J., Wu, D., Zhu, M., Yan, L., Mao, G., Ye, X., Linhardt, R.J. and Chen, S., 2019. Development of low molecular weight heparin by H₂O₂/ascorbic acid with ultrasonic power and its anti-metastasis property. *International Journal of Biological Macromolecules*, 133, pp.101–109.

Shivnanajaiah, H.N., Sailaja Kumari, K. and Geetha, M.S., 2020. Green mediated synthesis of lanthanum doped zinc oxide: Study of its structural, optical and latent fingerprint application. *Journal of Rare Earths*, 38(12), pp.1281–1287.

Shojaeiarani, J., Bajwa, D. and Holt, G., 2020. Sonication amplitude and processing time influence the cellulose nanocrystals morphology and dispersion. *Nanocomposites*, 6, pp.1–6.

Shreema, K., Mathammal, R., Kalaiselvi, V., Vijayakumar, S., Selvakumar, K. and Senthil, K., 2021. Green synthesis of silver doped zinc oxide nanoparticles using fresh leaf extract *Morinda citrifolia* and its antioxidant potential. *Materials Today: Proceedings*.

Shubha, P., Gowda, M.L., Namratha, K., Manjunatha, H.B. and Byrappa, K., 2019. In vitro and In vivo evaluation of green-hydrothermal synthesized ZnO nanoparticles. *Journal of Drug Delivery Science and Technology*, 49(December 2018), pp.692–699.

Siadatnasab, F., Farhadi, S., Dusek, M., Eigner, V., Hoseini, A.-A. and Khataee, A., 2020. Sonochemical synthesis and structural characterization of an organic-inorganic nanohybrid based on a copper-dithiocarbamate complex and PMo12O40³⁻ polyanion as a novel sonocatalyst. *Ultrasonics Sonochemistry*, 64, p.104727.

Siddique, M., Fayaz, N. and Saeed, M., 2021. Synthesis, characterization, photocatalytic activity and gas sensing properties of zinc doped manganese oxide nanoparticles. *Physica B: Condensed Matter*, 602, p.412504.

Sidik, D.A.B., Hairom, N.H.H., Ahmad, M.K., Madon, R.H. and Mohammad, A.W., 2020. Performance of membrane photocatalytic reactor incorporated with ZnO-Cymbopogon citratus in treating palm oil mill secondary effluent. *Process Safety and Environmental Protection*, 143, pp.273–284.

da Silva, A.F.V., Fagundes, A.P., Macuvele, D.L.P., de Carvalho, E.F.U., Durazzo, M., Padoin, N., Soares, C. and Riella, H.G., 2019. Green synthesis of zirconia nanoparticles based on *Euclea natalensis* plant extract: Optimization of reaction conditions and evaluation of adsorptive properties. *Colloids and Surfaces A: Physicochemical and Engineering Aspects*, 583, p.123915.

Singh, J., Kumar, S., Alok, A., Upadhyay, S.K., Rawat, M., Tsang, D.C.W., Bolan, N. and Kim, K.-H., 2019a. The potential of green synthesized zinc oxide nanoparticles as nutrient source for plant growth. *Journal of Cleaner Production*, 214, pp.1061–1070.

Singh, J., Rathi, A., Rawat, M., Kumar, V. and Kim, K.-H., 2019b. The effect of manganese doping on structural, optical, and photocatalytic activity of zinc oxide nanoparticles. *Composites Part B: Engineering*, 166, pp.361–370.

Singh, R., King, A. and Nayak, B.B., 2019. Reddish emission of europium doped zinc oxide nanophosphor prepared through precipitation route using sodium borohydride. *Journal of Alloys and Compounds*, 792, pp.1191–1199.

Singh, T.A., Das, J. and Sil, P.C., 2020. Zinc oxide nanoparticles: A comprehensive review on its synthesis, anticancer and drug delivery applications as well as health risks. *Advances in Colloid and Interface Science*, 286, p.102317.

Siti Azima, A.M., Noriham, A. and Manshoor, N., 2017. Phenolics, antioxidants and color properties of aqueous pigmented plant extracts: *Ardisia colorata* var. *elliptica*, *Clitoria ternatea*, *Garcinia mangostana* and *Syzygium cumini*. *Journal of Functional Foods*, 38(Part A), pp.232–241.

Siva, N., Sakthi, D., Ragupathy, S., Arun, V. and Kannadasan, N., 2020. Synthesis, structural, optical and photocatalytic behavior of Sn doped ZnO nanoparticles. *Materials Science and Engineering: B*, 253, p.114497.

Sofianos, V.M., Lee, J., Silvester, D.S., Samanta, P.K., Paskevicius, M., English, N.J. and Buckley, C.E., 2021. Diverse morphologies of zinc oxide nanoparticles and their electrocatalytic performance in hydrogen production. *Journal of Energy Chemistry*, 56, pp.162–170.

Soren, S., Kumar, S., Mishra, S., Jena, P.K., Verma, S.K. and Parhi, P., 2018. Evaluation of antibacterial and antioxidant potential of the zinc oxide nanoparticles synthesized by aqueous and polyol method. *Microbial Pathogenesis*, 119, pp.145–151.

Spooren, J., Binnemans, K., Björkmalm, J., Breemers, K., Dams, Y., Folens, K., González-Moya, M., Horckmans, L., Komnitsas, K., Kurylak, W., Lopez, M., Mäkinen, J., Onisei, S., Oorts, K., Peys, A., Pietek, G., Pontikes, Y., Snellings, R., Tripiana, M., Varia, J., Willquist, K., Yurramendi, L. and Kinnunen, P., 2020. Near-zero-waste processing of low-grade, complex primary ores and secondary raw materials in Europe: technology development trends. *Resources, Conservation and Recycling*, 160, p.104919.

Sravandas, P. and Alexander, L.K., 2021. Facile hydrothermal synthesis and sonophotocatalytic performance of novel Bi₂WO₆ structure on the degradation of rhodamine B. *Materials Today: Proceedings*, 46, pp.2925–2929.

Srimathi, K., Hussain, T., Panigrahi, P., Subramaniam, N.G. and Ahuja, R., 2020. Influence of Sodium Iodide doped polypyrrole on green synthesized aluminum doped ZnO for the enhanced charge separation at the interface. *Optical Materials*, 99, p.109568.

Srinivasan, S. and Sadasivam, S.K., 2021. Biodegradation of textile azo dyes by textile effluent non-adapted and adapted *Aeromonas hydrophila*. *Environmental*

Research, 194, p.110643.

Stanley, R., Jebasingh, J.A., Manisha Vidyavathy, S., Stanley, P.K., Ponmani, P., Shekinah, M.E. and Vasanthi, J., 2021. Excellent Photocatalytic degradation of Methylene Blue, Rhodamine B and Methyl Orange dyes by Ag-ZnO nanocomposite under natural sunlight irradiation. *Optik*, 231, p.166518.

Su, X., Jonnalagadda, U.S., Bharatula, L.D. and Kwan, J.J., 2021. Unsupported gold nanocones as sonocatalytic agents with enhanced catalytic properties. *Ultrasonics Sonochemistry*, 79, p.105753.

Subbiah, R., Muthukumar, S. and Raja, V., 2020. Biosynthesis, structural, photoluminescence and photocatalytic performance of Mn/Mg dual doped ZnO nanostructures using *Ocimum tenuiflorum* leaf extract. *Optik*, 208, p.164556.

Sudhakaran, S., Athira, S., Suresh Babu, S., Varma, H. and Mohanan, P., 2020. Determination of the bioavailability of zinc oxide nanoparticles using ICP-AES and associated toxicity. *Colloids and Surfaces B: Biointerfaces*, 188, p.110767.

Sühnhholz, S., Kopinke, F.-D. and Mackenzie, K., 2020. Reagent or catalyst? – FeS as activator for persulfate in water. *Chemical Engineering Journal*, 387, p.123804.

Sultana, H., Usman, M. and Farooqi, Z.H., 2021. Micellar flocculation for the treatment of synthetic dyestuff effluent: Kinetic, thermodynamic and mechanistic insights. *Journal of Molecular Liquids*, 344, p.117964.

Sultana, K.A., Islam, M.T., Silva, J.A., Turley, R.S., Hernandez-Viezcas, J.A., Gardea-Torresdey, J.L. and Noveron, J.C., 2020. Sustainable synthesis of zinc oxide nanoparticles for photocatalytic degradation of organic pollutant and generation of hydroxyl radical. *Journal of Molecular Liquids*, 307, p.112931.

Sun, H., Yu, B., Pan, X. and Liu, Z., 2022a. MOF Nanosheets-decorated electrospun nanofiber membrane with Ultra-high adsorption capacity for dye removal from aqueous solutions. *Journal of Molecular Liquids*, 367, p.120367.

Sun, Y., Li, X., Zong, Y., Lan, Y., Li, Z., Feng, J., Fan, H., Zhang, Z. and Zheng, X., 2017. Thermal decomposition synthesis of single-crystalline porous ZnO nanoplates self-assembled by tiny nanocrystals and their pore-dependent magnetic properties. *Ceramics International*, 43(8), pp.6029–6038.

Sun, Y., Yu, Y., Zhou, S., Shah, K.J., Sun, W., Zhai, J. and Zheng, H., 2022b. Functionalized chitosan-magnetic flocculants for heavy metal and dye removal modeled by an artificial neural network. *Separation and Purification Technology*, 282, p.120002.

Sutar, S.S., Patil, P.J., Tamboli, A.S., Patil, D.N., Apine, O.A. and Jadhav, J.P., 2019. Biodegradation and detoxification of malachite green by a newly isolated bioluminescent bacterium *Photobacterium leiognathi* strain MS under RSM optimized culture conditions. *Biocatalysis and Agricultural Biotechnology*, 20, p.101183.

Swamy, N.K., Mohana, K.N.S. and Yashas, S.R., 2022. GNR@CeO₂ heterojunction as a novel sonophotocatalyst: Degradation of tetracycline hydrochloride, kinetic modeling and synergistic effects. *Colloids and Surfaces A: Physicochemical and Engineering Aspects*, 639, p.128324.

Tabrizi Hafez Moghaddas, S.M., Elahi, B., Darroudi, M. and Javanbakht, V., 2019. Green synthesis of hexagonal-shaped zinc oxide nanosheets using mucilage from flaxseed for removal of methylene blue from aqueous solution. *Journal of Molecular Liquids*, 296, p.111834.

Tabrizi Hafez Moghaddas, S.M., Javanbakht, V. and Elahi, B., 2020. Biosynthesis of pure zinc oxide nanoparticles using Quince seed mucilage for photocatalytic dye degradation. *Journal of Alloys and Compounds*, 821, p.153519.

Tadjarodi, A., Imani, M., Izadi, M. and Shokrayian, J., 2015. Solvent free synthesis of ZnO nanostructures and evaluation of their capability for water treatment. *Materials Research Bulletin*, 70, pp.468–477.

Talukdar, K., Saravanakumar, K., Kim, Y., Fayyaz, A., Kim, G., Yoon, Y. and Park, C.M., 2021. Rational construction of CeO₂-ZrO₂@MoS₂ hybrid nanoflowers for enhanced sonophotocatalytic degradation of naproxen: Mechanisms and degradation pathways. *Composites Part B: Engineering*, 215, p.108780.

Tan Sian Hui Abdullah, H.S., Aqlili Riana Mohd Asseri, S.N., Khursyiah Wan Mohamad, W.N., Kan, S.-Y., Azmi, A.A., Yong Julius, F.S. and Chia, P.W., 2021. Green synthesis, characterization and applications of silver nanoparticle mediated by the aqueous extract of red onion peel. *Environmental Pollution*, 271, p.116295.

Tang, S.H. and Zaini, M.A.A., 2021. Microporous activated carbon prepared from yarn processing sludge via composite chemical activation for excellent adsorptive removal of malachite green. *Surfaces and Interfaces*, 22, p.100832.

Tanveer, R., Yasar, A., Nizami, A.-S. and Tabinda, A.B., 2022. Integration of physical and advanced oxidation processes for treatment and reuse of textile dye-bath effluents with minimum area footprint. *Journal of Cleaner Production*, p.135366.

Taran, M., Rad, M. and Alavi, M., 2018. Biosynthesis of TiO₂ and ZnO nanoparticles by *Halomonas elongata* IBRC-M 10214 in different conditions of medium. *BioImpacts*, 8(2), pp.81–89.

Tarwal, N.L., Patil, V.L., Rani, J.R., Gurav, K. V, Shaikh, J.S., Khandekar, M.S., Harale, N.S., Patil, P.S. and Jang, J.H., 2021. Plasmonic DSSC performance of spray deposited Ag-ZnO and Au-ZnO films. *Chinese Journal of Physics*, 73, pp.581–588.

Tavakoli, S., Kharaziha, M. and Nemati, S., 2021. Polydopamine coated ZnO rod-shaped nanoparticles with noticeable biocompatibility, hemostatic and

antibacterial activity. *Nano-Structures & Nano-Objects*, 25, p.100639.

Thambidurai, S., Gowthaman, P., Venkatachalam, M. and Suresh, S., 2020. Natural sunlight assisted photocatalytic degradation of methylene blue by spherical zinc oxide nanoparticles prepared by facile chemical co-precipitation method. *Optik*, 207, p.163865.

Thangamani, N. and Bhuvaneshwari, N., 2019. Green synthesis of gold nanoparticles using *Simarouba glauca* leaf extract and their biological activity of micro-organism. *Chemical Physics Letters*, 732, p.136587.

Thanh Tu, N.T., Thien, T.V., Du, P.D., Thanh Chau, V.T., Mau, T.X. and Khieu, D.Q., 2018. Adsorptive removal of Congo red from aqueous solution using zeolitic imidazolate framework-67. *Journal of Environmental Chemical Engineering*, 6(2), pp.2269–2280.

Thomas, B., Mary Vithiya, B.S. and Augustine Arul Prasad, T., 2019. Antioxidant and Photo Catalytic Activity Of Aqueous Leaf Extract Mediated Green Synthesis Of Silver Nanoparticles Using *Passiflora Edulis F.Flavicarpa*. *Materials Today: Proceedings*, 14(Part 2), pp.239–247.

Tiwari, H., Sonwani, R.K. and Singh, R.S., 2022. A comprehensive evaluation of the integrated photocatalytic-fixed bed bioreactor system for the treatment of Acid Blue 113 dye. *Bioresource Technology*, 364, p.128037.

Torres-Gómez, N., Nava, O., Argueta-Figueroa, L., García-Contreras, R., Baeza-Barrera, A. and Vilchis-Nestor, A.R., 2019. Shape Tuning of Magnetite Nanoparticles Obtained by Hydrothermal Synthesis: Effect of Temperature. *Journal of Nanomaterials*, pp.1–15.

Tóthová, E., Senna, M., Yermakov, A., Kováč, J., Dutková, E., Hegedüs, M., Kaňuchová, M., Baláž, M., Bujňáková, Z.L., Briančin, J. and Makreski, P., 2019. Zn source-dependent magnetic properties of undoped ZnO nanoparticles from mechanochemically derived hydrozincite. *Journal of Alloys and Compounds*, 787, pp.1249–1259.

Tripathi, R.M., Bhadwal, A.S., Gupta, R.K., Singh, P., Shrivastav, A. and Shrivastav, B.R., 2014. ZnO nanoflowers: Novel biogenic synthesis and enhanced photocatalytic activity. *Journal of Photochemistry and Photobiology B: Biology*, 141, pp.288–295.

Truong, T.K., Nguyen, T.Q., Phuong La, H.P., Le, H.V., Van Man, T., Cao, T.M. and Van Pham, V., 2021. Insight into the degradation of p-nitrophenol by visible-light-induced activation of peroxymonosulfate over Ag/ZnO heterojunction. *Chemosphere*, 268, p.129291.

Van Tuan, P., Phuong, T.T., Tan, V.T., Nguyen, S.X. and Khiem, T.N., 2020. In-situ hydrothermal fabrication and photocatalytic behavior of ZnO/reduced graphene oxide nanocomposites with varying graphene oxide concentrations. *Materials Science in Semiconductor Processing*, 115, p.105114.

Ullah, M., Chunlei, W., Su, W.-B., Manan, A., Ahmad, A.S. and Rehman, A.U., 2019. Thermoelectric properties of indium-doped zinc oxide sintered in an argon atmosphere. *Journal of Materials Science: Materials in Electronics*, 30(5), pp.4813–4818.

Umamaheswari, A., Prabu, S.L., John, S.A. and Puratchikody, A., 2021. Green synthesis of zinc oxide nanoparticles using leaf extracts of *Raphanus sativus* var. *Longipinnatus* and evaluation of their anticancer property in A549 cell lines. *Biotechnology Reports*, 29, p.e00595.

Umaralikhan, L. and Jaffar, M., 2017. Green synthesis of ZnO and Mg doped ZnO nanoparticles, and its optical properties. *Journal of Materials Science: Materials in Electronics*, 28(11), pp.7677–7685.

United Nations, 2022. *The Sustainable Development Goals Report 2022*. [online].

Uribe-López, M.C., Hidalgo-López, M.C., López-González, R., Frías-Márquez, D.M., Núñez-Nogueira, G., Hernández-Castillo, D. and Alvarez-Lemus, M.A., 2021. Photocatalytic activity of ZnO nanoparticles and the role of the synthesis method on their physical and chemical properties. *Journal of Photochemistry and Photobiology A: Chemistry*, 404, p.112866.

Vaiano, V., Matarangolo, M., Murcia, J.J., Rojas, H., Navío, J.A. and Hidalgo, M.C., 2018. Enhanced photocatalytic removal of phenol from aqueous solutions using ZnO modified with Ag. *Applied Catalysis B: Environmental*, 225, pp.197–206.

Valian, M., Khoobi, A. and Salavati-Niasari, M., 2020. Green synthesis and characterization of DyMnO₃-ZnO ceramic nanocomposites for the electrochemical ultratrace detection of atenolol. *Materials Science and Engineering: C*, 111, p.110854.

Vallero, D.A., 2019. Chapter 13 - Wastewater. In: T.M. Letcher and D.A.B.T.-W. (Second E. Vallero, eds. Academic Press.pp.259–290.

Vasantharaj, S., Sathiyavimal, S., Senthilkumar, P., Kalpana, V.N., Rajalakshmi, G., Alsehli, M., Elfasakhany, A. and Pugazhendhi, A., 2021. Enhanced photocatalytic degradation of water pollutants using bio-green synthesis of zinc oxide nanoparticles (ZnO NPs). *Journal of Environmental Chemical Engineering*, 9(4), p.105772.

Velsankar, K., Suganya, S., Muthumari, P., Mohandoss, S. and Sudhahar, S., 2021. Ecofriendly green synthesis, characterization and biomedical applications of CuO nanoparticles synthesized using leaf extract of *Capsicum frutescens*. *Journal of Environmental Chemical Engineering*, 9(5), p.106299.

Vergara-Llanos, D., Koning, T., Pavicic, M.F., Bello-Toledo, H., Díaz-Gómez, A., Jaramillo, A., Melendrez-Castro, M., Ehrenfeld, P. and Sánchez-Sanhueza, G., 2021. Antibacterial and cytotoxic evaluation of copper and zinc oxide nanoparticles as a potential disinfectant material of connections in implant

provisional abutments: An in-vitro study. *Archives of Oral Biology*, 122, p.105031.

Vidya Lekshmi, K.P., Yesodharan, S. and Yesodharan, E.P., 2018. MnO₂ efficiently removes indigo carmine dyes from polluted water. *Heliyon*, 4(11), p.e00897.

Vijayakumar, S., Saravanakumar, K., Malaikozhundan, B., Divya, M., Vaseeharan, B., Durán-Lara, E.F. and Wang, M.-H., 2020. Biopolymer K-carrageenan wrapped ZnO nanoparticles as drug delivery vehicles for anti MRSA therapy. *International Journal of Biological Macromolecules*, 144, pp.9–18.

Vinayagam, R., Selvaraj, R., Arivalagan, P. and Varadavenkatesan, T., 2020. Synthesis, characterization and photocatalytic dye degradation capability of Calliandra haematocephala-mediated zinc oxide nanoflowers. *Journal of Photochemistry & Photobiology, B: Biology*, 203, p.111760.

Vinoditha, U., Sarojini, B.K., Sandeep, K.M., Narayana, B. and Balakrishna, K.M., 2020. Phase segregation induced third order nonlinear saturable absorption behavior in Erbium doped ZnO nanoparticles synthesized by facile hydrothermal method. *Physica E: Low-dimensional Systems and Nanostructures*, 124, p.114281.

Vorobyova, V., Vasyliiev, G., Uschapovskiy, D., Lyudmyla, K. and Skiba, M., 2021. Green synthesis, characterization of silver nanoparticals for biomedical application and environmental remediation. *Journal of Microbiological Methods*, p.106384.

Vyas, N., Manmi, K., Wang, Q., Jadhav, A.J., Barigou, M., Sammons, R.L., Kuehne, S.A. and Walmsley, A.D., 2019. Which Parameters Affect Biofilm Removal with Acoustic Cavitation? A Review. *Ultrasound in Medicine & Biology*, 45(5), pp.1044–1055.

Wang, C.-C., Shieu, F.-S. and Shih, H.C., 2021. Ag-nanoparticle enhanced photodegradation of ZnO nanostructures: Investigation using photoluminescence and ESR studies. *Journal of Environmental Chemical Engineering*, 9(1), p.104707.

Wang, G., Ma, X., Liu, J., Qin, L., Li, B., Hu, Y. and Cheng, H., 2020a. Design and performance of a novel direct Z-scheme NiGa₂O₄/CeO₂ nanocomposite with enhanced sonocatalytic activity. *Science of The Total Environment*, 741, p.140192.

Wang, J., Jiang, Z., Zhang, Z., Xie, Y., Wang, X., Xing, Z., Xu, R. and Zhang, X., 2008. Sonocatalytic degradation of acid red B and rhodamine B catalyzed by nano-sized ZnO powder under ultrasonic irradiation. *Ultrasonics Sonochemistry*, 15(5), pp.768–774.

Wang, S., Chen, M., Shen, S., Cheng, C., Cai, A., Song, A., Lu, X., Gao, G., Ma, M., Zhang, Z. and Xu, X., 2022. Bifunctionalized Fe₇S₈@MoS₂-O core-shell

with efficient photocatalytic activity based on internal electric field. *Journal of Cleaner Production*, 335, p.130375.

Wang, X., Yu, S., Li, Z.-H., He, L.-L., Liu, Q.-L., Hu, M.-Y., Xu, L., Wang, X.-F. and Xiang, Z., 2021. Fabrication Z-scheme heterojunction of Ag₂O/ZnWO₄ with enhanced sonocatalytic performances for meloxicam decomposition: Increasing adsorption and generation of reactive species. *Chemical Engineering Journal*, 405, p.126922.

Wang, Y., Bi, N., Zhang, H., Tian, W., Zhang, T., Wu, P. and Jiang, W., 2020b. Visible-light-driven photocatalysis-assisted adsorption of azo dyes using Ag₂O. *Colloids and Surfaces A: Physicochemical and Engineering Aspects*, 585, p.124105.

Wang, Y., Yu, M., Huang, C., Zheng, Q., Zhou, H., Zhang, Z. and Zhao, S., 2020c. Infrared emission characteristic and microwave loss property of aluminum doped zinc oxide nanoparticles. *Ceramics International*, 47(2), pp.2456–2462.

World Health Organization, 2019. *Drinking-water*. [online].

Wu, X., Lin, Q., Belwal, T., Huang, H., Zou, L., Lv, W. and Luo, Z., 2022. Effect of advanced/hybrid oxidation process involving ultrasonication and ultraviolet radiation (sonophotolysis) on anthocyanin stability: Degradation kinetics and mechanism. *Food Chemistry*, 370, p.131083.

Xia, X., Zhu, F., Li, J., Yang, H., Wei, L., Li, Q., Jiang, J., Zhang, G. and Zhao, Q., 2020. *A Review Study on Sulfate-Radical-Based Advanced Oxidation Processes for Domestic/Industrial Wastewater Treatment: Degradation, Efficiency, and Mechanism*. *Frontiers in Chemistry*, .

Xiao, C., Li, H., Zhao, Y., Zhang, X. and Wang, X., 2020. Green synthesis of iron nanoparticle by tea extract (polyphenols) and its selective removal of cationic dyes. *Journal of Environmental Management*, 275, p.111262.

Xiong, X., Liu, X., Yu, I.K.M., Wang, L., Zhou, J., Sun, X., Rinklebe, J., Shaheen, S.M., Ok, Y.S., Lin, Z. and Tsang, D.C.W., 2019. Potentially toxic elements in solid waste streams: Fate and management approaches. *Environmental Pollution*, 253, pp.680–707.

Xu, L., Wang, S.-H., Jin, Y., Liu, N.-P., Wu, X.-Q. and Wang, X., 2021. Preparation of Cobalt tungstate nanomaterials and study on sonocatalytic degradation of Safranin t. *Separation and Purification Technology*, 276, p.119405.

Xu, L., Wang, X., Xu, M.-L., Liu, B., Wang, X.-F., Wang, S.-H. and Sun, T., 2019. Preparation of Zinc Tungstate Nanomaterial and Its Sonocatalytic Degradation of Meloxicam as a Novel Sonocatalyst in Aqueous Solution. *Ultrasonics Sonochemistry*, 61, p.104815.

Xu, Q., Wang, Z., Yang, H., Xiang, Y., Nie, G. and Yue, W., 2022. Synthesis of

hierarchical Cu₂CdSnS₄ by microwave-assisted transformation from precursor for photodegradation to malachite green. *Journal of Alloys and Compounds*, 904, p.163966.

Xu, R., Su, M., Liu, Y., Chen, Z., Ji, C., Yang, M., Chang, X. and Chen, D., 2020. Comparative study on the removal of different-type organic pollutants on hierarchical tetragonal bismutite microspheres: Adsorption, degradation and mechanism. *Journal of Cleaner Production*, 242, p.118366.

Yadavalli, R., Peasari, J.R., Mamindla, P., Praveenkumar, Mounika, S. and Ganugapati, J., 2018. Phytochemical screening and in silico studies of flavonoids from *Chlorella pyrenoidosa*. *Informatics in Medicine Unlocked*, 10, pp.89–99.

Yang, F., Jiang, G., Chang, Q., Huang, P. and Lei, M., 2021. Fe/N-doped carbon magnetic nanocubes toward highly efficient selective decolorization of organic dyes under ultrasonic irradiation. *Chemosphere*, 283, p.131154.

Yang, H.M., Zhang, X.C., Tang, A.D. and Ao, W.Q., 2004. Formation of zinc oxide nanoparticles by mechanochemical reaction. *Materials Science & Technology*, 20(11), pp.1493–1495.

Yaseri Nasab, F. and Bahiraei, H., 2020. High photocatalytic activity of magnetically separable ZnO and Ag/ZnO supported on Mg-ferrite nanoparticles. *Journal of Photochemistry and Photobiology A: Chemistry*, 394, p.112489.

Yentür, G. and Dükkancı, M., 2021. Synergistic effect of sonication on photocatalytic oxidation of pharmaceutical drug carbamazepine. *Ultrasonics Sonochemistry*, 78, p.105749.

Yousefi, H.R., Hashemi, B., Mirzaei, A., Roshan, H. and Sheikhi, M.H., 2020. Effect of Ag on the ZnO nanoparticles properties as an ethanol vapor sensor. *Materials Science in Semiconductor Processing*, 117, p.105172.

Yu, Y., Wu, Y., Xie, C., Sun, X., Wang, Y., Liu, P., Wang, Y., Liu, C., Wan, Y., Pan, W. and Li, T., 2022. High-flux, antifouling and highly hydrophilic tight ultrafiltration membranes based on crosslinked PEEKWC/PEI containing positively charged water channel for dyes removal. *Chemical Engineering Research and Design*, 188, pp.1–14.

Yulizar, Y., Apriandanu, D.O.B. and Ashna, R.I., 2020. La₂CuO₄-decorated ZnO nanoparticles with improved photocatalytic activity for malachite green degradation. *Chemical Physics Letters*, 755, p.137749.

Yusefi-Tanha, E., Fallah, S., Rostamnejadi, A. and Pokhrel, L.R., 2020. Zinc oxide nanoparticles (ZnONPs) as a novel nanofertilizer: Influence on seed yield and antioxidant defense system in soil grown soybean (*Glycine max* cv. Kowsar). *Science of The Total Environment*, 738, p.140240.

Zare, M., Namratha, K., Thakur, M.S. and Byrappa, K., 2019. Biocompatibility assessment and photocatalytic activity of bio-hydrothermal synthesis of ZnO

nanoparticles by *Thymus vulgaris* leaf extract. *Materials Research Bulletin*, 109, pp.49–59.

Zargar Shoushtari, M., Poormoghadam, A. and Farbod, M., 2017. The size dependence of the magnetic properties of ZnO and Zn_{1-x}Ni_xO nanoparticles. *Materials Research Bulletin*, 88, pp.315–319.

Zhan, L., Li, O. and Xu, Z., 2020. Preparing nano-zinc oxide with high-added-value from waste zinc manganese battery by vacuum evaporation and oxygen-control oxidation. *Journal of Cleaner Production*, 251, p.119691.

Zhang, H., Lu, Y., Zhang, Q., Yang, F., Hui, A. and Wang, A., 2022a. Structural evolution of palygorskite-rich clay as the nanocarriers of silver nanoparticles for efficient improving antibacterial activity. *Colloids and Surfaces A: Physicochemical and Engineering Aspects*, 652, p.129885.

Zhang, H., Zhang, K., Gao, M., An, Z., Tang, C. and Yan, X., 2022b. Degradation efficiency of the azo dye acid orange 2 and microbial community characteristics in a rotating algal biofilm reactor. *Journal of Water Process Engineering*, 50, p.103233.

Zhang, Q. and Bai, W., 2011. Synthesis and growth mechanism of macroscopic ZnO nanocombs and nanobelts. *Vacuum*, 86(4), pp.398–402.

Zhang, Q., Cheng, T., Lin, Q. and Fang, C., 2021a. Facile preparation of robust dual MgO-loaded carbon foam as an efficient adsorbent for malachite green removal. *Environmental Research*, 195, p.110698.

Zhang, Q., Fang, W., Wang, M., Tian, T., Li, G. and Zhao, Y., 2022c. Titanium dioxide nanofibers modified with iron oxide for the heterogeneous Fenton reaction. *Ceramics International*, 48(17), pp.25183–25190.

Zhang, T., Jin, X., Owens, G. and Chen, Z., 2021b. Remediation of malachite green in wastewater by ZIF-8@Fe/Ni nanoparticles based on adsorption and reduction. *Journal of Colloid and Interface Science*, 594, pp.398–408.

Zhang, W., Li, J., Li, J., Guo, J., Wang, Y., Zu, P. and Li, P., 2022d. Structural, optical, dielectric, and magnetic properties of Sr_{0.7}La_{0.3}Zn_{0.3}Fe_{11.7-x}Al_xO₁₉ hexaferrite synthesized by the solid-state reaction method. *Journal of Solid State Chemistry*, 306, p.122766.

Zheng, J., Li, Y., Xu, D., Zhao, R., Liu, Y., Li, G., Gao, Q., Zhang, X., Volodine, A. and Van der Bruggen, B., 2022. Facile fabrication of a positively charged nanofiltration membrane for heavy metal and dye removal. *Separation and Purification Technology*, 282, p.120155.

Zhong, X., Zhang, K.-X., Wu, D., Ye, X.-Y., Huang, W. and Zhou, B.-X., 2020. Enhanced photocatalytic degradation of levofloxacin by Fe-doped BiOCl nanosheets under LED light irradiation. *Chemical Engineering Journal*, 383, p.123148.

Ziylan-Yavas, A., Ince, N.H., Ozon, E., Arslan, E., Aviyente, V., Savun-

Hekimoğlu, B. and Erdinçler, A., 2021. Oxidative decomposition and mineralization of caffeine by advanced oxidation processes: The effect of hybridization. *Ultrasonics Sonochemistry*, 76, p.105635.

Zubair, N.F., Jamil, S., Fatima, S., Khan, S.R., Khan, M.U. and Janjua, M.R.S.A., 2020. Synthesis of needle like nano composite of rGO-Mn₂O and their applications as photo-catalyst. *Chemical Physics Letters*, 757, p.137874.

Zulfiqar, M., Chowdhury, S., Omar, A.A., Siyal, A.A. and Sufian, S., 2020. Response surface methodology and artificial neural network for remediation of acid orange 7 using TiO₂-P25: optimization and modeling approach. *Environmental Science and Pollution Research*, 27(27), pp.34018–34036.

LIST OF PUBLICATIONS

1. **Chan, Y.Y.**, Pang, Y.L., Lim, S., Chong, W.C. and Shuit, S.H., 2022. Plant-mediated synthesis of silver-doped ZnO nanoparticles with high sonocatalytic activity: Sonocatalytic behavior, kinetic and thermodynamic study. *Environmental Science and Pollution Research*, Article in Press.
2. **Chan, Y.Y.**, Pang, Y.L., Lim, S., Lai, C.W., Abdullah, A.Z., 2022, Plant based-biosynthesized silver doped zinc oxide for effective sonocatalytic degradation of malachite green: characterizations and optimization studies, *Desalination and Water Treatment*, 245, 270-285.
3. **Chan, Y.Y.**, Pang, Y.L., Lim, S., Chong, W.C., 2021, Facile green synthesis of ZnO nanoparticles using natural-based materials: Properties, mechanism, surface modification and application, *Journal of Environmental Chemical Engineering*, 9(4), 105417.
4. **Chan, Y.Y.**, Pang, Y.L., Lim, S., Chong, W.C., 2021, Sonocatalytic degradation of Congo red by using green synthesized silver doped zinc oxide nanoparticle, *Materials Today Proceedings*, 46, 1948-1953.
5. **Chan, Y.Y.**, Pang, Y.L., Lim, S., Lai, C.W., Abdullah, A.Z., Chong, W.C., 2020, Biosynthesized Fe- and Ag-doped ZnO nanoparticles using aqueous extract of *Clitoria ternatea* Linn for enhancement of sonocatalytic degradation of Congo red, *Environmental Science and Pollution Research*, 27(28), 34675–34691.
6. **Chan, Y.Y.**, Pang, Y.L., Lim, S., 2019, Heat treatment effect of zinc oxide on the sonocatalytic degradation of organic dyes, *AIP Conference Proceedings* 2157, 020009.